University of Bath

UNIVERSITY OF BATH

PHD

Development of Catalyst Characterisation Techniques

Gopinathan, Navin

Award date:
2013

Awarding institution:
University of Bath

Link to publication

DEVELOPMENT OF CATALYST CHARACTERISATION TECHNIQUES

NAVIN GOPINATHAN

A thesis submitted for the degree of Doctor of Philosophy

University of Bath

Department of Chemical Engineering

July 2012

"Man needs his difficulties because they are necessary to enjoy success"

- Dr. A. P. J. Abdul Kalam

Eminent Scientist and Former President of India

ഈ ഗവേഷണ പ്രബന്ധം ഞാൻ എന്റെ അച്ഛനും അമ്മക്കും അനുജത്തിക്കും ഹൃദയപൂർവം സമർപ്പിക്കുന്നു.

I dedicate this thesis wholeheartedly to my father, mother and sister.

TABLE OF CONTENTS

LIST OF FIGURES

CHAPTER 1 – INTRODUCTION

CHAPTER 2 – MERCURY POROSIMETRY

CHAPTER 3 – GAS ADSORPTION POROSIMETRY

CHAPTER 4 – INTEGRATED ADSORPTION OF NITROGEN AND WATER – N_2-H_2O-N_2 PROTOCOL

CHAPTER 5 – CATALYST CHARACTERISATION BY NUCLEAR MAGNETIC RESONANCE

CHAPTER 6 – SUMMARY AND FUTURE WORK

APPENDIX A – SUPPORTING INFORMATION FOR MERCURY POROSIMETRY

APPENDIX B – SUPPORTING INFORMATION FOR GAS ADSORPTION POROSIMETRY

APPENDIX C – SUPPORTING INFORMATION FOR N$_2$-H$_2$O-N$_2$ ADSORPTION EXPERIMENTS

APPENDIX D – SUPPORTING INFORMATION FOR LLE EXPERIMENTS

LIST OF TABLES

CHAPTER 4 – INTEGRATED ADSORPTION OF NITROGEN AND WATER – N_2-H_2O-N_2 PROTOCOL

CHAPTER 5 – CATALYST CHARACTERISATION WITH NUCLEAR MAGNETIC RESONANCE

CHAPTER 6 – SUMMARY AND FUTURE WORK

APPENDIX A – SUPPORING INFORMATION FOR MERCURY POROSIMETRY

APPENDIX B – SUPPORTING INFORMATION FOR GAS ADSORPTION POROSIMETRY

ACKNOWLEDGMENTS

ABSTRACT

Standard catalyst characterisation techniques such as gas adsorption porosimetry and mercury porosimetry only account for some of the physical heterogeneity of the catalyst surface. They completely ignore the chemical heterogeneity present and in most cases consider pores present in the medium to be independent of each other. Thus, most results of characterisation (pore space descriptors such as BET surface area, BJH pore size distribution, mercury porosimetry surface area, etc.) are not accurate. This has been a major issue that remains to be resolved during the characterisation of fresh and coked catalysts. In this thesis, the use of a multi-component adsorption system is recommended as a step-change solution to this limitation. Two approaches are adopted. Firstly, integrated nitrogen-water-nitrogen gas adsorption experiments are performed on fresh and coked catalysts. This established the significance of pore coupling by showing the presence of advanced adsorption. The method also helped to determine the location of coke deposits within catalysts and indicated that water vapour adsorption was a good probe to understand the sites responsible for coking. Secondly, coadsorption of immiscible liquids – cyclohexane and water – was performed on fresh and coked catalysts following which the displacement of cyclohexane by water was studied using NMR relaxometry and diffusometry. This novel approach takes the wettability of the surface into consideration, unlike the former methods. It is therefore a method that accounts for the chemical heterogeneity of the surface. It also helped determine the location of coke within catalysts. The different approaches are presented in the context of combustion of heavy oil in bitumen reservoirs, and the use of supercritical conditions that help to dissolve coke precursors in the isomerisation of 1-hexene. Thus, the solutions provided in this thesis are directions in which catalyst characterisation, especially distinguishing fresh and coked catalysts, and other porous materials, must be carried out.

NOTATION

A	Surface Area, m^2g^{-1}
A	Constant, Eq. (2.3)
A_{BET}	BET surface area, m^2g^{-1}
B	Constant, Eq. (2.3)
B_0	Static magnetic field, T
B_1	r.f. pulse in the form of a strong magnetic field, T
b	Langmuir constant
C	BET constant
D	FHH fractal dimension
D	Average diameter, nm
D	Diffusion coefficient, m^2s^{-1}
D_b	Free or bulk diffusion coefficient, m^2s^{-1}
D_k	Knudsen diffusion coefficient, m^2s^{-1}
D_p	Diffusion coefficient of liquid within the pores, m^2s^{-1}
D_{PFG}	Diffusion coefficient measured by PFG NMR, m^2s^{-1}
d_p	Pore diameter, m
$\dfrac{dM_{xy}(t)}{dt}$	Rate of change of the magnetization in the xy plane, $Am^{-1}s^{-1}$
$\dfrac{dM_z(t)}{dt}$	Rate of change of the magnetization in the z-direction, $Am^{-1}s^{-1}$
$\dfrac{d\overline{q}}{dt}$	Rate of mass uptake during adsorption, mgs^{-1}, Eq. (4.1)
dV	Incremental volume, cm^3g^{-1}
E	Energy for a spin state, J
E_1	Energy of adsorption in the first layer, $Jmol^{-1}$
E_L	Heat of condensation of the liquid adsorbate, $Jmol^{-1}$
F	Percolation probability
f	Bond occupation probability
G_z	Gradient in the applied magnetic field along the z-direction, Tm^{-1}, Eq. (5.9)
g	Gradient strength, Gcm^{-1} or (Tm^{-1}, 1 Gauss (G) = 10^{-4} Tesla (T)), Eq. (5.10a)
h	Planck's constant, 6.62608×10^{-34} Js
I	Spin quantum number
I	Intensity in the presence of diffusion, a.u
I_0	Intensity in the absence of diffusion, a.u
k	Permeability of the displacing or displaced fluid, m^2
k	Adsorption mass transfer coefficient, s^{-1}
k_N	Normalised adsorption mass transfer coefficient
L	Lattice size
M	Macroscopic magnetization, Am^{-1}
M_z	z-component of the macroscopic magnetization, Am^{-1}
M_{xy}	xy-component of the macroscopic magnetization, Am^{-1}
M_0	Absence of macroscopic magnetisation
M	Mobility ratio
M	Molecular weight
m_I	Magnetic quantum number
N_A	Avogadro Number, 6.62608×10^{23}
Nc	Capillary Number
N_{Kn}	Knudsen Number
n	Number of adsorbed layers, Eq. (3.5c)
n	Number of molecules per unit volume, nN_A/V , Eq. (4.5)
n_m	Amount adsorbed to form a monolayer, $V_m/22414$, Eq. (3.3d), $molg^{-1}$
P	Pressure, Pa
P	Angular momentum, Js
p	Fraction of the pore space contributing to the Langmuir component, Eq. (3.6b)
p_a	Fraction of liquid having diffusion coefficient D_a, Eq. (5.14b)

Symbol	Definition
p_b	Fraction of liquid present in the bulk in a pore, Eq. (5.8a)
p_b	Fraction of liquid having diffusion coefficient D_b, Eq. (5.14b)
p_i	Fraction of the pore space contributing to uptake defined by model i, Eq. (3.6a)
p_i	Fraction of liquid having diffusion coefficient D_i, Eq. (5.14a)
p_s	Fraction of liquid present near the surface of a pore, Eq. (5.8a)
$\bar{q}$	Average adsorbate uptake in the adsorbent particle, mg, Eq. (4.1)
q^*	Equilibrium adsorbate uptake by the adsorbent, mg, Eq. (4.1)
R	Ideal gas constant, $8.31447 \ JK^{-1}mol^{-1}$
R	Change in echo intensity
$\Re$	Spherical cavity radius, m
R_p	Particle radius or diffusion path length, m
R, r, r_p	Pore radius, m
r_1, r_2	Radii of curvature, m
$\langle r^2 \rangle$	Mean square displacement, m^2
S	Slope, Eq. (3.5a)
s/v	Surface area to volume ratio of a pore, m^{-1}
T	Temperature, K
TPV_{fresh}	Total pore volume of the fresh catalyst, cm^3g^{-1}
$TPV_{after \ H_2O \ adsorption}$	Total pore volume of nitrogen after water adsorption, cm^3g^{-1}
TPV_{C1}	Total pore volume of nitrogen before water adsorption in material C1, cm^3g^{-1}
$TPV_{C1 \ after \ H_2O \ adsorption}$	Total pore volume of nitrogen after water adsorption in material C1, cm^3g^{-1}
T_1	Longitudinal or spin lattice relaxation time, s
T_2	Transverse or spin-spin relaxation time, s
$T_2 \ C_6H_{12}$	Transverse relaxation time of cyclohexane phase, s
$T_2 \ H_2O$	Transverse relaxation time of water phase, s
T_{2b}	Transverse relaxation time of the bulk liquid, s
T_{2s}	Transverse relaxation time of the liquid at the surface, s
t_1	Initial time at which field gradient is applied, s
t	Thickness of the adsorbed film, m
t_p	Length or width of the pulse, s
v	Velocity of displacing fluid, ms^{-1}
V	Amount adsorbed, Eq. (3.1), cm^3g^{-1}STP
V_M	Molar volume, cm^3mol^{-1}
V_c	Incremental pore volume, cm^3g^{-1}
V_i	Incremental pore volume, cm^3g^{-1}
V_m	Amount adsorbed to form a monolayer, Eq. (3.1), cm^3g^{-1}STP
$V_{0.95}$	Volume adsorbed at $P/P_0 = 0.95$, cm^3g^{-1}STP, Eq. (3.7)
W_E	Withdrawal efficiency
$\bar{v}^l$	Average molar volume of mercury over the pressure range, cm^3mol^{-1}, (Eq. 2.4)
$x = P/P_0$	Relative pressure
x	Crystal size, nm
y	Total amount adsorbed, Eq. (3.6a)
Z	Coordination number or pore connectivity
z	Position vector of the spins, Eq. (5.9)

Greek letters

Symbol	Definition
α	Pulse or flip angle, degrees
β	Critical exponent, 0.41, Eq. (3.9)
γ	Surface tension, Nm^{-1}
γ	Gyromagnetic or Magnetogyric ratio, $T^{-1}s^{-1}$
Δ	Diffusion time, s
δ	Difference parameter used to determine the operating regime in fractal FHH model, $3(1+S)-2$
δ	Duration of the applied gradient, s
ΔE	Energy difference between spin states in the presence of magnetic field B_0, J
ΔP	Pressure difference across the curved mercury interface, Pa

ε_{fresh}	Porosity of the fresh catalyst
θ	Mercury contact angle, degrees
θ_A	Advancing mercury contact angle, degrees
θ_R	Receding mercury contact angle, degrees
λ	Mobility of displacing or displaced fluid, $m^2(Pas)^{-1}$
λ	Thickness of the thin layer over which surface relaxation takes place, m
λ	Mean free path of the gas molecule at specific temperature and pressure, m, Eq. (4.5)
μ	Viscosity of displacing or displaced liquid, Pas
μ^*	Change in chemical potential of mercury corresponding to change of its structure under the presence of a force field, $Jmol^{-1}$
μ	Magnetic moment, JT^{-1}
v	Critical exponent, 0.88, Eq. (3.9)
v	Frequency, Hz
v_0	Larmor frequency, Hz
π	Pi constant, 3.14
ρ	Surface relaxivity, ms^{-1}
σ	Oil-water interfacial tension, Nm^{-1}
σ	Molecular area of the adsorbate, nm^2
σ	Collision diameter of gas molecules, nm
σ	Standard deviation
τ	Time interval between 180° and 90° pulses in the inversion recover sequence to determine T_1, s
τ	Time delay between 90° and 180° pulses and after the 180° pulse in the CPMG pulse sequence to determine T_2, s
τ	Correction time between bipolar gradients, s
τ_p	Tortuosity of pore space probed by liquid molecules
τ_{C6H12}	Tortuosity of the cyclohexane phase
τ_{H2O}	Tortuosity of the water phase
ϕ	Potential due to dispersion force interaction with the solid, $Jmol^{-1}$
Ψ	Constant, Eq. (5.10)
ω_0	Angular frequency, Hz
ω_{0z}	Angular frequency varying along the direction of the applied gradient, Hz

Abbreviations

AC	Active Carbon
ACS	American Chemical Society
API	American Petroleum Institute
APD	Average Pore Diameter (4V/A)
ASAP	Accelerated Surface Area Porosimeter
BET	Brunauer-Emmett-Teller
BJH	Barrett-Joyner-Halenda
BOC	Provider of industrial gases, a commercial company
CAPRI®	CA-Catalyst, PRI-Petroleum Recovery Institute
CHOPS	Cold Heavy Oil Production with Sand
CPG	Controlled Pore Glass
CPMG	Carr-Purcell-Meiboom-Gill
CSS	Cyclic Steam Stimulation
CUS	Coordinatively Unsaturated Sites
CXT	Computerised X-ray Tomography
DFT	Density Functional Theory
DNAPL	Dense Non-Aqueous Phase Liquids
FCC	Fluid Catalytic Creacking
FID	Free Induction Decay
FHH	Frenkel-Halsey-Hill
GCMC	Grand Canonical Monte Carlo
HDA	Hydrodeasphalting
HDM	Hydrodemetallisation
HDN	Hydrodentirogenation
HDS	Hydrodesulphurisation

HTO	High Temperature Oxidation
IGA	Intelligent Gravimetric Analyser
ISC	In Situ Combustion
IUPAC	International Union of Pure and Applied Chemistry
LDF	Linear Driving Force
LHS	Left Hand Side
LLE	Liquid-Liquid Exchange
LTO	Low Temperature Oxidation
LTS	Low Temperature Shift
MAP	Macropore Alumina
Mbopd	Thousand barrels of oil per day
MC	Monte Carlo
MF-DFT	Mean-Field Density Functional Theory
MFT	Mean Field Theory
MOZ	Mobile Oil Zone
MRI	Magnetic Resonance Imaging
NAPL	Non-Aqueous Phase Liquids
NLDFT	Non-Local Density Functional Theory
NMR	Nuclear Magnetic Resonance
PC	Personal Computer
PFG	Pulsed Field Gradient
RHS	Right Hand Side
rms	Root mean square
r.f.	Radiofrequency
SAGD	Steam Assisted Gravity Drainage
SAXS	Small Angle X-ray Scattering
SANS	Small Angle Neutron Scattering
SVE	Soil Vapour Extraction
TAN	Total Acid Number
THAI®	Toe to Heel Air Injection
TOS	Time On Stream
TPV	Total Pore Volume
VAPEX	Vapour Extraction
WGS	Water-Gas Shift
3D	Three Dimensional

CHAPTER 1 – INTRODUCTION

Chapter 1 of this thesis introduces the reader to the role of catalysts in the oil industry and why they require characterisation and design. It also discusses the different heavy oil recovery methods, focusing primarily on thermal recovery methods. An overview of the THAI®-CAPRI® process which is likely to be a major thermal recovery method in the near future is given. The reader will begin to understand that this process and the catalysts involved are expected to play an important role in recovering upgraded oil that meets standard refinery requirements. It will also be seen that the properties of catalysts applicable for the THAI®-CAPRI® process are similar to those used in the refinery processing of heavy crudes. As a result, different catalysts used for the refinery processing of heavy crudes reported in the literature have also been evaluated. It will be seen that the survey clearly identifies the need for the structural characterisation of catalysts used in the THAI®-CAPRI® process and thereby the need to optimise the THAI®-CAPRI® process itself. Thus, Chapter 1 sets the scene for the subsequent chapters where catalyst characterisation is performed by different techniques.

1.1 INTRODUCTION

Today catalysts play a vital role in the manufacture of commercial products that affect most aspects of our lives; be it in the fertilizer or petroleum refining industry, in the production of food and medicine or in the manufacture of different polymers, or even in our daily use of transport vehicles. An essential objective or requirement of all industries is to make optimal use of catalysts. However, a major problem that spans the industry is catalyst deactivation. This can lead to economic losses to the tune of millions of dollars especially in critical industrial sectors like petroleum and refining. Deactivation may be due to sintering, carbon deposition, improper control of reaction conditions, impurities in the feedstock, etc. In the petroleum and refining industry, which is related to the work discussed in this thesis, catalyst deactivation by carbon deposition or coking is a common issue. Coking directly impacts the physical or structural properties of the catalyst. These properties include surface area, pore size and pore volume. It is the measurement of these properties that this thesis deals with. The information obtained can be used to design better catalysts that will help achieve greater reaction performance. Though it may be

possible to reduce deactivation effects by changing the chemistry of the catalyst, unfavourable physical properties will definitely reduce the activity of the catalyst or in some cases the reaction of interest may not even take place. Hence, there is a need for efficient catalyst characterisation techniques. In this thesis, conventional characterisation techniques that are widely practised in the industry have been used to estimate catalyst properties. More importantly, conventional techniques are prone to certain disadvantages. Thus, new methods of catalyst characterisation are required. As part of the work presented here, the reader will also be introduced to a new characterisation technique that employs nuclear magnetic resonance (NMR) spectroscopy to differentiate between fresh and coked catalysts. Apart from this, separate work was also completed by adapting a conventional characterisation technique in a new manner to reveal the structural properties of catalysts. Before introducing the different techniques of catalyst characterisation that were pursued, a brief introduction on the properties of the heavy oil feedstock, and how it is derived and processed are given.

1.2 HEAVY OIL RECOVERY

The rapid development of human society has been anchored on the availability of energy through the use of oil in its different forms. With oil prices hovering at around 85-100 USD/bbl (Anon, 2012a; Anon, 2012b) and the rise in energy consumption of the developed and developing economies, a decline in the availability of light oil and further price rises are clearly foreseeable. In order to sustain the world economy before it is possible to make a transition to an oil-free energy world there is a need to exploit heavy oil resources which are present in much larger amounts than light oil resources. In 2010, Alberta in Canada had the third largest oil reserves in the world at 170.8 billion barrels. Of this, approximately 99% was in the form of bitumen reserves (Government of Alberta Energy, 2012a). Highly dense and viscous crude oil with a high boiling point and API gravity[1] less than 25 is defined as heavy oil. Bitumen is a thick form of crude oil that is extremely heavy and viscous such that it does not flow unless heated or diluted with lighter hydrocarbons. Compared to conventional crude oil, bitumen contains more sulphur, metals and hydrocarbons. Bitumen reserves that are mixed with sand, clay or other minerals are termed as oil

---

[1] API gravity - Gravity of crude oil or petroleum fraction may be reported as specific gravity SG 60/60 °F [measured at 60 °F (15.6 °C) and referred to water at 60 °F (15.6 °C)] or commonly as API gravity. API gravity = 141.5/(SG 60/60 °F) -131.5. Water has an API gravity of 10, and most crude oils and petroleum fractions have API gravity in the range of 10 to 80 (Doherty et al., 2008).

sands (Government of Alberta Energy, 2012b). Most refineries across the world are not capable of processing these heavy crudes without the use of expensive large capacity hydrogen upgraders or thermal cokers. This gap can be filled by the toe to heel air injection (THAI®) process – an in situ combustion (ISC) process that helps in recovering upgraded oil from heavy oil and bitumen reservoirs. A further development of the THAI® process is CAPRI®, wherein the cracked THAI® oil is allowed to fall through a catalyst bed aiding further upgrading.

1.3 NON THERMAL METHODS OF HEAVY OIL RECOVERY

Before reviewing THAI® and CAPRI® processes, other heavy oil recovery methods are briefly reviewed to help understand the importance and advantages of the THAI® and CAPRI® processes. Initial or primary recovery of mobile heavy oil is usually done by water flooding, cold heavy oil production with sand (CHOPS), or by mining. However, recovery factors are extremely low, usually between 3 and 10% (Selby et al., 1989; Dusseault, 1993). Secondary water flooding is a common practice but it also results in low recovery factors. Thin reservoir formations (formation thickness < 5 m) are usually subjected to chemical flooding techniques or immiscible carbon dioxide (CO_2) flooding. These liquid-liquid or gas-liquid displacement techniques usually work by reducing the oil-water interfacial tension or the mobility ratio. Reducing the oil-water interfacial tension increases capillary number N_C, which is expressed as:

$$N_C = \frac{\mu v}{\sigma}.$$
(1.1)

The capillary number measures the significance of viscous forces over capillary forces. In Eq. (1.1), μ is the displacing fluid viscosity, v is the fluid velocity and σ is interfacial tension between the displacing and displaced fluid. Higher capillary number implies greater ease in recovering oil due to the reduction in oil-injected fluid interfacial tension. Mobility ratio M:

$$M = \frac{\lambda_{ing}}{\lambda_{ed}} = \frac{(k/\mu)_{ing}}{(k/\mu)_{ed}},$$
(1.2)

is defined as the ratio of the mobility of displacing λ_{ing} and displaced λ_{ed} fluids. k and μ denote the permeability and viscosity of the two fluids. Mobility ratios greater than 1 do not favour oil recovery since under such conditions, the displacing fluid flows more easily and channels past the displaced fluid. As with primary recovery methods, low oil recovery factors are characteristic of chemical methods as well (Selby et al.,

1989; Thomas et al., 2001; Thomas, 2008). Unlike the former methods (which have witnessed limited growth especially in the past decade (Koottungal, 2010)), thermal recovery techniques have been more successful and are able to achieve greater recovery factors especially when used in oil sands and bitumen reservoirs.

1.4 THERMAL METHODS OF HEAVY OIL RECOVERY

1.4.1 STEAM INJECTION PROCESSES

Thermal recovery techniques are usually based on steam injection or air injection (to achieve ISC) based processes. Cyclic steam stimulation (CSS) is a process that employs steam injection into the heavy oil reservoir for a set duration (see Fig. 1.1). The reservoir is then shut and the steam is allowed to soak the reservoir for some time. During the soaking period, the steam condenses and heats the oil within the reservoir allowing it to be mobile. After the soaking period, the well is put into production mode (Thomas, 2008). Another process, steam assisted gravity drainage (SAGD), developed relatively recently, makes use of horizontal wells to carry out oil displacement over very short distances. The process utilises two parallel horizontal wells aligned on top of each other (see Fig. 1.2). The steam injection well (located on the top) produces a rising steam chamber which systematically spreads causing the heated oil to drain towards the bottom producer well (Butler, 1994). Similar well configurations can also be used for the injection of hydrocarbon solvents alone or in combination with steam. Such a process called vapour extraction (VAPEX) has the potential to produce upgraded oil since the process has the potential to strip bitumen of extremely heavy components by precipitation of asphaltenes (James et al., 2008).
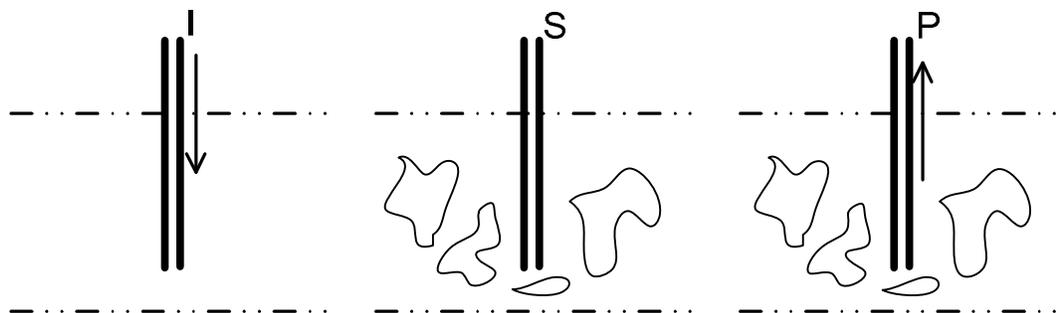
Fig. 1.1. Schematic showing the well configuration for the CSS process - I (steam injection), S (steam soak) and P (production).

Steam based processes are highly demanding with CSS requiring proper control of steam injection pressure. Moreover, the reservoir formation must be

4

susceptible to proper heat distribution. Recovery factors are usually between 10 and 40% (Thomas, 2008). On the other hand, SAGD is a gravity controlled process which achieves slightly greater recovery factors, usually > 50%. But they are applicable only in reservoirs with formation thicknesses > 12 m and permeability > 5000 mD. Heterogeneity in vertical permeability or undulation in the wells can cause the steam front to channel decreasing oil recovery. Similarly, communication between different sets of wells or heat losses to adjacent formation must also be prevented. Proper control and optimisation of the process is required as these processes are highly complex and labour intensive (Butler, 1994; Turta and Singhal, 2004). Finally, steam based processes consume a large amount of water and natural gas.
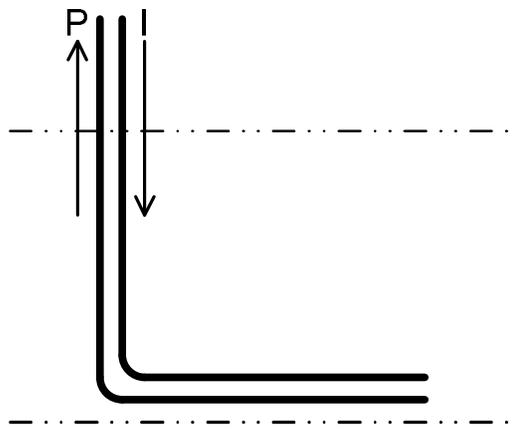
Fig. 1.2. Schematic showing the well configuration for SAGD and VAPEX processes. The upper horizontal well is the steam injection well (I) and lower horizontal well is the oil producer well (P).

1.4.2 IN SITU COMBUSTION (ISC)

1.4.2.1 CONVENTIONAL IN-SITU COMBUSTION
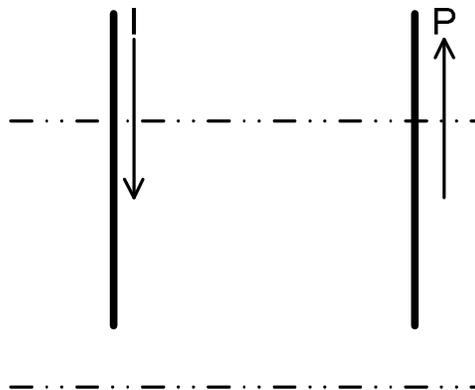
Fig. 1.3. Schematic showing the well configuration for conventional ISC - I (vertical air injector well) and P (vertical producer well). A similar well configuration may also be used for non-thermal heavy oil recovery methods.

In contrast to steam based processes, thermal recovery of oil by in ISC uses free air (at high fluxes) as the injection fluid with vertical injection and vertical producer well combinations (see Fig. 1.3). The injected air undergoes exothermic oxidation reactions with hydrocarbons present in the reservoir aiding the recovery of oil. Conventional ISC is a dynamic displacement process that involves low temperature oxidation (LTO, < 350 °C) reactions, high temperature oxidation (HTO, > 350 °C) reactions, and gas phase combustion intertwined with complex organic reactions. LTO reactions are usually oxygen addition reactions and therefore tend to increase oil viscosity and gravity while HTO reactions are bond scission reactions (Nodwell et al., 2000). Hence, it is essential for an ISC process to operate in the HTO regime. Conventional ISC is a long distance displacement process as oil heated near the injector is forced to travel the entire length of the reservoir section. As a result, heterogeneity in reservoir permeability can cause the displacement front to destabilise. Any instability in the displacement front can easily transfer the oxidation regime from HTO mode to LTO mode and eventually cause an extinction of the combustion reaction. Further, even when operating in HTO mode, all the produced oil has a tendency to be banked in the downstream cold heavy oil region. This may cause the temperature to drop changing the reaction conditions from HTO mode to LTO mode. Finally, at intermediate stages of operation once a burned zone is established, conventional ISC is susceptible to gravity segregation of the injected fluid. Gravity separation causes the injected air to channel past the reservoir section and make contact with the producer well. Thereafter, the reservoir is no longer productive (Xia et al., 2003; Turta and Singhal, 2004). Thus, conventional ISC can also be a demanding process. Nevertheless, there are successful field scale projects where careful monitoring of the displacement front is carried out.

1.4.2.2 TOE TO HEEL AIR INJECTION (THAI®)

THAI® is the most modern of all thermal recovery processes. Like SAGD, it is a short distance displacement process and uses horizontal wells, but in a different configuration. The process utilises vertical injection and horizontal production wells with the toe of the producer well located in proximity to the shoe of the vertical injection well (see Fig. 1.4a). After preheating the reservoir and establishing communication between the shoe and toe (of the injector and producer wells), the heavy residues or coke fractions are burned by the injected air by combustion. The high temperatures generated by the combustion reaction causes viscosity reduction and an increase in mobility of the heated oil. This mobile oil along with the

6

combustion gases and steam are restricted to a narrow region called the mobile oil zone (MOZ) and forced into the producer well. The MOZ is located between the coke zone and the cold downstream region. The coke zone provides the fuel for sustaining the combustion front while the cold downstream region acts as an imaginary wall (that gets swept by the combustion front) and comprises the original bitumen present in the reservoir (see Fig. 1.4b). Unlike conventional ISC, the produced oil and gas are immediately drawn into the horizontal well. Thus, little banking of oil takes place and the entire process occurs at HTO conditions. This ensures that the combustion front traces a quasi-vertical or quasi-perpendicular path to the horizontal producer well with minimal gas override. Further, the short displacement distance ensures that the mobility ratio of the fluids does not dominate the process and any formed fingers are not too large. Thus, oil production can be achieved with minimum effect of the permeability heterogeneity (Xia et al., 2003; Turta and Singhal, 2004).
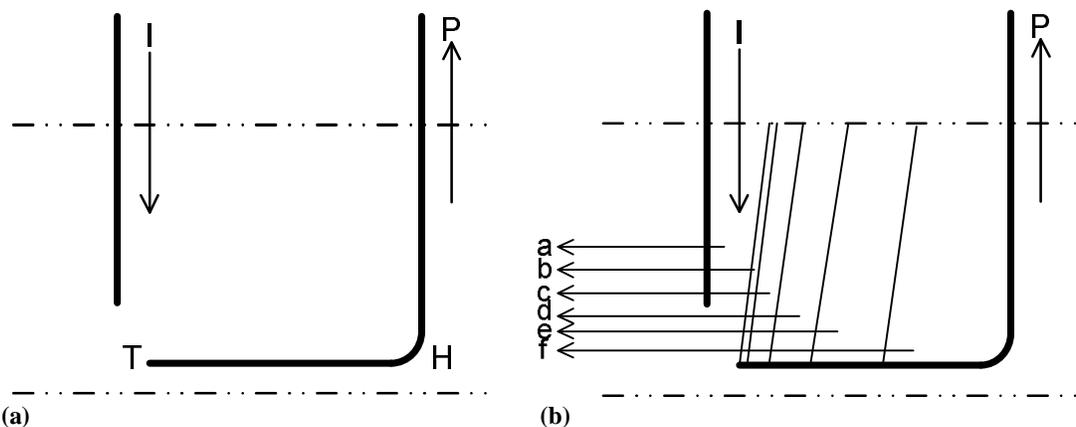
(a)   **(b)**

Fig. 1.4. (a) Schematic of the well configuration for the THAI® process - I (vertical air injection well), P (horizontal producer well), T (toe of the horizontal well), H (heel of the horizontal well). (b) The different zones present in a typical THAI® process - a (burnt zone), b (combustion zone), c (coke zone), d (steam zone), e (banked oil zone), f (cold oil zone). The figure has been adapted from Xia et al. (2005) and Greaves et al. (2011c).

Destabilisation of the combustion front can easily take place if the injected air were to channel directly into the horizontal producer well. However, the presence of coke deposits ahead of the combustion front and the presence of burnt residues behind the combustion front ensure almost complete consumption of injected oxygen. Thus, conditions under which the THAI® process takes place allow the sustenance of HTO reactions from the toe to the heel of the horizontal well (Xia et al., 2005). THAI® process also has the potential to be applied under different conditions – higher air fluxes, wet combustion conditions achieving very high recovery factors (> 75%). Relative to other processes discussed earlier, THAI® also offers the benefit of producing upgraded oil with favourable properties (see Table 1.1).

7

Up to 8 API gravity points above the original crude and more than 2 order of magnitude drop in viscosity have been obtained in experiments conducted in 3D combustion cells. It has also been possible to simulate the 3D combustion cell experiments and obtain a good match using a computer model. This was done most recently by Greaves et al. (2011a, 2011c), giving rise to better insights into the fluid transport within the MOZ. They reported the presence of a steam zone that travels faster than the combustion zone. Further advances to this work were also obtained by Greaves et al. (2011b), where they performed field scale simulations which delivered promising results confirming their modelling approach.

Table 1.1
Experimental results of Xia and Greaves (2002b) for THAI® process in a 3D combustion cell. The viscosity and saturates readings were averaged over an experimental time of 9.5 h.

	Athabasca bitumen	THAI® (Run 2000-01)
Viscosity (mPas)	1.8×10^4-1×10^6 (15 °C)	211(50) (20 °C)
API gravity	8	16
Saturates (wt %)	14.52	62.3(3.8)
Sulphur (%)	4.6-5.6	3.93
Ni (ppm)	60-100	11
V (ppm)	160-300	23
Oil recovery (wt %)		81.5

( ) Errors are quoted in brackets.

All advantages of the THAI® process cannot be realised in reservoirs with large pay thicknesses, since the chances of gravity override and the creation of an unstable displacement front is more probable (Turta and Singhal, 2004). However, the THAI® process is not as demanding as steam based processes and does not consume water or natural gas. The produced oil usually requires little use of diluent when transported or pipelined to refineries. It also offers the ability to thoroughly recover oil from reservoirs that have already undergone production by other processes, e.g. SAGD, and other new reservoirs. Presently, Petrobank Energy and Resources Ltd. are operating commercial scale THAI® projects (Kerrobert and Dawson) located (respectively in Saskatchewan and Alberta) in Canada. The projects are expected to produce 7 Mbopd[2] of upgraded oil from Kerrobert and 10-20 Mbopd of upgraded bitumen from Dawson (Petrobank Energy and Resources Ltd., 2012).

---

[2] Mbopd - Thousand barrels of oil per day

1.5 DOWNHOLE UPGRADING

The potential of downhole upgrading (i.e. upgrading of oil within the reservoir itself) has been discussed widely in the literature. Aquathermolysis[3], mineral or rock matrix reactions can take place when catalytic solutions containing VO^{2+}, Ni^{2+} and Fe^{2+} are added to the reservoir following the injection of steam (Fan and Liu, 2002; Liu and Fan, 2002). Similar experiments involving the addition of hydrogen donors (examples include tetralin or methane) to steam also reportedly produces upgraded oil (Ovalles et al., 2003). Very limited upgrading is achieved in these processes and reaction mechanisms are highly dependent on the physical and chemical characteristics of the reservoir. They are yet to take off on a commercial scale. Besides these processes, as mentioned earlier in Section 1.4.1, partial upgrading can also be achieved by the VAPEX process due to solvent deasphalting of the heavy crude. However, solvent requirements for the VAPEX process, their proper control during operation and recovery, can become complex issues.

As seen in the earlier section, ISC processes provide favourable conditions for producing upgraded oil. The high temperatures generated during combustion reactions promote thermal cracking of heavy hydrocarbon molecules producing lighter molecules and greater oil mobility. The resins are converted to aromatics, and aromatics to saturates. The heavy asphaltene fractions produce coke which serves as fuel for combustion reactions. It can be expected that clays, minerals and formation water may play an important role in facilitating the upgrading process. Further, hydrogen may also be generated via coke gasification or water-gas shift reactions (WGS). The presence of a catalyst layer within the producer well or the addition of dispersed phase catalysts[4] allows the reservoir to act as an efficient chemical reactor similar to a surface heavy duty hydroprocessing unit.

Conventional ISC experiments along with downhole upgrading of Middle Eastern heavy crude oil and Llancanelo heavy oil using $NiMo/Al_2O_3$ catalysts were conducted by Moore et al. (1999) and Cavallaro et al. (2008). An increase of approximately 10 API gravity points was found in both instances. Recovery factors of 55% and 73.6% were obtained. These recovery factors are lower than those found

---

[3] Aquathermolysis describes the reactions occurring between steam, heavy oil and minerals in the oil reservoir that result in the production of more saturates and aromatics while decreasing the amount of resins and asphaltenes (Liu and Fan, 2002).

[4] The use of dispersed phase catalysts will not be discussed as no experiments using these types of catalysts were pursued as a part of this project. However, this is an alternative route to obtain catalytically upgraded good quality oil and may need to be considered in future. A wide literature on the use of different types of dispersed phase catalysts for processing heavy crudes is available. Reviews by Del Bianco et al. (1993) and Chapter 12 in Furimsky (2007) provide in depth details on the use of dispersed phase catalysts.

with the THAI® process. As mentioned earlier, it is likely that the producer well was blocked by the presence of coke and extremely heavy oil. It must be highlighted that direct field scale development of these experiments is not possible since they were performed in one dimensional combustion tubes. The evolution of the combustion front in a combustion tube is unlikely to be valid in the field (where the combustion front travels in three dimensions).

The catalytic add on to the THAI® process; called CAPRI®, allow the possibility of further upgrading the THAI® cracked oil by bringing it in contact with an annular layer of catalysts placed along the perforated section of the horizontal producer well (see Fig. 1.5). Prior to the work presented in this thesis, CAPRI® experiments using two types of hydrodesulphurisation (HDS) catalysts (NiMo and CoMo), and a fluid catalytic cracking (FCC) catalyst were performed on Wolf Lake heavy oil using a 3D combustion cell by Xia and Greaves (2002a). Table 1.2 provides a summary of the results from their experiments. They found that the produced oil was significantly upgraded but the type of the HDS catalysts used did not make any major difference. The low recovery factor obtained for the experiment using fluid catalytic cracking (FCC) catalysts was attributed to the small particle size of these catalysts which caused the well to become blocked with coke. The other runs had greater than 80% recovery factors (Xia and Greaves, 2002a). Similar tests were also performed by Xia and Greaves (2002b) with Athabasca bitumen using a NiMo hydrotreating catalyst. As seen in Table 1.3, the produced oil was slightly more upgraded in the CAPRI® experiment.
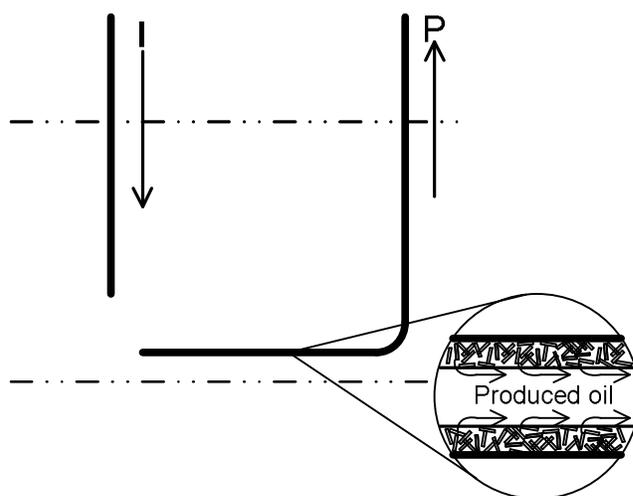
Fig. 1.5. Location of catalysts placed in the horizontal producer well (P) in the THAI®-CAPRI® process.

Considering all the work completed prior to this project in relation to the development of the THAI®-CAPRI® process, it is clear that there some upgrading is available from the process. However, importantly, no clear understanding of the form of upgrading was achieved. Previous work has been unable to clearly ascertain whether the form of upgrading achieved was thermal or catalytic. Furthermore, no characterisation studies were performed on any of the catalysts subjected to the 3D combustion cell experiments. Thus, a natural subsequent step would be to optimise the THAI®-CAPRI® process by conducting experiments under different reaction conditions similar to that in the field using a microreactor. Such an approach can be expected to help understand the different mechanisms of upgrading and the transport of fluids within the reservoir and the catalyst bed. The approach can also allow recovery of catalysts at the end of experiments. These aged, coked or spent catalysts may then be characterised using different techniques and their properties can be compared with those of the respective fresh counterparts. Such steps would help provide an understanding of the optimal catalyst type or structure required for the THAI®-CAPRI® process. These steps were carried out and will be discussed in Section 1.7 which details the approach and background to this thesis. But, before that, it is necessary to see how heavy oil feedstocks are currently processed in refineries (is the process catalytic or thermal?), if catalytic the different types of catalysts used in surface upgrading processes, and the reaction conditions employed as such catalysts may also be appropriate for the THAI®-CAPRI® process. This will also help understand the differences and similarities between the THAI®-CAPRI® and surface upgrading processes.

Table 1.2
Experimental results of Xia and Greaves (2002a) for THAI®-CAPRI® process in a 3D combustion cell containing Wolf Lake heavy oil.

	Wolf Lake heavy oil	THAI (Run 984)	HDS (NiMo) (Run 989)	HDS (CoMo) (Run 9901)	FCC (Run 986)
API Gravity	10.5	~15	25.3	21.77	19
Viscosity (mPas)	48500 (15 °C) 24400 (20 °C)	N/A	~20.5	~59	N/A
Oil Recovery (%)		85	85.5	83	55
Expt duration (combustion) (h)		~11	11	11	11

Table 1.3
Experimental results of Xia and Greaves (2002b) for the THAI®-CAPRI® process in a 3D combustion cell containing Athabasca bitumen. Properties of the THAI® pilot oil from Shah et al. (2011) are also provided.

	Athabasca bitumen	THAI (Run 2000-01)	NiMo (Run 2000-02)	THAI® pilot oil
API Gravity	8	16	~19	13
Viscosity (mPas)	1.8×10^4-1×10^6 (15 °C)	211	N/A	0.577 (20 °C)
Recovery factor (%)		81.5	43.5	
Expt duration (combustion) (h)		9	5.7	

1.6 SURFACE UPGRADING

The catalysts used in the above experiments are similar to those used for surface upgrading in hydroprocessing reactors. Before considering the different catalyst characterisation techniques pursued in this thesis, it is essential to understand how refineries carry out surface upgrading processes and the properties of catalysts used in these processes. In a way, the THAI®-CAPRI® process essentially replaces the surface upgrading process into a heavy oil reservoir, i.e. the underground reservoir serves as the chemical reactor. Processing of heavy crude oil and their fractions in refineries is normally carried out by carbon rejection or hydrogen addition processes. Carbon rejection processes are non-catalytic and are also called thermal cracking processes. Hydrogen addition processes are catalytic and involve either hydrotreatment or hydrocracking reactions which are carried out in reactors with high hydrogen partial pressures (~13 MPa) and at elevated temperatures (~400 °C). The objective of both these processes is to increase the H/C ratio of the produced oil. Heavy crudes processed in upgraders contain more asphaltenes, resins, organometallic compounds, heteroatomic compounds, water soluble salts and mineral matter relative to saturates and aromatics. This is also the case for bitumen and THAI® produced oil (though lesser than the bitumen itself). It is therefore conceivable that catalysts used for hydroprocessing are likely to be applicable for the THAI®-CAPRI® process as well. Hence, some of the catalyst structural and physical properties applicable for surface upgrading are also expected to be applicable for the THAI®-CAPRI® process. The structural properties and design of catalysts for the treatment of heavy oil are greatly dependent on oil composition especially its

asphaltenes and heavy metals content, since these are the two main components responsible for the catalyst deactivation. Apart from these, the presence of large quantities of sulphur and nitrogen within the oil can also cause catalyst deactivation.

1.6.1 CATALYST DEACTIVATION BY COKING

Catalyst deactivation can be broadly divided into three main categories. They are sintering (or aging), coking (or fouling), and poisoning. Catalyst deactivation due to the deposition of carbonaceous residues from the reactant, product or any intermediate is termed as coking (Fogler, 2006; Froment and Bischoff, 1979). As the reactions studied in this project deals with heavy hydrocarbons, coking can be considered to be the major factor responsible for catalyst deactivation. The reservoir feedstock contains heavy and light oil fractions along with some formation water. The heavy oil fractions constitute asphaltenes and resins. Asphaltenes are organic materials consisting of long chains of aromatic and naphthenic ring compounds (containing nitrogen, sulphur and oxygen molecules). They are the heaviest fraction of the crude oil with boiling points greater than 525 °C. They also possess a high C/H ratio and are responsible for the decay in catalyst activity as the deposits are highly carbon rich. Apart from asphaltenes, organometallic compounds of vanadium and nickel, and heteroatomic compounds containing nitrogen and sulphur are also responsible for reducing the activity of the catalyst. Coking deactivates the catalyst by blocking access to pore space, and/or due to active site coverage. This is the reason behind using catalysts that have specific functionalities like hydrodeasphalting (HDA), hydrodemetallisation (HDM), hydrodenitrogenation (HDN), and hydrodesulphurisation (HDS).

1.6.2 TYPES OF CATALYST

The most common supported catalysts used are Mo or W containing γ-Al$_2$O$_3$ supports with Co or Ni as the metal ingredient. They are active in the sulphided state and are generally accepted to increase the rate of hydrodemetallisation (HDM), hydrodeasphalting (HDA) and conversion of heavy fractions to light distillates. Research has shown that the alumina catalyst surface is partially covered by slabs of MoS$_2$ or WS$_2$ in the sulphided state. Under intense hydroprocessing conditions, these sulphur ions are removed forming coordinatively unsaturated sites (CUS). These sites have a Lewis acid character and are responsible for the adsorption of N-bases and

hydrogen activation by splitting hydrogen molecules to form Mo–H and S–H groups. Reactant molecules that are adsorbed on or near the CUS receive hydrogen from these groups. Though the bare support is susceptible to coke deposition, some of the active hydrogen can be split over the support allowing regions of the active MoS_2 or WS_2 slabs to be free of coke. The CUS and the rate of hydrogen activation increase in the presence of promoters (Co or Ni). At temperatures above 400 °C, S–H groups have a Bronsted acid character supplying the necessary hydrogen for hydrodenitrogenation (HDN). Over time, access to these active sites becomes highly restricted due to clogging or blockage of routes by coke. The V content in the feedstock can also poison active sites causing their deactivation. Further details on how these catalysts function and the reasons for deactivation can be found in Furismsky and Massoth (1999) or Furimsky (2007).

The high susceptibility of conventional Al_2O_3 catalysts to deactivation by nitrogen compounds and coke deposition has directed research towards the use of more efficient supports especially those that offer less acidic or neutral character. Table 1.4 lists some of the different supports that have been investigated in the literature.

Table 1.4
Different supported catalysts that have been investigated in the literature.

Active metals	Supports	Characteristics
CoMo	TiO_2-Al_2O_3	High activity for HDS due to favourable metal support interaction, mesopore structure
Fe	Active Carbon	Mesopore structure, neutral surface
CoMo	Zeolite/Al_2O_3	Bimodal porosity, acidic nature
NiMo	NaOH/Al_2O_3	High HDS activity, reduced coke deposition, better asphaltene removal

The neutral or weak base active carbon (AC) catalysts have been shown to display greater adsorption selectivity to asphaltenes and an ability to restrict coke formation during the hydrocracking of vacuum residues relative to conventional Al_2O_3 catalysts (Fukuyama et al., 2004). Under moderate pressures (7 MPa) and temperatures (380-420 °C) zeolite based CoMo/Al_2O_3 catalysts showed better HDS, HDM and asphaltene cracking ability of Maya heavy crude oil. This performance was attributed to the acidity of the catalyst. However, at higher temperatures, this acidity level increased the rate of hydrocracking and reduced catalyst resistance to coke and metal deposition due to asphaltene precipitation and coke forming reactions (Rana et

al., 2008). Earlier, Rana et al. (2005b) also reported the preparation of mixed oxide catalysts (CoMo/TiO$_2$-Al$_2$O$_3$) where the introduction of TiO$_2$ altered the nature of metal interaction with the support by allowing greater dispersion of the active phase on the support surface aiding greater HDS activity of Maya heavy crude oil relative to commercial CoMo/Al$_2$O$_3$ catalysts. Similarly, Richardson and Gray (1997) found that hydroprocessing of Athabasca bitumen with alkali metal hydroxides doped on NiMo/γ-Al$_2$O$_3$ catalysts improved HDS activity and asphaltene removal with reduced coke deposition relative to untreated NiMo/γ-Al$_2$O$_3$ catalysts.

From the preceding discussion, it is evident that catalyst chemistry is important in the selection of a catalyst for the heavy oil upgrading. However, their physical properties also need to be optimised and understood so as to increase their lifetime and utilisation. This approach is critical and been followed by most investigators in this area of research. The mesopore structure of the AC catalyst mentioned in the preceding paragraph helped in realising significant HDM and conversion of heavy hydrocarbons into lighter fractions (Fukuyama et al., 2004). The zeolite based CoMo/Al$_2$O$_3$ catalysts that showed better HDS, HDM and asphaltene cracking ability of Maya heavy crude oil was also bimodal in its pore size distribution. Thus, it is the combination of a suitable pore size distribution and surface area along with the right catalyst support chemistry that provides an ideal catalyst. Usually, high surface areas are required for high activity of catalysts. However, for heavy crude oil, surface area is not a key parameter, but catalyst pore size distribution, pore volume and average pore size are the major properties that play critical roles in determining the HDM, HDA, HDS and HDN activities. Ancheyta et al. (2005) reported that HDS requires a high dispersion of active sites (which implies greater surface area) and moderate pore volume catalysts. However, sufficient HDM and HDA activity require low surface area, high pore volume catalysts, i.e. catalysts with pore size greater than 20 nm (Fukase and Akashah, 2004, cited by Ancheyta et al. 2005, p.8 and Furimsky 2007, p. 29). The large asphaltene molecules and organometallic compounds present in the heavy crude oil can be easily accommodated by large pore volume catalysts since these molecules will travel comfortably through the pores without facing any restrictions. This is the reason why FCC microporous catalysts are not suitable for the treatment of heavy crude oil (due to the transport restrictions faced by larger molecules)[5].

---

[5] The International Union of Pure and Applied Chemistry (IUPAC) has classified pore sizes in porous media as follows: all pores with widths > 50 nm are termed macropores, those with widths between 2 and 50 nm are termed mesopores and those with widths < 2 nm are termed micropores (Sing et al., 1985).

For the same surface area, bimodal catalysts are more active than unimodal catalysts. However, this bimodal pore size range is critical. Any bimodality seen in the micropore or lower mesopore range can cause transport restrictions causing the catalyst to be ineffective (Ancheyta et al., 2005; Furimsky, 2007). Ternan (1998) reported the hydrocracking of Athabasca vacuum residue using macropore alumina (MAP) catalysts and commercial standard bimodal catalysts. The MAP catalysts containing 15% alumina were found to be more effective in residue conversion giving greater yields of distillates and greater HDS, HDN and HDM conversions. Their performance was correlated with the mesopore surface area of the active catalyst having access to large macropores. This in turn allowed large residue molecules to enter and gain access to the active sites available. Similar work by Yang et al. (1996) also showed that MAP catalysts provided greater nitrogen conversion of Athabasca vacuum bottoms than a unimodal catalyst. Thus, catalysts with macropores providing access to larger or moderate size mesopores seem to be a good choice for processing heavy feeds.

Refinery strategy to cope with processing heavy oil feeds is to operate multiple reactors or a single reactor with different catalysts. Each catalyst has a specific function. For example, at the front end, it may be better to have a guard bed that removes asphaltenes and metals present in the oil. This may be followed by a bed containing HDS/HDN catalysts. The catalyst life can be expected to increase under such arrangements and the produced oil would also be of better quality. As mentioned earlier, surface upgrading processes are characterised by high hydrogen partial pressures (~13 MPa) on an industrial scale in the absence of steam and at temperatures of 350 °C or greater. In the THAI®-CAPRI® process, whether such similar conditions can be achieved is yet to be ascertained. Most recently, Shah et al. (2011) reported that the addition of hydrogen did not have any significant effect on the produced oil. The role of hydrogen has not been completely elucidated and though the potential of WGS reactions has been hinted at, there is however no evidence yet. Recent simulation work of the THAI® process by Greaves et al. (2011b, 2011c) showed the presence of a steam front that is located ahead of the combustion front. It is highly likely that this steam front plays a critical role in oil displacement but whether it contributes to any reactions requires further investigation. The presence or the effect of formation water also requires further investigation. Once the wells have been drilled into place, communication between the wells is established by steaming. This is certain to increase the mobility of bitumen allowing it fall over the bed and may be even wet the catalyst bed prior to exposure or contact with the

combustion front. Additionally, Ayasse et al. (2005) reported that the horizontal well has a steaming line which can be used to prevent thermal shock between the combustion front and the catalyst bed. Clearly, such an atmosphere is far from ideal on-surface hydroprocessing conditions and can have a severe effect on catalyst activity. Hence, the need for determination of catalyst pore properties and to use this information for the optimisation of the THAI®-CAPRI® process.

1.7 BACKGROUND WORK TO THIS THESIS

As a part of the detailed investigation of the THAI®-CAPRI® process carried out in this project, an extensive array of reaction engineering experiments were performed at the School of Chemical Engineering in the University of Birmingham. An experimental CAPRI® rig was commissioned by the group led by Dr Joseph Wood[6]. The rig comprises two reactors and can simulate field scale THAI®-CAPRI® processes[7] by allowing the THAI® pilot oil[8] to flow over the catalyst bed. The CAPRI® microreactor is a fixed bed catalyst reactor with a 10.2 mm diameter cylindrical core of length 110 mm. This can be assumed to represent an annular layer of catalyst within the horizontal producer well. The catalyst bed is located in a furnace and the gap between the reactor and the furnace is filled with marble chips. The trace heated THAI® feed oil (at a temperature of 300 °C) is allowed to enter a chamber where it gets mixed with reaction gases. The gaseous-fluid mixture then enters the microreactor bed from the top. The reactor can withstand temperatures up to 500 °C and a maximum system pressure of 10 MPa (100 bar). A whole matrix of reaction studies was conducted using the above set-up. This included an assessment of the effect of different catalysts (fresh and pre-treated), different run times for the same catalyst, change in temperature, pressure, reactant gas composition and feedstock. The work concluded that under the investigated conditions little additional upgrading of the feed THAI® pilot oil took place and this upgrading was mainly dependent on temperature and oil flow rate. Most of this upgrading was likely to be due to further thermal reactions or a filtering effect provided by the catalyst bed. High temperature

---

[6] The Universities of Bath and Birmingham are collaborators in this project. The CAPRI® reactions were performed in Birmingham and Bath performed the characterisation of catalysts.
[7] A field pilot of the THAI®-CAPRI® process initiated in 2006 was operated by WHITESANDS INSITU Ltd. (a subsidiary of Petrobank Energy and Resources Ltd.) in a 1.3 billion barrel bitumen lease 10 km west of Conklin, Alberta, Canada (Ayasse et al., 2005). Oil production from the CAPRI® well began in August 2008 (Petrobank Energy and Resources Ltd., 2008).
[8] The THAI® pilot oil was supplied by Petrobank Enegy and Resources Ltd. from their WHITESANDS THAI® pilot trial near Conklin in Alberta, Canada (Ayasse et al., 2005). Its properties can be seen in Table 1.3, taken from Shah et al. (2011).

reactions produced highly upgraded oil (~6 API gravity points increase) similar to that seen in 3D combustion cell tests of Xia and Greaves (2002b). However, this was at the expense of extremely short catalyst bed life times. An optimum microreactor operating temperature of 420 °C at a pressure of 2 MPa (20 bar) was suggested for moderate upgrading (i.e. an additional ~3 API gravity points increase) with large catalyst bed life times. A comprehensive discussion of the results from these experiments can found in Shah et al. (2011) or Shah (2011). Three different catalysts were used in these simulated CAPRI® experiments. This thesis will deal with the characterisation of these catalysts in their fresh forms. Amongst them, one of the catalysts, denoted sample A, was studied by the Birmingham group in more detail, so this catalyst was also studied in its coked form. A difficult and challenging issue faced was the inability to recover catalysts at the end of the reaction/experiment without causing grave structural damage to the reactor or catalysts themselves. On termination of the experiment, it was found that catalysts were surrounded or immersed by coke and oil residue deposits[9]. Since none of the catalysts used produced oil with appreciably enhanced properties, further analyses of these catalysts were not undertaken in this work. As a result, the new NMR method was developed on another catalyst. This was the same catalyst used in the work done on the supercritical isomerisation of 1-hexene discussed previously by Wang et al. (2009).

1.8 THESIS STRUCTURE

The determination of different catalyst pore properties used in these CAPRI® experiments will be pursued in this thesis by first following conventional methods of characterisation, namely mercury porosimetry and gas adsorption porosimetry. These two techniques will be discussed in Chapter 2 and Chapter 3 respectively. Chapter 4 will then introduce the reader to a new integrated gas adsorption technique, where nitrogen and water vapour will be used, one after the other, to study the pore characteristics of fresh and coked catalysts. Chapter 5 will introduce the reader to a new liquid-liquid exchange (LLE) technique where NMR will be used in a novel manner to differentiate between fresh and coked catalysts[10] by determining the spatial location of coke. Each of these chapters will introduce the technique, discuss the principles involved and provide a literature overview which presents their application to characterising catalysts or support materials. This is followed by a description of

---

[9] An example of the catalyst bed cross section can be seen in Fig. 9 of Shah et al. (2011).
[10] The catalysts were obtained from previous work conducted by Wang et al. (2009).

the experiments carried out and a discussion of the significance of the results obtained. Chapter 6 will summarise the work and conclusions of this thesis, and simultaneously also describe the lines of work that ought to be taken in future.

REFERENCES

ANCHEYTA, J., RANA, M. S. & FURIMSKY, E. 2005. Hydroprocessing of heavy petroleum feeds: Tutorial. *Catalysis Today,* 109**,** 3-15.

ANON 2012a. US Crude Prices. *Oil & Gas Journal.* 15 June 2012 ed.: PennEnergy Research Center. Available from: http://www.ogj.com/industry-stats.html [Accessed 27 June 2012].

ANON 2012b. World Crude Prices. *Oil & Gas Journal.* 15 June 2012 ed.: PennEnergy Research Center. Available from: http://www.ogj.com/industry-stats.html [Accessed 27 June 2012].

AYASSE, C., BLOOMER, C., LYNGBERG, E., BODDY, W., DONNELLY, J. & GREAVES, M. 2005. First Field Pilot of the THAI^{TM} Process. *Canadian International Petroleum Conference,* 07-09 June 2005. Calagary, Alberta, Canada: Society of Petroleum Engineers (successor to Petroleum Society of Canada).

BUTLER, R. M. 1994. Steam-Assisted Gravity Drainage - Concept, Development, Performance and Future. *Journal of Canadian Petroleum Technology,* 33**,** 44-50.

CAVALLARO, A. N., GALLIANO, G. R., MOORE, R. G., MEHTA, S. A., URENBACH, M. G., ZALEWSKI, E. & PEREIRA, P. 2008. In situ upgrading of Llancanelo heavy oil using in situ combustion and a downhole catalyst bed. *Journal of Canadian Petroleum Technology,* 47**,** 23-31.

DEL BIANCO, A., PANARITI, N., DI CARLO, S., ELMOUCHNINO, J., FIXARI, B. & LE PERCHEC, P. 1993. Thermocatalytic Hydroconversion of Heavy Petroleum Cuts with Dispersed Catalyst. *Applied Catalysis A: General,* 94**,** 1-16.

DOHERTY, M. F., FIDKOWSKI, Z. T., MALONE, M. F. & TAYLOR, R. 2008. Petroleum and Complex-Mixture Distillation. *In:* PERRY, R. H. & GREEN, D. W. (eds.) *Perry's chemical engineers' handbook.* 8th ed. / prepared by a staff of specialists under the editorial direction of editor-in-chief, Don W. Green, late editor, Robert H. Perry. ed. New York: McGraw-Hill Professional ; London : McGraw-Hill [distributor].

DUSSEAULT, M. 1993. Cold Production and Enhanced Oil-Recovery. *Journal of Canadian Petroleum Technology,* 32**,** 16-18.

FAN, H. & LIU, Y. 2002. Downhole catalyst upgrades heavy oil. *Oil & Gas Journal,* 100, 4.

FOGLER, H. S. 2006. *Elements of chemical reaction engineering,* Upper Saddle River ; N.J., Prentice Hall PTR/Pearson Education International.

FROMENT, G. F., BISCHOFF, K. B. *Chemical reactor analysis and design.* New York ; Chichester, John Wiley & Sons.

FURIMSKY, E. 2007. *Catalysts for upgrading heavy petroleum feeds,* Amsterdam ; Oxford, Elsevier.

FURIMSKY, E. & MASSOTH, F. E. 1999. Deactivation of hydroprocessing catalysts. *Catalysis Today,* 52, 381-495.

GOVERNMENT OF ALBERTA ENERGY. 2012a. *Facts and Statistics* [Online]. Edmonton, Alberta, Canada: Goverment of Alberta Energy. Available from: http://www.energy.gov.ab.ca/OilSands/791.asp [Accessed 07 February 2012].

GOVERNMENT OF ALBERTA ENERGY. 2012b. *Oil Sands Glossary* [Online]. Edmonton, Alberta, Canada: Government of Alberta Energy. Available from: http://www.energy.gov.ab.ca/OilSands/1708.asp#O [Accessed 07 February 2012].

GREAVES, M., DONG, L. L. & RIGBY, S. P. 2011a. Understanding the Mobile Oil Zone in the Toe-to-Heel Air Injection (THAI) Process. *16th European Symposium on Improved Oil Recovery,* 12-14 April 2011. Cambridge, United Kingdom: EAGE.

GREAVES, M., DONG, L. L. & RIGBY, S. P. 2011b. Upscaling THAI: Experiment to Pilot. *Canadian Unconventional Resources Conference,* 15-17 November 2011. Calgary, Alberta, Canada: Society of Petroleum Engineers.

GREAVES, M., DONG, L. L. & RIGBY, S. P. 2011c. Validation of THAI Bitumen Recovery Using 3D Combustion Cell Results. *SPE EUROPEC/EAGE Annual Conference and Exhibition,* 23-26 May 2011. Vienna, Austria: Society of Petroleum Engineers.

JAMES, L. A., REZAEI, N. & CHATZIS, I. 2008. VAPEX, warm VAPEX and hybrid VAPEX - The state of enhanced oil recovery for in situ heavy oils in Canada. *Journal of Canadian Petroleum Technology,* 47, 12-18.

KOOTTUNGAL, L. 2010. Special Report: EOR/Heavy Oil Survey: 2010 worldwide EOR survey. *Oil & Gas Journal,* 108, 41-53.

LIU, Y. J. & FAN, H. F. 2002. The effect of hydrogen donor additive on the viscosity of heavy oil during steam stimulation. *Energy & Fuels,* 16, 842-846.

MOORE, R. G., LAURESHEN, C. J., MEHTA, S. A., URSENBACH, M. G., BELGRAVE, J. D. M., WEISSMAN, J. G. & KESSLER, R. V. 1999. A

Downhole Catalytic Upgrading Process for Heavy Oil Using In Situ Combustion. *Jounal of Canadian Petroleum Technology,* 38, 1-8.

NODWELL, J., MOORE, R. G., URSENBACH, M. G., LAURESHEN, C. J. & MEHTA, S. A. 2000. Economic considerations for the design of in situ combustion projects. *Journal of Canadian Petroleum Technology,* 39, 34-41.

OVALLES, C., VALLEJOS, C., VASQUEZ, T., ROJAS, I., EHRMAN, U., BENITEZ, J. L. & MARTINEZ, R. 2003. Downhole upgrading of extra-heavy crude oil using hydrogen donors and methane under steam injection conditions. *Petroleum Science and Technology,* 21, 255-274.

PETROBANK ENERGY AND RESOURCES LTD. 2008. *PETROBANK ANNOUNCES FIRST THAI™/CAPRI™ PRODUCTION* [Online]. Alberta: Petrobank Energy and Resources Ltd. Available from: http://www.petrobank.com/files/392.PBG_2008_09_22.pdf [Accessed 08 February 2012].

PETROBANK ENERGY AND RESOURCES LTD. 2012. *WHITESANDS* [Online]. Alberta: Petrobank Energy and Resources Ltd. Available from: http://www.whitesandsinsitu.com/ [Accessed 08 February 2012].

SELBY, R., ALIKHAN, A. A. & ALI, S. M. F. 1989. Potential of Non-Thermal Methods for Heavy Oil-Recovery. *Journal of Canadian Petroleum Technology,* 28, 45-59.

SHAH, A., FISHWICK, R. P., LEEKE, G. A., WOOD, J., RIGBY, S. P. & GREAVES, M. 2011. Experimental Optimization of Catalytic Process In Situ for Heavy-Oil and Bitumen Upgrading. *Journal of Canadian Petroleum Technology,* 50, 33-47.

SHAH, A. A. 2011. *Experimental Optimization of the CAPRI Process.* PhD, University of Birmingham.

TERNAN, M. 1998. Product fractions obtained by hydrocracking vacuum residue from athabasca bitumen using bimodal catalysts of varying macropore volume. *Energy & Fuels,* 12, 239-247.

THOMAS, S. 2008. Enhanced oil recovery - An overview. *Oil & Gas Science and Technology-Revue De L Institut Francais Du Petrole,* 63, 9-19.

THOMAS, S., ALI, S. M. F., SCOULAR, J. R. & VERKOCZY, B. 2001. Chemical methods for heavy oil recovery. *Journal of Canadian Petroleum Technology,* 40, 56-61.

TURTA, A. T. & SINGHAL, A. K. 2004. Overview of short-distance oil displacement processes. *Journal of Canadian Petroleum Technology,* 43**,** 29-38.

WANG, J., CHIGADA, P. I., RIGBY, S. P., AL-DURI, B. & WOOD, J. 2009. Prolonging catalyst lifetime in supercritical isomerization of 1-hexene over a platinum/alumina catalyst. *Chemical Engineering Science,* 64**,** 3427-3436.

XIA, T. X. & GREAVES, M. 2002a. 3D Physical Model Studies of Downhole Catalytic Upgrading of Wolf Lake Heavy Oil using THAI. *Journal of Canadian Petroleum Technology,* 41**,** 58-64.

XIA, T. X. & GREAVES, M. 2002b. Upgrading Athabasca tar sand using toe-to-heel air injection. *Journal of Canadian Petroleum Technology,* 41**,** 51-57.

XIA, T. X., GREAVES, M. & TURTA, A. 2005. Main mechanism for stability of THAI - Toe-to-heel air injection. *Journal of Canadian Petroleum Technology,* 44**,** 42-48.

XIA, T. X., GREAVES, M., TURTA, A. T. & AYASSE, C. 2003. THAI - A 'short-distance displacement' in situ combustion process for the recovery upgrading of heavy oil. *Chemical Engineering Research & Design,* 81**,** 295-304.

YANG, D. S., DUREAU, R., CHARLAND, J. P. & TERNAN, M. 1996. Hydrodenitrogenation of vacuum residue with a large-pore catalyst. *Fuel,* 75**,** 1199-1205.

CHAPTER 2 – MERCURY POROSIMETRY

Chapter 2 of this thesis introduces the reader to the first catalyst characterisation technique that has been investigated in this work. Mercury intrusion-extrusion porosimetry is one of the most popular methods and has been in use for more than six decades for pore size measurement. This chapter will first provide the reader with an introduction to the fundamentals of the technique. The method is not ideal and it has advantages and disadvantages. The prevalence of the technique within the literature will also be briefly discussed. The method has been used in the characterisation of three industrially relevant catalysts in this work. The reasons for the different intrusion-extrusion behaviours are discussed. One of the catalysts was scrutinised in detail with a scanning loop, gravimetry and light microscopy to understand intrusion-extrusion mechanisms. The significance of the results discussed here are mainly two fold. Firstly, they show that, unlike model materials which are relatively physically and chemically homogeneous, catalysts are extremely complex due to their inherent chemical and physical heterogeneity. This is likely to be responsible for an enhancement in hysteretic effects. Secondly, the three catalysts show completely different pore properties – surface area, pore volume, percentage mercury entrapment. They provide clues as to why these catalysts did not perform as expected in the THAI®-CAPRI® reactions (which will be discussed in Chapter 3). This investigation also proved to be a motivating factor behind work done using NMR characterisation techniques discussed in Chapter 5.

2.1 INTRODUCTION – CONCEPT, THEORY AND BACKGROUND

The capillary law for non-wetting liquids (e.g. mercury) requires an excess hydrostatic pressure to force the liquid into a pore. The Young-Laplace law (Eq. 2.1), which relates the pressure difference across an interface of two fluids to its radii of curvature, was used by Washburn (1921) in a cylindrical capillary model of a porous medium. This law forms the basis of intrusion methods that are used to characterise porous solids (Van Brakel et al., 1981; Giesche, 2002). Mercury porosimetry is one such technique. The Washburn equation is:

$$\Delta P = \gamma \left(\frac{1}{r_1} + \frac{1}{r_2} \right) = -\frac{2\gamma \cos\theta}{r} , \qquad (2.1)$$

where ΔP is the pressure difference across the curved mercury interface, γ is interfacial tension of mercury (0.485 Nm^{-1}), r_1 and r_2 describe the radii of curvature of that interface, θ is the mercury contact angle, and r is the pore radius. The greatest advantage of this characterisation technique is its ability to measure a large pore diameter range that varies from ~360 μm to ~3 nm. This covers macropores and mesopores which is the pore size range of interest in this work. Unlike other characterisation techniques, a typical mercury porosimetry experiment can also determine bulk and skeletal density in addition to pore characteristics like pore volume, surface area, and porosity. Data acquisition in this work was completed by controlling the mercury pressure and recording the intruded mercury volume. Other methods that can be followed include a control over the volume of mercury that is injected and a time controlled mercury invasion (Cerepi et al., 2002). In this work pore volume, surface area, and percentage (%) mercury entrapment for three different catalysts will be determined from raw data. The porosimeter directly calculates the volume of mercury intruded. This volume increment (dV) at each pressure can then be integrated using the relationship given by Rootare and Presnzlow (1967):

$$A = -\frac{1}{\gamma \cos\theta} \int_0^V P dV , \tag{2.2}$$

to obtain the surface area (A). Withdrawal efficiency (W_E) is a ratio (expressed as a percentage) of the amount of mercury extruded to the total volume intruded before extrusion began. Percentage mercury entrapment will therefore be $100 - W_E$. Percentage entrapment is an important parameter available only from intrusion or displacement based experiments. It has immense significance in the oil industry especially in water flooding processes. In fact, a typical mercury porosimetry experiment can provide data similar to a water flood in an oil reservoir (Vavra et al., 1992). Both are displacement experiments with the only difference being that air-mercury is a gas-liquid displacement process while water-oil or brine-hydrocarbon is a liquid-liquid displacement process. Further, in catalysis, this parameter can also be related to coking as entrapped regions tend to be surrounded by small throats which can be easily blocked by carbon deposition or poisoning causing pore blockage and diffusion limitations.

Despite these advantages, there are a number of issues which can lead to inaccuracies in the data obtained. Firstly, Eq. (2.1) was derived by Washburn for a parallel bundle of cylindrical pores. Real materials need not have regular cylindrical pores. Both surface tension and contact angle are usually assumed to be constant during a typical experiment. This is only assumed for convenience. There is clear

evidence that surface tension and contact angle change within pores, depending on their surface curvature, geometry and topology, during intrusion and/or extrusion processes (Van Brakel et al., 1981; Kloubek, 1981). Further, the pore diameter, as determined by Eq. (2.1), corresponds to the entrance size of the pore during an intrusion process. On the other hand, the extrusion process provides a measure of the pore body rather than the entrance depending on their ratio. There will definitely be regions where small pores mask or shield larger pores. As a result, the pore size distribution becomes skewed to smaller pore sizes. Finally, equilibration time, which is the time delay allowed before the pressure of the mercury stream is incremented, can bias the pore size distribution. Short equilibration time will skew the distribution to lower pore sizes and lower pore volumes in the intrusion process as enough time is not provided for the mercury menisci to detect the presence of pores. This also means that the extrusion process will be characterised by large entrapment values since enough time is not provided for the mercury stream to extrude. Snap off, or break off, of mercury menisci is artificially forced under such conditions (Van Brakel et al., 1981). These factors are key to understanding mercury porosimetry data before considering them to be accurate or representative of the material studied.

It is expected that, in an ideal cylindrical pore, mercury will intrude and extrude at the same pressure. However, in reality, this is not the case. A volumetric hysteresis can be clearly observed, where for a given pressure, a greater volume of mercury is within the pore space in the extrusion cycle than in the intrusion cycle. Many explanations have been suggested for this hysteresis. They include contact angle hysteresis, and structural hysteresis which comprises the ink-bottle theory or the presence of interconnected networks within a porous medium. These will be explained below.

There is a difference in the advancing (intrusion) and receding (extrusion) contact angle, with the former being greater than the latter (Adamson, 1982). As mentioned in the preceding paragraph, contact angle can vary depending on the surface curvature, pore size, surface roughness and surface chemistry. The effects of these parameters can be studied by experiments. Previous work by Liabastre and Orr (1978) included a study of the morphology of controlled pore glasses (CPG) by comparing the pore diameters obtained from electron microscopy and mercury porosimetry. Kloubek (1981) used their data to obtain correlations that determine the variation of the product $\gamma \cos \theta$ as a function of the pore radius for the advancing and receding mercury menisci. Rigby and Edler (2002) then inserted the Kloubek correlations into the Washburn equation (Eq. 2.1) to obtain equations of the form of:

$$P = \frac{-A + \sqrt{A^2 - 2PB}}{r},$$ (2.3)

which accounted for the variation in contact angle and surface tension. Here A and B are constants depending on the material and whether the mercury menisci is advancing or receding, P is the pressure and r is the pore radius[11]. However, this equation is not universal and is only applicable for systems that exhibit a piston type or parallel intrusion-extrusion mechanism as seen in Fig. 2.1.

(a) Raw data   **(b)**   **(c) Analysed data**
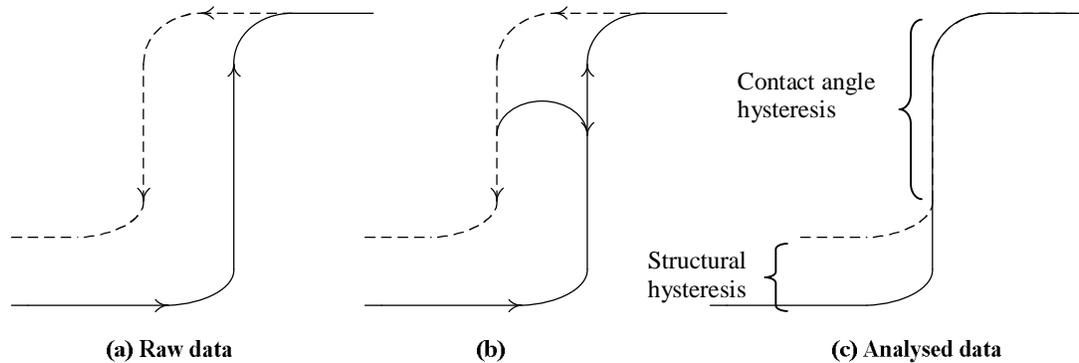
Fig. 2.1. (a) Piston type mercury intrusion-extrusion behaviour for a porous material which is the raw data. (b) The extrusion curve can be superimposed on the intrusion curve using equations of the form derived by Rigby and Edler (2002) from the Kloubek correlations (Kloubek, 1981) and the Washburn equation (Eq. 2.1). (c) This procedure removes contact angle hysteresis showing only structural hysteresis.

Other systems show irreversible extrusion curves that have been found to depend strongly on the interaction between mercury and the chemical substrate (polar or non-polar) present on the pore surface (Moscou and Lub, 1981; Lowell and Shields, 1982; Milburn et al., 1994) or artificially when high pressure mercury streams crush the sample fragmenting it (Pirard et al., 1995). Though there have been attempts to classify the major intrusion-extrusion behaviours exhibited by porous materials as seen in Day et al. (1994), they are not widely used in contrast to the classification proposed for gas adsorption porosimetry (as will be seen in Chapter 3).

Ink-bottle theory, and its extension to a continuous network in porous materials, provides a reasonable explanation for structural hysteresis observed in most porous materials (Van Brakel et al., 1981; Lowell et al., 2006). Real materials rarely have parallel uniform cylindrical pores. A small pore can be connected to a larger pore forming an ink-bottle like system. Consider the system shown in Fig. 2.2, where adjacent pores form an ink-bottle structure. The pressure required for intrusion of mercury is dependent on the entrance size, i.e. radius of pore 1. Once the pressure exceeds that corresponding to this pore size, the mercury stream enters pores 1 and 2.

---

[11] For more details, please refer Section A.2 in Appendix A.

As pressure is reduced, extrusion begins from pore 1 causing a snap-off of the mercury thread. Thus, some of the mercury remains irreversibly trapped in the larger pore as seen in Fig. 2.2c.

This principle can be further extended to interconnected networks where hysteresis is observed when a set of cavities, or large pores, are surrounded by regions containing smaller pores. In such a scenario, large pores will remain filled with mercury at the end of the extrusion step if they have lost connection to the path traversed by mercury streams. In such networks, the condition for a pore to be filled during intrusion is that its diameter must be greater than, or equal to, the pore size corresponding to the applied pressure and a continuous path of mercury also leads to that pore. Thus, in networks, connectivity also plays an important role.

(a) (b) (c)
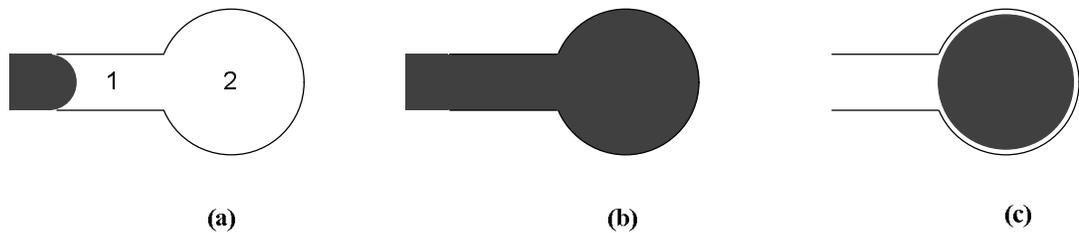
Fig. 2.2. (a,b) Mercury intrusion into an ink-bottle system represented by pores 1 and 2 occurs once the pressure corresponds to the size of pore 1. However, this fills up both pores 1 and 2. (c) On extrusion, entrapment of mercury takes place in pore 2.

Work done earlier with the aid of glass micro-models has enabled a deeper understanding of structural hysteresis, and the mechanisms and factors responsible for entrapment of fluids by snap-off (or break-off) of their threads. Work by Li and Wardlaw (1986a, 1986b) showed that the aspect ratio (pore to throat diameter ratio) can strongly influence the extrusion cycle as it plays a key role in snap-off of mercury thread. Wettability and topology are key factors responsible for snap-off. Using glass micro-models they also showed that interface movements are influenced by pore size, shape and topology of pores and throats in the direction of the displacing fluid front. Other studies include an analysis of pore network effects (Androutsopoulos and Mann, 1979), location of different sized regions within a network (Wardlaw and McKellar, 1981), spatial distribution of pore size in porous materials (Rigby and Edler, 2002), and surface roughness and surface chemistry (Lowell and Shields, 1982).

Apart from the above interpretations, another theory suggested by Giesche (1995, 2006) is the requirement of extra energy to generate free menisci during the retraction (extrusion) process in a single through cylindrical pore (i.e. open at both ends) or from an interconnected porous network relative to the intrusion process in

the same. From a theoretical perspective, there is still no single unified theory or approach which can be applied to all porous media to help understand hysteresis mechanisms. From the work conducted here and that presented in the current literature, it can be said that both contact angle and structural hysteresis can be seen in some systems while in other systems one of the two mechanisms tends to be a controlling factor.

Recently, mean-field density functional theory (MF-DFT) calculations have been used to model the intrusion and extrusion of mercury into a model mesoporous material (Vycor glass) by Porcheron et al. (2005). They found that the generated isotherms agreed well with experimental observations. The extrusion process from the material was found to be similar to that from an ink-bottle pore. Further, they also found that mercury entrapment was a time dependent process. Greater details and insight into the intrusion and extrusion process in slit pore models, ink-bottle pore models, and Vycor glass model, were given by Porcheron and Monson (2005). Their modelling work showed that mercury intrusion was a nucleation process where filling of pores took place after vapour diffusion into the specific pore. Their work also revealed that for Vycor glass, intrusion was close to (but not exactly) a percolation process while extrusion was dominated by cavitation and fragmentation (and not a percolation process). They suggested that mercury entrapment in Vycor glass was caused by a decrease in the rate of mass transfer caused by the fragmentation of mercury during extrusion. These results were attributed to the small pore size of Vycor glass (2 nm to 12 nm) by Porcheron et al. (2007), where they also showed that for larger pore sized CPG (7 nm to 12 nm) intrusion was a percolation process but extrusion was dominated by cavitation (just as for Vycor glass). In other work, Rigby and Chigada (2010) used MF-DFT and mercury porosimetry experiments of silica materials to show that the width between the intrusion and extrusion cycles (hysteresis width) was dependent on the surface roughness factor of the material. They found that for silica materials the hysteresis width decreased with increasing surface roughness. Though much work has been done on the use of MF-DFT for model materials and homogenous silica materials, to date, no work has been done on catalysts using such computational methods. It is likely that the methods have not developed yet to begin modelling the interactions between mercury atoms and atoms present on the surface of the chemically heterogeneous catalysts.

2.1.1 CHEMICAL HETEROGENEITY EFFECTS ON MERCURY POROSIMETRY

Homogeneous model materials usually exhibit clear characteristic properties when characterised using mercury porosimetry (or nitrogen gas adsorption as will be seen later in Chapter 3). In a real cylindrical pore, intrusion and extrusion of mercury take place at different pressures. This could be due to a change in the contact angle or due to some structural effects. The contact angle can be considered a measure of wettability of the surface by the probe liquid, and is subject to change, due to one or more of variation in surface roughness, non-uniformity in pore shape, or due to the chemical heterogeneity of the catalyst surface.

Catalysts, especially those considered in this project display a heterogeneous surface. For example, samples A and B used in this chapter (and in Chapter 3) possess supports comprising alumina and precipitated silica while sample C possess supports comprising copper oxide, zinc oxide and alumina. Thus, the presence of different chemical atoms on the catalyst surface leads to a variable interaction with mercury atoms (or any other probe fluid). In the literature, chemical heterogeneity of the material has been discussed by comparing the mercury intrusion and extrusion curves of materials where mercury comes into contact with polar or non-polar surfaces. It was found that more mercury was entrapped as the polarity of the surface increased (Lowell and Shields, 1982). Such systems usually display large hysteresis loops with irreversible extrusion curves. This irreversibility has been found to depend on the interaction between mercury and the chemical substrate (polar or non-polar) present on the pore surface. Catalysts similar to samples A and B have been studied earlier by Moscou and Lub (1981), and Milburn et al. (1984), who found that the MoO_3 concentration within the catalyst was critical for determining the shape of mercury porosimetry curves for these catalysts. Their experiments showed that the greater the percentage of MoO_3 within the catalyst, the greater was the amount of non-recoverable mercury. Thus, high van der Waals forces of adsorption, leading to an enhancement in pore potential between the mercury atoms and metal atoms on the catalyst surface, can change the contact angle of mercury leading to its non-recoverability. Such high levels of entrapment or non-recoverability of mercury are also found when using alumina samples containing $CuSO_4$ (similar to sample C). Thus, for chemically heterogeneous surfaces with small mesopores, mercury intrusion is likely to provide pore structural information, but extrusion curves are likely to be flat or horizontal due to an enhancement in pore potential. This enhanced pore

potential causes a change in the mercury contact angle and trapping it within the pores of the catalyst.

In this thesis, mercury porosimetry has been used to characterise industrial grade catalysts. Before proceeding to the investigations carried out on these catalysts, an overview is first presented demonstrating the prevalence of this technique in the literature. It appears that mercury porosimetry is still a popular technique used in characterising catalysts, especially to determine the presence of macropores. Importantly, the technique's application has been mainly focused on trying to generally derive quick catalyst porosity characteristics like pore volume, pore size, etc. There is no mention of equilibration time used or entrapment properties of the catalyst. Examples of work include the use of mercury porosimetry in coal based monoliths (Gatica et al., 2010) and natural sepiolite catalysts containing Co, K, and Ba (Milt et al., 2010). In another investigation, He and co-workers (2010) used mercury porosimetry along with other characterisation techniques to determine the properties of fresh and coked $PtSnK/Al_2O_3$ catalysts. They found that the coke narrowed the pores present in their original catalysts. This caused a lowering of the pore volumes and surface area of the spent sample. It must be stressed that high pressures generated by a porosimeter can move or displace coke. This is one of the reasons why this technique was not used to characterise coked catalysts in this work. Further, mercury is also known to wet Pt (Rigby et al., 2011) or interact with Pt to form amalgams (Catchpole, 2009). Hence, it is possible to question such an approach. Other approaches include an investigation to obtain useful catalyst property information by comparing the data obtained from two different characterisation techniques, e.g. mercury porosimetry and multiscale tomography. Such an approach has been pursued by Tariq et al. (2011) where one catalyst showed the availability of large motorways for molecules unlike the other catalyst. In this work, three different catalysts will be investigated to reveal their pore properties and reasons for their intrusion-extrusion behaviour are investigated. Each of the three catalysts will be reported individually with their respective results and discussion. The work will be summarised at the end.

2.2 MATERIALS AND METHODS

Two types of industrially relevant hydroprocessing catalysts, denoted A and B, and a low temperature shift (LTS) catalyst, denoted C, sourced from commercial vendors were used for characterisation experiments in this work. The samples were

characterised in their whole and powdered form, and were used under different reaction conditions in the THAI®-CAPRI® microreactor experiments at the University of Birmingham. The properties and features of the fresh samples are summarised in Table 2.1.

Mercury porosimetry experiments (using 99.99% Hg[12]) were performed with the aid of a Micromeritics Autopore III 9420 apparatus. Fresh catalyst samples were packed and sealed in a penetrometer using a light coating of vacuum grease along the lip of the penetrometer bulb. This setup was then carefully loaded into the low pressure port available in the apparatus with $\frac{1}{4}$ of its stem coated with a thin coating of silicone high vacuum grease. Then the set up was evacuated to a pressure of ~6.7×10^{-6} MPa (~50 μm Hg) in order to remove all the physisorbed water and air from the sample and the penetrometer bulb. All control of the apparatus was possible through an interface controller that was attached to a lab PC. Immediately after degassing, the apparatus performed a low pressure analysis during which pressure was increased stepwise from 0.0035 MPa up to atmospheric pressure (~0.1 MPa). Next the penetrometer assembly containing mercury was carefully removed and the silicone high vacuum grease along the stem wiped off. The assembly weight was noted. This sealed assembly was then transferred to a high pressure port after which the port was filled with a high pressure fluid up to the ledge level, and closed tightly to ensure no oil leakage. Once this setup was arranged, the high pressure analysis was initiated. This involved pressure steps from atmospheric pressure (0.1 MPa) to 413 MPa, the maximum achievable pressure of the apparatus. The equilibration times selected for analysis ranged from 10 s to 30 s and depended on the sample. Initial analysis was conducted by assuming a constant contact angle θ of 130°, and the mercury surface tension γ was assumed to be 0.485 Nm^{-1}. Prior to performing mercury porosimetry experiments on samples, blank runs and reference material tests using the same penetrometers and ports were performed. This helped to minimise errors related to compression and heating, and also confirm that the results obtained were representative of the material studied.

In addition to the above standard mercury intrusion-extrusion experiment, catalyst sample A was subjected to gravimetry and a scanning loop experiment. After a typical mercury intrusion and extrusion experiment, the sample mass that had mercury intruded into it was measured and compared to the initial mass of the fresh sample. This helped to confirm if mercury had indeed intruded the sample. The

---

[12] 99.99% Hg sourced from Micromeritics Ltd was used for all mercury porosimetry experiments.

intruded sample was also subjected to light microscopy after freezing the mercury by dipping it in liquid nitrogen. This helped to see the mercury patches on the catalyst surface. For the scanning loop experiment, pressure was initially raised stepwise to 189 MPa and then reduced to 4 MPa. At 189 MPa, the sample was only partially filled with mercury. After extrusion to 4 MPa, re-intrusion was initiated and this time mercury was allowed to intrude the entire sample as pressure was allowed to increase stepwise up to 412 MPa. This was followed by a final extrusion stepwise to atmospheric pressure.

Table 2.1
Composition and physical properties of catalysts studied by mercury porosimetry as specified by the manufacturer.

Sample	Name	Composition (% W/W)	Appearance	Colour	Odour	Melting point (°C)	Bulk density (kgm^{-3})	Length (mm)	Diameter (mm)
A	Ketjenfine hydroprocessing catalysts-CoMo type	Precipitated silica: 0-6							
		Cobalt (II) oxide: 1-10							
		Molybdenum (VI) oxide: < 25	Extrudates	Blue	Odourless	> 800	550-900	~7	~1
		Phosphorus pentoxide: 0-4							
B	Ketjenfine hydroprocessing catalysts-NiMo type	Aluminium oxide: balance Precipitated silica: < 10							
		Nickel (II) oxide: < 10							
		Molybdenum (VI) oxide: < 30	Extrudates	Yellow	Odourless	> 800	550-950	~7	~1
		Phosphorus pentoxide: 0-9							
C	C18 HA LTS	Aluminium oxide: balance Copper oxide: 56							
		Zinc oxide: 31							
		Aluminium oxide: 11	Tablets	Black	Odourless	N/A	1050	~2.4	~4.5
		Sulphur: < 0.02							
		Chlorine: <0.01							

2.3 RESULTS – SAMPLE A

A typical raw mercury porosimetry intrusion-extrusion experiment for catalyst sample A using an equilibration time of 30 s over the complete pressure range available from the apparatus is presented in Fig. 2.3. This was transformed into a pore diameter vs. cumulative pore volume plot by applying the Washburn equation (Eq. 2.1) and removing the inter-particle intrusion volume, as seen in Fig. 2.4. Here, another set of data obtained previously for catalysts from the same batch using an equilibration time of 10 s is also presented.
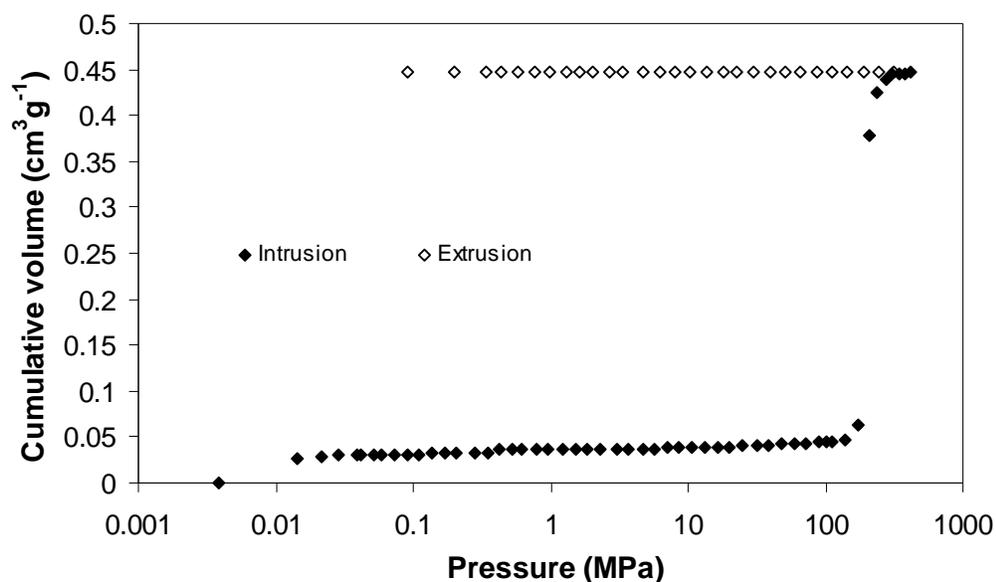
Fig. 2.3. Typical raw mercury intrusion and extrusion data for catalyst sample A (whole). The equilibration time was set at 30 s.

As is evident in Fig. 2.4, little difference can be seen in the experiments conducted at different equilibration times. This slight difference can be attributed to minor intra-batch non-uniformities or variability in the pore structure. Also the measured pore volume agreed well with that determined by nitrogen gas adsorption as will be seen later in Chapter 3. The catalyst sample A displayed a steep intrusion curve which plateaus as the intrusion pressure reaches 413 MPa, indicating complete filling of the pore volume. The following horizontal extrusion step indicates that most of the mercury was unable to be recovered from the pores of the catalyst. The structural properties of catalyst sample A obtained from the intrusion and extrusion steps are presented in Table 2.2. The surface area was determined by the Rootare-Prenzlow equation (Eq. 2.2).
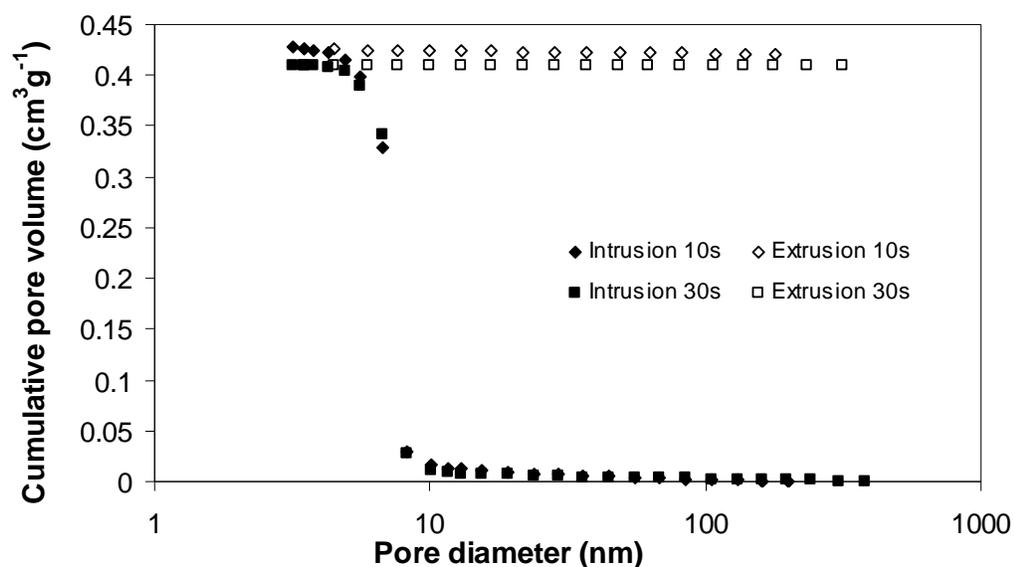
Fig. 2.4. Intra-particle cumulative pore volume data for catalyst sample A (whole) obtained from mercury porosimetry at different equilibration times. Both sample sets belong to the same batch.

Table 2.2
Typical structural properties of catalyst sample A (whole) obtained from mercury porosimetry.

Sample	Entrapment percentage (%)	Pore volume (cm^3g^{-1})	Surface area (m^2g^{-1})
A	99.23(0.77)	0.42	283(8)

( ) Errors are quoted in brackets.

In order to achieve a greater understanding of the reason behind the inability of mercury to extrude from sample A, further work involved a verification of whether the sample underwent a buckling phenomenon, gravimetric analysis, the use of a scanning loop and a powdered sample instead of the whole. High entrapment has been previously shown to be an artefact for aerogels by Pirard et al. (1995). These workers found that the aerogels buckled being unable to withstand the stress and high pressures of the mercury front. However, as seen in Fig. 2.5, sample A does not undergo any buckling. The intruded sample displayed a greyish silver sheen and clearly visible mercury blobs relative to the fresh sample. When weighed, the intruded sample weight was at least 6 times the weight of the fresh sample proving that mercury definitely intruded the sample. This observation was also consistent with product of pore volume and the density of mercury present in the literature (13.5336 gcm^{-3} at 298 K) (Forsythe, 1954; 2003). Light microscopy also revealed the presence of mercury blobs on the surface of the catalyst as seen in Fig. 2.6. Further information on the extrusion mechanism was revealed by a scanning loop experiment on sample A and use of a powdered sample instead of a whole sample. As seen in Fig. 2.7, the scanned region leads to > 95% mercury entrapment. Re-intrusion followed the same

36

path as the first extrusion step and completely filled the sample pore space. The final extrusion step also revealed greater than > 95% mercury entrapment.
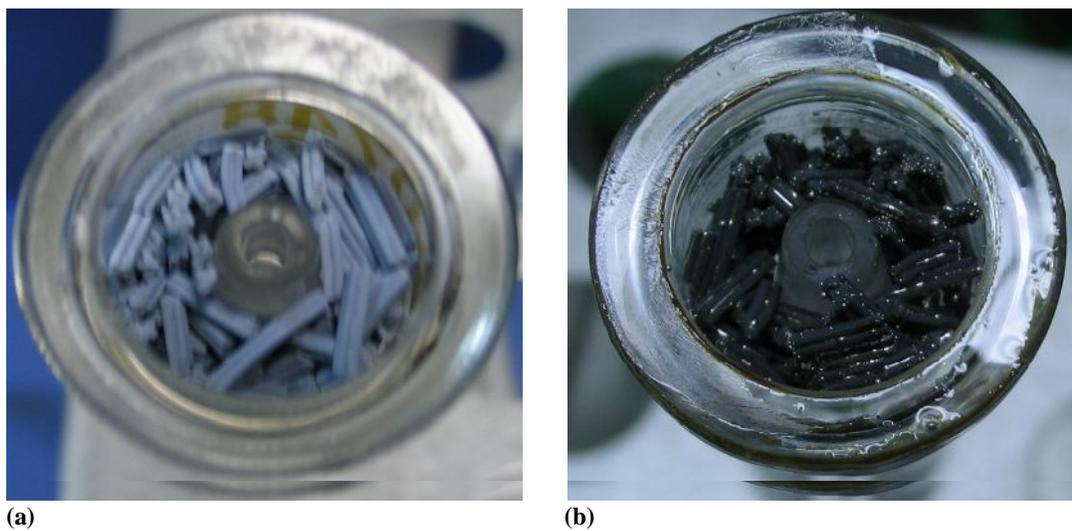
(a)   **(b)**

Fig. 2.5. (a) Fresh sample A extrudates and (b) mercury intruded sample A extrudates showing blobs of mercury in the sample holder (penetrometer) used for mercury porosimetry experiments. The colour of the catalyst changed following mercury intrusion.
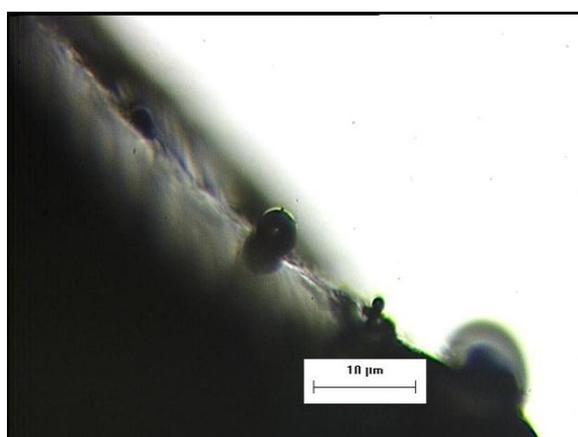
Fig. 2.6. Mercury blobs and patches seen on the surface of the catalyst sample A. The mercury intruded sample weighed at least 6 times the fresh sample.
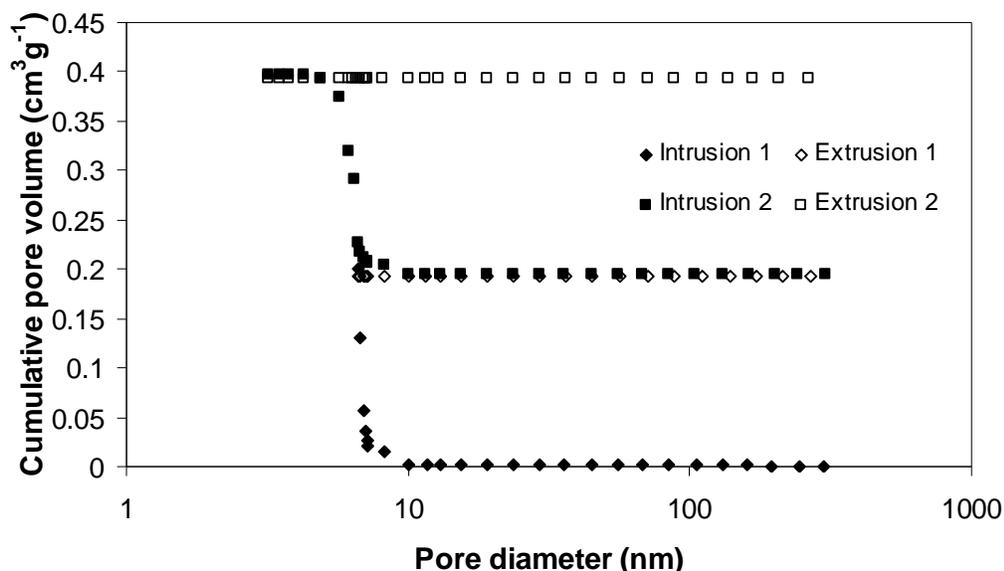
Fig. 2.7. Intra-particle cumulative pore volume data obtained for catalyst sample A (whole) in a mercury porosimetry experiment. Step 1 represents the scanning loop. Intrusion 1 represents the partial intrusion of the sample with mercury and extrusion 1 represents the following desaturation. This step is followed by an intrusion cycle that fills up the entire pore volume which is then extruded, i.e. step 2. Equilibration time was 30 s.

Similar to the results obtained for the whole sample, Fig. 2.8 and Fig. 2.9 display the results obtained for a powdered sample. It was found that the powdered sample had less pore volume than the fresh sample and some of the mercury could be extruded. However, similar to the fresh sample, there was an initial region where there was no extrusion of mercury.
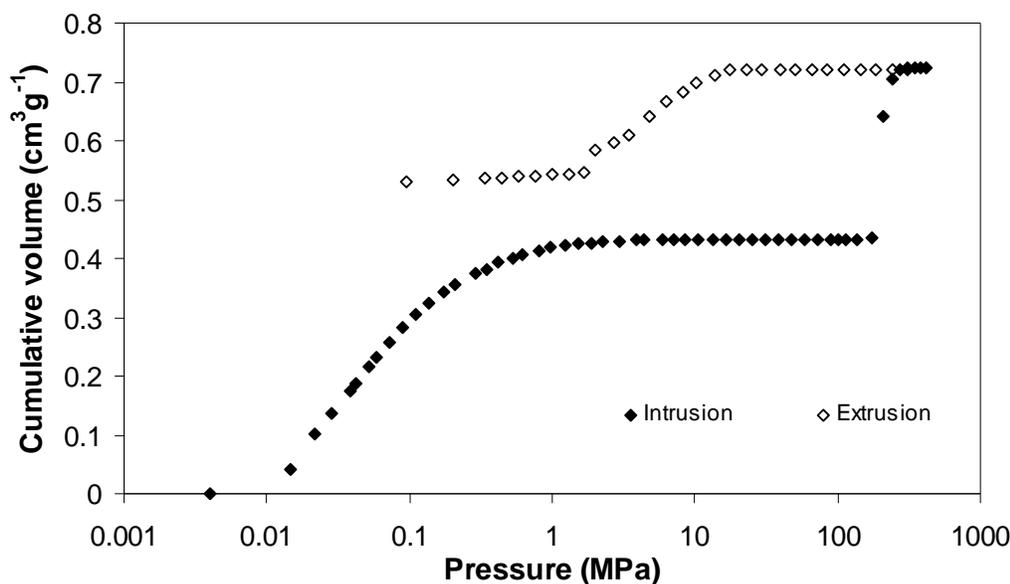
Fig. 2.8. Typical raw mercury intrusion and extrusion data for catalyst sample A in its powdered form. The equilibration time was set at 30 s.

38
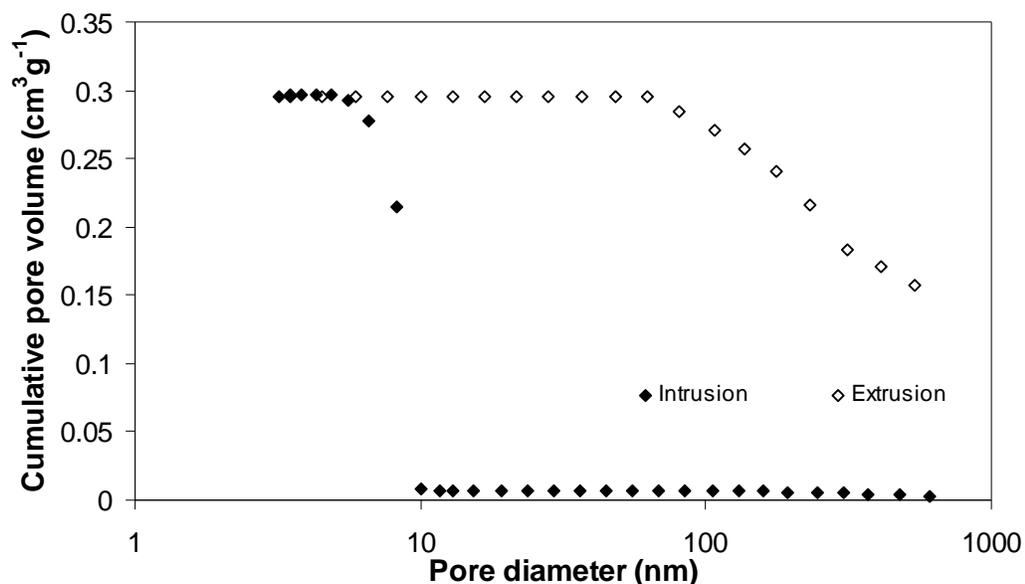
Fig. 2.9. Intra-particle cumulative pore volume data for catalyst sample A in its powdered form obtained from mercury porosimetry. The equilibration time was 30 s.

2.4 DISCUSSION – SAMPLE A

Sample A revealed a characteristic flat extrusion curve that gave high mercury entrapment values, be it in the whole or powdered form. Equilibration time can sometimes be a factor as greater equilibration time gives greater time for mercury threads to move. However, this did not seem to be a factor as there was no change in mercury intrusion or extrusion characteristics when the experiment was run with an equilibration time of 10 s or 30 s. The powdered sample revealed a slightly lower pore volume than the whole sample and a flat extrusion curve initially which later became gradual. The lower pore volume was likely to be due to intra-batch variability or the destruction of some of the pores available in the fresh catalyst. The extrusion cycle displayed a flat region initially which gradually sloped. During the extrusion process, as the pressure was decreased stepwise, mercury receded from the smallest pores. But for catalyst sample A, it was found that no extrusion could take place in these pressures. However, once the characteristic size was larger and becomes of the order of inter-particulate gaps, extrusion was possible. So, it can be confirmed that both whole and powder samples display very similar characteristics.

High entrapments usually occur in networks where large pores or cavities are surrounded by a region of smaller pores. Porous media containing such networks belong to class III, according to the classification provided by Day et al. (1994). But there is evidence from previous work by Pirard et al. (1995) that high entrapment may also be an artefact because the porous material undergoes a buckling phenomenon

39

(due to the high pressures of the mercury front). This can be discounted for sample A as the sample did not appear in a fragmented/powdery form following mercury intrusion and extrusion. Besides, it was seen that the sample weight following mercury porosimetry was far greater than the fresh sample. This was proof that mercury indeed intruded the sample.

From the scanning loop experiment, it was seen that partial mercury intrusion also led to > 95% mercury entrapment. In a scanning loop experiment, free menisci are already available for mercury to extrude. This should theoretically allow easier extrusion relative to an experiment where no scanning loop was performed as mercury extrusion can only initiate once free menisci are generated. Thus, it seems that once mercury has intruded into the pores of sample A, it is unable to extrude even at atmospheric conditions. It remains to be seen how low a pressure is required for mercury to extrude from the pores of sample A.

Moscou and Lub (1981), Lowell and Shields (1982) and Milburn et al. (1994) observed that mercury entrapment was dependent on whether the porous materials are impregnated with polar or non-polar materials. Work by Moscou and Lub (1981) and Milburn et al. (1994) are particularly interesting. Moscou and Lub found that for increasing concentration of molybdenum oxide (MoO_3), mercury intrusion process revealed increasing pore radius (even though nitrogen adsorption-desorption isotherms revealed a decrease in the pore size with increasing concentration of MoO_3)[13]. Milburn et al. (1994) found that mercury intrusion was independent of the MoO_3 concentration for alumina supported catalysts while extrusion curves were dependent on MoO_3 concentration. Horizontal flat extrusion curves similar to those observed for sample A was also found by Milburn and co-workers for samples having > 10% MoO_3 concentration. This observation was in agreement with Moscou and Lub (1981) who found a similar effect (i.e. the greater the percentage of MoO_3, the greater the amount of non-recoverable mercury, see Fig. 10 in Moscou and Lub (1981)) and attributed it to the change in contact angle or shape of the pore. The observations from these cited works are in line with those seen for sample A, which has < 25% MoO_3 (see Table 2.1), gave a horizontal extrusion curve, and showed a colour change after the extrusion process (see Fig 2.5).

The classical Washburn equation (Eq. 2.1) accounts only for the mechanical equilibrium between the pressure and capillary forces in pores > 40 nm. Most of the pores in sample A are definitely between 6 and 14 nm (as will be seen using nitrogen

---

[13] Note that the nitrogen adsorption-desorption isotherms are not given in Moscou and Lub (1981). It is only stated.

adsorption in Chapter 3). Van der Waals adsorption forces in small pores are extremely high making it necessary to account for them depending on the pore geometry and dimension. This insight has been provided by Kadlec (1989) who derived a refined Washburn equation:

$$P = \frac{-2\gamma\cos\theta}{r} + \frac{\phi}{\bar{v}^l} + \frac{\mu^*(r)}{\bar{v}^l},$$
(2.4)

from the Gibb's condition of thermodynamic equilibrium that accounts for both mechanical and potential forces. In Eq. (2.4), ϕ is the potential due to the dispersion force interaction with the solid, $\bar{v}^l$ is the average value of the liquid molar volume over the pressure range, and μ^* is the change in chemical potential of mercury corresponding to the change of its structure under the presence of a force field and the other terms are as defined earlier.

Sample A contains a whole host of ingredients (see Table 2.1), making its surface chemically heterogeneous in addition to the physical heterogeneity. The atoms in sample A are highly electron rich creating deep potential wells with significant van der Waals forces. Thus, once mercury falls into the well of a pore, it is unable to overcome the force field present in the pore (even at atmospheric conditions). This interpretation is supported by previous work done by Lowell and Shields (1982), Kadlec (1989) and Milburn et al. (1994). The high dispersion forces in the pores of sample A may even possibly cause a dramatic change in the mercury surface tension and contact angle. This effect is likely to be more significant for the sample A in its whole form rather than the powder form. This is why the extrusion curve for the powdered sample is initially flat but gradually slopes. At lower pressures, greater amounts of mercury are extruded since the distance for the mercury stream to travel is less (relative to sample A in its whole form). Thus, the chemistry of the catalyst surface creates a strong pore potential which manifests itself as an enhancement in contact angle or structural hysteresis.

2.5 RESULTS – SAMPLE B

The results for sample B from a typical mercury porosimetry intrusion-extrusion experiment over the complete pressure range available from the apparatus are presented in Fig. 2.10. No change was observed in the intrusion and extrusion data for this catalyst when the equilibration time was increased from 10 s to 30 s. The path traversed by the mercury curve during a second intrusion step was similar to the initial intrusion step, as seen in Fig. 2.11.
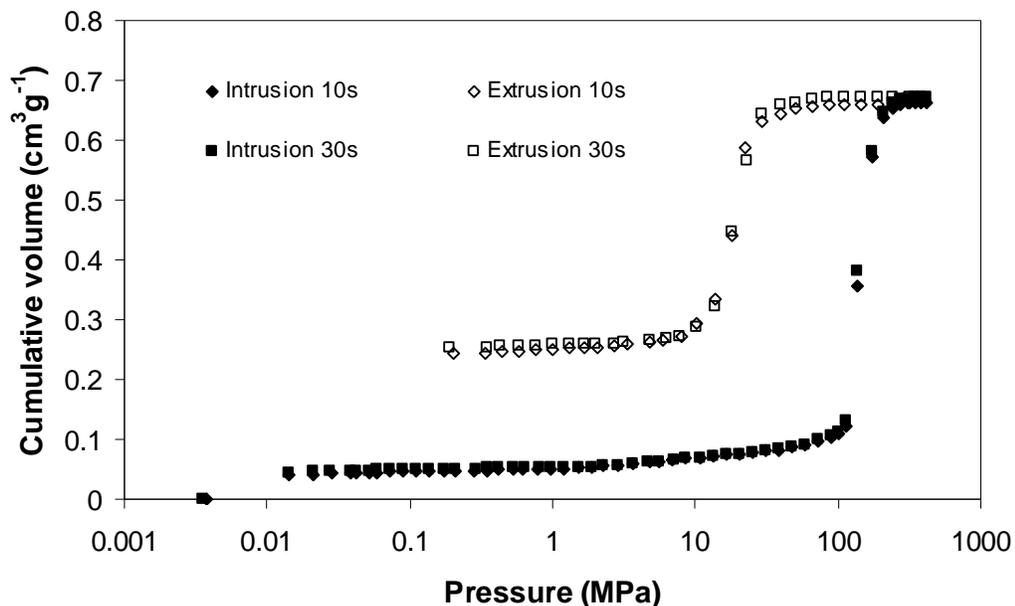
Fig. 2.10. Typical raw mercury intrusion and extrusion data for catalyst sample B (whole) at an equilibration time of 10 and 30 s.

Application of the Washburn equation (Eq. 2.1) allowed the transformation of the pressure points in Fig. 2.10 into their corresponding pore sizes as seen in Fig. 2.12. The inter-particle volume has also been deducted to only provide pore volume data in Fig. 2.12. The catalyst pore volume was 0.62 cm^3g^{-1}, and the surface area was 306 m^2g^{-1} as determined by the Rootare-Prenzlow equation (Eq. 2.2). The incomplete extrusion indicates that ~30% of the intruded mercury was entrapped within the pore network of catalyst B. This suggests that ~70% of the pore volume was accessible to mercury in a manner that it could intrude and extrude freely from. These major properties are tabulated in Table 2.3. The parallel nature of the intrusion and extrusion steps at high pressures (> 10 MPa) is evidence of the presence of both contact angle and structural hysteresis. The contact angle hysteresis was removed by application of Rigby-Edler equations (Eq. 2.3) using the parameters in Table 2.4. This enabled the transformation of Fig. 2.12 into Fig. 2.13. The coincidence of the intrusion and extrusion curves (above 10 nm) can be clearly noted. Thus, structural hysteresis was responsible for mercury entrapment in catalyst B.
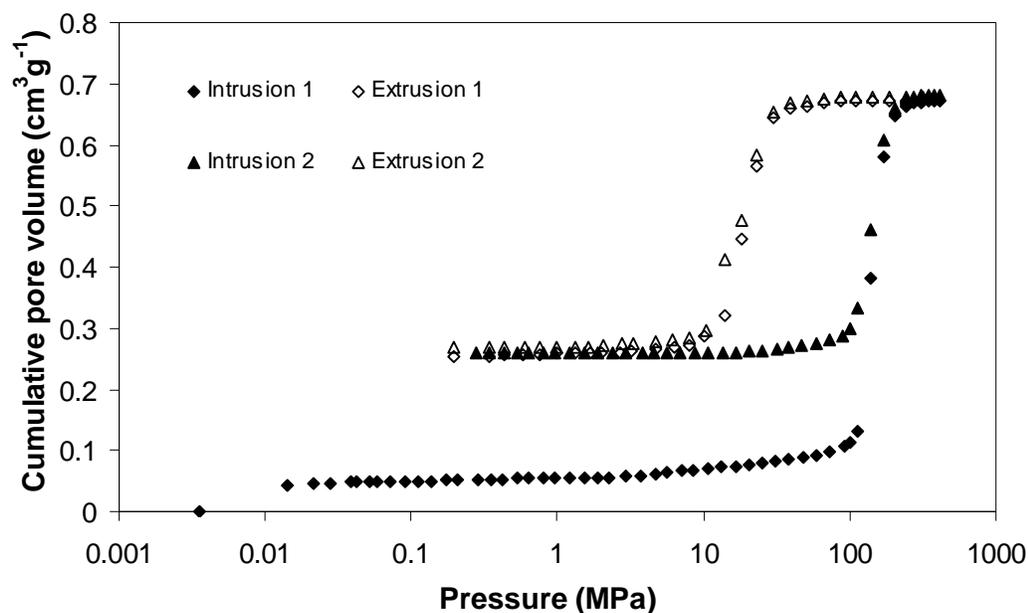
Fig. 2.11. Typical raw mercury intrusion and extrusion data for catalyst sample B (whole) at an equilibration time of 30 s. The plot shows a re-intrusion step (Intrusion 2) following the same path as the primary intrusion cycle (Intrusion 1). The same also applies for the extrusion cycle. The equilibration time was 30 s.

Table 2.3
Typical structural properties of catalyst sample B (whole) obtained from mercury porosimetry.

Sample	Entrapment percentage (%)	Pore volume (cm^3g^{-1})	Surface area (m^2g^{-1})
B	30.75(0.46)	0.62(0.02)	306(7)

( ) Errors are quoted in brackets.

Table 2.4
Parameters obtained when the Rigby-Edler equations are applied to catalyst sample B.

	A	B
Mercury intrusion	-302.533	-0.739
Mercury extrusion	-5	-135

43
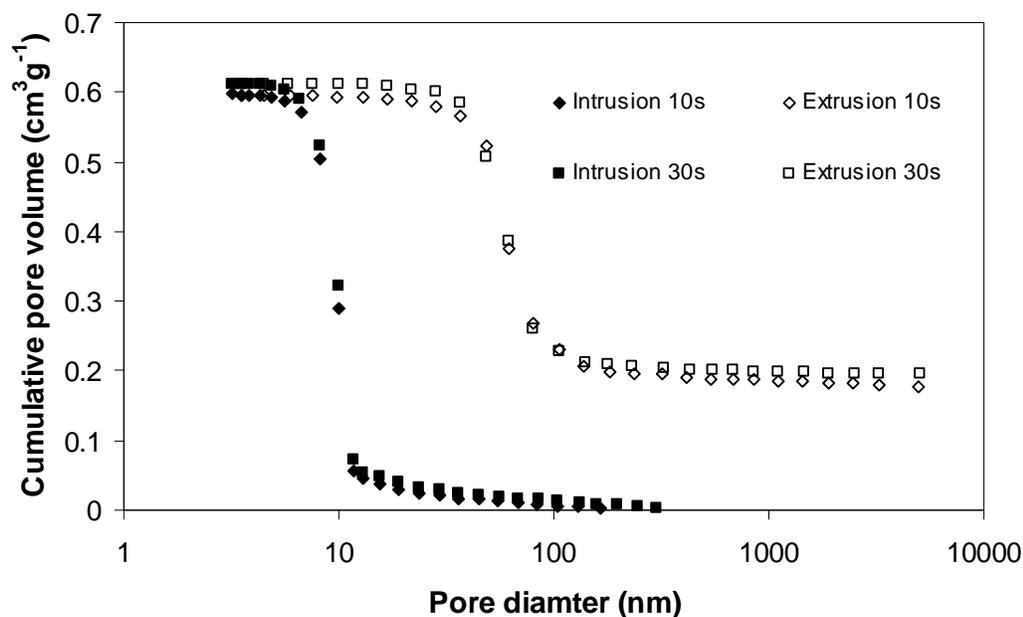
Fig. 2.12. Intra-particle cumulative pore volume data for catalyst sample B (whole) obtained from mercury porosimetry at different equilibration times. Both sample sets belong to the same batch.
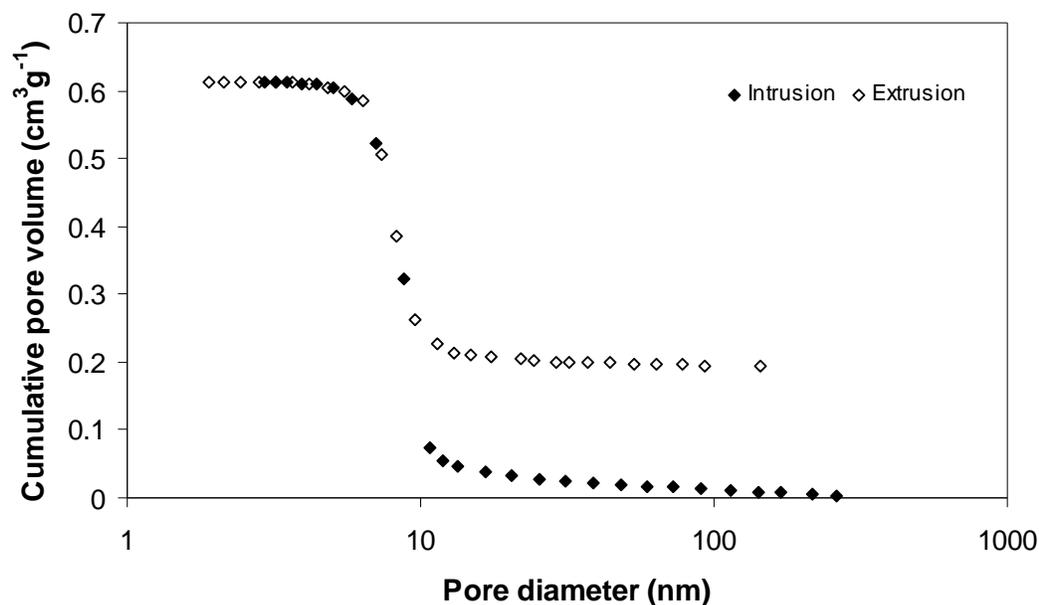
Fig. 2.13. Intra-particle cumulative pore volume data for catalyst sample B (whole) where contact angle hysteresis has been removed after application of the Rigby-Edler equations using the constants in Table 2.4. The equilibration time was 30 s.

For the powder sample investigated, the results obtained are presented Figs. 2.14, 2.15 and 2.16. Once again, like the whole sample, the paths traversed by the mercury curve during the second intrusion and extrusion cycles are similar to the primary step. This confirmed no destruction of the pore structure took place during the experiment. The powdered sample had a percentage entrapment similar to the whole catalyst. However, the pore volume and surface area are lower, as shown in

44

Table 2.5. This is likely to be due to the destruction of some pores during the powdering process leading to a reduction in available surface area and pore volume. Another difference observed between intrusion and extrusion cycles of the whole and powdered samples are the difference in knee shapes during intrusion and extrusion steps. It is also found that the same constants present in Table 2.4 enabled the removal of contact angle hysteresis for the powdered sample as well.
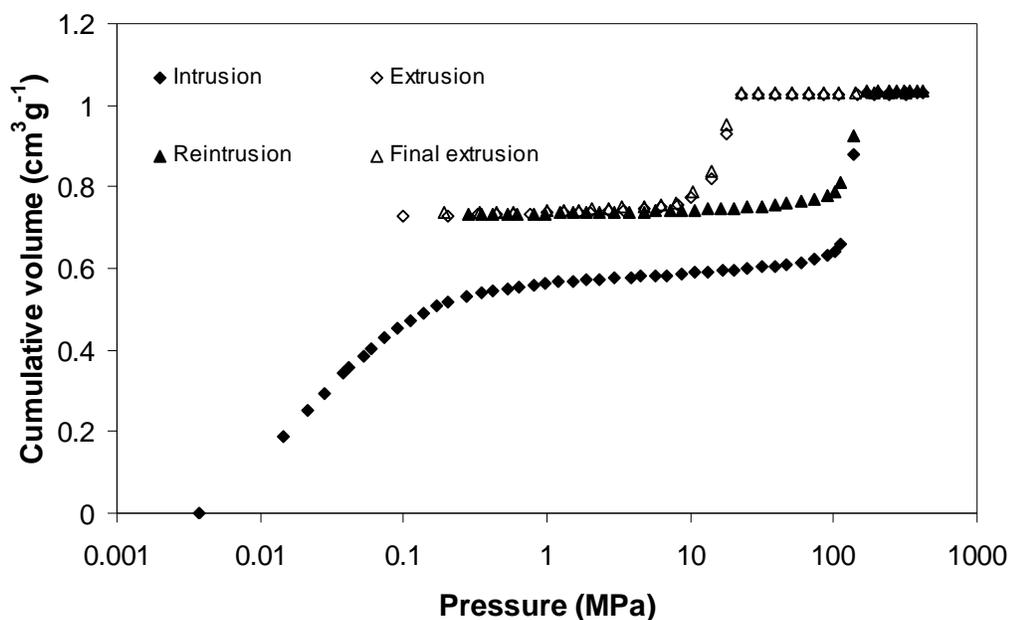
Fig. 2.14. Typical raw mercury intrusion and extrusion data for catalyst sample B in its powdered form at an equilibration time of 30 s. The re-intrusion step followed the path of the primary intrusion step and the same applied for the extrusion cycles as well.

Table 2.5
Typical structural properties of catalyst sample B (powdered) obtained from mercury porosimetry.

Sample	Entrapment percentage (%)	Pore volume (cm³g⁻¹)	Surface area (m²g⁻¹)
B - Powder	32.85	0.45	197
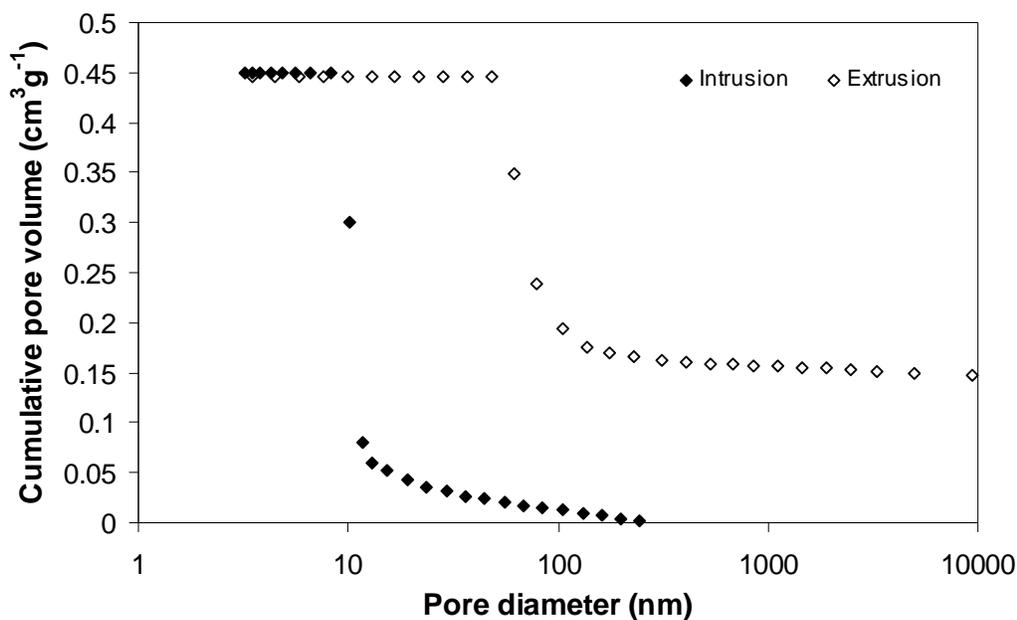
Fig. 2.15. Intra-particle cumulative pore volume data for catalyst sample B in its powdered form obtained from mercury porosimetry at an equilibration times of 30 s.
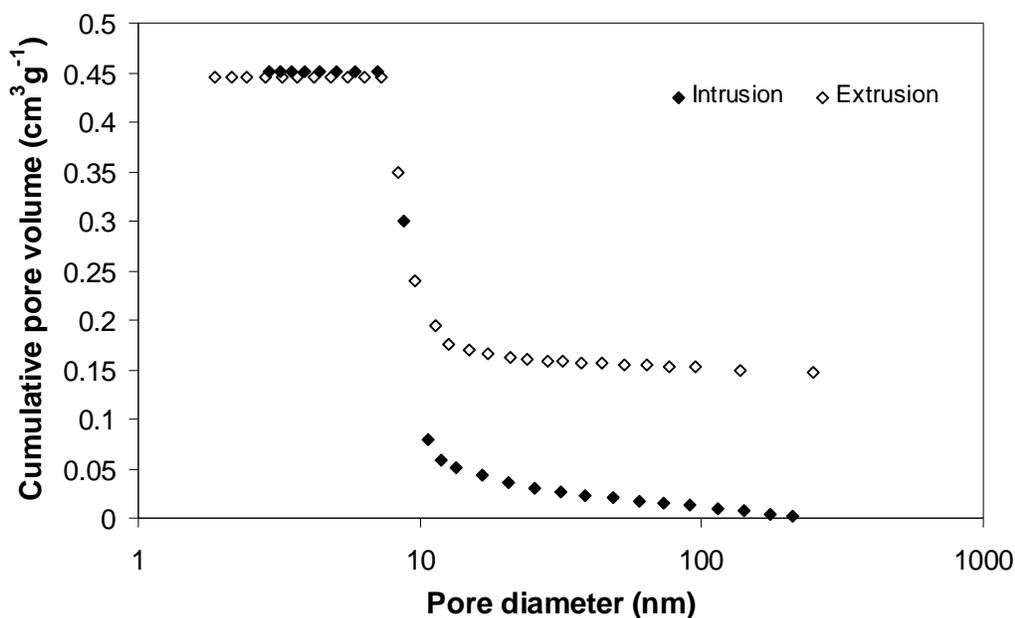
Fig. 2.16. Intra-particle cumulative pore volume data for catalyst sample B (powdered) where contact angle hysteresis has been removed after application of the Rigby-Edler equations using the same constants in Table 2.4. The equilibration time was 30 s.

2.6 DISCUSSION – SAMPLE B

Mercury porosimetry revealed that key characteristic properties of hydroprocessing catalyst sample B are unlike those obtained for sample A. The intrusion cycle revealed a steep step leading to complete saturation of all the pores as seen by the ultimate flat plateau in the pore volume. The following extrusion step was

found to follow a parallel path with a gradual knee leading finally to a smaller degree of entrapment relative to sample A. Such behaviour in catalyst sample B is representative of a narrow unimodal system. No destruction of the pore structure was observed in both whole and powdered samples. The hysteresis observed between the intrusion and extrusion steps for catalyst sample B is similar to pore networks that belong to Class I according to the classification provided by Day et al. (1994). Additionally, the parallel nature of the intrusion and extrusion cycle allowed the use of Rigby-Edler equations (Eq. 2.3) to remove contact angle hysteresis. This helped understand that the majority of the pore volume (~70%) showed reversible contact angle hysteresis (see Figs. 2.13 and 2.16) and it occurred in pores that varied in size from ~6 nm to ~11 nm. This suggests that these pores were likely to be together in the pore network space of catalyst B since superimposition of the intrusion and extrusion curves in this region implied no significant pore shielding. Structural hysteresis as expected was found to occur in larger pores. This is conceivable as the extrusion step is dependent on the pore aspect ratio and the presence or availability of the connecting mercury stream. In large pores, once the mercury stream is disconnected or snapped off, entrapment takes place with no further access to the withdrawing mercury stream. It is likely that some large pores are surrounded by some smaller pores causing this effect.

A major difference between the whole and powdered sample is their respective knee shapes during extrusion. Instead of a gradual knee as seen in the whole sample, a sharp knee is present in the powdered sample. This sharpness was also present in the intrusion step. It appears as though as there is cohesion and breakage of the mercury menisci at the respective points. The effect was found to be repeatable for samples from the same batch (see Fig. A.2.1 in Appendix A) and was not a fault/blip in the machine. It was more likely to be an artefact of the particle size used and can be confirmed by conducting mercury porosimetry experiments on different sized powdered fractions.

It was earlier suggested that catalysts having > 10% MoO_3 displayed flat extrusion curves resulting in very high entrapment of mercury. Though this behaviour was visible in sample A, it was not observed in sample B. It must be noted that this characteristic was despite the fact that both Co and Ni as elements lie next to each other in the periodic table. Further, both catalysts had an alumina support. A difference was clearly visible in the extrusion steps of the two materials even though intrusion steps in both materials are characterised by steep uptakes. Both catalysts were sourced from the same company and the ingredients present in the catalysts are

listed in the materials description in Table 2.1. It appears that the presence of > 10% MoO_3 and 1-10% of CoO_2 caused the non-recoverability of mercury due to some chemical effect. However, the replacement of CoO_2 with NiO_2 does not cause any apparent chemical effect. The mercury stream was able to access the entire pore surface and only 30% of the mercury remained entrapped. Hence, it was likely that there was a significant difference in MoO_3 concentrations within the two catalysts or some difference in the preparation procedures that gave rise to this effect.

2.7 RESULTS – SAMPLE C

A typical mercury intrusion-extrusion experiment performed on sample C at an equilibration time of 10 seconds over the entire pressure range available from the apparatus is displayed below in Fig. 2.17. The pore volume detected by mercury after removal of the inter-particle volume was plotted as a function of the pore diameter calculated by application of the Washburn equation (Eq. 2.1) in Fig. 2.18. The structural properties determined from the intrusion and extrusion steps are tabulated in Table 2.8. The intrusion cycle showed a plateau at high pressures indicating all the available pore volume present within the catalyst was filled. It also displayed a steep slope which was absent in the extrusion cycle. No mercury could be extruded up to atmospheric pressure as seen earlier for sample A.
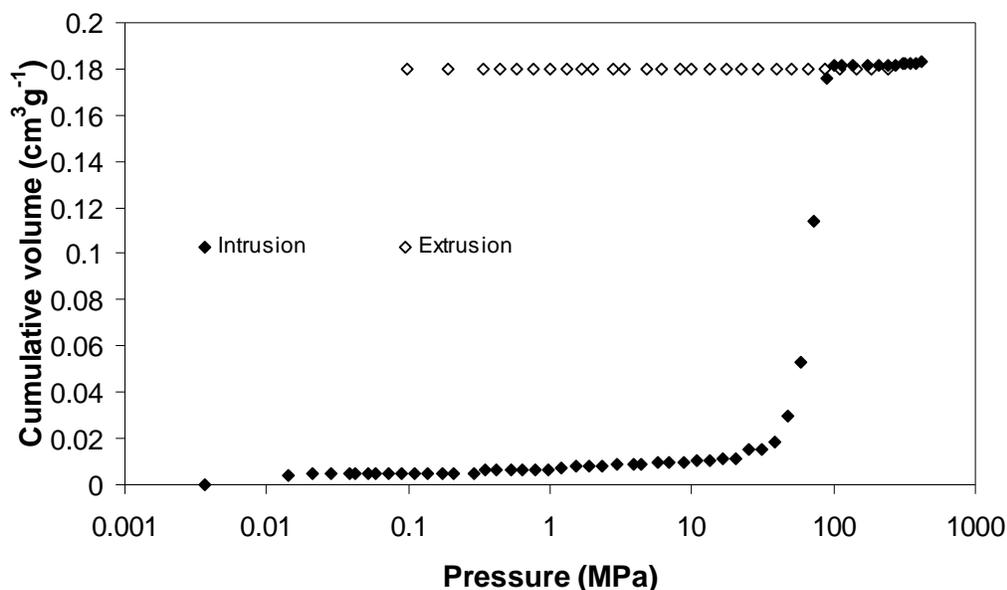
Fig. 2.17. Typical raw mercury intrusion and extrusion data for catalyst sample C (whole) at an equilibration time of 10 s.
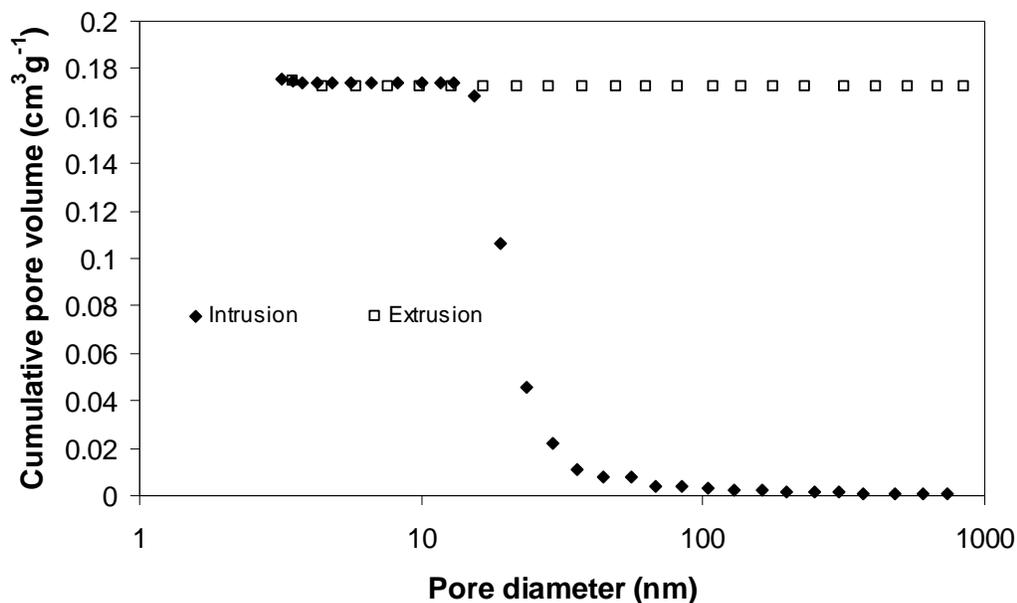
Fig. 2.18. Intra-particle cumulative pore volume data for catalyst sample C (whole) obtained from mercury porosimetry at an equilibration time of 10 s.

Table 2.6
Typical structural properties of catalyst sample C (whole) obtained from mercury porosimetry.

Sample	Entrapment percentage (%)	Pore volume (cm^3g^{-1})	Surface area (m^2g^{-1})
C	99(0.49)	0.18	43

( ) Errors are quoted in brackets.

2.8 DISCUSSION – SAMPLE C

Mercury porosimetry was found to reveal key characteristic properties of the LTS catalyst sample C. The sample exhibited properties different to samples A and B. The catalyst sample C has a significantly smaller pore volume and surface area compared to samples A and B. It is likely that these properties of sample C are favourable in the LTS stage of the WGS reaction. The intrusion cycle in sample C revealed a steep slope and was found to completely saturate the available pore volume. However, the extrusion step exhibited a trend similar to sample A. Approximately 100% of the mercury intruded was unable to be recovered when the system pressure was reduced stepwise from the maximum available pressure (412 MPa) to atmospheric conditions. It remains to be seen if further lowering of the pressure can allow mercury to extrude. Such high entrapment values can only be obtained if the sample studied had a broad distribution of pores or regions having large cavities surrounded by narrow entrances, i.e. a Class III material according to the classification provided by Day et al. (1994). As discussed in Section 2.1, it is well

49

known that mercury interacts with Cu and other metals to form amalgams (Catchpole, 2009; Hadden and Moss 2010). Further, previous work by Lowell and Shields (1982) stressed the importance of pore potential, and the entrapment and hysteresis behaviour when porous samples were impregnated with polar or non-polar materials. They observed that mercury entrapment increased when increasing amounts of polar materials were added to the porous sample. Fig. 2d of this reference must be cited here as this displays the mercury intrusion-extrusion characteristics of an alumina sample treated with 40% $CuSO_4$. Similar to sample C, their alumina sample displayed ~91% mercury entrapment and a flat extrusion curve. From Table 2.3, it is noted that sample C contains 56% copper oxide. Thus, it is likely that the presence of such a high concentration of copper oxide increases the field intensity within the pores and this high pore potential caused the entrapment of mercury within the pores of sample C.

2.9 CONCLUSIONS

Considering all the three samples, the mercury porosimetry analyses showed that samples A and C exhibited horizontal flat extrusion curves giving large entrapment values unlike sample B. The theory of van der Waals forces seemed to be only valid for samples A and C, but not sample B. The promoters present in the three catalysts Co, Ni and Cu and Zn all lie next to each other in increasing order of atomic number (27-30) in the periodic table. Mo is even larger with an atomic number of 42. The properties provided by the vendors in Table 2.1 do not explicitly state the concentration of the different ingredients within samples A and B. It is possible that sample B had less percentage of Ni and Mo, thereby giving rise to parallel intrusion and extrusion steps. The greater percentage of promoters in samples A and C (relative to sample B) means greater dispersion forces between the mercury atoms and atoms present on the catalyst pore surface. This resulted in the inability of mercury to be removed from them during the extrusion process giving rise to apparently greater entrapment of mercury. Thus, mercury porosimetry did not reveal sufficient information for samples which exhibited high pore potential or have a tendency to allow mercury to wet its surface. Thus, there is a need for an alternative catalyst pore characterisation technique.

REFERENCES

ADAMSON, A. W. 1982. *Physical chemistry of surfaces,* New York ; Chichester, Wiley.

ANDROUTSOPOULOS, G. P. & MANN, R. 1979. Evaluation of Mercury Porosimeter Experiments Using a Network Pore Structure Model. *Chemical Engineering Science,* 34, 1203-1212.

CATCHPOLE, S. 2009. Mercury removal in hydrocarbon streams *Petroleum Technology Quarterly* 14, 39-45.

CEREPI, A., HUMBERT, L., & BURLOT, R. 2002. Dynamics of capillary flow and transport properties in porous media by time-controlled porosimetry. *Colloids and Surfaces A: Physicochemical and Engineering Aspects,* 206, 425-444.

DAY, M., PARKER, I. B., BELL, J., FLETCHER, R., DUFFIE, J., SING, K. S. W. & NICHOLSON, D. 1994. Modeling of Mercury Intrusion and Extrusion. *In:* ROUQUEROL, J., RODRIGUEZ-REINOSO, F., SING, K. S. W., UNGER, K. K., eds. *IUPAC Symposium on Characterisation of Porous Solids (COPS III),* 09-12 May 1993. Marseille, France. Studies in Surface Science and Catalysis, 87, Amsterdam: Elsevier Science, 225-234.

FORSYTHE, W. E. 1954; 2003. Table 291. Density and Volume of Mercury -10° to +360°C. *Smithsonian physical tables (9th revised edition).* 9th ed.: Knovel. Available from: http://www.knovel.com/web/portal/browse/display?_EXT_KNOVEL_DISPLAY_bookid=736&VerticalID=0 [Accessed 10 July 2012].

GATICA, J. M., HARTI, S. & VIDAL, H. 2010. Changing the adsorption capacity of coal-based honeycomb monoliths for pollutant removal from liquid streams by controlling their porosity. *Applied Surface Science,* 256, 7111-7117.

GIESCHE, H. 1995. Interpretation of hysteresis 'fine-structure' in mercury-porosimetry measurements. *In:* KOMERNENI, S., SMITH, D. M., BECK, J. S., eds. *Symposium on Advances in Porous Materials, at the 1994 MRS Fall meeting,* 28 November – 01 December 1994. Boston, MA. Materials Research Society Symposium Proceesdings, 371, Pittsburgh: Materials Research Soc, 505-510.

GIESCHE, H. 2002. Mercury Porosimetry. *In:* SCHÜTH, F., SING, K. S. W. & WEITKAMP, J. (eds.) *Handbook of porous solids.* Weinheim: Wiley-VCH.

GIESCHE, H. 2006. Mercury porosimetry: A general (practical) overview. *Particle & Particle Systems Characterization,* 23, 9-19.

HADDEN, R. & MOSS, T. 2010. Dealing with mercury in refinery processes. *Petroleum Technology Quarterly,* 15**,** 29-37.

HE, S. B., SUN, C. L., YANG, X., WANG, B., DAI, X. H. & BAI, Z. W. 2010. Characterization of coke deposited on spent catalysts for long-chain-paraffin dehydrogenation. *Chemical Engineering Journal,* 163**,** 389-394.

KADLEC, O. 1989. On the Theory of Capillary Condensation and Mercury Intrusion in Determining Carbon Porosity. *Carbon,* 27**,** 141-155.

KLOUBEK, J. 1981. Hysteresis in Porosimetry. *Powder Technology,* 29**,** 63-73.

LI, Y. & WARDLAW, N. C. 1986a. The Influence of Wettability and Critical Pore Throat Size Ratio on Snap-Off. *Journal of Colloid and Interface Science,* 109**,** 461-472.

LI, Y. & WARDLAW, N. C. 1986b. Mechanisms of Nonwetting Phase Trapping during Imbibition at Slow Rates. *Journal of Colloid and Interface Science,* 109**,** 473-486.

LIABASTRE, A. A. & ORR, C. 1978. An evaluation of pore structure by mercury penetration. *Journal of Colloid and Interface Science,* 64**,** 1-18.

LOWELL, S. & SHIELDS, J. E. 1982. Influence of Pore Potential on Hysteresis and Entrapment in Mercury Porosimetry - Pore Potential Hysteresis Porosimetry. *Journal of Colloid and Interface Science,* 90**,** 203-211.

LOWELL, S., SHIELDS, J. E., THOMAS, M. A. & THOMMES, M. 2006. *Characterization of porous solids and powders: surface area, pore size and density,* Dordrecht, Kluwer Academic Publishers.

MILBURN, D. R., ADKINS, B. D. & DAVIS, B. H. 1994. Alumina-Supported Molybdenum and Tungsten-Oxide Catalysts - Surface-Area and Pore-Size Distribution from Nitrogen Adsorption and Mercury Penetration. *Applied Catalysis A: General,* 119**,** 205-222.

MILT, V. G., BANUS, E. D., MIRO, E. E., YATES, M., MARTIN, J. C., RASMUSSEN, S. B. & AVILA, P. 2010. Structured catalysts containing Co, Ba and K supported on modified natural sepiolite for the abatement of diesel exhaust pollutants. *Chemical Engineering Journal,* 157**,** 530-538.

MOSCOU, L. & LUB, S. 1981. Practical Use of Mercury Porosimetry in the Study of Porous Solids. *Powder Technology,* 29**,** 45-52.

PIRARD, R., BLACHER, S., BROUERS, F. & PIRARD, J. 1995. Interpretation of mercury porosimetry applied to aerogels. *Journal of Materials Research,* 10**,** 2114-2119.

PORCHERON, F. & MONSON, P. A. 2005. Dynamic aspects of mercury porosimetry: A lattice model study. *Langmuir,* 21, 3179-3186.

PORCHERON, F., MONSON, P. A. & THOMMES, M. 2005. Molecular Modeling of mercury porosimetry. *Adsorption-Journal of the International Adsorption Society,* 11, 325-329.

PORCHERON, F., THOMMES, M., AHMAD, R. & MONSON, P. A. 2007. Mercury porosimetry in mesoporous glasses: A comparison of experiments with results from a molecular model. *Langmuir,* 23, 3372-3380.

RIGBY, S. P. & CHIGADA, P. I. 2010. MF-DFT and Experimental Investigations of the Origins of Hysteresis in Mercury Porosimetry of Silica Materials. *Langmuir,* 26, 241-248.

RIGBY, S. P., CHIGADA, P. I., WANG, J. W., WILKINSON, S. K., BATEMAN, H., AL-DURI, B., WOOD, J., BAKALIS, S. & MIRI, T. 2011. Improving the interpretation of mercury porosimetry data using computerised X-ray tomography and mean-field DFT. *Chemical Engineering Science,* 66, 2328-2339.

RIGBY, S. P. & EDLER, K. J. 2002. The influence of mercury contact angle, surface tension, and retraction mechanism on the interpretation of mercury porosimetry data. *Journal of Colloid and Interface Science,* 250, 175-190.

ROOTARE, H. M. & PRENZLOW, C. F. 1967. Surface Areas from Mercury Porosimeter Measurements. *The Journal of Physical Chemistry,* 71, 2733-2735.

TARIQ, F., HASWELL, R., LEE, P. D. & MCCOMB, D. W. 2011. Characterization of hierarchical pore structures in ceramics using multiscale tomography. *Acta Materialia,* 59, 2109-2120.

VAN BRAKEL, J., MODRY, S. & SVATA, M. 1981. Mercury Porosimetry - State of the Art. *Powder Technology,* 29, 1-12.

VAVRA, C. L., KALDI, J. G. & SNEIDER, R. M. 1992. Geological Applications of Capillary-Pressure - a Review. *AAPG Bulletin-American Association of Petroleum Geologists,* 76, 840-850.

WARDLAW, N. C. & MCKELLAR, M. 1981. Mercury Porosimetry and the Interpretation of Pore Geometry in Sedimentary-Rocks and Artificial Models. *Powder Technology,* 29, 127-143.

WASHBURN, E. W. 1921. The Dynamics of Capillary Flow. *Physical Review Series II,* 17, 273-283.

CHAPTER 3 – GAS ADSORPTION POROSIMETRY

Chapter 3 of this thesis introduces the reader to the second conventional catalyst characterisation technique that has been investigated in this work. Gas (nitrogen) adsorption porosimetry is another popular method with the first reported investigations taking place more than two centuries back. This chapter will first provide the reader with an introduction to the fundamentals of the technique. The determination of catalyst surface area, fractal dimension, pore volume have been briefly explained and the origin of hysteresis in adsorption-desorption isotherms are also given. The reader will then begin to understand that like mercury porosimetry, the method is not ideal and has advantages and disadvantages. Incorrect use of nitrogen adsorption-desorption isotherms within the literature has also been highlighted. In this work, the method has been used in the characterisation of three industrially relevant catalysts (that were investigated earlier using mercury porosimetry). Their key characteristic properties like BET surface area, fractal dimension, pore volume, pore size distribution are studied and they are compared with results from mercury porosimetry. Results obtained are in line with mercury porosimetry in that all samples are mesoporous but nitrogen adsorption showed the presence of some microporosity in these catalysts. The reasons regarding their performance in the microreactor experiments are also discussed. The work has revealed that surface area, pore volume and pore size are key properties especially for catalysts used in heavy oil upgrading reactions.

3.1 INTRODUCTION – CONCEPT AND THEORY

Adsorption is a separation process which involves the transfer of molecules from a fluid phase to a solid surface. It has gained significance and widespread use due to its ease of applicability in the determination of catalyst characteristic properties like surface areas, pore volumes and pore size distributions of porous materials, particularly catalysts and adsorbents. From a reaction engineering perspective, reaction rate is determined by the internal surface area of the catalyst apart from temperature, particle or pellet size and reactant(s) concentration. Reactant molecules adsorb on the active sites present in the catalyst surface to undergo reaction. Catalyst activity is determined by the availability of active sites to reactant molecules and this in turn tends to depend on the available catalyst surface area. Every catalytic chemical

reaction depending on reaction conditions will require catalysts with certain physical properties that provide optimum performance. However, the presence of side reactions, contaminants within the feedstock, improper reaction control, etc. can cause catalysts to perform in an inadequate manner. To aid the design of the right catalyst, determination of the above mentioned physical properties are essential. This will be focus of the work in this chapter.

Adsorption is classified into two types, namely physisorption and chemisorption. In physisorption or physical adsorption, gas molecules are attracted to the solid (or catalyst) surface by van der Waals forces of attraction. They undergo a momentary retention before being replaced by other gas molecules when attractive forces between the solid and the gas are greater than those between the gas molecules itself. No chemical bond is formed between the adsorbed gas molecules and molecules of the catalyst. Thus, only low heats of adsorption are observed and they do not cause any structural change to the catalyst surface. The process is fully reversible and the number of layers adsorbed can build up giving rise to multilayer adsorption. In contrast, chemisorption or chemical adsorption involves the formation of a chemical bond between the gas molecule and the solid giving large heats of adsorption. The process is irreversible and is limited to the formation of a single layer. In the adsorption process, the solid is usually called the adsorbent, the gas molecules are called the adsorptive and when bound on the catalyst surface are termed as adsorbate (Gregg and Sing, 1982; Rouquerol et al., 1999; Lowell et al., 2006). The work presented in this chapter deals with physisorption of gases (i.e. nitrogen gas only) where the amount adsorbed is expressed as a function of increasing pressure at constant temperature. Data expressed in this manner are called adsorption isotherms. Adsorption of gases on porous solids can be determined either volumetrically or gravimetrically. The experiments discussed in this chapter follow the method of volumetric adsorption.

When gas molecules are confined in the pore space of a solid, the size of the pores can have a strong effect on the interaction forces that exist between the adsorbate-adsorbate and adsorbate-adsorbent molecules. This directly has an effect on the isotherm shapes obtained. The different classes of pore size[14] proposed by the International Union of Pure and Applied Chemistry (IUPAC) (as mentioned earlier in Section 1.6 in Chapter 1) were primarily derived due to the apparent differences in the adsorption mechanisms of each class of pores. Adsorbate molecules when confined in

---

[14] For reference, all pores with widths > 50 nm are termed macropores, those with widths between 2 and 50 nm are termed mesopores and those with widths < 2 nm are termed micropores (Sing et al., 1985).

each of the above classes of pores experience different interaction strengths. In macropores, adsorbate-adsorbate interactions tend to dominate with little adsorbent-adsorbate interactions. However, mesopores and micropores display significant differences. In mesopores, both adsorbate-adsorbate and adsorbent-adsorbate interactions are equally important. A thin film is formed along the surface of the mesopore that builds up in thickness due to cooperative effects between the adsorbed molecules eventually condensing to a liquid. Micropores display a rapid filling mechanism; this is mainly due to the overlap of interaction forces from opposite walls in the tiny pores (Gregg and Sing, 1982; Rouquerol et al., 1999; Lowell et al., 2006). In typical porous media, it is natural that there may be a distribution of different pore sizes or the material may only consist of a single pore size. In some cases, however, the material may even be non-porous. Depending on the distribution of different sized pores, the IUPAC (Sing et al., 1985) also proposed a classification comprising six characteristic adsorption isotherms that are normally observed for porous materials. Type I is a reversible isotherm that is concave to the relative pressure P/P_0 axis. It is given by microporous solids where the amount adsorbed approaches a limiting value as the relative pressure approaches unity. Type II isotherms are reversible and represent unrestricted monolayer-multilayer adsorption on non-porous or macroporous materials. A distinct point, termed B, is usually visible which indicates the formation of a statistical monolayer. This point is usually followed by a linear region representing multilayer adsorption. Type III isotherms are reversible but convex to the P/P_0 axis and therefore there is no point B. Such isotherms are representative of weak attractive forces between the adsorbate and the adsorbent. Type IV isotherms display a point B and exhibit a reversible multilayer region similar to Type II isotherms. However, at intermediate and high relative pressures, capillary condensation takes place within the pores. This causes the system to display hysteresis. This type of isotherm is usually given by mesoporous solids and will be seen for the catalysts investigated in this work. Type V isotherms are similar to type IV in that they also have a hysteresis loop. However, they do not have a point B and are convex to the P/P_0 axis. Hence, low pressure regions are similar to Type III isotherms. Type VI isotherms represent step-wise multilayer adsorption on a uniform non-porous surface. The step shape depends on the adsorbent surface, adsorptive and the temperature of adsorption (Gregg and Sing, 1982; Sing et al., 1985). The chemical inertness of nitrogen towards most solid surfaces, its ability to exhibit sufficient but not excessive specificity of adsorption to give a well defined monolayer on most surfaces, its low cost and ease of operation of commercial equipments has made it an

adsorbate of choice for gas adsorption experiments (Sing, 2001). Nitrogen will be the adsorbate for the three catalysts investigated in this chapter.

3.1.1 BET SURFACE AREA BY ADSORPTION

Earlier, in the preceding paragraph, it was mentioned that Type II and IV isotherms are concave to the P/P_0 axis and display a region of linear uptake called the multilayer adsorption region. A theoretical model was developed by Brunauer, Emmett and Teller (1938) describing multilayer adsorption by extending the Langmuir theory of monomolecular adsorption to infinite layers. The model named after them, the BET isotherm, is given by:

$$\frac{V}{V_m} = \frac{Cx}{(1-x)(1-x+Cx)}. \tag{3.1}$$

It has been universally used to estimate the surface area of mesoporous materials. In Eq, (3.1), $x = P/P_0$ is the relative pressure of the adsorbate, V and V_m are the amount adsorbed, and amount adsorbed to form a monolayer respectively, and C is the BET constant which is given by:

$$C = \exp\left(\frac{E_1 - E_L}{RT}\right). \tag{3.2}$$

C measures the strength of adsorption. It is related to the difference in energy of adsorption in the first layer (E_1) and the heat of condensation of the liquid adsorbate (E_L). In Eq. (3.2), R is the ideal gas constant and T is the adsorption temperature. However, there are a few matters of concern with the BET model. The BET equation (Eq. 3.1) is only valid at low relative pressures and, often only over a specific range which is highly dependent on the system studied. Generally, the amount adsorbed can be fitted to the linear form of the BET equation over the relative pressure range $0.05 \leq P/P_0 \leq 0.3$. The BET model assumes that all adsorption sites are energetically equivalent and that adsorption occurs on a flat surface. Further, the model also assumes no lateral interaction between the adsorbed molecules. Finally, to estimate the surface area of a porous material, it is necessary to assume a molecular area for the adsorbed molecule (Gregg and Sing, 1982; Rouquerol et al., 1999; Sing, 2001; Lowell et al., 2006).

The surface area of a porous solid can be determined from the BET model (Eq. 3.1) in two steps. Firstly, the standard model (Eq. 3.1) is transformed to a straight line model:

$$\frac{x}{V(1-x)} = \frac{1}{V_m C} + \frac{C-1}{V_m C} x ,$$ (3.3a)

which is fitted to the experimental data in the multilayer adsorption region. The slope:

$$Slope = \frac{C-1}{V_m C} ,$$ (3.3b)

and intercept:

$$Intercept = \frac{1}{V_m C} ,$$ (3.3c)

can then be used to determine the monolayer capacity V_m and the BET C constant. The second stage involves the use of the monolayer capacity V_m to evaluate the BET surface area A_{BET} of the porous medium or catalyst using the following expression:

$$A_{BET} = \frac{V_m}{22414} \sigma N_A = n_m \sigma N_A .$$ (3.3d)

Here an assumption is made regarding the value of the molecular area σ occupied by the adsorbate in the completed monolayer. In Eq. (3.3d), n_m is the monolayer capacity and N_A is the Avogadro number. The molecular area σ used is usually based on the assumption that the molecules are spherical and rest on a plane surface with a packing similar to that in the bulk liquid. However, in reality most adsorbate molecules of interest are not spherical. Nitrogen gas molecules, the adsorbate of interest in this chapter, are not spherical and can adsorb on the surface in a flat or upright position. Nitrogen molecules also possess a quadrupole moment. This causes nitrogen molecules to adsorb in a localised manner on some surfaces mimicking the effect of the formation of a monolayer even though no monolayer has been formed in reality (Gregg and Sing, 1982; Sing, 2001; Lowell et al., 2006). Thus, chemical heterogeneity of the surface can have a strong effect on the molecular area of adsorbed molecules. High energy sites tend to have strong interactions with nitrogen molecules causing them to pack in a denser manner relative to low energy sites. Thus, in reality only an apparent area is determined. Karnaukhov (1985) has elaborated on the above effect and has plotted the variation of the nitrogen molecular area as a function of the BET C constant (in Fig. 7 of this reference). This plot was used to determine the molecular area in the estimation of BET surface areas of catalysts investigated in this work. In order to accurately estimate the BET surface area of catalysts, the selection of correct relative pressure range involving multilayer adsorption and the use of the correct molecular area of the adsorbate is most critical.

3.1.2 FRACTALS

The tendency of nitrogen to adsorb locally on certain adsorbents prevents the determination of the exact BET surface area. Under such conditions different adsorptives such as argon, carbon dioxide, butane, water vapour, etc. may be used. But the BET surface area determined need not match with those obtained using nitrogen. It will scale depending on the molecular area of the adsorbate. A similar issue is also present during the adsorption of nitrogen on preadsorbed and immobilised films. It is necessary to understand if the film adsorbed uniformly or in an irregular manner (as will be seen in Chapter 4). The presence of different surfaces means different interaction strengths and thus different molecular areas. The fractal theory presents a solution to this dilemma as it provides a unique value called the surface fractal dimension D. Surfaces that possess a property of self similarity or geometric invariance when scaled over different length scales are called fractal surfaces. The fractal approach involves the study of how a property varies depending on the resolution of its measurement. It may be defined by a scaling power law of the following manner:

$$Amount\ of\ a\ surface\ property \propto resolution\ of\ analysis^{D}. \qquad (3.4)$$

Fractal surfaces look the same at all levels of magnification. The degree of roughness of catalysts can be characterised by the surface fractal dimension D which is a value between 2 and 3 using different techniques like adsorption, small angle x-ray scattering, neutron scattering, etc. (Rouquerol et al., 1994; Neimark, 2002). In this chapter (and Chapter 4), the fractal form of the Frenkel Halsey Hill (FHH) theory is used to measure the roughness of the catalyst surface. This parameter is independent of the molecular area. The method also has the advantage that it requires only the use of a single adsorptive.

The FHH theory is an alternative to the BET model for describing multilayer adsorption. Unlike the BET model, which considers the adsorption of individual molecules on different sites to build up layers, the FHH model considers the influence of the surface on the thickness of each layer of adsorbed film. Once the film thickness increases to two or three molecular layers, the influence of the surface is smoothed out due to surface tension effects and the adsorbed film can be considered as a liquid (Gregg and Sing, 1982). Thus, the thickness of the slab of adsorbed films acts as the varying ruler in this model. During the initial stages of multilayer formation, the interaction between the gas molecules and the surface is governed by van der Waals attraction forces (Ismail and Pfeifer, 1994; Sahouli et al., 1997). In this regime, the FHH fractal dimension D can be estimated from:

$$\ln \frac{V}{V_m} = K + \left(\frac{D-3}{3} \right) \left[\ln \left[\ln (P_0 / P) \right] \right]. \tag{3.5a}$$

However, as the number of layers increases, there is an enhancement of surface tension effects and the regime changes. In the capillary condensation regime, the FHH fractal dimension D can be estimated from:

$$\ln \frac{V}{V_m} = K + (D-3) \left[\ln \left[\ln (P_0 / P) \right] \right]. \tag{3.5b}$$

In both regimes, the number of adsorbed layers n can be determined from:

$$n = \left(\frac{V}{V_m} \right)^{1/D-3}, \tag{3.5c}$$

which gives a sense of the length scale over which the fractal dimension is valid. In order to determine which regime is operating, the difference $\delta = 3(1+S) - 2$ (where S is the slope from Eq. 3.5a) is determined. The influence of surface tension is negligible if $\delta > 0$ and Eq. (3.5a) determines the fractal dimension of the surface. On the other hand, if $\delta < 0$, surface tension effects are non-negligible and Eq. (3.5b) determines the fractal dimension of the surface (Pfeifer and Ismail, 1994). K is the proportionality constant in Eq. (3.5a) and Eq. (3.5b). A value of 2 for the fractal dimension indicates a smooth Euclidean surface while a value close to 3 represents a surface with increasing roughness. For all the catalysts investigated in this work, the FHH fractal dimension D was determined from the capillary condensation regime.

3.1.3 DUAL SURFACE THEORY OR HOMOTATTIC PATCH MODEL

Most adsorption models assume the solid surface to be geometrically and chemically homogeneous. However, it is possible to gain an understanding of the heterogeneity present in the solid phase by modelling adsorption using a homotattic patch model (McMillan, 1947) such as by the application of a dual surface theory (Walker and Zettlemoyer, 1948). For example, if the surface of a porous medium consists of only micropores and mesopores, the micropore region can be defined by a model that accounts for the rapid filling mechanism, while the remaining pore space which contains larger mesopores may be defined by a model that describes multilayer adsorption. Recently, Chua et al. (2010) applied this model to PtH–ZSM–5 catalysts in their fresh and coked forms. They described nitrogen and argon uptake of the zeolitic catalyst by a Langmuir component and a BET component to find that the presence of coke caused a change in the fraction of the pore space that contributed to each uptake model. Thus, the model provided an understanding of whether coke was

located in the micropores and/or mesopores. Different uptake models may be combined to create an equation of the following form:

$y = p_1(model\ 1) + p_2(model\ 2) + .. + p_i(model\ i)$ such that $p_1 + p_2 + .. p_i = 1$, (3.6a)

where y is the total amount adsorbed, p_i is fraction of the pore space contributing to the uptake defined by *model i*. One of the catalysts studied in this work exhibited a surface that could be described by a two-component (Langmuir and BET) model. Such a model will have the following equation:

$$V = (1-p)\left(\frac{V_m bx}{1+bx}\right) + p\left(\frac{V_m Cx}{(1-x)(1-x+Cx)}\right),$$ (3.6b)

where V is the total volume adsorbed, p is the fraction of the pore space contributing to the BET component, V_m is the monolayer capacity, b is the Langmuir constant, x is the relative pressure P/P_0 and C is the BET constant.

3.1.4 PORE VOLUME

Micropore filling contributes to adsorption before the multilayer adsorption region and capillary condensation takes place above the multilayer adsorption region. As the number of layers increases, lateral interactions between adsorbate volumes assume significance since the influence of the force field from the catalyst surface decreases. In mesopores, the adsorbed molecules within the pores of the solid condense to a liquid. This phenomenon is termed capillary condensation. At saturation conditions, i.e. at $P/P_0 =$ ~0.95, the amount adsorbed can be converted to determine the total volume of pores present in the catalyst that is accessible to any adsorptive (Lowell et al., 2006). This volume is also called the Gurvitsch volume and can be determined by the following equation:

$$Gurvitsch\ volume = \left(\frac{V_{0.95}}{22414}\right) \times 34.68,$$ (3.7)

where $V_{0.95}$ is the volume adsorbed at $P/P_0 = 0.95$, and 34.68 cm^3mol^{-1} is the molar volume of liquid nitrogen at 77 K. Higher relative pressures may be used provided accurate pressure readings are available.

3.1.5 MESOPORE ANALYSIS

The Kelvin equation:

$$\gamma V_M\left(\frac{1}{r_1} + \frac{1}{r_2}\right) = RT \ln\left(\frac{P}{P_0}\right),$$ (3.8a)

derived from the Young-Laplace equation, relates the change in vapour pressure for a curved surface such as a liquid in a capillary to the size of the capillary. It is a fundamental relationship that helps to measure pore sizes in the mesoporous region and understand capillary condensation and hysteresis (Adamson, 1982; Gregg and Sing, 1982; Lowell et al., 2006). In Eq. (3.8a), γ is the surface tension of the adsorbate, V_M is the molar volume of the adsorbate, r_1 and r_2 are the radii of curvature that define the curved surface, R is the ideal gas constant, T the temperature. For a cylindrical pore, the radii of curvature r_1 and r_2 are r and ∞ respectively. Substituting r and ∞ for r_1 and r_2 respectively, the final form of the Kelvin equation will be obtained:

$$\gamma V_M \left(\frac{1}{r} + \frac{1}{\infty} \right) = -RT \ln \left(\frac{P}{P_0} \right),$$
(3.8b)

$$\ln \left(\frac{P}{P_0} \right) = -\frac{\gamma V_M}{RT} \left(\frac{1}{r} \right).$$
(3.8c)

The radius obtained from the Kelvin Equation is not the actual pore radius since prior to condensation adsorption has already taken place along the pore walls in the form of a thin film. Conversely, an adsorbed film remains on the pore wall during desorption as well since evaporation of only the core takes place, Therefore, it is the sum of the thickness t and the Kelvin radius r obtained from Eq. (3.8c) that gives the pore radius r_p:

$$r_p = r + t.$$
(3.8d)

The thickness t of the adsorbed film is the number of adsorbed layers times the thickness of one layer. It is a function of the adsorbate pressure and molecular size. For a particular system, it is assumed that the thickness of the adsorbed film that is formed in the pores would be similar to that on a similar non-porous surface. For an alumina surface, Harkins and Jura (1944) derived the thickness equation:

$$t = \left[\frac{13.99}{\log(P_0/P) + 0.034} \right]^{1/2},$$
(3.8e)

which was developed by Boer et al. (1966).

The Kelvin equation along with the thickness equation for the respective material can be included in the Barrett, Joyner and Halenda (BJH) algorithm (Barrett et al., 1951) to determine the pore volume distribution as a function of the pore size. Care must be taken to ensure that the right choice of the sorption branch is made for determining the pore size distribution. A study of the origin of hysteresis by various workers has revealed that the obtained BJH pore size distribution is not entirely accurate especially in the microporous and lower mesoporous regions. Recent work

has argued the use of density functional theory (DFT) (Neimark and Ravikovitch, 2001) and grand canonical Monte Carlo (GCMC) simulations (Coasne et al., 2008a, 2008b) which describe the local fluid structure using statistical mechanics to determine pore size distributions. In contrast to this is the evidence provided by Rigby et al. (2008) where the Kelvin equation along with the correct thickness equation described the pore characteristics of a mesoporous catalyst support. Presently, the above mentioned computational methods (DFT and GCMC), though remarkable in their development, are still at a nascent stage in their applications to generating the pore size distribution of the type of catalysts investigated in this work. This has been primarily due to the difficulty in modelling the geometrical and chemical heterogeneity present in catalysts. Recently, a chemically heterogeneous model was used by Rasmussen et al. (2012), where a single non-wetting site in a simulated structure was used to study cavitation[15] during nitrogen desorption.

3.1.6 HYSTERESIS

Mesoporous solids are characterised by adsorption-desorption isotherms where for a given relative pressure greater volumes of adsorbate are present in the desorption branch relative to the adsorption branch. This irreversibility of adsorption-desorption isotherms is called hysteresis. In addition to the general classification of adsorption isotherms proposed by the IUPAC (Sing et al., 1985), a general classification of the hysteresis loops was also given. Type H1 isotherms consist of parallel adsorption and desorption branches which close at relative pressures $P/P_0 \sim 0.4$. They are representative of mesoporous materials that have a narrow uniform pore size distribution. Type H2 isotherms (as will be seen in the work done here) have a wide (non-parallel) hysteresis loop and are representative of mesoporous materials that have a wide pore size distribution. Type H3 loops do not exhibit any limiting uptake at high relative pressures and are usually observed for aggregates of plate-like particles that have slit-shaped mesopores. Type H4 loops are characteristic of aggregates with narrow slit-shaped mesopores that also have some microporosity (Sing et al., 1985).

Initially, as with mercury porosimetry, hysteresis in gas adsorption was also attributed to contact angle hysteresis (Zsigmondy 1911, cited by Adamson 1982, p. 585) due to the presence of impurities. Such an adsorption-desorption isotherm was irreversible over the entire relative pressure range and did not agree with the observations that showed a closure of the hysteresis loop at intermediate relative

---

[15] Refer Section 3.1.6 for more details on cavitation.

pressures. Two major models can be invoked to understand the origin of hysteresis. They include the independent pore model and the network model.

An independent or single pore model can be used to describe systems that display Type H1 isotherms. The foundation for this model can be attributed to Cohan (1938) who suggested that capillary condensation was responsible for hysteresis by applying the Kelvin equation (Eq. 3.8) in an open cylindrical pore. The Cohan theory argues that the different radii of curvature for the menisci formed during adsorption and desorption was responsible for hysteresis. However, later developments and theories argued that hysteresis was caused by the presence of metastable states of the pore fluids during the capillary condensation transition and such effects were not present during capillary evaporation or desorption (Sing and Williams, 2004; Lowell et al., 2006). The development and the use of templated or ordered mesoporous materials that possess regular geometry and narrow uniform pore size distribution has greatly advanced the understanding of the different factors responsible for hysteresis by performing adsorption experiments with them (Morishige and Shikimi, 1998).

In contrast to the single pore model, the network model relies on the interconnectivity between the pores to explain hysteresis. Such a model is applicable for materials exhibiting Type H2 hysteresis. Porous materials may comprise of ink-bottle like pores or regions which cause pore blocking effects delaying desorption. Apart from pore blocking effects, desorption branches are also amenable to a cavitation phenomena. Experimental evidence of the different mechanisms of desorption found for ordered mesoporous materials was provided by Ravikovitch and Neimark (2002), where they showed pore blocking only occurred when the desorption pressure was larger than the cavitation pressure but less than the pressure required for desorption from the cavity. However, if the desorption pressure became less than the cavitation pressure, a gas bubble would be induced within the cavity causing its spontaneous desorption. Their work was developed further by Morishige et al. (2006) where cross over from pore blocking to cavitation was clearly observed in ordered mesoporous materials as the adsorption-desorption temperature increased. The former work on cavitation phenomena can be closely linked to the classical tensile strength effect as propounded by Burgess and Everett (1970) and Gregg and Sing (1982). These workers obtained evidence that the hysteresis loop for various porous materials closed at a relative pressure P/P_0~0.42-0.5 for nitrogen sorption at 77 K. This is because further reduction of pressure would be unable to suppress the nucleation of gas bubbles and the condensed liquid state is no longer thermodynamically favourable. The single pore model and the network model can be imagined to be the two poles in

the interpretation of hysteresis in gas adsorption-desorption isotherms. It must be noted that there is also evidence where the pore network of catalyst supports show menisci geometry effects similar to a single pore as in Rigby et al. (2008).

From the preceding paragraphs in this section, and Section 3.1.5, it is clear that every isotherm has to be thoroughly analysed to determine whether the adsorption isotherm or desorption isotherm produces the pore size distribution that is representative of the material. Materials which possess type H2 hysteresis loop are composed of networks which give some degree of pore blocking and in some cases cavitation as well. Since the adsorption isotherm is not prone to either mechanism, it is better to select the adsorption isotherm to generate the pore size distribution. On the other hand, recent investigators have started to discuss the effect of advanced adsorption (Felipe et al., 2006; Hitchcock et al., 2010), where pores fill up much earlier than the actual equilibrium relative pressure corresponding to them. Under these scenarios, it may be better to use the desorption isotherm to obtain the pore size distribution or use the adsorption isotherm of a sample that does not display advanced adsorption effects.

The literature presents several instances of the use of nitrogen gas adsorption porosimetry in the characterisation of catalyst pore textural properties and surface area. Nevertheless, there is evidence of the use of non-equilibrated or non-isothermal adsorption isotherms as seen in Weissman and Edwards (1996), Rana et al. (2005a, 2005b), and Rayo et al. (2008). The adsorption-desorption isotherms in these references are characterised by hysteresis loops which close at relative pressures < 0.4 and some even have desorption isotherms with a greater volume desorbed than was initially adsorbed at saturation conditions ($P/P_0 = 1$). From the theory of gas adsorption porosimetry, it is clearly understood that such isotherms need not be representative of the porous material these workers studied and doubts can be raised on the assessed catalyst properties.

3.1.7 PERCOLATION ANALYSIS (SEATON, 1991)

It is possible to gain structural information, i.e. connectivity Z and lattice size L, of a porous medium from experimental nitrogen gas adsorption data by constructing a pore network model that maps the pore structure of the real sample to an array of lattice sites. Connectivity Z is the number of pores connected to a pore and lattice size L is the average linear dimension representing the length of the microparticles of the pellet or the distance between adjacent macropores. The size of

the pores in the simulated network can be adjusted to match the pore size distribution of the sample. The procedure to determine Z and L is based on percolation theory and was conceived by Seaton (1991).

Seaton (1991) used a random pore bond network model to represent the bidisperse pore structure of catalyst pellets. Each pellet was assumed to be an aggregate of microparticles that are smaller than the pellet itself. Thus, pore spaces within the microparticles are micro or mesoporous while those between the different particles formed a macropore network which spanned the solid. The method provides structural information of only the micro-mesoporous network, since macropores are unfilled in nitrogen gas adsorption. Details regarding the procedure to determine Z and L can be seen in Seaton (1991). It is only summarised here. Firstly, the BJH pore size distribution is obtained for the catalyst. Following this, the ratio of the percolation probability to the bond occupation probability F/f is calculated from the adsorption and desorption isotherms. This can then be related to the pore size by using the Kelvin equation (Eq. 3.8) (along with the appropriate film thickness equation). The BJH pore size distribution can then be used to calculate the bond occupation probability f. The percolation probability F is now obtained as both F/f and f is known. Z and L can then be obtained by fitting the set of experiment scaling data (f,F) to the generalised scaling relation h:

$$L^{\beta/\nu}ZF = h\left[(Zf - 3/2)L^{1/\nu}\right],$$ (3.9)

between f and F. In Eq. (3.9), $\beta = 0.41$ and $\nu = 0.88$ are the critical exponents. The scaling relation was constructed using the simulation data of Kirkpatrick (1979, cited by Seaton 1991, p.1899).

The parameters Z and L are used to characterise the accessibility of the pore network and the shape of the hysteresis loop in sorption isotherms. Highly accessible pore networks are usually characterised by large values of Z and smaller values of L while the converse is true for less accessible networks. The knee of the desorption isotherm coincides with the percolation threshold of the network and also represents the onset of penetration of the vapour phase into the porous medium. In general, for a small, highly-connected random pore bond network, the onset of percolation occurs earlier. Thus, highly connected networks are characterised by narrow hysteresis loops (Rigby and Fletcher, 2004).

3.1.8 CHEMICAL HETEROGENEITY EFFECTS ON GAS ADSORPTION

The presence of different metal atoms, or different functional groups, on the surface of a catalyst can also affect the adsorption of nitrogen or other adsorbates such as water. Samples A and B studied in this thesis contain alumina and precipitated silica which usually have hydroxyl groups attached to them. Their effect on adsorption can be easily determined by obtaining the BET surface area of catalysts. The molecular area occupied by adsorbate molecules varies depending on the interaction strength between the gas adsorbate molecules and those present on the surface. For example, the presence of hydroxyl groups on the surface can affect the adsorption of nitrogen due to its quadrupole moment. Similarly the presence of oxygen atoms on carbonised surfaces can also affect the adsorption of water, as they tend to become sites for hydrogen bonding. Thus, the packing of nitrogen or water molecules can be localised giving an apparent effect of monolayer formation. As mentioned earlier in section 3.1.1, high energy sites tend to have strong interactions with nitrogen molecules causing them to pack in a denser manner relative to low energy sites (Gregg and Sing, 1982). The relative strength of interaction between the gas adsorbate molecules and the adsorbent can be estimated from the BET C constant, which also depends upon the molecular area of the adsorbate as shown by Karnaukhov (1985). A similar procedure has been followed in this thesis during the characterisation of the different catalyst samples. With respect to water adsorption (which will be discussed in Chapter 4), the literature reveals that the isotherms for many catalyst materials are Type III (Gregg and Sing, 1982), indicating specific adsorption on sparse sites. However, for catalysts studied in this thesis, water adsorption is of Type IV which is similar to that exhibited by nitrogen. Further, the BET surface areas obtained using nitrogen and water showed little difference implying that the two adsorbates perceived similar surfaces. The effect of water adsorption and its freezing on nitrogen adsorption which is discussed in the Chapter 4 takes place at higher pressures, i.e. once capillary condensation is achieved. At these stages, surface chemistry will not have a strong effect as it will be covered with adsorbate multilayers, but pore size and geometry will (Refer Chapter 4 for further information).

In this chapter, volumetric nitrogen gas adsorption has been used to study the physical properties of three industrial grade catalysts. Coked versions of sample A have also been examined. The other coked samples were unrecoverable and have not

been included here[16]. Each of the three catalysts is reported individually with their respective results and discussion. The reasons for their reaction performance are also discussed. Seaton's connectivity analysis was applied to two catalysts (sample A and sample C) to determine their respective connectivity and lattice size. The work will be summarised at the end.

3.2 MATERIALS AND METHODS

Nitrogen[17] gas adsorption-desorption isotherms for three industrial grade catalysts[18] (that were investigated using mercury porosimetry in Chapter 2) were obtained by using a commercial Micromeritics accelerated surface area porosimeter (ASAP 2010) apparatus. The sample preparation involved taking the weight of the catalyst before and after degassing. Initially, the sample tube was rinsed with acetone and distilled water using a sample tube brush. The cleaned tube was then placed in a drying oven overnight. The dried tube was plugged with a seal frit and weighed. Between 0.1 and 0.5 g of the catalyst was weighed and transferred carefully to the cleaned sample tube which was immediately plugged with the seal frit and weighed again. Then the cold trap dewar was filled with liquid nitrogen[19]. The plugged tube containing the catalyst was screwed tightly into the degassing port of the system with a connector nut and o-ring. With the controls available on the system, the sample tube was first filled with the backfill gas (nitrogen). When atmospheric pressure was attained, the backfill gas was switched off and vacuum was applied. Once virtual vacuum conditions (~0.00067 MPa/5 mm Hg) were attained, the sample was heated with the help of a heating mantle system using a thermocouple. The thermal pre-treatment temperature was set at 90 ºC for one hour which ensured the removal of all the moisture present on the surface. This was followed by a more rigorous heat treatment where the temperature was raised to 350 ºC. These settings were finalised after repeated analysis under different conditions. The primary objective of pre-treatment was to ensure the complete removal of moisture from the sample without any destruction of the pore structure. After approximately four hours, heating was stopped and the tube was

---

[16] There was difficulty in recovering coked catalysts from the microreactor as they were firmly held by the unreacted oil and coke. It was not possible to recover them without causing excessive damage to the catalysts themselves. Further, these catalysts did not show any appreciable performance as the oil produced did not show any significant upgrading. The recovery of the coked catalyst of type sample A was possible since it belonged to the series of short interval experiments. Please refer Section 1.7 for further details.

[17] Nitrogen (oxygen free) gas was sourced from BOC.

[18] Please refer Table 3.1 for properties of the catalysts investigated.

[19] Liquid nitrogen was sourced from BOC.

allowed to cool to room temperature. The sample tube was unloaded and re-weighed to determine the dry mass of the sample. The plugged sample tube (containing the dried sample) was then inserted into an isothermal jacket and then screwed tightly into the analysis port of the system with a connector nut and o-ring. The saturation pressure tube was then attached to the tube. The analysis dewar was filled with liquid nitrogen to the required volume with the help of a dewar depth gauge and placed carefully on the elevator so that the round bottom sample tube was positioned at the centre. The computer connected was then used to set the parameters, select the data required, and run the analysis. The apparatus performed a leak test and then carried out the analysis over the entire relative pressure range.

While the above protocol was followed for fresh catalysts A and C, the coked version of catalyst sample A was exposed to a temperature of 90 °C for 1 h followed by 150 °C for more than 12 h (refer Appendix B for more details). The coked catalysts were obtained from Runs P21 and P23 Top. In Run P21, 5 g of sample A was exposed to 500 cm^3min^{-1} of nitrogen and 1 cm^3min^{-1} of THAI® field oil at 400 °C and 2 MPa pressure for 1 h, where as in Run P23 Top, 5 g of sample A was exposed to 500 cm^3min^{-1} of nitrogen gas and 1 cm^3min^{-1} THAI® field oil at 400 °C and 2 MPa pressure for 8 h. 'Top' indicates that the catalyst extrudates were located at the top of the reactor. Results presented for sample B was obtained from runs where the samples were heated to 150°C for more than 12 h[20].

---

[20] Similar results were obtained for sample B when treated at 90 °C for 1 h and 350 °C for 4 h.

Table 3.1
Composition and physical properties of catalysts studied by nitrogen gas adsorption.

Sample	Name	Composition (% W/W)	Appearance	Colour	Odour	Melting point (°C)	Bulk density (kgm^{-3})	Length (mm)	Diameter (mm)
A	Ketjenfine hydroprocessing catalysts – CoMo type	Precipitated silica: 0-6							
		Cobalt (II) oxide: 1-10							
		Molybdenum (VI) oxide: < 25	Extrudates	Blue	Odourless	> 800	550-900	~7	~1
		Phosphorus pentoxide: 0- 4							
		Aluminium oxide: balance							
A Coked	Run P21 Run P23 Top	N/A	Extrudates	Black	N/A	N/A	N/A	N/A	N/A
B	Ketjenfine hydroprocessing catalysts – NiMo type	Precipitated silica: < 10							
		Nickel (II) oxide: < 10							
		Molybdenum (VI) oxide: < 30	Extrudates	Yellow	Odourless	> 800	550-950	~7	~1
		Phosphorus pentoxide: 0-9							
		Aluminium oxide: balance							
C	C18 HA LTS	Copper oxide: 56							
		Zinc oxide: 31							
		Aluminium oxide: 11	Tablets	Black	Odourless	N/A	1050	~2.4	~4.5
		Sulphur: < 0.02							
		Chlorine: <0.01							

3.3 RESULTS – SAMPLE A

Nitrogen gas adsorption-desorption isotherms obtained for sample A seen in Fig. 3.1 were of type IV according to the IUPAC classification with a reproducible Type H2 hysteresis loop. The isotherms were reversible in the multilayer adsorption region and the lower closure point of the hysteresis loop was ~0.5. The Gurvitsch pore volume (see Table 3.2 and Fig. 3.1) obtained when sample A was exposed to vacuum conditions at 100 °C for more than 12 hours was found to be less than that obtained when the same sample was given an intense heat treatment (90 °C for 1 h followed by 350 °C for 4 h) under similar vacuum conditions. It was found that there was no change in the isotherm obtained when the equilibration time was changed from 60 to 90 s confirming that equilibrated isotherms for sample A can be obtained for any time between 45 and 60 s.

Fig. 3.1. Typical nitrogen adsorption-desorption isotherms obtained for sample A (whole) at different equilibration times and sample pre-treatment conditions. The isotherm obtained for an equilibration time of 45 s was given a pre-treatment of 100 °C for more than 12 hours.

Sample A was characterised by a rapid initial uptake of nitrogen at low relative pressures (that gives a sharp point B) followed by a region of multilayer adsorption and eventually capillary condensation. The different regions are marked in Fig. 3.2. A plateau was also found in the isotherm at saturation conditions indicating that the all of the pore space present in the sample was accessible to nitrogen. The typical physical properties of sample A as obtained from the isotherms are presented in Table

3.2. It was found that the pore volume measured by nitrogen adsorption was greater (~10%) than that obtained from mercury intrusion and the surface area of sample A measured by mercury porosimetry was ~20% higher than that obtained from nitrogen gas adsorption.
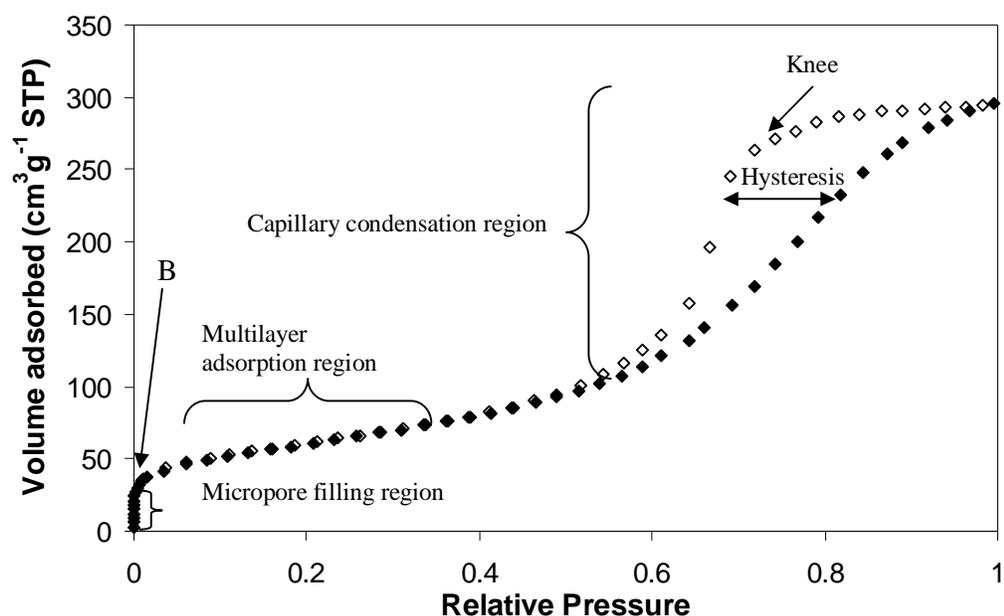
Fig. 3.2. Typical nitrogen adsorption-desorption isotherm for sample A (whole) showing the different regions associated with different mechanisms of adsorption.

Table 3.2
Physical properties obtained for sample A (whole) from the isotherms presented in Fig. 3.1 and repeats performed which are not presented here.

Equilibration time (s)	Gurvitsch pore volume at $P/P_0 = 0.95$ (cm^3g^{-1})	BET surface area (m^2g^{-1})	BET C constant	FHH fractal dimension D
60	0.46	222(12)	115(4)	2.53
90	0.44	215(10)	100(4)	2.50
Averaged values	0.47(0.02)	226(8)	108(4)	2.52(0.01)
Hg porosimetry (Table 2.2)	0.42	283(8)		

( ) Errors are quoted in brackets.

The BET surface area was ~226 m^2g^{-1} and the BET C constant was ~108 according to the procedure given in Section 3.1.1. An example of the BET straight line plot obtained for sample A is represented in Fig. 3.3a. The residuals, i.e. the difference

obtained between the experimental value and that obtained from the straight line fit are shown in Fig. 3.3b.
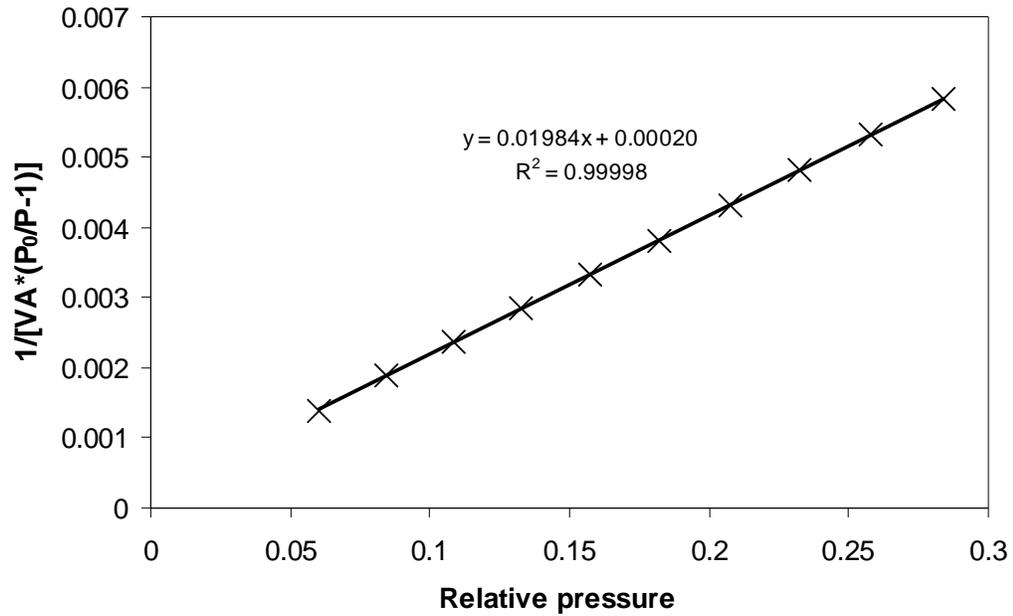
(a)
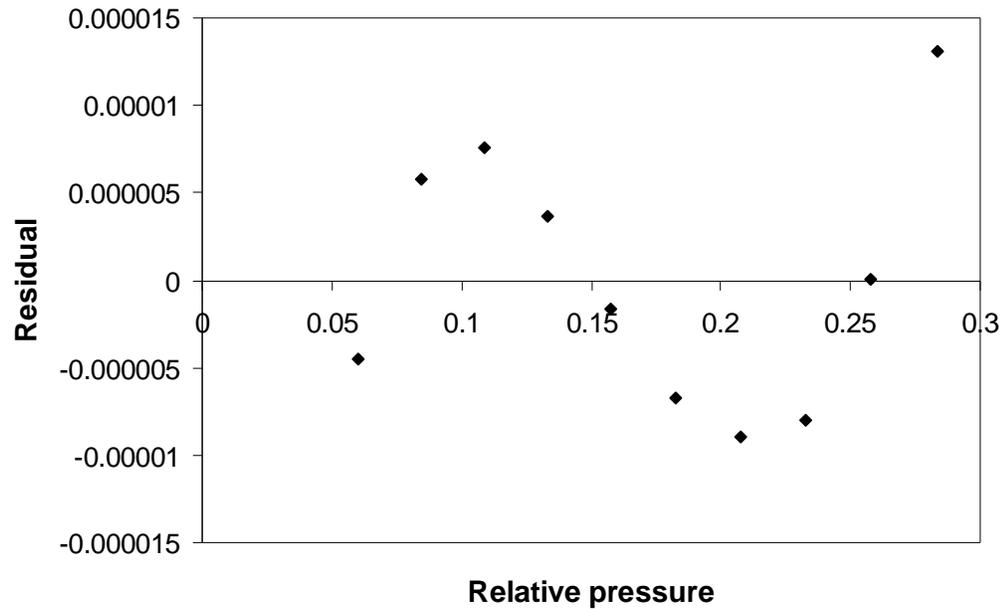
(b)
Fig. 3.3. (a) Typical BET surface area plots obtained for sample A (whole). (b) Residuals obtained for the straight line fit presented in Fig. 3.3a.

The FHH surface fractal dimension from Fig. 3.4a in the pore condensation regime was ~2.52 indicating a rough surface in the pore interiors. The BJH pore size distribution displayed in Fig. 3.5 had its adsorbed film thickness described by the Harkins-Jura thickness equation (Eq. 3.8e). Sample A was found to have a broad size

distribution of large pores centred around ~10 nm in the adsorption branch and a narrow distribution of pores centred around ~6 nm in the desorption branch. The t method was used to determine the presence of micropore volume within sample A by employing the former thickness equation. A typical t plot obtained for sample A is presented in Fig. 3.6. The presence of a positive intercept implied the presence of micropores. The micropore volume was estimated to be ~0.004 cm^3g^{-1}.
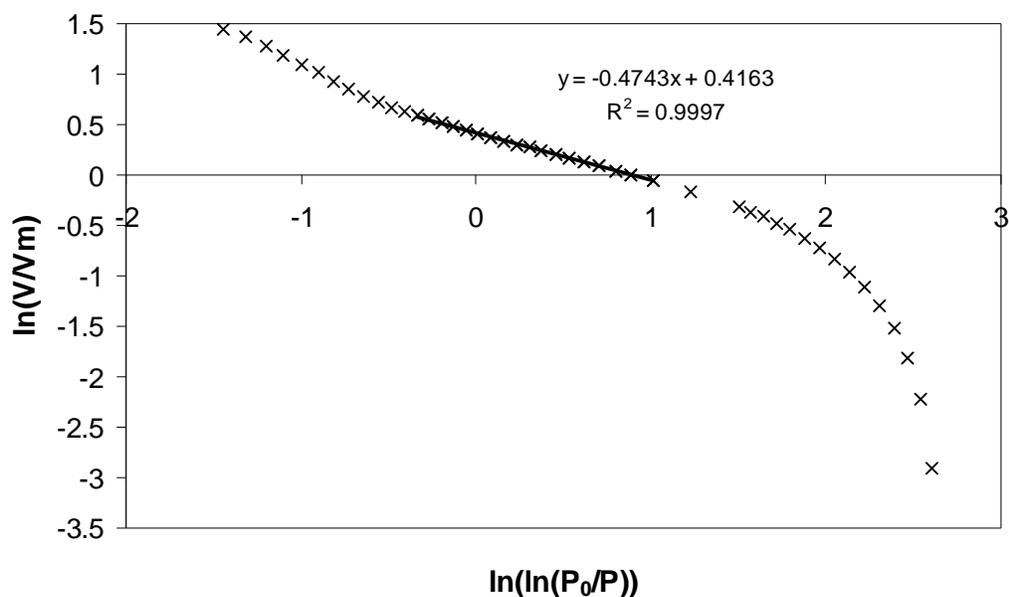
(a)
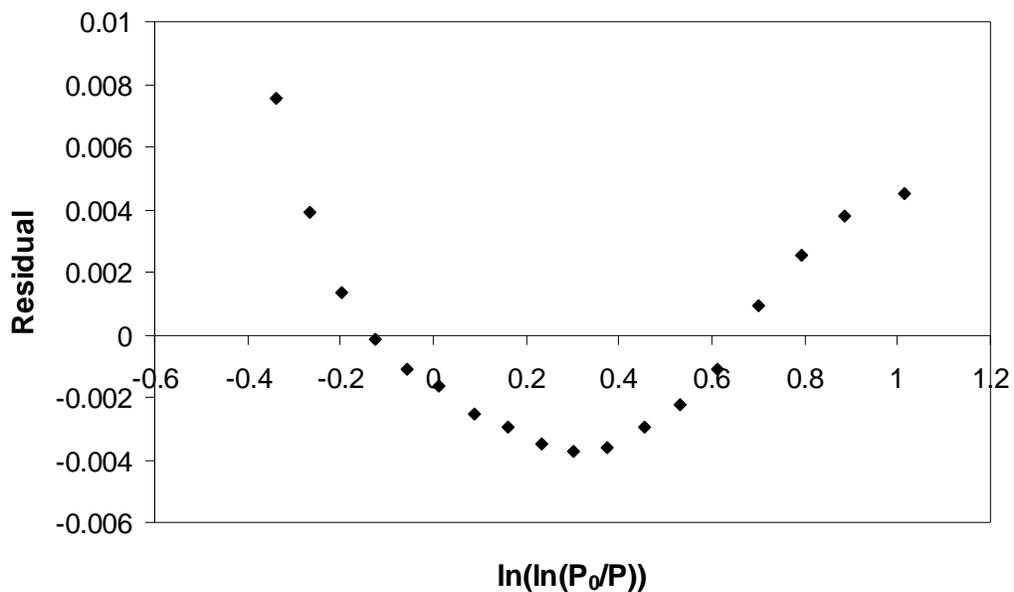
(b)

Fig. 3.4. (a) Typical FHH fractal dimension plot obtained for sample A (whole). (b) Residuals obtained for the straight line fit presented in Fig. 3.4a.
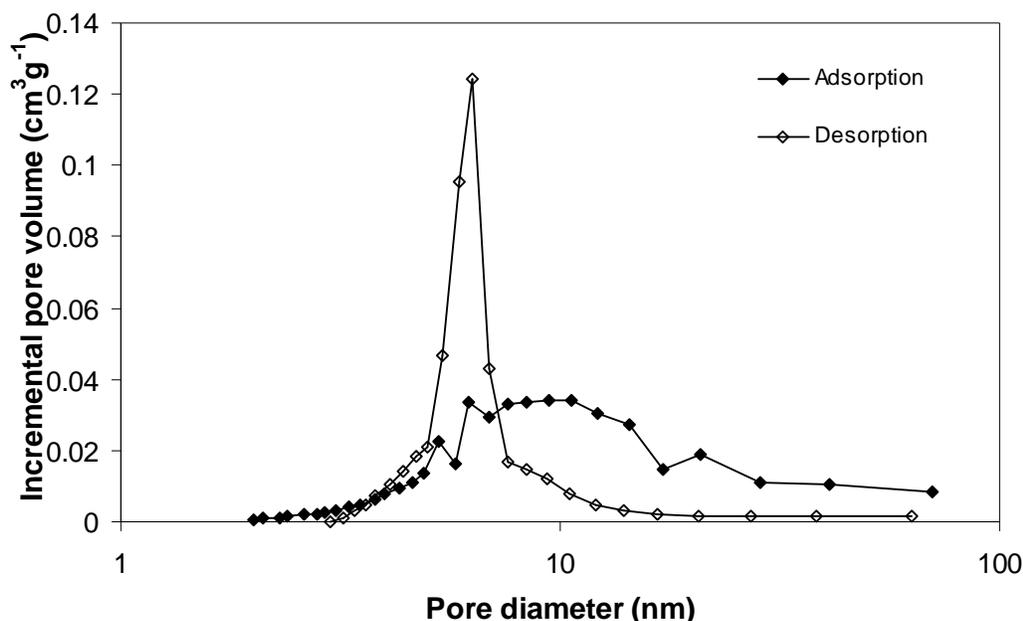
Fig. 3.5. Typical BJH pore size distribution plots obtained for sample A (whole). The distributions were obtained under the assumption that there were no pores open at both ends.

$$y = 0.2128x + 0.0038$$
$$R^2 = 1$$
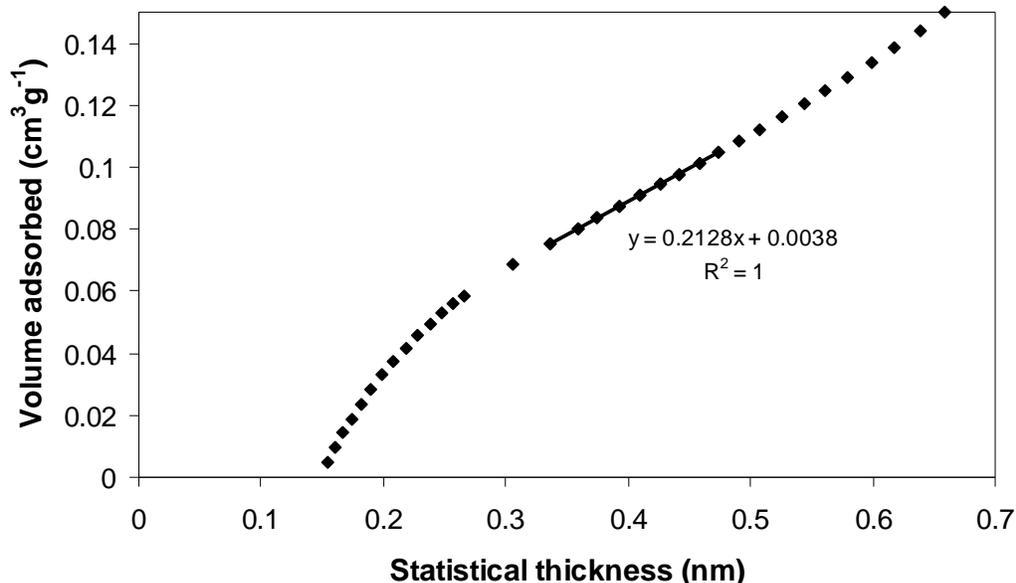
Fig. 3.6. Typical *t* plot obtained for sample A (whole). The positive intercept implied the presence of a micropore volume within sample A.

The uptake of nitrogen at the lowest relative pressures and in the multilayer adsorption region was fitted to various two-component and single-component adsorption models as seen in Fig. 3.7 using the Solver function within Microsoft® Office Excel 2003. However, none of them provided a satisfactory fit. The fitting indicated that the micropore filling at the lowest relative pressures could not be described by a Langmuir adsorption model. Figs. 3.7a, b, and c display the

75

experimental data along with the different two-component and single-component models used.
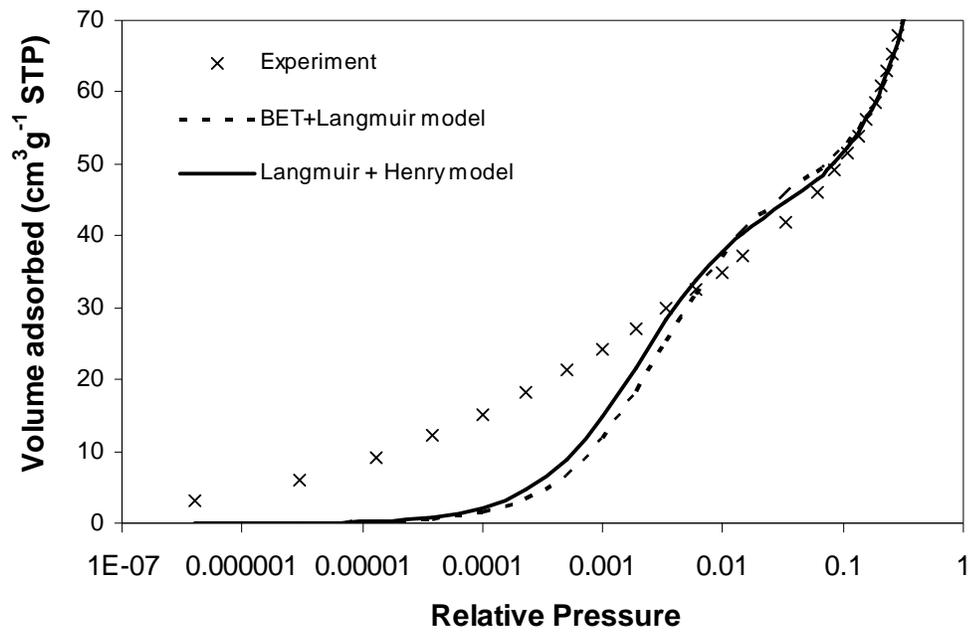
(a)
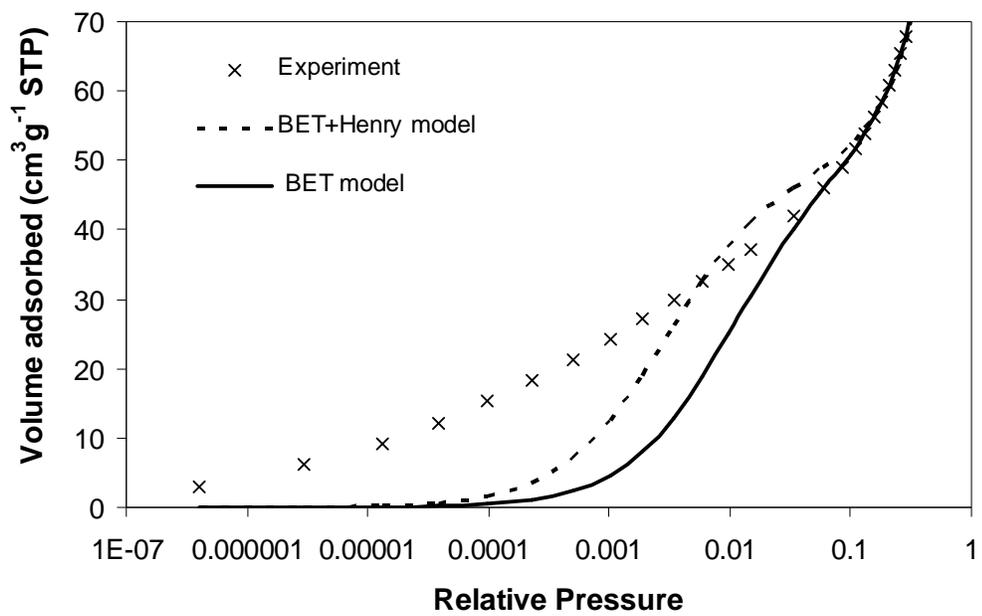
(b)
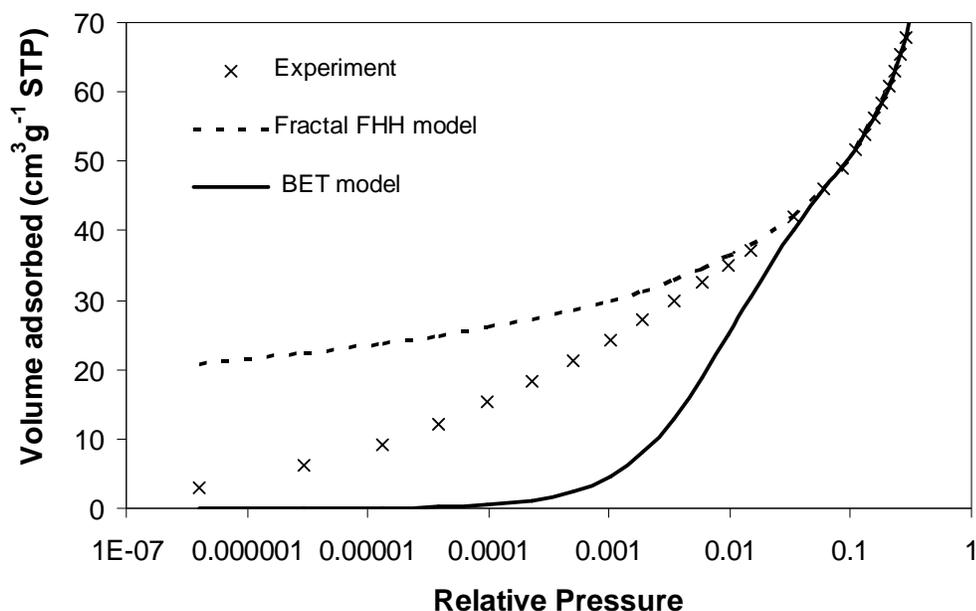
(c)

Fig. 3.7. Different two-component and single component models fitted to nitrogen uptake for sample A (whole) in the micropore region and region representing multilayer adsorption. The relative pressure is represented in the logarithmic scale to verify whether fitting took place at low relative pressures. Models fitted include (a) BET + Langmuir and Langmuir + Henry, (b) BET + Henry and BET model, (c) Fractal FHH model and BET model. It can be seen that though the models fitted in the multilayer region, none of them fitted in the micropore region.

Since nitrogen fully filled sample A, the accessibility of the mesopore network was analysed to determine the lattice size L and connectivity Z using the method, due to Seaton (1991), based on percolation theory. The fit of the nitrogen sorption data for sample A to the generalised scaling function for the Seaton (1991) method is presented in Fig. 3.8. The values of L and Z obtained from the fit are presented in Table 3.3.

Table 3.3
Value of pore connectivity and lattice size of sample A (whole) obtained from percolation analysis of the nitrogen adsorption isotherms using the Seaton (1991) method.

Sample	Z	L
A	5	7

In contrast to sample A in its fresh form, it was found that the coked versions provided linear nitrogen adsorption isotherms. Under the reaction conditions investigated, the nitrogen adsorption-desorption isotherms provided by the coked samples seemed to be independent of the time on stream (TOS). A linear isotherm was obtained for both coked samples. The catalysts were on stream for 1 h and 8 h respectively. Figs. 3.9a and b display the nitrogen adsorption-desorption isotherms for

sample A from the THAI®-CAPRI® experiments where the TOS was 1 h and 8 h respectively.
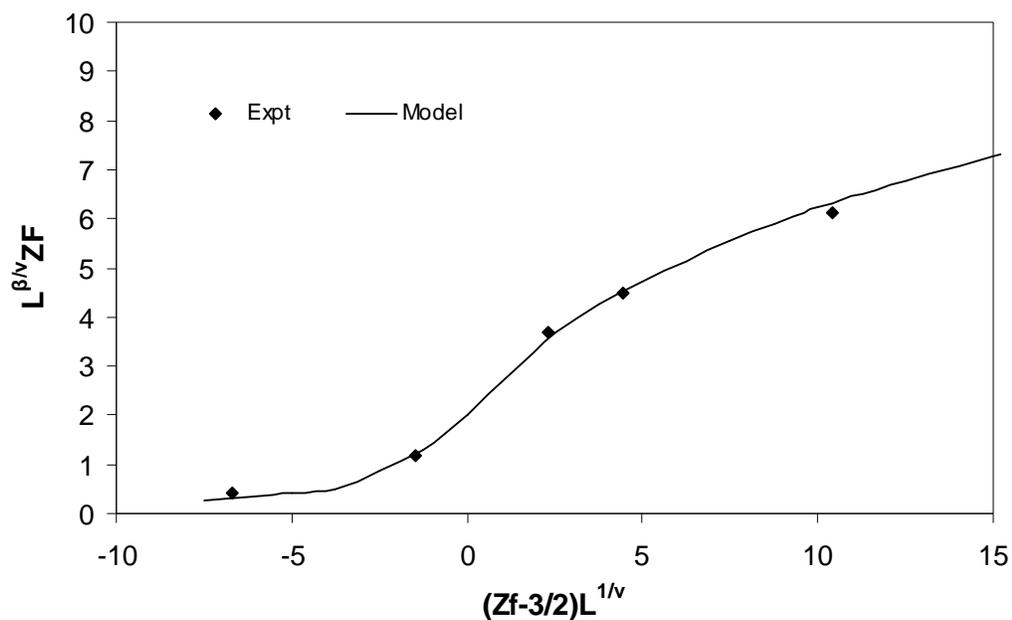
Fig. 3.8. Fit of the nitrogen sorption experimental data of sample A (whole) to the generalised scaling function using the method due to Seaton (1991). The values obtained from the fit are given in Table 3.3.
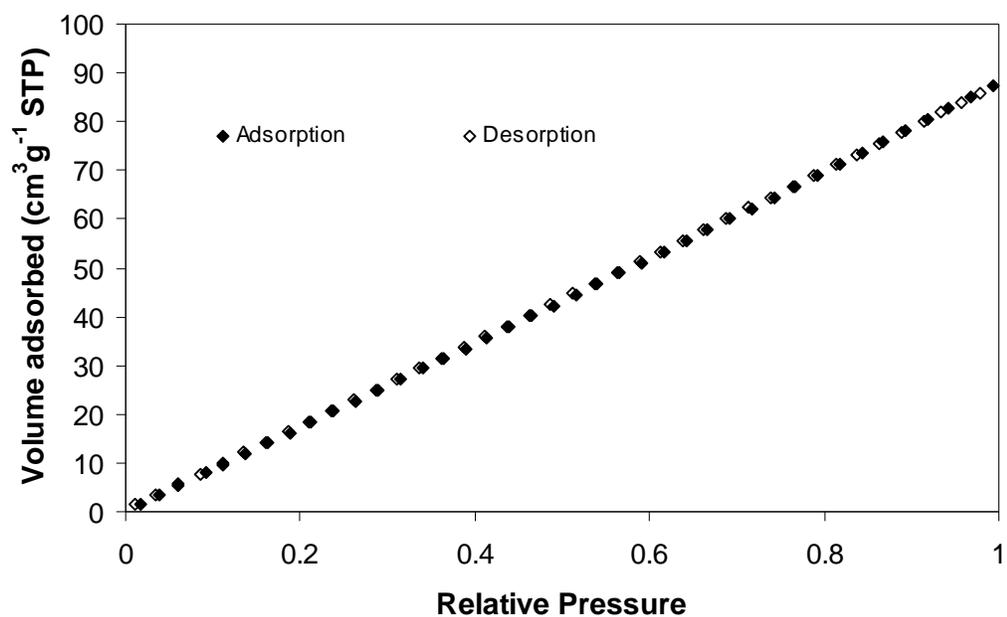
(a)
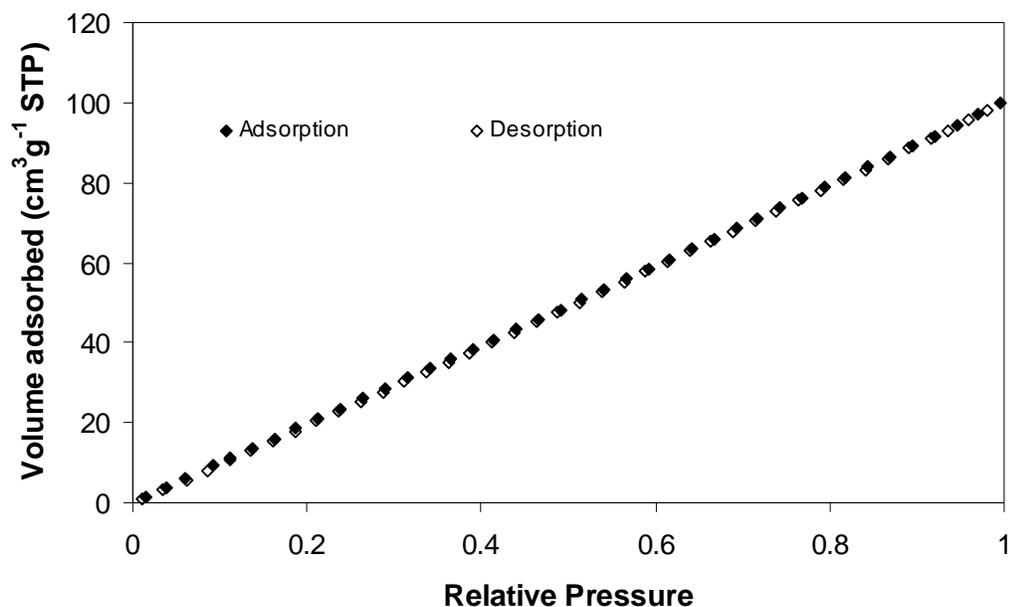
(b)
Fig. 3.9. Nitrogen adsorption-desorption isotherms for coked sample A (whole). The coked catalysts were on stream in the reactor for (a) 1h and (b) 8h.

3.4 DISCUSSION – SAMPLE A

Nitrogen gas adsorption porosimetry has revealed properties in sample A that were not understood earlier from mercury porosimetry. The type IV isotherm with a reproducible hysteresis loop was clear evidence that sample A possessed a mesoporous structure. Sample pre-treatment and equilibration time were shown to be critical factors in these gas adsorption experiments. This has been specifically emphasised here due to the evidence of the use of non-equilibrated or non-isothermal nitrogen adsorption-desorption isotherms for the characterisation of hydroprocessing catalysts within the recent literature (refer to Section 3.1.6). The physical properties of sample A evaluated from gas adsorption revealed that it had a pore volume of ~0.47 cm^3g^{-1}. This was close to that determined from mercury intrusion porosimetry. However, the surface area detected by mercury intrusion was slightly higher. This may mean that the assumed contact angle and surface tension required change or it could be due to the presence of some pore shielding effects. The BET C constant for catalyst sample A was ~108. A value between 50 and 200 for nitrogen adsorption at 77 K is consistent with the formation of a well defined monolayer (Rouquerol et al., 1999). But the t plot confirmed the presence of micropores with a positive intercept. Usually, the presence of localised adsorption is evident when C values are > 200 and when there is a contribution of micropores (Rouquerol et al., 1999). It is possible that localised adsorption of nitrogen may be taking place within the pores of catalyst

79

sample A due to presence of some micropores. Further, the catalyst support is also chemically heterogeneous at the atomic scale with the presence of active metal components like Co and Mo (see Table 3.1). It can be expected that the nitrogen molecules will experience large van der Waals forces due to the presence of such big atoms on the pore surface. The force field is likely to cause nitrogen molecules to adsorb strongly (due to its quadrupole moment) on certain sites relative to others. The chemistry of the catalyst surface was also discussed in Section 2.4 with respect to mercury porosimetry. Mercury porosimetry revealed that sample A was mesoporous. However, nitrogen gas adsorption conveyed that sample A actually contained micropores and mesopores with a rough texture as determined by the FHH fractal dimension.

Though attempted two-component fits to the micropore filling and multilayer adsorption region did not provide any satisfactory fit to the adsorption isotherm considered here, it can be said that adsorption in the microporous region required a more complex model than a simple Langmuir model (that described the formation of a monolayer).

Seaton's connectivity analysis was performed on sample A to determine its pore connectivity and lattice size. This would have been beneficial to compare with coked catalysts. However, the coked versions of sample A studied here produced linear nitrogen adsorption isotherms. This can be interpreted as complete blockage or filling up of the pores with coke. As a result, the catalyst behaved essentially like a weakly adsorbing non-porous material giving a characteristic straight line isotherm. The result also suggested that the TOS was not a factor in the investigated reaction conditions as similar isotherms were obtained for the catalyst when the TOS was 1 h or 8 h. However, it remains to be seen if complete pore blockage of the catalysts takes place for samples when the TOS was < 1 h. Such reaction runs were, however, not conducted in this project.

This clearly implied that under the investigated conditions, once the feedstock (cracked THAI® oil, combustion gases) came in contact with the catalyst, there was a rapid and immediate coking causing blockage of all the pores within sample A. It is certain that the timescale involved would be of the order of minutes. The activity of the catalyst completely disappears making it act like a filter bed. The author believes that the use of a micro-mesoporous catalyst was likely to be the major cause for this quick loss in activity. The BJH pore size distribution for sample A had a broad mode around ~10 nm. It is better to consider the adsorption branch since the desorption branch is prone to pore blocking or network effects. This pore size is smaller than the

size of heavy oil molecules trying to access active sites. For example, Zhao and Shaw (2007, 2008) reported Athabasca bitumen asphaltene (heaviest component of the bitumen) aggregate size distribution range from 5 nm to more than 100 nm in diameter. Though there is little overlap between the pore size of sample A and the size distribution of asphaltene aggregates, it is certain that most of the molecules will experience hindrances and accessibility issues. With the presence of a certain distribution of micropores, size difference between the pores and the oil molecules can be expected to be far greater. Under these conditions, the reaction was therefore highly diffusion limited. Thus, it may be necessary to use a macroporous or meso-macroporous catalyst that had a large pore volume and low surface area. Such catalysts would be more likely to have pores that allow greater accessibility for the THAI® oil reactant molecules to the active sites.

Apart from physical properties, the chemistry of the catalyst must also be optimised by taking into account the acid number[21] of THAI® oil. The acidity of the hydroprocessing catalyst is known to be responsible for cracking activity. Hydroprocessing of heavy feeds in refineries are conducted in reactors which have a high partial pressure of hydrogen – more than 125 times the atmospheric pressure (Furimsky, 2007). Reservoir pressures are usually less by an order of magnitude. As catalyst sample A was not designed for this purpose, it was expected that this would also contribute to the mediocre performance of sample A in the THAI®-CAPRI® reactions. An ideal catalyst must consider the above mentioned factors.

3.5 RESULTS – SAMPLE B

Type IV adsorption isotherms (Fig. 3.10) according to the IUPAC classification along with a reproducible classical type H2 hysteresis loop were exhibited by catalyst sample B. The isotherms obtained were reversible in the multilayer adsorption region. The lower closure point of the hysteresis loop was located at a relative pressure ~0.64. The sample preparation technique was checked by first performing the experiment on a sample heated at 150 °C for more than 12 h and an equilibration time of 45 s. However, a slightly greater uptake was found when the heating conditions were changed to 90 °C for 1 hour and 350 °C for 4 hours at the same equilibration conditions. Results similar to this run were obtained when the sample was treated at 150 °C for more than 12 h and the equilibration time increased

---

[21] Total acid number (TAN) measurements determine the acid content of the oil, i.e. the amount of KOH in mg required to neutralise 1 g of oil (Sheng, 2011). The acid number of Athabasca bitumen is 2.11 – 3.21 mgKOH/gbitumen (Wallace et al., 1983).

to 60 s and 90 s (see Fig. 3.11). Thus, an equilibration time between 45 and 60 s was necessary for sample B to get reproducible isotherms.
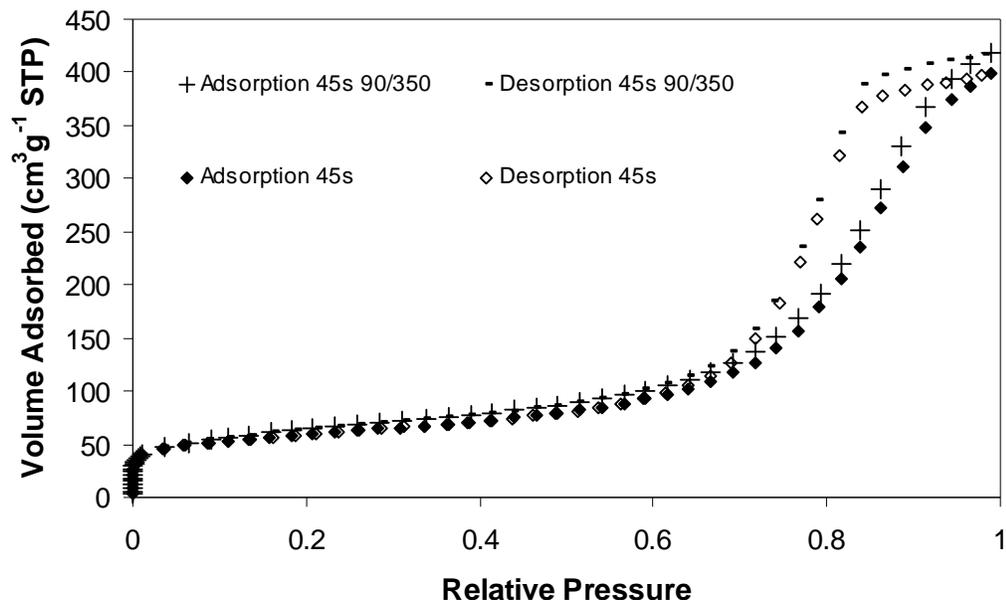
Fig. 3.10. Typical nitrogen adsorption-desorption isotherms obtained for sample B (whole) under different sample pre-treatment conditions. The isotherm obtained for an equilibration time of 45 s was given a pre-treatment of 150 °C for more than 12 hours.

Sample B was characterised by a high initial uptake of nitrogen at low relative pressures that established a monolayer, followed by clear multilayer adsorption and capillary condensation regions. At saturation, a clear plateau was not found in the isotherm like sample A. The typical physical properties of sample B are presented in Table 3.4. It was found that the BET surface area of the catalyst was ~230 m^2g^{-1} with a BET C constant of ~150 which is similar to sample A (see Figs. 3.12a and b). However, the Gurvitsch pore volume in sample B was slightly higher than that for sample A. It was also found that the pore volumes measured by nitrogen adsorption and mercury intrusion are similar but the surface area of sample B measured by mercury porosimetry was higher (~35%) than that obtained from nitrogen gas adsorption. The FHH surface fractal dimension from Fig. 3.12a in the pore condensation regime was ~2.53 indicating a rough surface in the pore interiors. This was similar to that for sample A. The t method was also used to determine the micropore volume using the Harkins-Jura thickness equation (Eq. 3.8e). Approximately 0.01 cm^3g^{-1} of sample B comprised micropores (see Fig. 3.14). The BJH pore size distribution with thickness described using the Harkins-Jura equation

from the adsorption branch was broad and centred around ~17 nm while the desorption branch had a mode centred around ~10 nm as seen in Fig. 3.15.
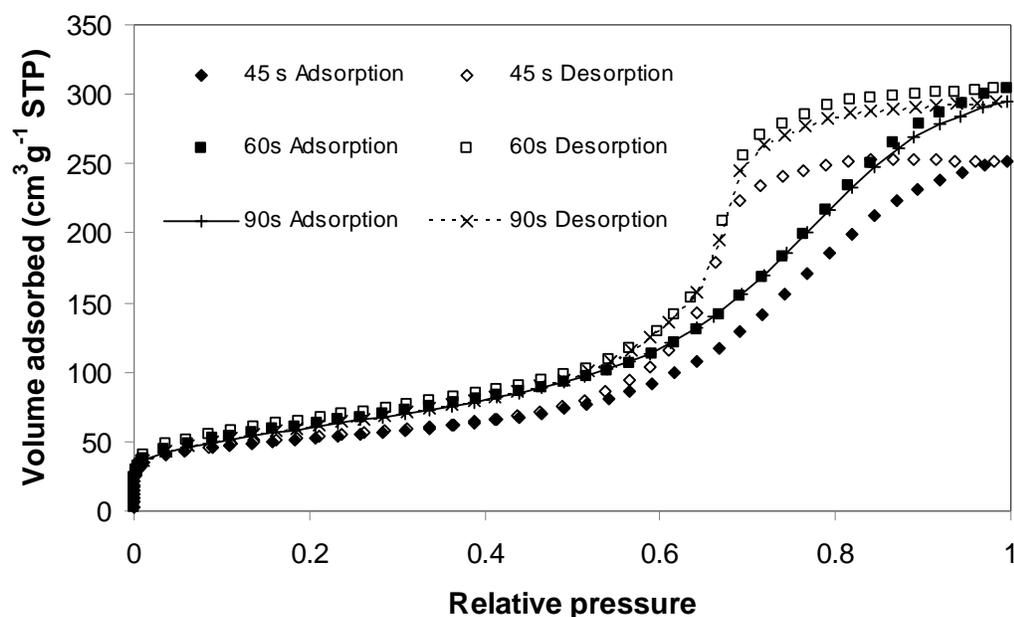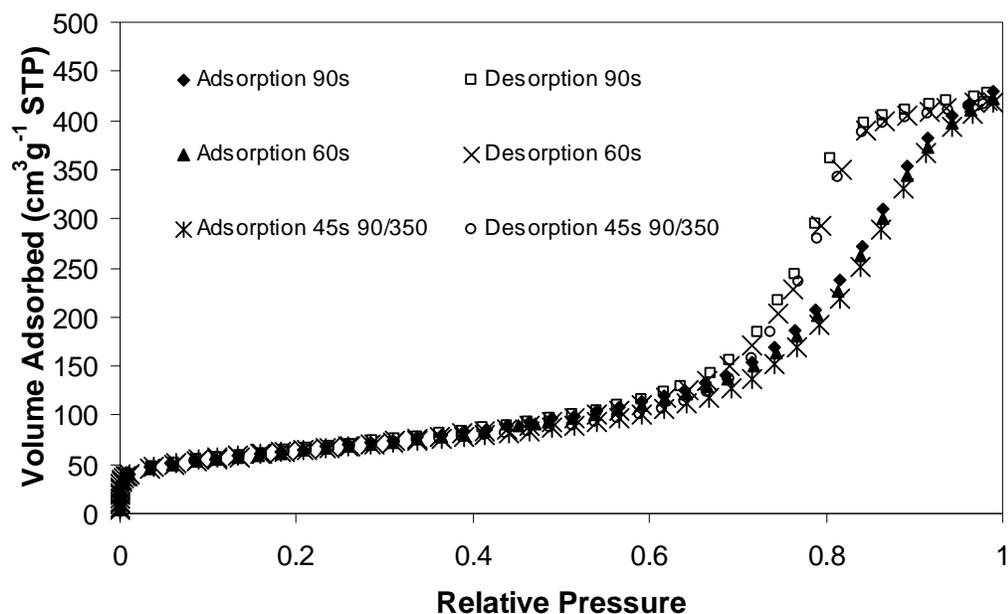

Fig. 3.11. Typical nitrogen adsorption-desorption isotherms obtained for sample B (whole) at different equilibration times and same sample pre-treatment conditions.

Table 3.4
Physical properties obtained for sample B (whole) from the nitrogen adsorption isotherms presented in Fig. 3. 11.

Equilibration time (s)	Gurvitsch pore volume at P/P_0 = 0.95 (cm³g⁻¹)	BET surface area (m²g⁻¹)	BET C constant	FHH fractal dimension D
60	0.62	195(11)	162(7)	2.54
90	0.63	200(10)	131(4)	2.53
Averaged values	0.625(0.005)	197(3)	146(16)	2.535(0.005)
Hg porosimetry (Table 2.3)	0.62	306(7)		

( ) Errors are quoted in brackets.
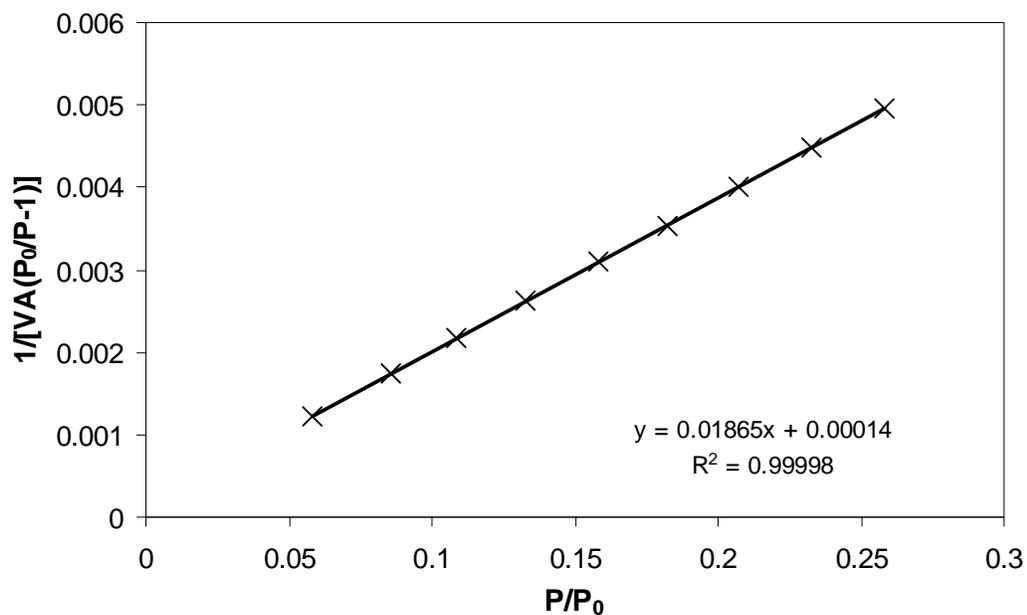
(a)
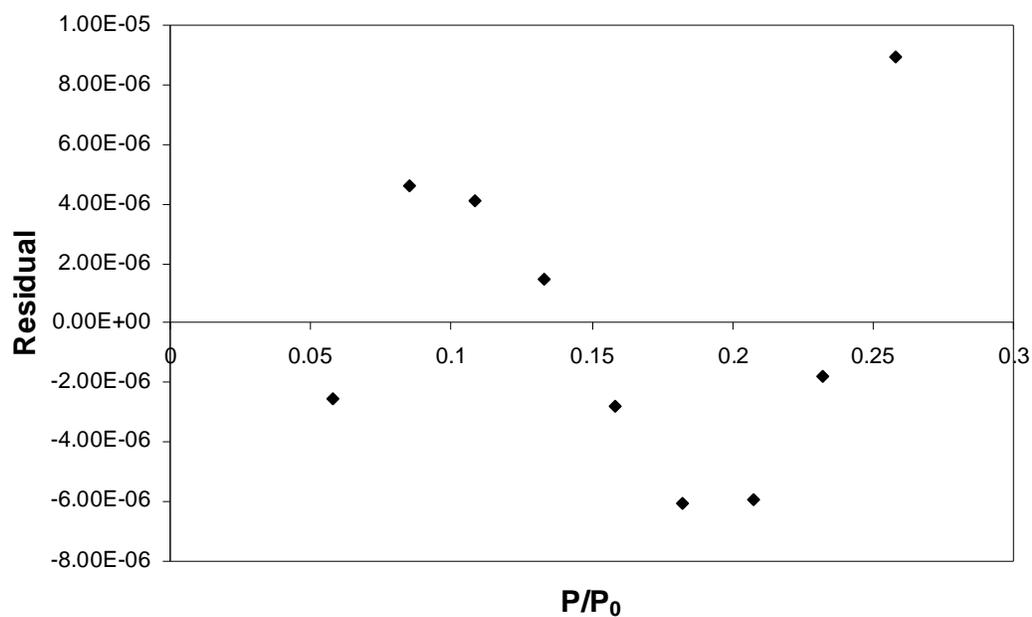
(b)
Fig. 3.12. (a) Typical BET surface area plots obtained for sample B (whole). (b) Residuals obtained for the straight line fit presented in Fig. 3.12a.
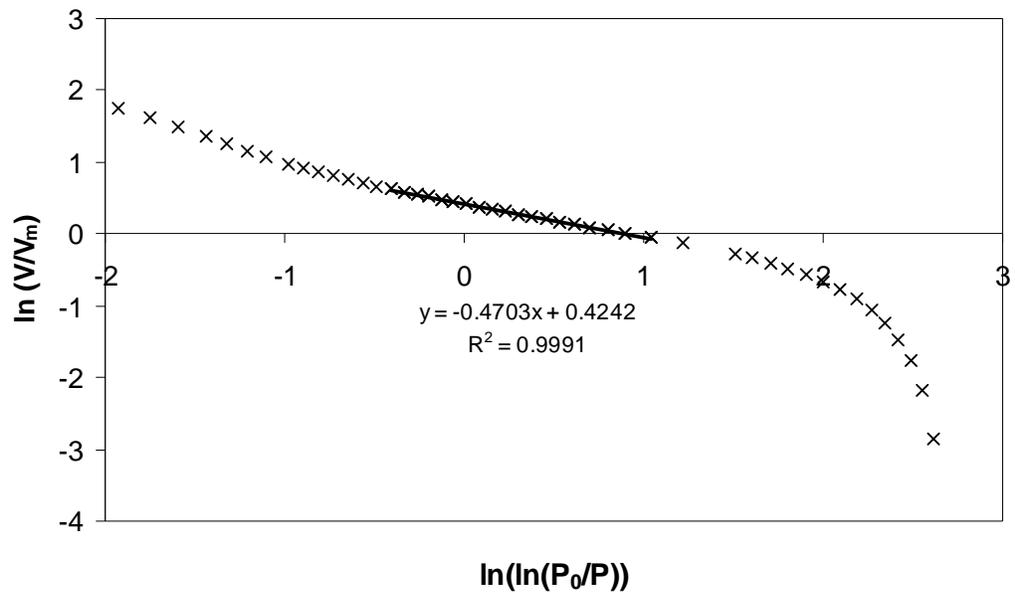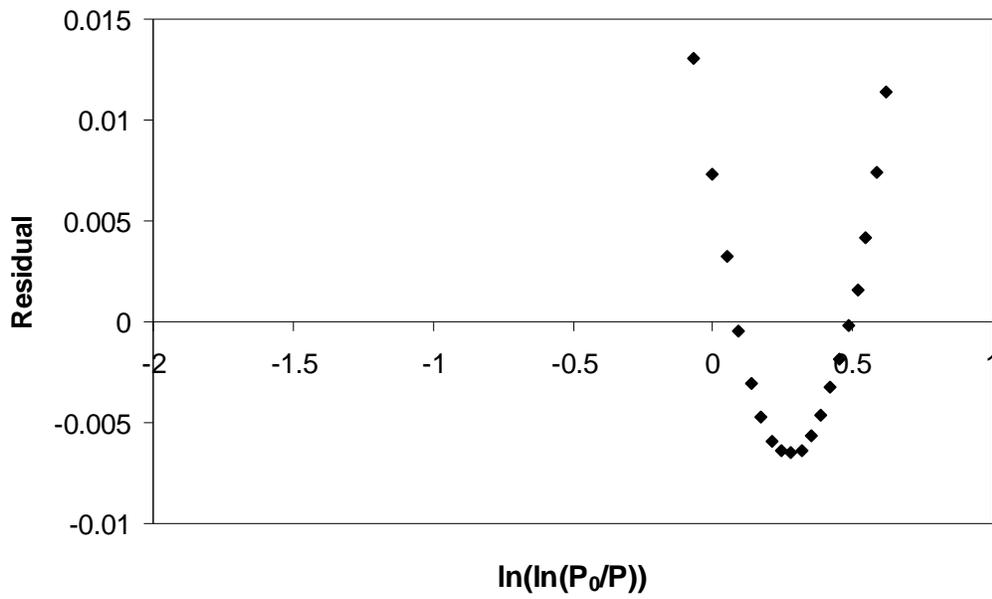
Fig. 3.13. (a) Typical FHH fractal dimension plot obtained for sample B (whole). (b) Residuals obtained for the straight line fit presented in Fig. 3.13a.
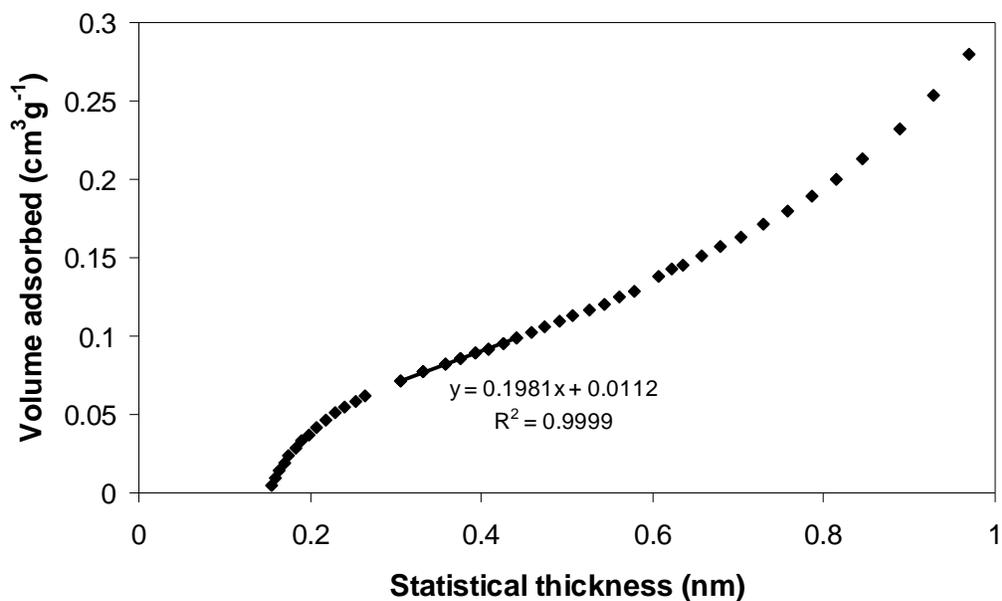
Fig. 3.14. Typical *t* plot obtained for sample B (whole). The positive intercept implied the presence of a micropore volume within sample B.
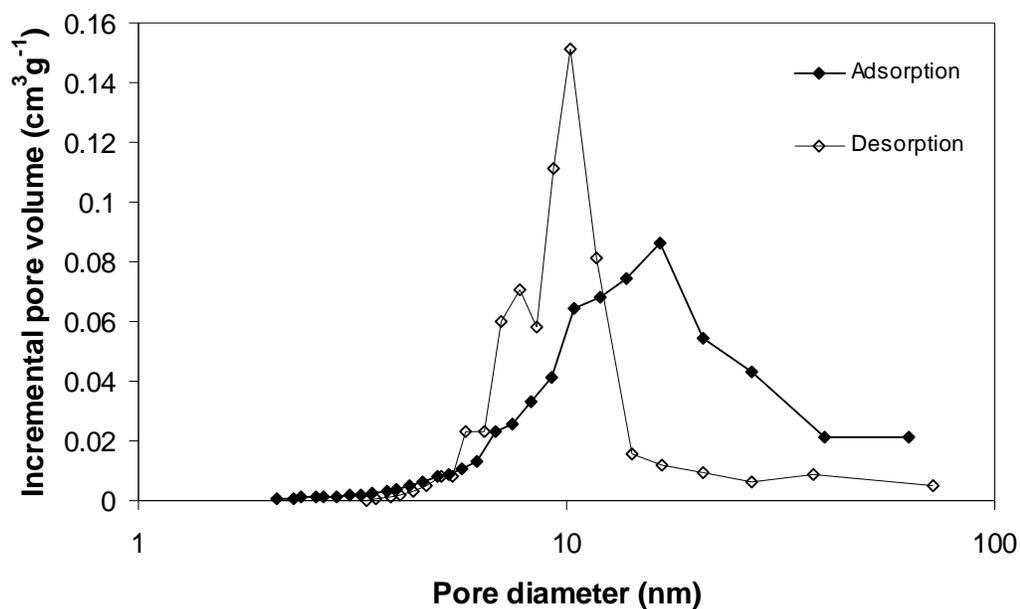
Fig. 3.15. Typical BJH pore size distribution plots obtained for sample B (whole). The distributions were obtained under the assumption that there were no pores open at both ends.
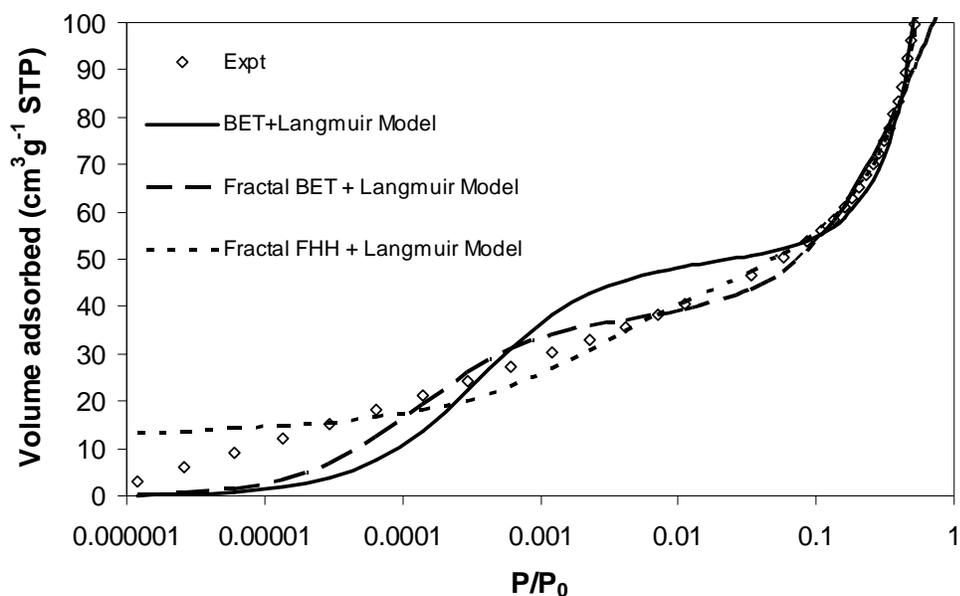
Fig. 3.16. Different two component models fitted to the experimental nitrogen uptake for sample B (whole) in the micropore region and region representing multilayer adsorption. The relative pressure is represented in logarithmic scale to verify whether fitting took place at low relative pressures. Models fitted include BET + Langmuir, Fractal BET + Langmuir and Fractal FHH + Langmuir. It can be seen that though the models fitted in the multilayer region, none of them fitted in the micropore region.

Apart from the determination of standard catalyst properties, nitrogen uptake at low relative pressures and in the multilayer region was tested by fitting different two-component models as discussed earlier in Section 3.1.3. However, none of the models provided a good fit (see Fig. 3.16). It was likely that a more complex multi–component model may be required to fit the experimental data.

3.6 DISCUSSION – SAMPLE B

The type IV nitrogen adsorption isotherm of sample B along with its Type H2 classical hysteresis loop was clear evidence of the presence of substantial mesoporosity in the catalyst. There was a rapid initial uptake of nitrogen at very low relative pressures which led to the formation of a sharp point B indicating the formation of the monolayer. This rapid uptake may be the evidence of the presence of some micropores in the sample. Indeed, this agreed with the presence of micropore volume as detected by the *t* method. Approximately 1.5% of the pore volume in sample B consisted of micropores which was larger than that in sample A. There was evidence of localised adsorption of nitrogen in sample B as the BET *C* constant was ~150 and there was also a micropore contribution. It is likely that the highly polarisable surface exhibited by the catalyst due to the presence of different active metal components (Ni

and Mo) caused nitrogen molecules to adsorb strongly (due to its quadrupole moment) on certain sites relative to others mimicking the effect of a monolayer formation. If these micropores were interspersed among the 17 and 10 nm mesopores (as determined by the BJH pore size distribution) then they definitely are pores that undergo coking due to diffusion limitations. Catalytic upgrading would be limited which agreed with the results from the microreactor experiments.

At saturation conditions, a plateau was not seen in the adsorbed amount. Usually, this indicated the presence of some unfilled macropores. However, the Gurvitsch pore volume measured by nitrogen adsorption agreed well with that obtained from mercury porosimetry suggesting that most pores were filled. Any macropores not detected during mercury intrusion is evidence of it being shielded by smaller pores. It is likely that this may be case with sample B, as the pore size distributions obtained for sample B during mercury intrusion do not show the presence of macropores but the extrusion cycle does (see Fig. B.4.1 in Appendix B). These shielded large pores may actually be responsible for the structural hysteresis (mentioned earlier in Section 2.6) for sample B.

Desorption branches in gas adsorption are usually susceptible to cavitation or pore blocking. However, the knee and the lower closure point in sample B (and for sample A) was higher than a relative pressure ~0.42. This implied that pore blocking was probably taking place in sample B during desorption. Mercury intrusion process is similar to desorption and is affected by pore blocking or shielding affects. There was an agreement in the modes provided by the mercury intrusion process and nitrogen desorption (see Fig. B.4.2 in Appendix B). An approximation can be made that the pore network in sample B contained throats, windows or bonds ~10 nm in size providing access to larger cavities. As discussed for sample A, such pore sizes are in the lower mesopore range. It is likely that reactant molecules would find it difficult to travel through the small pores to reach the larger pores present in sample B. This would result in diffusion limitations causing coking and deactivation of the catalyst sample B just as with sample A. With the presence of some micropores, the deactivation effect would likely be enhanced.

3.7 RESULTS – SAMPLE C

Typical nitrogen gas adsorption-desorption isotherms obtained for catalyst sample C at different equilibration times (45, 60 and 90 s) are displayed in Fig. 3.17a. They were of Type IV according to the IUPAC classification and possessed a

reproducible narrow hysteresis loop that was of type H2. The lower closure point of the hysteresis loop was located at a relative pressure of ~0.74 (see Fig. 3.17c). The figure shows a clear shift in the isotherm to higher relative pressures when the experiment was performed with an equilibration time of 60 and 90 s relative to an experiment at 45 s. The isotherms obtained with an equilibration time of 60 and 90 s are nearly coincident suggesting that equilibration time for this catalyst was between 45 and 60 s. The multilayer adsorption region was reversible (Fig. 3.17b) and could be clearly distinguished from the capillary condensation region (Fig. 3.17c). Unlike samples A and B, little uptake was observed at the lowest relative pressures (P/P_0~9×10^{-5} to 5×10^{-3}). Further, sample C was also characterised by a narrow hysteresis loop in contrast to samples A and B. The pore properties of the material, i.e. pore volume according to the Gurvitsch rule, BET surface area, BET C constant, and FHH fractal dimension are listed in Table 3.5. The BET surface area was ~50 m^2g^{-1} with a high BET C constant. A typical BET fit and the residuals obtained for sample C are presented in Figs. 3.18a and b respectively. The FHH fractal dimension (see Figs. 3.19a and b) in the pore condensation regime was ~2.57 indicating a rough surface. The BJH pore size distributions displayed in Fig. 3.20 has its adsorbed film thickness described by the Harkins-Jura equation (Eq. 3.8e). The adsorption pore size distribution displayed a mode at ~40 nm, while the desorption pore size distribution revealed a mode at ~30 nm. The micropore volume in sample C was determined using the t method employing the former thickness equation. Fig. 3.21 presents the t plot obtained for sample C. A positive intercept was obtained. The micropore volume in sample C was ~0.003 cm^3g^{-1}. This contributes ~1.7% of the total pore volume present in sample C.

Table 3.5
Physical properties of catalyst sample C (whole) obtained from nitrogen adsorption isotherms.

Equilibration time (s)	Gurvitsch pore volume at P/P_0 = 0.95 (cm^3g^{-1})	BET surface area (m^2g^{-1})	BET C constant	FHH fractal dimension D
60	0.18	43(3)	160(9)	2.55
90	0.18	38(3)	214(12)	2.59
Averaged values	0.18	40(3)	187(27)	2.57(0.02)
Hg porosimetry (Table 2.6)	0.18	43		

( ) Errors are quoted in brackets.
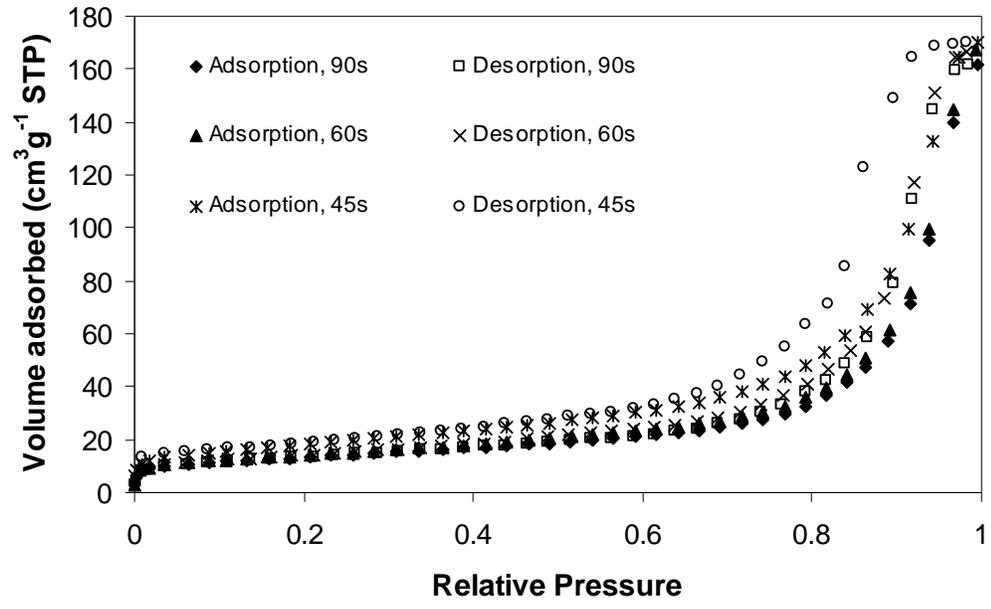
(a)
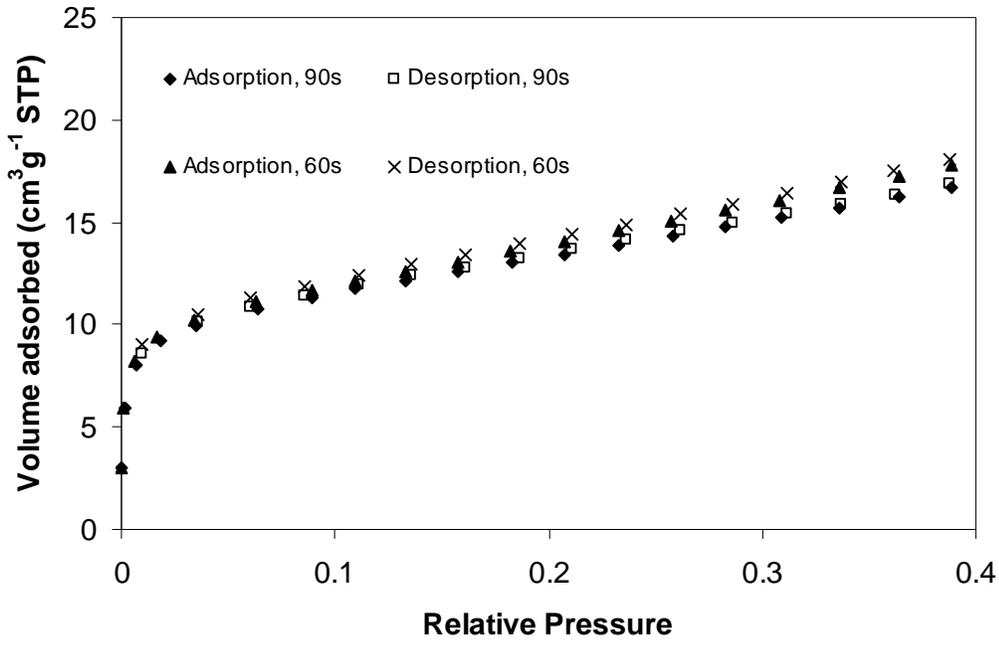
(b)
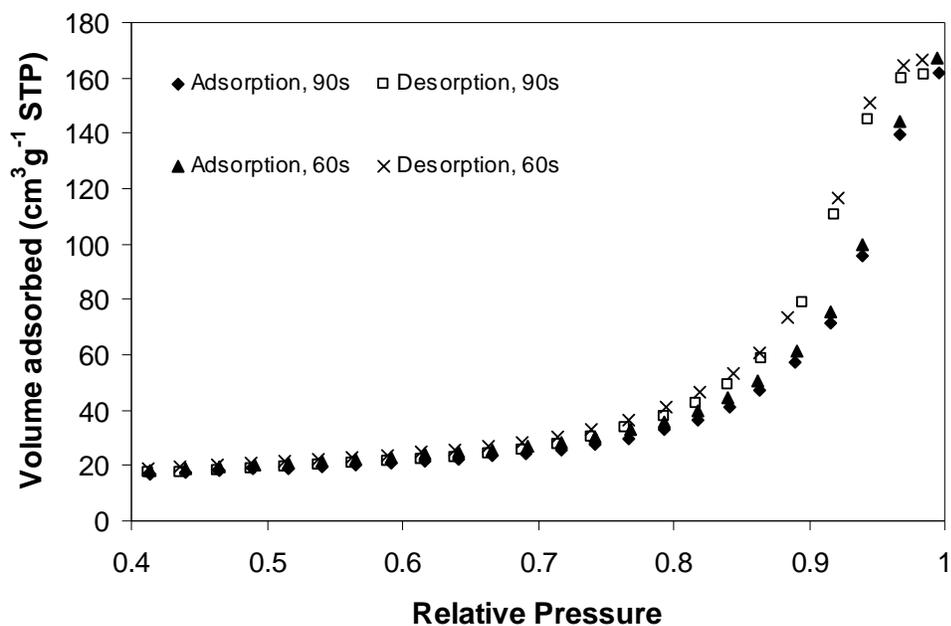
(c)

Fig. 3.17. (a) Typical nitrogen adsorption-desorption isotherms obtained for sample C (whole) at different equilibration times. The sample pre-treatment condition was 90 °C for 1 h followed by 350 °C for 4 h for all experiments. (b) Low pressure range of the equilibrated isotherms showing the formation of the monolayer. Also very low uptake is seen in this sample relative to samples A and B. (c) Capillary condensation region in sample C characterised by a narrow hysteresis loop for the two isotherms presented in Fig. 3.17b.

$$y = 0.09180x + 0.00043$$
$$R^2 = 0.99999$$

(a)
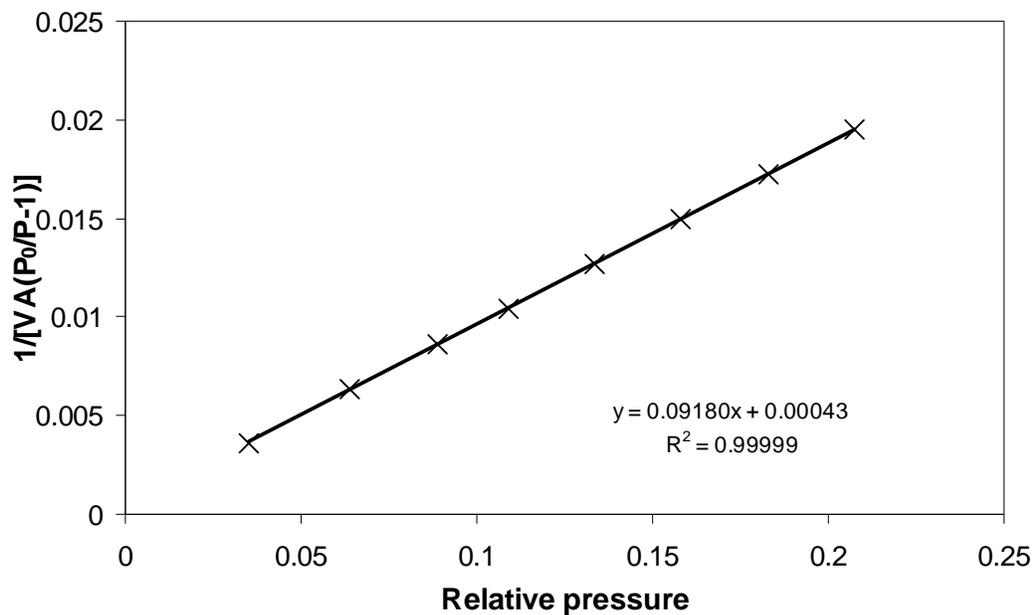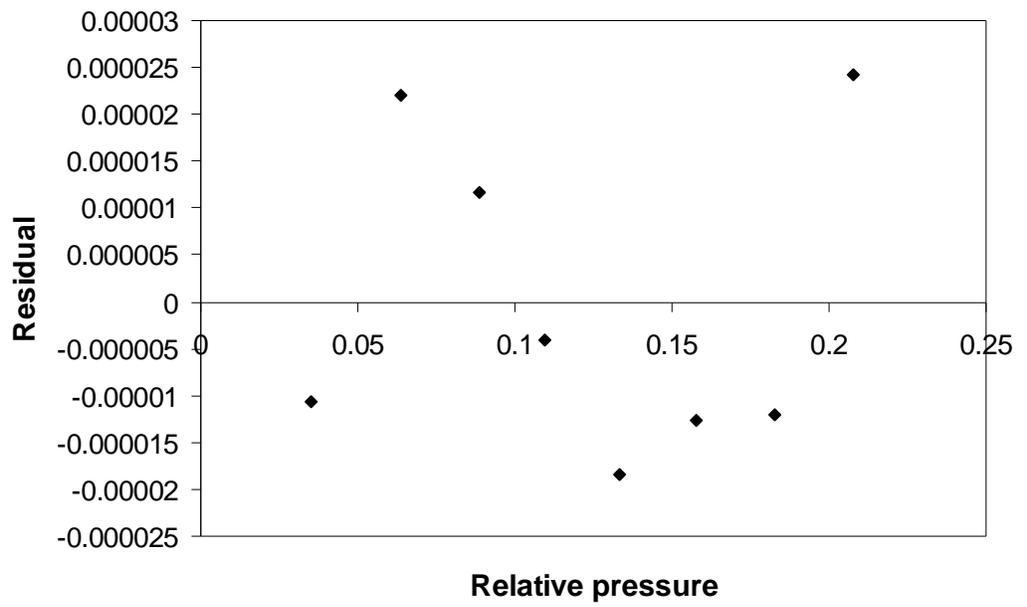
Fig. 3.18. (a) Typical BET surface area plot obtained for sample C (whole). (b) Residuals obtained for the straight line fit presented in Fig. 3.18a.

$y = -0.407x + 2.7865$

$R^2 = 0.9997$

(a)
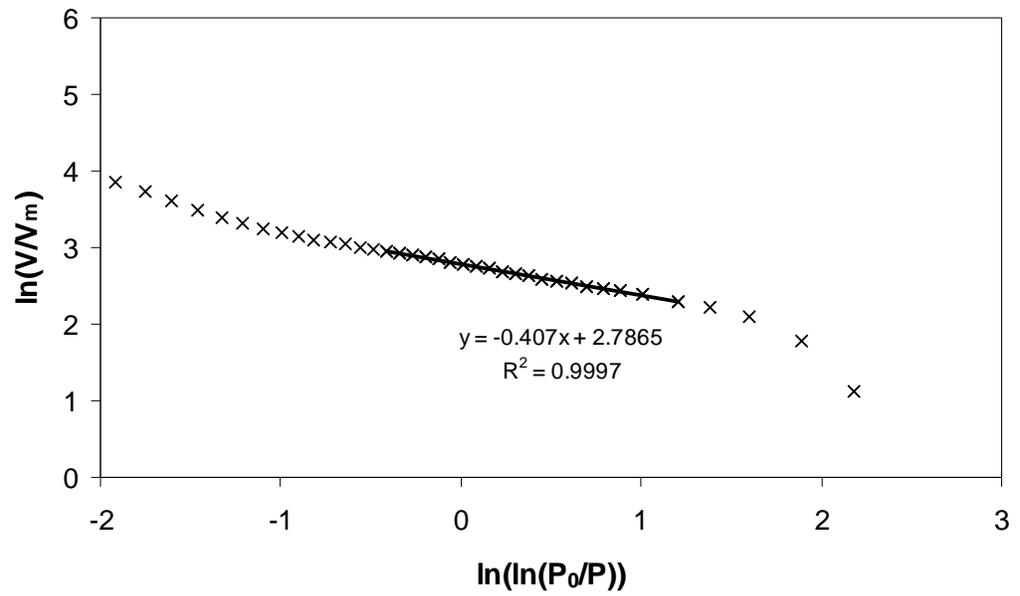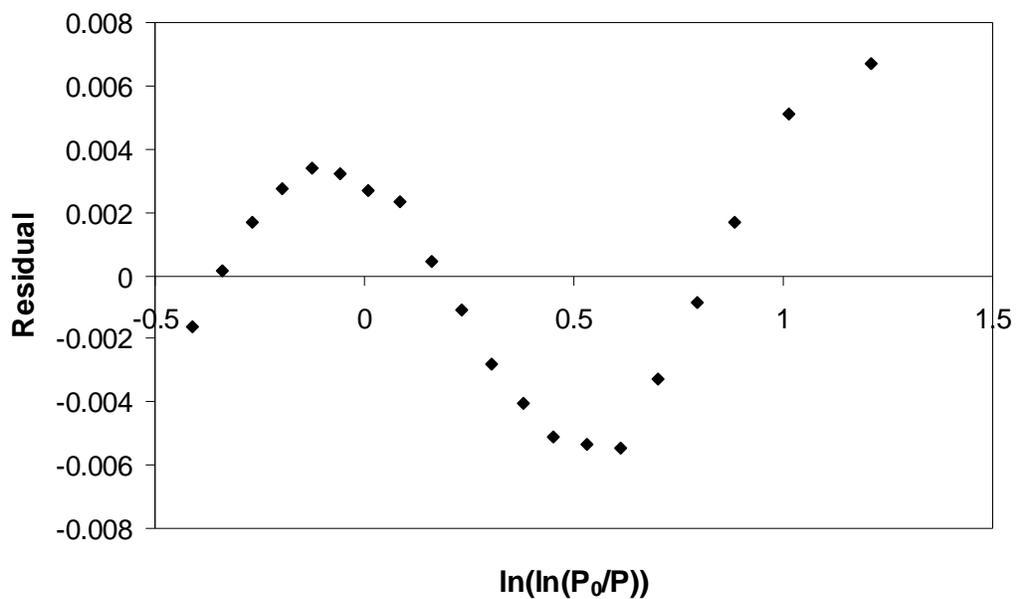
Fig. 3.19. (a) Typical FHH fractal dimension plot obtained for sample C (whole). (b) Residuals obtained for the straight line fit presented in Fig. 3.19a.
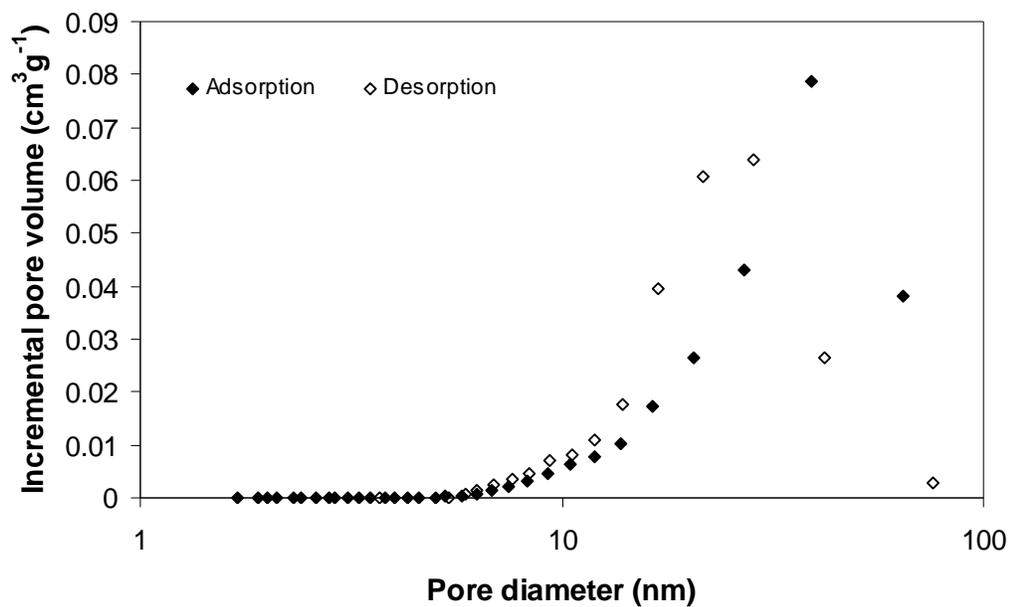
Fig. 3.20. Typical BJH pore size distribution plots obtained for sample C (whole). The distributions were obtained under the assumption that there were no pores open at both ends.
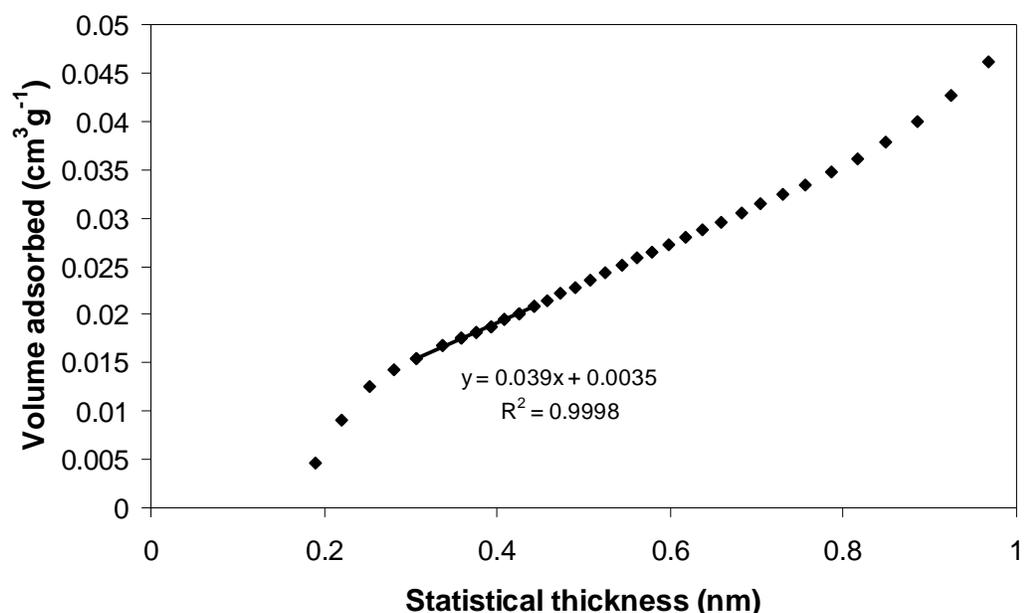
Fig. 3.21. Typical *t* plot obtained for sample C (whole). The positive intercept implied the presence of a micropore volume within sample C.

Apart from standard catalyst properties as seen earlier in Table 3.4, nitrogen uptake at low relative pressures and in the multilayer region was tested by fitting different two-component models as discussed earlier in Section 3.1.3. It was found that the experimental data were best defined by a two-component (Langmuir and BET) model. The fit of this model to the experimental data and the parameters obtained are presented in Fig. 3.22 and Table 3.6a. Results of the fit showed that ~40% of the catalyst surface contained micropores and the remaining 60% was responsible for multilayer adsorption and presumably contained mesopores. Table 3.6b contains the sum of the squares of the residuals of the fits to the experimental data for the different models.

Table 3.6
(a) Parameters that satisfy the fit of the Langmuir + BET model to the adsorption isotherm of sample C (whole). (b) Sum of the squares of the residuals obtained for different models.

(a)

Model	p	b	BET C constant	V_m (cm^3g^{-1} STP)	Surface area (m^2g^{-1})
Langmuir + BET	0.6	23	4225	12	54

(b)

	Langmuir + BET	Langmuir + Fractal BET	Langmuir + Fractal FHH
$\Sigma(Residual)^2$	0.64	11.5	33
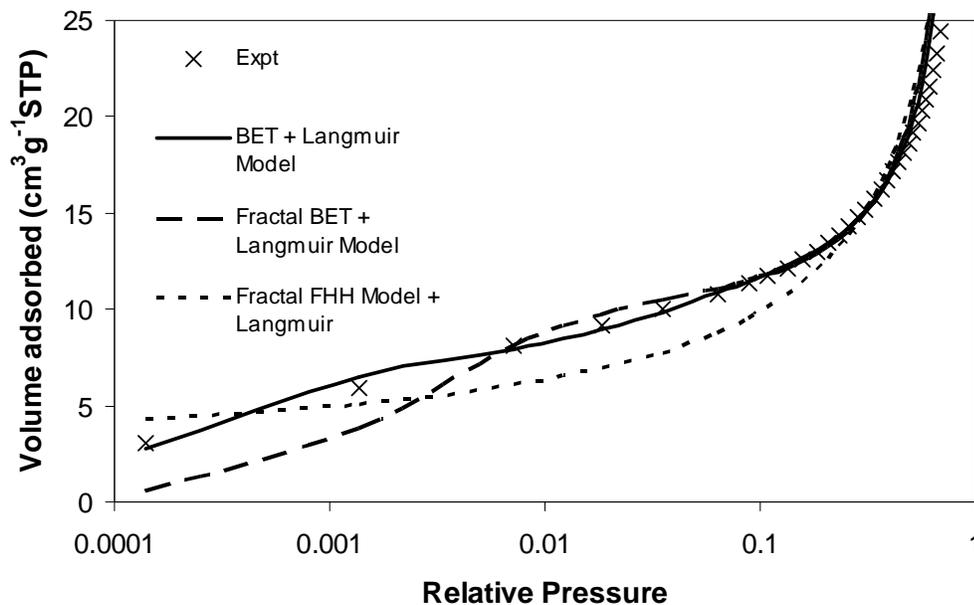
Fig. 3.22. Different two component models fitted to the nitrogen uptake in the micropore region and multilayer adsorption region in sample C (whole). Relative pressures are represented in the logarithmic scale to verify whether fitting took place at low relative pressures. Models fitted include BET + Langmuir, Fractal BET + Langmuir model, and Fractal FHH + BET model. It can be seen that the BET + Langmuir model fitted over multilayer and micropore regions. The parameters can be seen in Table 3.6a.
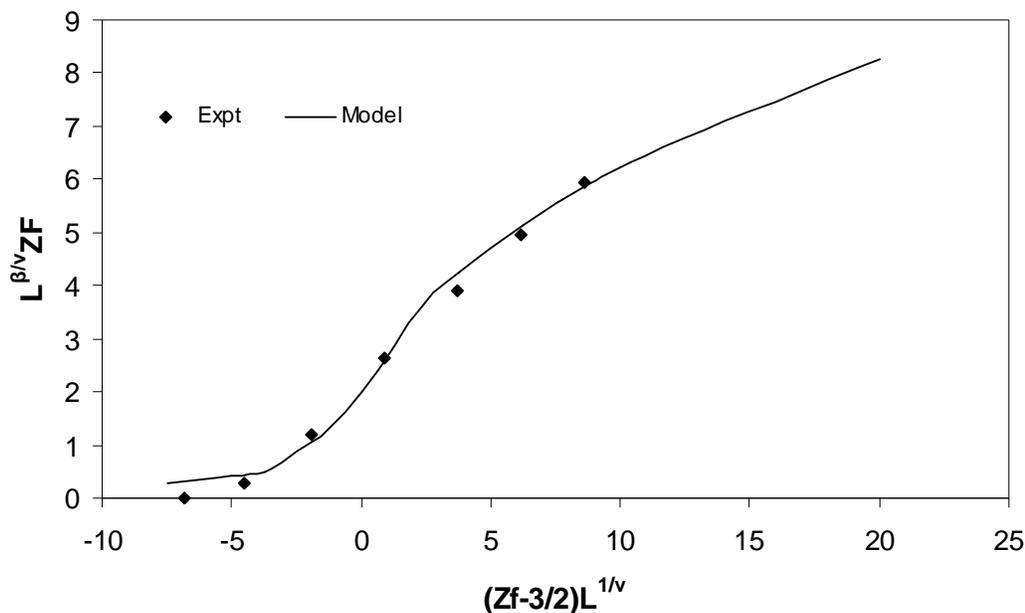
Fig. 3.23. Fit of the nitrogen sorption experimental data of sample C (whole) to the generalised scaling function using the method due to Seaton (1991). The values obtained from the fit are given in Table 3.7.

Since the nitrogen fully filled the sample, the accessibility of the mesopore network was analysed to determine lattice size L and connectivity Z using the method, due to Seaton (1991), based on percolation theory. The fit of nitrogen sorption data

for sample C to the generalised scaling function for the Seaton (1991) method is presented in Fig. 3.23. The values of L and Z obtained from the fit are presented in Table 3.7.

Table 3.7
Value of pore connectivity and lattice size of sample C (whole) obtained from percolation analysis of the nitrogen sorption isotherms using the Seaton (1991) method.

Sample	Z	L
C	7	4

3.8 DISCUSSION – SAMPLE C

Nitrogen gas adsorption porosimetry has revealed properties in sample C that were not understood earlier from mercury porosimetry. Although there was an agreement between the pore volume and surface area determined by the two techniques, mercury intrusion determined only the presence of mesopores. The mercury extrusion process for sample C showed that ~100% of the intruded mercury was not recoverable. In contrast, nitrogen adsorption on this catalyst revealed a Type IV isotherm that was representative of micro-mesoporous material with a narrow Type H2 hysteresis loop. This narrow hysteresis loop implied the existence of good connectivity among the pores present in catalyst sample C which was in line with the pore connectivity and lattice size obtained from the Seaton method (see Table 3.7). The lattice size was smaller than that for sample A and the pore connectivity was better too. The narrow hysteresis loop obtained from nitrogen gas sorption also suggested that little structure shielding or pore blocking was likely to exist among the pores of sample C. This disagreement between the nitrogen gas adsorption-desorption isotherm and mercury intrusion-extrusion behaviour suggested that mercury was unrecoverable from the pores of sample C due to the chemistry effect discussed in Section 2.8. As a result, the mercury extrusion process was unlikely to give any pore structure information. The BET surface area and pore volume present in sample C was far less than that available in samples A and B. The BJH pore size distribution revealed a modal pore diameter of ~40 nm, much larger than pores present in samples A and B.

Similar to samples A and B, sample C was also characterised by localised adsorption effects as evident from the BET C constant of ~187. Clearly, the quadrupole moment of nitrogen was being effected by the chemistry of the surface due to the presence of active metal components like Zn and Cu. Hence, adsorption on certain sites was expected to be stronger than the others.

96

Two-component fits using different models were completed to gain an understanding of the micropore and mesopore region. The Langmuir + BET model indicated that ~40% of the pore space was occupied by micropores and the remaining by mesopores. This information would have been handy to compare it with adsorption data from coked catalysts as it may give essential information as to whether coking actually took place in the micropore and/or mesopore regions. As mentioned earlier, sample C did not give sufficient upgrading under the reaction conditions investigated. Further, these catalysts could not be removed without causing extra damage to them and the reactor.

For sample C, the low upgrading performance can also be related to the chemistry of the catalyst. This catalyst was designed for LTS reactions and was used to test whether any hydrogen could be fixed as the THAI® oil and gas fell on the catalyst bed. Gas analysis did not reveal the presence of any hydrogen content. The catalyst was not designed to handle contaminants of the nature seen in heavy oil. Though pore size present in sample C can be considered to be favourable, it may however be better to have catalysts that contained macropores only, and also had a larger pore volume.

3.9 CONCLUSIONS

Considering all the three samples, the analyses showed that all samples were primarily mesoporous with some distribution of micropores. None of the catalysts showed cavitation effects in their respective desorption branches. This indicated that pore blocking was probably influential, especially in samples A and B. Sample B showed evidence of the presence of macropores, however, they were shielded. Hence, it was unlikely that the reactant molecules would encounter it initially. Sample C was an LTS catalyst with a better connectivity than sample A. However, under the investigated conditions, it did not lead to any substantial upgrading of the feed (THAI® field oil) by the addition of hydrogen. The mesoporous character of all three samples was likely to be the major reason behind their mediocre performance in upgrading the feed. Sample A in it coked form was analysed by nitrogen adsorption. It gave evidence of rapid coking and blockage of the entire pore space within an hour. Hence, the next step would be to look at conducting experiments with catalysts that have a substantial macropore size distribution, thereby tackling the diffusion limitations caused by the unfavourable size ratio of the pores present in the catalysts and oil molecules investigated in this work.

REFERENCES

ADAMSON, A. W. 1982. *Physical chemistry of surfaces,* New York ; Chichester, Wiley.

BARRETT, E. P., JOYNER, L. G. & HALENDA, P. P. 1951. The Determination of Pore Volume and Area Distributions in Porous Substances. I. Computations from Nitrogen Isotherms. *Journal of the American Chemical Society,* 73, 373-380.

BOER, J. H. D., LIPPENS, B. C., LINSEN, B. G., BROEKHOFF, J. C. P., HEUVEL, A. V. D. & OSINGA, T. J. 1966. The *t*-curve of multimolecular N_2-adsorption. *Journal of Colloid and Interface Science,* 21, 405-414.

BRUNAUER, S., EMMETT, P. H. & TELLER, E. 1938. Adsorption of Gases in Multimolecular Layers. *Journal of the American Chemical Society,* 60, 309-319.

BURGESS, C. G. V. & EVERETT, D. H. 1970. Lower Closure Point in Adsorption Hysteresis of Capillary Condensation Type. *Journal of Colloid and Interface Science,* 33, 611-614.

CHUA, L. M., VAZHNOVA, T., MAYS, T. J., LUKYANOV, D. B. & RIGBY, S. P. 2010. Deactivation of PtH-MFI bifunctional catalysts by coke formation during benzene alkylation with ethane. *Journal of Catalysis,* 271, 401-412.

COASNE, B., DI RENZO, F., GALARNEAU, A. & PELLENQ, R. J. M. 2008a. Adsorption of simple fluid on silica surface and nanopore: Effect of surface chemistry and pore shape. *Langmuir,* 24, 7285-7293.

COASNE, B., GALARNEAU, A., DI RENZO, F. & PELLENQ, R. J. M. 2008b. Molecular simulation of adsorption and intrusion in nanopores. *Adsorption-Journal of the International Adsorption Society,* 14, 215-221.

COHAN, L. H. 1938. Sorption Hysteresis and the Vapor Pressure of Concave Surfaces. *Journal of the American Chemical Society,* 60, 433-435.

FELIPE, C., ROJAS, F., KORNHAUSER, I., THOMMES, M. & ZGRABLICH, G. 2006. Mechanistic and experimental aspects of the structural characterization of some model and real systems by nitrogen sorption and mercury porosimetry. *Adsorption Science & Technology,* 24, 623-643.

FURIMSKY, E. 2007. *Catalysts for upgrading heavy petroleum feeds,* Amsterdam ; Oxford, Elsevier.

GREGG, S. J. & SING, K. S. W. 1982. *Adsorption, surface area and porosity.* 2nd ed. London: Academic Press Inc. Ltd.

HARKINS, W. D. & JURA, G. 1944. Surfaces of Solids. XIII. A Vapor Adsorption Method for the Determination of the Area of a Solid without the Assumption

of a Molecular Area, and the Areas Occupied by Nitrogen and Other Molecules on the Surface of a Solid. *Journal of the American Chemical Society,* 66, 1366-1373.

HITCHCOCK, I., CHUDEK, J. A., HOLT, E. M., LOWE, J. P. & RIGBY, S. P. 2010. NMR Studies of Cooperative Effects in Adsorption. *Langmuir,* 26, 18061-18070.

ISMAIL, I. M. K. & PFEIFER, P. 1994. Fractal Analysis and Surface-Roughness of Nonporous Carbon-Fibers and Carbon-Blacks. *Langmuir,* 10, 1532-1538.

KARNAUKHOV, A. P. 1985. Improvement of Methods for Surface-Area Determinations. *Journal of Colloid and Interface Science,* 103, 311-320.

LOWELL, S., SHIELDS, J. E., THOMAS, M. A. & THOMMES, M. 2006. *Characteriszation of porous solids and powders: surface area, pore size and density,* Dordrecht, Kluwer Academic Publishers.

MCMILLAN, W. G. 1947. Multilayer Gas Adsorption on Composite Surfaces. *The Journal of Chemical Physics,* 15, 390-397.

MORISHIGE, K. & SHIKIMI, M. 1998. Adsorption hysteresis and pore critical temperature in a single cylindrical pore. *Journal of Chemical Physics,* 108, 7821-7824.

MORISHIGE, K., TATEISHI, M., HIROSE, F. & ARAMAKI, K. 2006. Change in desorption mechanism from pore blocking to cavitation with temperature for nitrogen in ordered silica with cagelike pores. *Langmuir,* 22, 9220-9224.

NEIMARK, A. V. 2002. Fractal Analysis. *In:* SCHÜTH, F., SING, K. S. W. & WEITKAMP, J. (eds.) *Handbook of porous solids.* Weinheim: Wiley-VCH.

NEIMARK, A. V. & RAVIKOVITCH, P. I. 2001. Capillary condensation in MMS and pore structure characterization. *Microporous and Mesoporous Materials,* 44, 697-707.

RANA, M. S., ANCHEYTA, J., MAITY, S. K. & RAYO, P. 2005a. Characteristics of Maya crude hydrodemetallization and hydrodesulfurization catalysts. *Catalysis Today,* 104, 86-93.

RANA, M. S., ANCHEYTA, J., MAITY, S. K. & RAYO, P. 2005b. Maya crude hydrodemetallization and hydrodesulfurization catalysts: An effect of TiO_2 incorporation in Al_2O_3. *Catalysis Today,* 109, 61-68.

RASMUSSEN, C. J., GOR, G. Y. & NEIMARK, A. V. 2012. Monte Carlo Simulation of Cavitation in Pores with Nonwetting Defects. *Langmuir,* 28, 4702-4711.

RAVIKOVITCH, P. I. & NEIMARK, A. V. 2002. Experimental confirmation of different mechanisms of evaporation from ink-bottle type pores: Equilibrium, pore blocking, and cavitation. *Langmuir,* 18**,** 9830-9837.

RAYO, P., RANA, M. S., RAMIREZ, J., ANCHEYTA, J. & AGUILAR-ELGUEZABAL, A. 2008. Effect of the preparation method on the structural stability and hydrodesulfurization activity of NiMo/SBA-15 catalysts. *Catalysis Today,* 130**,** 283-291.

RIGBY, S. P., CHIGADA, P. I., PERKINS, E. L., WATT-SMITH, M. J., LOWE, J. P. & EDLER, K. J. 2008. Fundamental studies of gas sorption within mesopores situated amidst an inter-connected, irregular network. *Adsorption-Journal of the International Adsorption Society,* 14**,** 289-307.

RIGBY, S. P. & FLETCHER, R. S. 2004. Interfacing mercury porosimetry with nitrogen sorption. *Particle & Particle Systems Characterization,* 21**,** 138-148.

ROUQUEROL, F., ROUQUEROL, J. & SING, K. S. W. 1999. *Adsorption by powders and porous solids : principles, methodology and applications,* London, Academic Press.

ROUQUEROL, J., AVNIR, D., FAIRBRIDGE, C. W., EVERETT, D. H., HAYNES, J. H., PERNICONE, N., RAMSAY, J. D. F., SING, K. S. W. & UNGER, K. K. 1994. Recommendations for the Characterization of Porous Solids. *Pure and Applied Chemistry,* 66**,** 1739-1758.

SAHOULI, B., BLACHER, S. & BROUERS, F. 1997. Applicability of the fractal FHH equation. *Langmuir,* 13**,** 4391-4394.

SHENG, J. 2011. *Modern chemical enhanced oil recovery : theory and practice,* Burlington, Gulf Professional Publishing.

SING, K. 2001. The use of nitrogen adsorption for the characterisation of porous materials. *Colloids and Surfaces A: Physicochemical and Engineering Aspects,* 187**,** 3-9.

SING, K. S. W., EVERETT, D. H., HAUL, R. A. W., MOSCOU, L., PIEROTTI, R. A., ROUQUEROL, J. & SIEMIENIEWSKA, T. 1985. Reporting Physisorption Data for Gas Solid Systems with Special Reference to the Determination of Surface-Area and Porosity (Recommendations 1984). *Pure and Applied Chemistry,* 57**,** 603-619.

SING, K. S. W. & WILLIAMS, R. T. 2004. Physisorption hysteresis loops and the characterization of nanoporous materials. *Adsorption Science & Technology,* 22**,** 773-782.

WALKER, W. C. & ZETTLEMOYER, A. C. 1948. A Dual-Surface B.E.T. Adsorption Theory. *The Journal of Physical Chemistry,* 52, 47-58.

WALLACE, E. D., LOTT, R. K., DAIGNEAULT, L. E., SHELLY, N., IVORY, J., KUMAR, D., FRAUENFELD, T. & SINGH, B. 1983. Some Physical Properties of Bitumen and Oil Sand, Revision 2. *In:* PROWSE, D. R. (ed.). Edmonton, Alberta: Alberta Research Council.

WEISSMAN, J. G. & EDWARDS, J. C. 1996. Characterization and aging of hydrotreating catalysts exposed to industrial processing conditions. *Applied Catalysis A: General,* 142, 289-314.

ZHAO, B. & SHAW, J. M. 2007. Composition and size distribution of coherent nanostructures in Athabasca bitumen and Maya crude oil. *Energy & Fuels,* 21, 2795-2804.

ZHAO, B. & SHAW, J. M. 2008. Impact of asphaltene-rich aggregate size on coke deposition on a commercial hydroprocessing catalyst. *Energy & Fuels,* 22, 1080-1092.

CHAPTER 4 – INTEGRATED ADSOPRTION OF NITROGEN AND WATER – N₂-H₂O-N₂ PROTOCOL

Chapter 4 of this thesis introduces the reader to a catalyst characterisation technique that has been adapted from conventional gas adsorption. Here, two adsorbates will be used. After adsorption of the first component, it is made immobile by freezing. This is then followed by the adsorption of a second component. The technique is introduced by recalling the absence of such an approach in the literature to distinguish fresh and aged/coked catalysts. It will be seen that the literature reveals the use of other related similar techniques such as the preadsorption of different films, and the use of integrated N_2-Hg-N_2 experiments on model materials. Thus, the absence of application of the above technique to characterising fresh and aged catalysts proved to be a motivating factor in developing the same. A brief description of the theory used to derive adsorption mass transfer coefficients is also given. The integrated N_2-H_2O-N_2 adsorption experiment will be performed on fresh sample A (discussed earlier in Chapter 2 and Chapter 3) and a coked counterpart. This experiment will establish the significance of pore coupling by showing the presence of advanced adsorption. The kinetic data obtained during the adsorption of nitrogen will also be used to help determine the location of coke.

4.1 INTRODUCTION

To understand and model the kinetics of catalyst deactivation, it is necessary to determine how coke or carbon deposition takes place on the pores of the catalyst. An important role in modelling catalyst deactivation is the comparison of pore properties of the fresh and carbon deposited or aged catalysts. The literature reveals that an understanding can be achieved by considering the coke to be deposited in the form of a uniform or non-uniform layer where the latter scenario leads to instances of pore blocking or filling. Such modelling requires the need to consider pores present in the catalyst pellet to assume a geometric shape. Thus, the simplest model assumes pores present in the catalyst have a cylindrical shape and form a parallel bundle. This model has been used by Menéndez and Braña (1994) to describe the pore structure present in fresh and aged Cr_2O_3/Al_2O_3 catalysts by using mercury porosimetry and thermogravimetry. They found that coke deposition within aged catalysts could be described by a cylindrical parallel pore bundle model with a uniform layer of coke.

However, such a model need not accurately describe the pore structure of all catalysts. It is well known that pores present in catalysts are not regular and assume various shapes. Hence, more complex models such as a cross linked pore model or a percolation model may be required to describe the pore topology of catalysts.

Unlike the approach adopted by Menéndez and Braña (1994), García-Ochoa and Santos (1996) used nitrogen gas adsorption to estimate pore properties and pulse chromatography to determine the effective diffusion coefficients of an Ar-He system in two different sets of catalysts (fresh Pt-Al$_2$O$_3$ and Ni-Mo-Al$_2$O$_3$, and their aged counterparts sourced from different reactions). They used a cylindrical bundle pore model, cross linked pore model and a percolation model to interpret the diffusion measurements. They found that the percolation model used (i.e. a Bethe network) could not describe the topology of Pt-Al$_2$O$_3$ catalysts. This was mainly attributed to the high initial porosity of Pt-Al$_2$O$_3$ catalysts (0.93) which possibly implied a greater number of inter-pore connections or branches than that described by the Bethe network. It is possible that some other form of network may describe the pore topology of Pt-Al$_2$O$_3$ catalysts; however this has not been discussed by García-Ochoa and Santos (1996). In contrast to the Pt-Al$_2$O$_3$ catalysts, the percolation model described the pore topology of Ni-Mo-Al$_2$O$_3$ catalysts. With coordination number $Z = 4$, the model accurately predicted the evolution of the effective diffusion coefficients in Ni-Mo-Al$_2$O$_3$ catalysts. In the above work, the focus has been mainly on modelling the catalyst pore topology from the pore properties obtained using conventional characterisation techniques, namely mercury porosimetry and nitrogen gas adsorption.

In contrast to the above approaches, traditional characterisation techniques have also undergone major developments in the recent past. An example of this development is the integration of nitrogen gas adsorption and mercury porosimetry. Here, nitrogen adsorption experiments are performed prior to, and post, mercury intrusion porosimetry on a sample. This technique has been used in different formats (complete or scanning loops for mercury porosimetry) to determine the distribution of pore length with diameter for porous materials (Rigby et al., 2005), the spatial distribution of different pore sizes (Rigby et al., 2004), and test for the presence of any pore blocking effects (Rigby and Fletcher, 2004). They have also been used to deconvolve adsorption and desorption behaviour within pore necks and pore bodies, especially when the latter is filled with entrapped mercury. The results from the latter were also supported by mean field theory (MFT) simulations which revealed that adsorption in an open ink bottle pore (having pore neck to pore body size ≥ 0.9)

occurred at a relative pressure corresponding to that for a cylindrical meniscus if the neck was short (Rigby and Chigada, 2009). However, the technique is yet to be utilised in a practical application to differentiate between fresh and aged catalysts. Further, Rigby and Chigada (2009) also highlight that the traditional method of characterising porous materials (such as either using the Kelvin equation in the BJH algorithm or even employing alternative methods such as non-local density functional theory (NLDFT)) involves an assumption of the absence of any pore-pore cooperative or coupling effects, i.e. the porous material void space is assumed to take the form of a parallel bundle. This assumption can lead to inaccuracies in the characterisation of fresh and aged catalysts. This cooperative effect, termed advanced condensation or advanced adsorption, has also been discussed earlier by Mayagoitia et al. (1985) and Esparza et al. (2004). They proposed that for a through ink-bottle pore, if the radii of the shielding necks (located on either side of the pore body) are greater than half the radius of the pore body, then all will fill at the same pressure. This is because once condensation takes place in the necks (from a cylindrical meniscus as given by the Cohan form of the Kelvin equation Eq. (3.8)), it provides the hemispherical menisci for the pore body, allowing the condensate to fill the body (since hemispherical menisci requires lesser pressure to condense). Carbon deposition can take place in pore necks or pore bodies causing a change in pore neck to pore body size ratio relative to the fresh catalyst. Thus, such a cooperative effect can have implications on the interpretations of characterisation data for coked catalysts.

Similar to the integrated nitrogen gas adsorption and mercury porosimetry experiments pursued by Rigby and co-workers, Morishige and Kanzaki (2009) examined the pore structure of ordered silicas (SBA-16 and KIT-5) by successive adsorption of water and nitrogen. In their work, adsorption of water was performed at 283 K to different filling fractions. The adsorbed water was then frozen after which nitrogen adsorption at 77 K was performed on the ordered silica material. The method identified that water tended to fill the necks, and, on freezing, blocked most pores thereby reducing the accessibility of nitrogen and also revealing the cage like nature of pores in SBA-16 and KIT-5. Further, they also found that, for SBA-16 and KIT-5 samples with larger necks, pore condensation of water occurred simultaneously in large cavities and a high fraction of necks, indicating that this sample subset had pores with an undulating character rather than cage-like features. Further experiments by Morishige and Yoshida (2010), involving successive adsorption of water and nitrogen, and water and argon, were performed on ordered mesoporous silica (FDU-12) which contained larger cavities (relative to SBA-16 and KIT-5). Results similar to

those obtained for SBA-16 and KIT-5 were obtained. The amount of nitrogen and argon that condensed inside cavities decreased rapidly over a relatively small range of water filling with an increase in water filling. This once again indicated the cage like character of the pores in FDU-12. Morishige and Yoshida (2010) also argue that the gradual desorption isotherm observed for ordered mesoporous silicas (FDU-12) was not due to the wide distribution of neck sizes but due to a desorption mechanism that involves bubble formation at the microscopic meniscus of the emptied pore.

Other investigations, which involve the presence of two adsorbed phases, include a study of the fractal properties of porous supports by the distribution of a host phase within them, modification of the support surface by the addition of different functional groups or preadsorption of films of varying thicknesses. Neimark et al. (1993) determined the surface fractal dimension of a porous silica support into which polybutadiene was impregnated in different amounts. The pre- and post-addition nitrogen gas adsorption isotherms at 77 K were used to determine the surface fractal dimension. They found that the addition of greater amounts of polybutadiene decreased the available pore volume and BET surface area. However, the surface fractal dimension did not change significantly from that obtained for the raw support. This implied the presence of a random distribution of the polymer in the porous support in the form of different sized ganglia (see Fig. 3 of Neimark et al. (1993)), since a uniform coating of the polymer along the entire pore space would have changed the surface fractal dimension significantly and also produced a change in the hydraulic radius (which was not observed). Hua and Smith (1992) studied the change in surface area, surface texture, pore size distribution and total pore volume of different silica samples (CPG, Vycor and silica xerogels) modified with different functional groups, i.e. alkylsilylation was performed to different degrees of coverage. Alkylsilylation was performed using trimethylchlorosilane, triethylchlorosilane, and tri-n-propylcholorosilane. They found that the surface area and pore volume of the different silica samples decreased rapidly with increased silylation of the raw silica surface. The pore size distribution narrowed significantly and also seemed to show a loss of larger pores. The surface fractal dimension as determined from the power law relation between film surface area and film volume agreed with the interpretation from small angle x-ray scattering (SAXS) analyses. Silylation increased the smoothness of the surface; larger the size of the silylating functional group, more smooth the surface. Pfeifer et al. (1991) determined the surface fractal dimension of different porous silicas (Cab-O-Sil fumed silicas, CPG, Vycor, and silica xerogels) by varying the surface area of an adsorbed film of water as a function of its volume. This

preadsorbed water was then frozen and nitrogen gas adsorption was used to determine the film area. The power law relation between the film area and film volume helped yield the surface fractal dimension which agreed well with that determined by other methods such as SAXS, small angle neutron scattering (SANS) and molecular tiling.

The review of the literature showed that the integrated or the successive adsorption method, or even the preadsorption of water or hydrocarbon films, has only to date been applied to ordered and disordered homogeneous materials. None of the above techniques have been applied in the characterisation of catalysts, be they in the fresh or aged form[22]. Further, they have also not been used to assess the impact of advanced adsorption effects in coked catalysts. In this chapter, adsorption experiments will be carried out in the following sequence: (1) nitrogen adsorption and desorption on a catalyst sample, (2) water adsorption on the same sample which will then be frozen, and (3) nitrogen adsorption and desorption on the sample containing the frozen water. Thus, like the integrated experiments performed by Rigby and co-workers and the successive adsorption experiments of Morishige and co-workers, integrated N_2-H_2O-N_2 adsorption experiments will be performed on fresh and aged catalysts. This will then be used to assess advanced adsorption effects in coked catalysts and determine the location of coke deposits within the catalyst.

4.2 THEORY

It was pointed out earlier in Chapter 3 that adsorption isotherms can be obtained either by a gravimetric or volumetric mode of operation. All experiments presented in this chapter were performed gravimetrically. In this mode of operation, equilibrium adsorption uptake is obtained by following a series of changes in gas pressure, and also simultaneously recording the mass uptake by the porous medium. Equilibrium mass uptake at a particular pressure is attained when there is no change in mass for that pressure. The timescale required for mass uptake is generally variable and depends on the material, gas, temperature, and will also vary as a function of composition of adsorbate within the material.

Since the increment in mass is recorded, it is possible to use this technique to gain an understanding of the kinetics of adsorption. There are different models that

---

[22] At the most, it can be said that any application of these advanced techniques in the characterisation of catalysts is not available in the open literature.

can be used to describe the adsorption kinetics in porous materials. Among them, the linear driving force (LDF) model:

$$\frac{d\overline{q}}{dt} = k\left(q^* - \overline{q}\right),$$ (4.1)

as suggested by Glueckauf and Coates (1947) and Glueckauf (1955), has been regarded as a convenient model to represent and analyse the overall rate of uptake of adsorbate molecules in adsorption systems (Sircar and Hufton, 2000). In Eq. (4.1), k is the effective LDF mass transfer coefficient, $\overline{q}$ is the average adsorbate uptake in the adsorbent particle, q^* is the equilibrium adsorbate uptake in the adsorbent particle at the specific pressure and adsorbent temperature and $\frac{d\overline{q}}{dt}$ is the rate of mass uptake during adsorption.

Glueckauf and Coates (1947) and Glueckauf (1955) solved the mass balance equation for adsorption in a spherical pellet and derived solutions for the uptake rate when the concentration increased linearly. Their solution represented by:

$$\frac{\partial \overline{q}}{\partial t} = \frac{15D}{R_p^2}\left(q^* - \overline{q}\right),$$ (4.2)

is valid for a spherical pellet. Thus, from Eqs. (4.1) and (4.2):

$$k = \frac{15D}{R_p^2},$$ (4.3a)

where D is the diffusion coefficient and R_p is the particle radius or diffusion path length. For other geometries, the LDF approximations have been provided by Patton et al. (2004). For a cylindrical adsorbent pellet, mass transfer coefficient is related to the effective diffusivity by the following relation:

$$k = \frac{8D}{R_p^2}.$$ (4.3b)

For most adsorbent particle geometries, the general relation between the LDF mass transfer coefficient and the path length can be probed by applying the following relation:

$$k \propto \frac{D}{R_p^2}.$$ (4.3c)

The LDF model uses a lumped parameter approach that helps to avoid the complexity of dealing with different operating diffusion mechanisms. Unlike other models, which are highly complex and require large computational time, the LDF model is mathematically simple (a linear equation). However, the LDF model

assumes that the adsorbent particle temperature is uniform at all times and does not vary across its radius (Sircar and Hufton, 2000; Crittenden, 2006). Integrating Eq. (4.1) with an initial condition where the adsorbent particle is free of all adsorbate and then instantaneously exposed to a constant surface concentration provides:

$$\frac{\overline{q}}{q^*} = 1 - \exp(-kt).$$

(4.4)

This equation has been used in Section 4.4.2 to determine the mass transfer coefficients in fresh and aged catalysts.

Diffusion in the gas phase results from collisions of gas molecules among themselves. However, when entering a pore, the diffusion process is dominated either by collision between the molecules themselves, or by collisions between the molecules and the pore wall, or an intermediate regime where the former two mechanisms operate. This is dependent on the mean free path λ:

$$\lambda = \frac{1}{\sqrt{2}n\pi\sigma^2} = \frac{RT}{\sqrt{2}\pi\sigma^2 N_A P},$$

(4.5)

of the gas molecules at the specific temperature and pressure. In Eq. (4.5), R is the ideal gas constant, T is the temperature, σ is the collision diameter of the gas molecules ($\sigma = 0.3$ nm for nitrogen), N_A is the Avogadro number, and P is the pressure. An estimate of the mean free path λ can be readily obtained on Nave (2010). When the mean free path of gas molecules is far less than the diameter of the pore, diffusion is dominated by collisions of the gas molecules and the process is called Maxwellian, bulk or molecular diffusion. However, when the mean free path of gas molecules is far greater than the pore diameter, diffusion occurs due to collision of gas molecules with the pore wall. This diffusion regime is termed Knudsen diffusion and the Knudsen diffusion coefficient D_k is given by:

$$D_k = \frac{2}{3}r\left(\frac{8RT}{\pi M}\right)^{1/2},$$

(4.6)

where R is the ideal gas constant, T is the temperature, M is the molecular weight ($M = 28.01$ for nitrogen), and r is the pore radius (Yang, 1987; Thomas and Crittenden, 1998). The relative importance of the two different diffusion mechanisms is determined by the Knudsen number N_{Kn}:

$$N_{Kn} = \frac{\lambda}{d_p},$$

(4.7)

which is the ratio of the mean free path λ to the pore diameter d_p. As a rule of thumb, molecules are in the Knudsen diffusion regime when $N_{Kn} > 10$ (Yang, 1987; Geankoplis, 2003). Since the Knudsen diffusion regime is dominated by collisions of

the gas molecules with the pore wall, it is possible to gain an understanding of the influence of the structure of the porous medium on the diffusion coefficient (or the mass transfer coefficient) of the adsorbate.

The diffusion coefficient in the Knudsen diffusion regime is proportional to $T^{1/2}$ as given in Eq. (4.6). Since $k \propto D$ (see Eq. 4.3c), this implies $k \propto T^{1/2}$ in the Knudsen diffusion regime. Hence, the obtained mass transfer coefficient can be normalised (as given by Eq. 4.8):

$$k_N = \left(\frac{k_1}{k_2}\right)\left(\frac{T_2}{T_1}\right)^{1/2},$$ (4.8)

to take account of any minor variation in temperature due to apparatus limitations on stability. This normalised mass transfer coefficient will be used in Section 4.4.2.

Apart from the normalised mass transfer coefficients, physical properties of the catalysts are also evaluated. In the evaluation of the BET surface area, the molecular area of nitrogen was determined from Fig. 7 in Karnaukhov (1985), who determined the variation of the nitrogen molecular area as a function of the BET C constant. It will be noted that in Section 4.4, for some cases two BET surface areas are present (each at different molecular areas). This has only been done as the general trend in the literature is to use a molecular area of 0.16 nm^2.

4.3 MATERIALS AND METHODS

An industrially-relevant, hydroprocessing catalyst sourced from a commercial vendor, denoted A, and its coked counterparts C1 and C2 were used for characterisation experiments in this work. The samples were characterised in their whole form, i.e. in the form of extrudates with length ~7 mm and diameter ~1 mm. Coked samples were obtained after allowing a model feed to undergo reactions in the CAPRI® microreactor at the University of Birmingham. The oil simulant fed into the reactor was decane at 1 mlmin^{-1}. The reaction was conducted at 425 °C and pressure was fixed at 2 MPa (20 bars). The operation time was 60 min. The properties and features of the samples are summarised in Table 4.1.

Gravimetric nitrogen[23] adsorption on fresh and coked catalyst samples was performed using a Hiden intelligent gravimetric analyser (IGA-002) system. The IGA SS316N chamber was opened and ~100 mg of the catalyst was loaded on to the sample hammock which was hung from a microbalance. The reactor chamber was then sealed tightly and the sample was evacuated to vacuum and heated to 90 °C for

---

[23] Nitrogen (oxygen free) gas was sourced from BOC.

an hour followed by a more intense heat treatment at 350 °C for four hours. This heat treatment was applied for fresh catalysts. Coked catalysts were heat treated at 150 °C for approximately twelve hours under similar vacuum conditions. After completing the heat treatment, the IGA reactor was allowed to cool to room temperature and an insulation jacket was placed around the reactor. The reactor was then immersed in a liquid nitrogen[24] dewar, that was regularly topped at 3-4 hour intervals to maintain isothermal conditions, to obtain the nitrogen adsorption isotherm.

After re-preparing the sample, water vapour adsorption was done using the same system by changing the valve position and installing a supply of ~20 ml of water in a vapour reservoir. The shifting of the valve position allowed the machine to operate in the vapour mode. The vapour reservoir was cleaned and dried in an oven before adding ultrapure water[25]. This water supply was then degassed. The partial saturation of the catalyst with water vapour was done after re-preparing the catalyst samples as above and ending the water vapour isotherm at a pressure of ~22 mbars which corresponded to a relative pressure of ~0.7 at 298 K instead of the saturation vapour pressure. This was achieved using the pressure control system available in the machine. At this pressure, there was sufficient capillary condensation to ensure that some of the pores in the catalyst were filled. A full water vapour isotherm performed prior to the partial water vapour adsorption experiment helped confirm this observation.

All water vapour adsorption experiments were performed at 298 K. At this temperature, the IGA SS316N reactor was surrounded by an ethylene glycol jacket. The jacket was connected to an external chiller which could be topped with ethylene glycol and had an automated temperature control system. To ensure complete equilibrium of the process, the catalyst was maintained at relative pressure of 0.7 for approximately 12 hours. At the end of the partial saturation, the ethylene glycol jacket was manually removed and the sample chamber was covered with an insulation jacket. A liquid nitrogen dewar half filled with liquid nitrogen was placed below the IGA reactor. The atmospheric water vapour present in the reactor was removed by outgassing at 1000 Pamin^{-1} (10 mbarsmin^{-1}) [26]. This low rate of degassing ensured that

---

[24] Liquid nitrogen was sourced from BOC.

[25] Ultrapure water having a resistivity of 18.2 MΩ-cm was used for the experiments.

[26] Further details on the switch from vapour to gas mode. The vapour reservoir was then disconnected by turning the PIV4 valve up. The vapour reservoir connection point was kept open (with the access panel on) for ~10 min. This helped to drain the water vapour in the line. The line was then shut with a stopper. PIV4 valve was then turned right and valve EV1 was also turned down slowly and carefully. At this stage, the turbo pump was cut off and it began to spin down. The vent on the pump was opened until the pressure was maintained between 0.03-0.04 MPa (300-400 mbars) and left for 15 min. The vent valve was then closed and the backing pressure was found to return to approximately 400 Pa (4 mbars) in 5 min. At this point, the turbo

atmospheric water vapour was removed. Subsequently, the remaining half of the dewar was filled with liquid nitrogen and the mass reading was allowed to stabilise. The nitrogen adsorption isotherm for the same sample after partial saturation with water was then obtained by bringing the machine back to gas mode and performing the experiment.

---

pump was switched on and outgas was also started at 1000 Pamin^{-1} (10 mbarsmin^{-1}). The weight was observed to go up and then down. Once the weight stabilised and the temperature reached the lowest possible value, nitrogen isotherm analysis was carried out on a catalyst sample that had frozen water.

Table 4.1
Composition and physical properties of samples used for nitrogen adsorption. Integrated N_2-H_2O-N_2 experiments were performed on sample A and C1.

Sample	Name	Composition (% W/W)	Appearance	Colour	Odour	Melting point (°C)	Bulk density (kgm^{-3})	Length (mm)	Diameter (mm)
A	Ketjenfine hydroprocessing catalysts-CoMo type	Precipitated silica: 0-6 Cobalt (II) oxide: 1-10 Molybdenum (VI) oxide: < 25 Phosphorus pentoxide: 0-4 Aluminium oxide: balance	Extrudates	Blue	Odourless	> 800	550-900	~7	~1
C1 (Coked)	Ketjenfine hydroprocessing catalysts-CoMo type	N/A	Extrudates	Brownish	N/A	N/A	N/A	~6	~1
C2 (Coked)	Ketjenfine hydroprocessing catalysts-CoMo type	N/A	Extrudates	Dark brown	N/A	N/A	N/A	~5	~1

4.4 RESULTS

4.4.1 ADSORPTION ISOTHERMS – SAMPLE A (FRESH AND COKED)
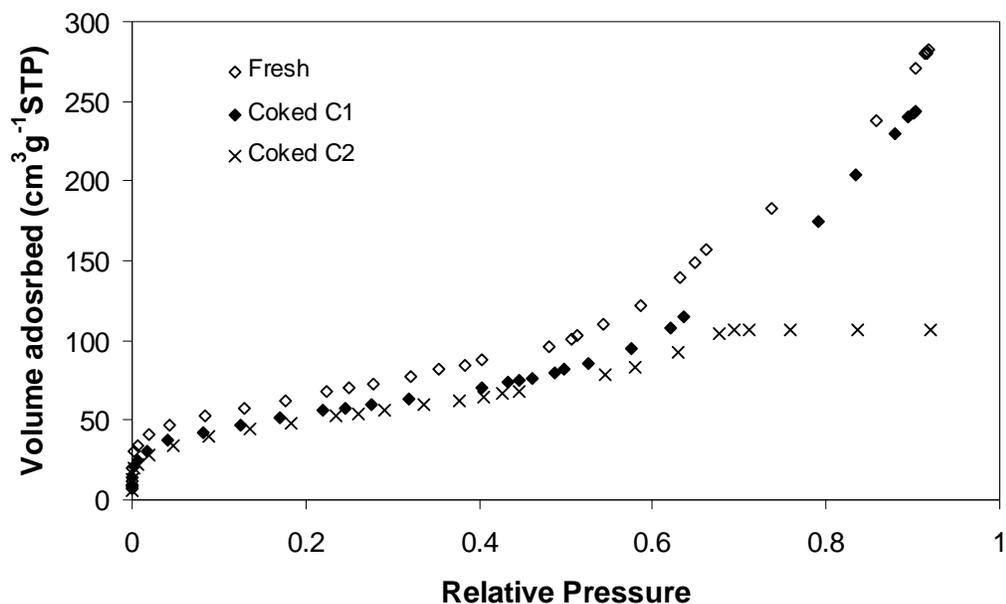
Fig. 4.1. Typical nitrogen adsorption isotherms obtained for sample A (whole) and its coked counterparts C1 (whole) and C2 (whole).

Fig. 4.1 presents the nitrogen gas adsorption isotherms obtained for sample A in its fresh form and its coked counterparts. The coked counterparts, denoted C1 and C2, are different subsets of catalysts from the same batch. The three isotherms were characterised by a rapid initial uptake at low relative pressures that formed a sharp point B. This was followed by multilayer adsorption and capillary condensation regions. Adsorption data only up to relative pressure $P/P_0 = 0.9$ was obtained for sample A in its fresh form and for the coked catalyst C1. The pore volumes for the two sets are presented in Table 4.2. It was observed that there was ~14% fall in pore volume following the reaction. However, this did not seem to affect the BET surface area and BET C constant drastically. Most of the surface area was still available and there was only a slight fall in the BET C constant. The FHH analysis showed that there was also a slight increase in roughness.

The nitrogen adsorption isotherm of coked catalyst C2, as seen in Fig. 4.1, indicated complete saturation at $P/P_0 = 0.7$. This was very different to the former two sets, i.e. the fresh sample and coked sample C1. As seen in Table 4.2, there was ~61% drop in the pore volume when compared to the fresh catalysts. The FHH fractal dimension was consistent showing slightly greater roughness compared to the fresh

catalysts. There was also a loss in the BET surface area. The APD indicated a fall from 7.6 nm for the fresh sample to ~7 nm for C1 and 3.4 nm for C2.

Table 4.2
Physical properties obtained for sample A (whole) and its coked counterparts C1 (whole) and C2 (whole) from isotherms presented in Fig. 4.1.

	Fresh A	C1	C2
BET surface area (m^2g^{-1})	233(8) ($\sigma = 0.16$ nm^2)	219(28) ($\sigma = 0.18$ nm^2) 195(25) ($\sigma = 0.16$ nm^2)	202(17) ($\sigma = 0.18$ nm^2) 179(15) ($\sigma = 0.16$ nm^2)
BET C constant	88(2)	74(7)	74(4)
Monolayer capacity V_m $(cm^3g^{-1}$ STP)	54(2)	45(6)	42(4)
Pore volume (cm^3g^{-1})	0.44	0.38	0.17
FHH fractal dimension D	2.47(0.01)	2.52(0.01)	2.50(0.01)
APD (nm)	7.6	6.9	3.4

( ) Errors are quoted in brackets.

To gather more information, a series of experiments, following the integrated method of gas adsorption, were performed. As mentioned in Section 4.3, initially nitrogen was adsorbed onto the sample and then desorbed. This was followed by water adsorption up to relative pressure of 0.7 which was then frozen. Finally, another nitrogen adsorption experiment was performed on the sample which contained frozen water. Integrated or sequential N_2-H_2O-N_2 gas adsorption experiments were performed on fresh sample A and coked C1 samples. The second coked sample will not be considered as most of the pore volume was already occupied by coke.

Nitrogen adsorption isotherms obtained for fresh catalyst sample A before and after water adsorption are displayed in Fig. 4.2a. The adsorption isotherm obtained after water vapour adsorption and freezing was adjusted, by linear interpolation, to the same relative pressure points as that obtained for the isotherm before water adsorption. The nitrogen adsorption isotherm, water adsorption isotherm and the adjusted isotherm obtained after freezing the adsorbed water are presented in Fig. 4.2b. As expected, the presence of frozen water within the sample decreased the subsequent nitrogen uptake. The nitrogen isotherms obtained before and after water adsorption were characterised by rapid initial uptakes with well distinguished multilayer and capillary condensation regions. The characteristic physical properties of sample A before and after water adsorption are presented below in Table 4.3.
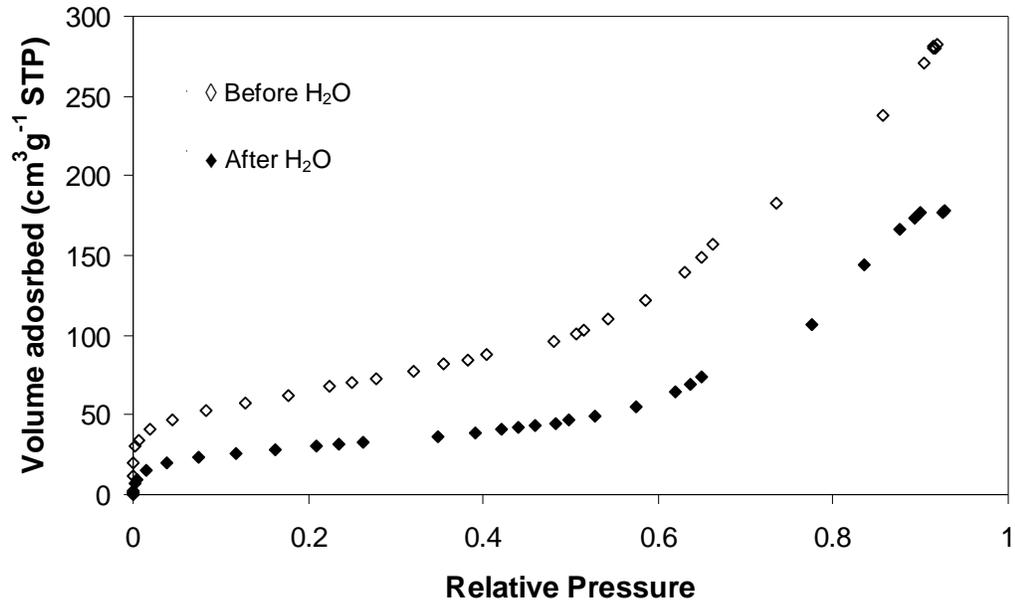
(a)
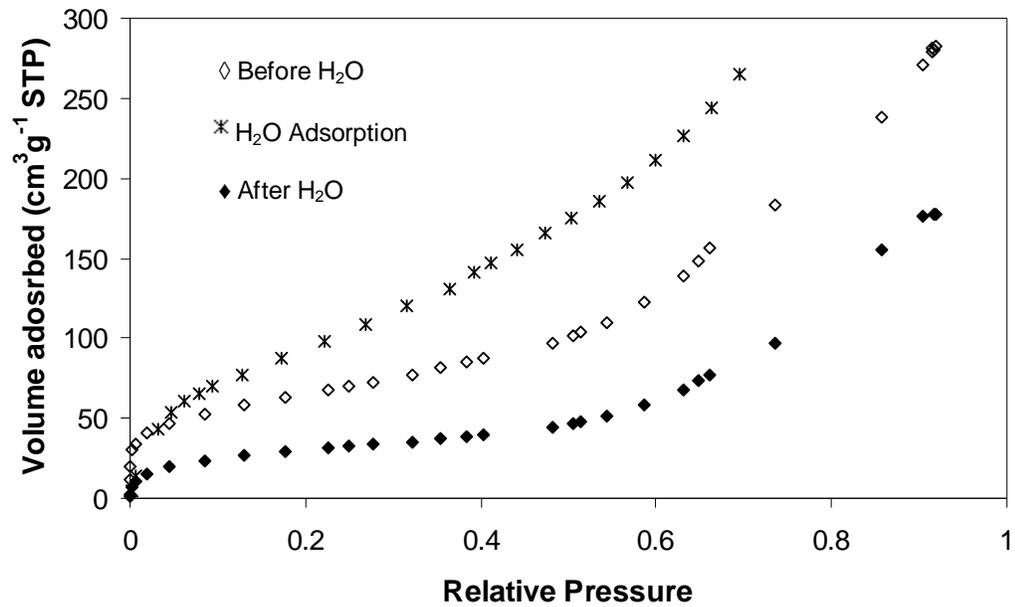
(b)
Fig. 4.2. (a) Raw nitrogen gas adsorption isotherm obtained before and water adsorption for sample A (whole). (b) Nitrogen gas adsorption isotherms adjusted to the same relative pressure along with the water adsorption isotherm for sample A (whole).

The presence of frozen water was found to alter the properties of the sample initially determined. There was ~48% fall in the nitrogen BET surface area after water adsorption. The BET C constant was also found to decrease by ~16%. These observations were in line with the drop in monolayer capacity following water adsorption. The volume of water adsorbed and that corresponding to nitrogen after

water adsorption added up to the original total pore volume detected by nitrogen adsorption. The FHH fractal dimension following water adsorption on the fresh catalyst was found to be very similar to that prior to water adsorption.

Table 4.3
Physical properties obtained for sample A (whole) from the nitrogen gas adsorption isotherms presented in Fig. 4.2a before and after water adsorption.

Fresh	Before H_2O	After H_2O
BET surface area (m^2g^{-1})	233(8) ($\sigma = 0.16$ nm^2)	122(14) ($\sigma = 0.185$ nm^2) 105.5(3.5)($\sigma = 0.16$ nm^2)
BET C constant	88(2)	73.5(7.5)
Monolayer capacity V_m (cm^3g^{-1} STP)	54(2)	24.5(0.5)
Pore volume (cm^3g^{-1})	0.44	0.26(0.01)
FHH fractal dimension D	2.47	2.48
APD	7.6	8.5

( ) Errors are quoted in brackets.
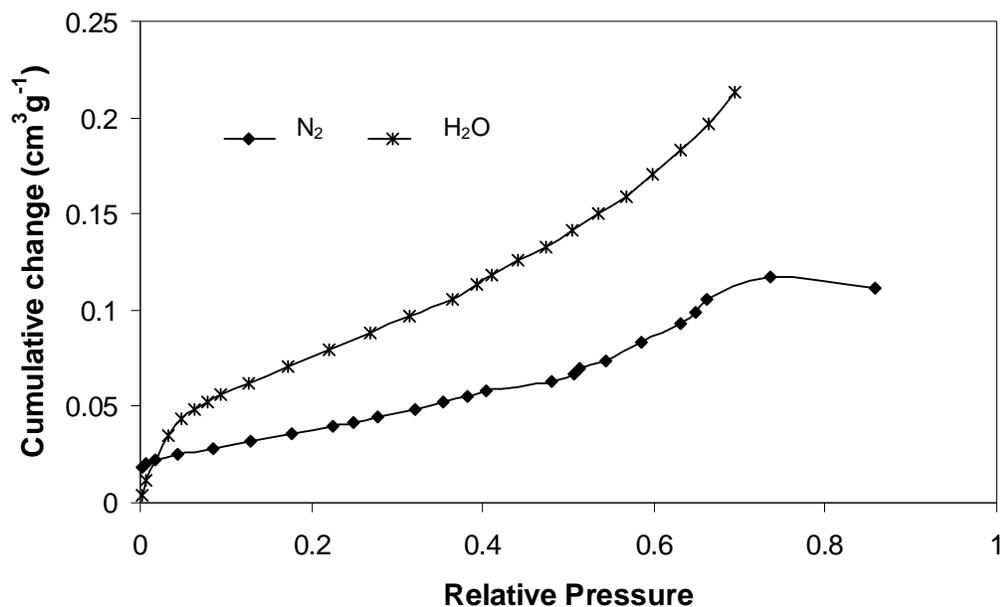
Fig. 4.3. Cumulative change in the amount of nitrogen and water adsorbed as condensed liquid as a function of the relative pressure for sample A (whole).

Considering the entire pore volume of the fresh catalyst, it was possible to understand the cumulative volume of nitrogen that condensed within the regions where water adsorbed. This was determined by taking the difference between the incremental amounts of nitrogen adsorbed before water adsorption from that after water adsorption for the same relative pressure points. This differential amount

adsorbed was then summed in order of increasing pressure to determine the cumulative change in the amount adsorbed. This summation was done as it would lead to reduced errors compared with those associated with an incremental or differential plot. This cumulative change was then converted to the condensed liquid volume. Thus, it was possible to gain an understanding of the filling mechanism within regions of the void space occupied by water. Fig 4.3 shows the cumulative change in the amount of nitrogen adsorbed as condensed liquid against relative pressure. Also shown in Fig 4.3 is the amount of water adsorbed as condensed liquid within the pores of sample A as a function of the relative pressure. It was observed that there was an increasing trend in the cumulative amount of nitrogen adsorbed as condensed liquid up to $P/P_0 = 0.66$. This also agreed with the filling of water within the pores of fresh catalyst sample A which displayed a similar trend. However, after $P/P_0 = 0.66$, there was little difference in the nitrogen adsorbed, giving rise to a plateau.

Nitrogen adsorption isotherms obtained for catalyst C1 before and after water adsorption are displayed in Fig. 4.4a. The nitrogen adsorption isotherm obtained after water adsorption was adjusted to the same relative pressure points as that obtained for the nitrogen adsorption before water adsorption. The primary nitrogen adsorption isotherm, water adsorption isotherm and the adjusted nitrogen adsorption isotherm obtained after freezing the adsorbed water are presented in Fig. 4.4b.

(a)

117
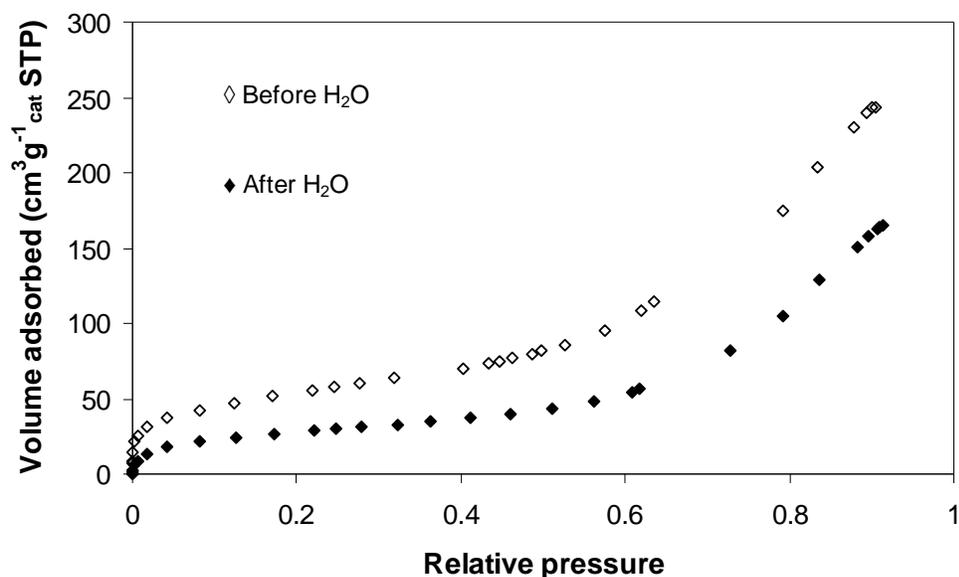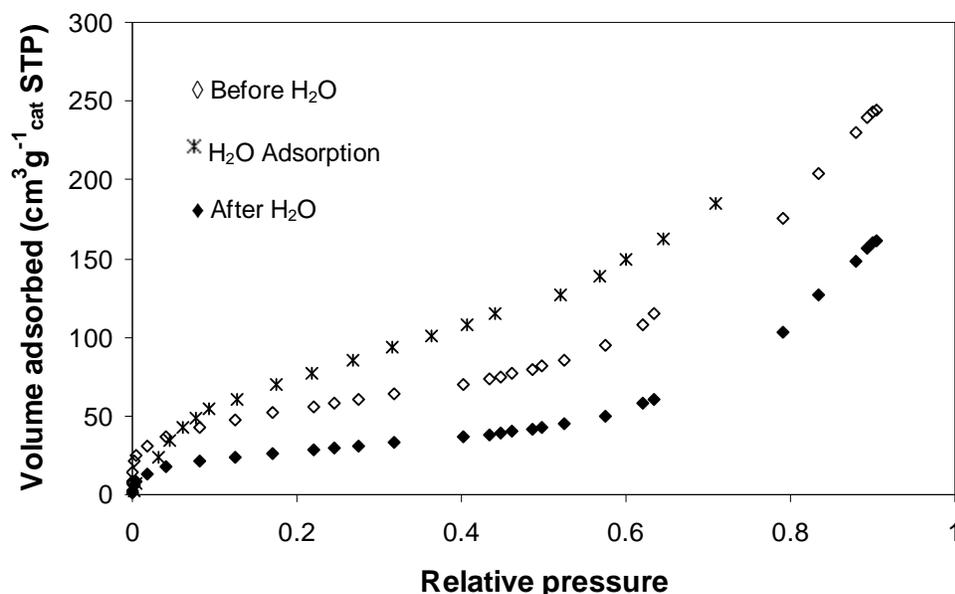
Fig. 4.4. (a) Raw nitrogen gas adsorption isotherms obtained before and after water adsorption for coked sample C1 (whole). (b) Nitrogen gas adsorption isotherms adjusted to the same relative pressure along with the water adsorption isotherm for coked sample C1 (whole).

As expected, the presence of frozen water within the sample decreased the subsequent nitrogen uptake. The nitrogen isotherms obtained before and after water adsorption were characterised by rapid initial uptakes with well distinguished multilayer and capillary condensation regions. The characteristic physical properties of sample C1 before and after water adsorption are presented in Table 4.4.

Table 4.4
Physical properties obtained for coked sample C1 (whole) from nitrogen gas adsorption isotherms presented in Fig. 4.4a before and after water adsorption.

C1	Before H_2O	After H_2O
BET surface area (m^2g^{-1})	213(6) ($\sigma = 0.17$ nm^2)	126.5(5.5) ($\sigma = 0.205$ nm^2)
	200.5(6.5) ($\sigma = 0.16$ nm^2)	98.5(1.5) ($\sigma = 0.16$ nm^2)
BET C constant	89(15)	58.75(5.25)
Monolayer capacity V_m (cm^3g^{-1} STP)	46.5(1.5)	22.75(0.25)
Pore volume (cm^3g^{-1})	0.37	0.25
FHH fractal dimension D	2.53(0.01)	2.46(0.01)
APD	6.9	7.9

( ) Errors are quoted in brackets.

The presence of frozen water was found to alter the properties of the sample initially determined. There was ~40% fall in the nitrogen BET surface area after water

118

adsorption. The BET C constant and the monolayer capacity decreased by ~34% and 51% respectively relative to what was obtained before water adsorption. The pore volume corresponding to the amount of water adsorbed and that corresponding to nitrogen after water adsorption was close to that measured initially by nitrogen adsorption before water adsorption. The FHH fractal dimension was also found to be less after water adsorption, indicating nitrogen molecules detected a relatively smoother surface.

As previously done for the fresh catalyst, the cumulative volume of liquid nitrogen that condensed within the regions where water adsorbed was also determined for coked sample C1. This was determined by taking the difference between the incremental amounts of nitrogen adsorbed before water adsorption from that obtained after water adsorption for the same relative pressure points. This differential amount adsorbed was then summed in order of increasing pressure to determine the cumulative change in the amount adsorbed. This summation was done as it would lead to reduced errors compared with those associated with an incremental or differential plot. This cumulative change was then converted to the condensed liquid volume. Thus, it was possible to gain an understanding of the filling mechanism of nitrogen within regions of the void space occupied by water. Fig 4.5 showed the cumulative change in the amount of nitrogen adsorbed as condensed liquid against relative pressure. Also shown in Fig 4.5 is the amount of water adsorbed as condensed liquid within the pores of coked sample C1 as a function of the relative pressure.

It was observed that there was an increase in the cumulative change in the amount of nitrogen adsorbed as condensed liquid even after $P/P_0 = 0.66$. The increasing trend was maintained up to $P/P_0 = 0.9$. This was different to that observed for sample A where at $P/P_0 > 0.66$, the trend was approximately flat and prior to that filling trend was similar to that of water. Hence, it was found that that the presence of coke altered the adsorption of water and reduced the amount of nitrogen adsorbing at higher relative pressures. The relevance of these observations will be discussed in Section 4.5.
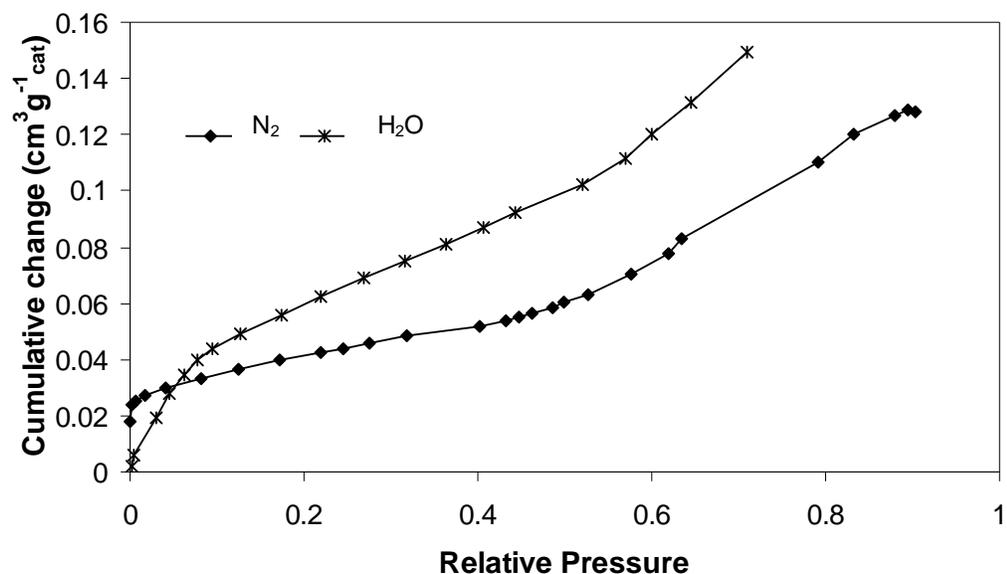
Fig. 4.5. Cumulative change in the amount of nitrogen and water adsorbed as condensed liquid as a function of the relative pressure for coked sample C1 (whole).

4.4.2 ADSORPTION KINETICS – SAMPLE A (FRESH AND COKED)

4.4.2.1 Fresh catalyst – Sample A

As mentioned in Section 4.2, adsorption kinetics in the Knudsen diffusion region were used to determine the adsorption mass transfer coefficient by employing the LDF equation as given by Eq. (4.4). The mass transfer coefficient was determined by analysing the individual mass uptake vs. time data for each relative pressure point in the isotherms given in Section 4.4.1. An example of the mass uptake vs. time data obtained at a relative pressure 0.0843 is provided in Fig. 4.6. The fitting was done using the non-linear curve fitting program available in Origin 6.1. At this relative pressure, the LDF mass transfer coefficient was 0.48243 ± 0.00028. The R^2 value obtained for the fit was 0.99969. Repeating this procedure for different relative pressures provided the respective LDF mass transfer coefficients.

Following this, the respective LDF mass transfer coefficients were normalised for the variation in sample temperature using Eq. (4.8) (refer Section 4.2). This allowed plotting the variation in normalised mass transfer coefficient as a function of the fraction of the pore volume occupied by condensed liquid nitrogen. The fraction of the pore volume occupied by condensed liquid nitrogen was obtained by taking the ratio of the amount condensed at a particular relative pressure to that obtained at the top of the isotherm or at saturation. Such a plot obtained for catalyst sample A is presented in Fig. 4.7a for two conditions, i.e. before and after water adsorption. From Fig. 4.7a, it was noted that the normalised mass transfer coefficient seemed to fall as

120

the fraction of the pore volume occupied by condensed liquid nitrogen increased before reaching a minimum and then rose. This same pattern could also be seen for sample A after water adsorption. Further, it was also noted that the first few points, at low occupancy of nitrogen, showed a much larger change in the normalised mass transfer coefficients compared to those at intermediate and greater nitrogen occupancies. More importantly, the normalised mass transfer coefficients were less than that obtained before water adsorption.

Fig. 4.6. Nitrogen mass uptake by sample A (whole) plotted as a function of time at a relative pressure of 0.0843.

It must be noted that the starting point for the two data sets are not the same. Hence, the fraction of the pore space occupied by condensed liquid nitrogen in sample A before and after water adsorption would be different. To facilitate comparison between the two different conditions, the normalised mass transfer coefficient was plotted as a function of the accessible porosity in Fig. 4.7b. Accessible porosity can be defined by the following expression:

$$\text{Accessible porosity} = \left[1 - \left(\text{fraction occupied by liquid } N_2\right)\right]\varepsilon_{fresh} \text{,} \tag{4.9a}$$

$$\text{Accessible porosity} = \left[1 - \left(\frac{\text{vol of condensed liquid } N_2}{TPV_{fresh}}\right)\right]\varepsilon_{fresh} \text{,} \tag{4.9b}$$

for nitrogen adsorption before water adsorption, and as:

$$\text{Accessible porosity} = \left[1 - \left(\begin{array}{l}\text{fraction occupied by } H_2O + \\ \left(\text{fraction occupied by liquid } N_2\right)_{after\,H_2O\,adsorption}\end{array}\right)\right]\varepsilon_{fresh} \text{,} \tag{4.10a}$$

121

$$\text{Accessible porosity} = \left[1 - \left[\left(\frac{\left(\begin{array}{l}vol\,of\,condensed\,liquid\,N_{2\,before\,H_2O\,adsorption} - \\ vol\,of\,condensed\,liquid\,N_{2\,after\,H_2O\,adsorption}\end{array}\right)}{TPV_{fresh}}\right) + \left(\frac{vol\,of\,condensed\,liquid\,N_2}{TPV}\right)_{after\,H_2O\,adsorption}\right]\right]\varepsilon_{fresh}, \quad (4.10b)$$

for nitrogen adsorption after water adsorption. In the above equations, TPV_{fresh} is the total pore volume of the fresh catalyst and ε_{fresh} is the porosity of the fresh catalyst and $TPV_{afterH_2O\,adsorption}$ is the total pore volume of nitrogen after water adsorption. Additionally, the starting conditions or the starting porosities have also been marked by vertical lines in Fig. 4.7b. For the fresh catalyst sample A, the starting porosity was 0.62 (see Appendix C for more details). On the other hand, after water adsorption and freezing, the starting porosity was 0.37. Thus, it was found that following water adsorption, there was a shift in the normalised mass transfer coefficients to lower porosities. The two conditions can be compared by transforming this plot into the one given in Fig. 4.7c where reduced porosity represented the change in porosity due to the adsorption of nitrogen, i.e. difference between the starting porosity and the accessible porosity at each experimental point. From Fig. 4.7c, it was found that for the same changes in porosity, the normalised mass transfer coefficient was lower following water adsorption and there seemed to be greater change in the mass transfer coefficients initially than at intermediate and later stages.

As said previously, it was also found that the normalised mass transfer coefficient decreases reaching a minimum and then again rises gradually. This fall and rise was observed for normalised mass transfer coefficients before and after water adsorption. The red diamonds in Fig. 4.7 correspond to the minimum in the normalised mass transfer coefficients. Referring the isotherms of catalysts sample A reported earlier (zoomed isotherms are presented in Fig. 4.8), it was noted that the minimum in the normalised mass transfer coefficient was obtained after the completion of the formation of the monolayer.
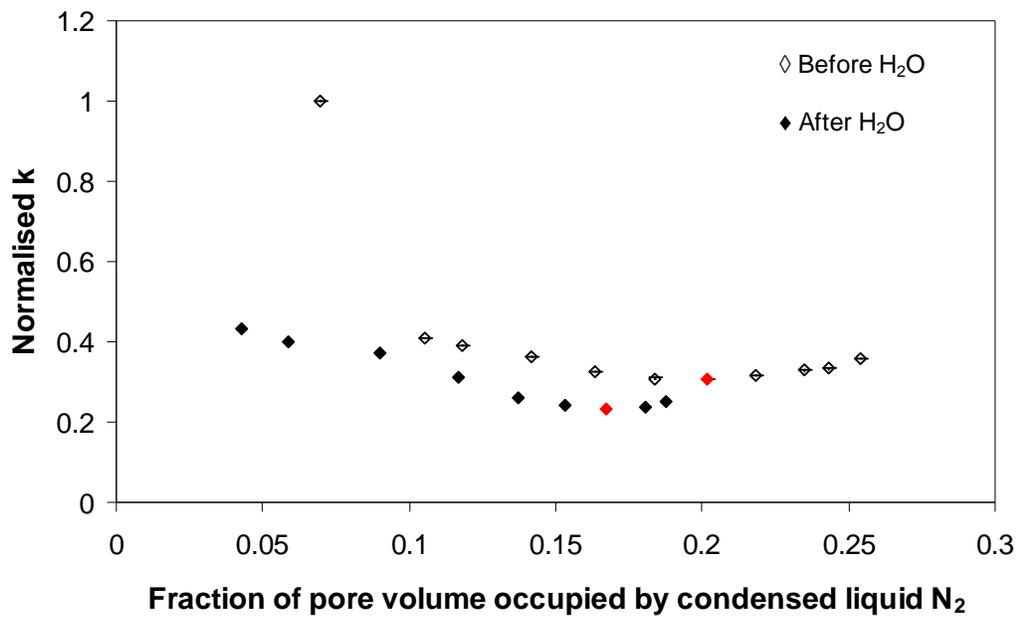
(a)
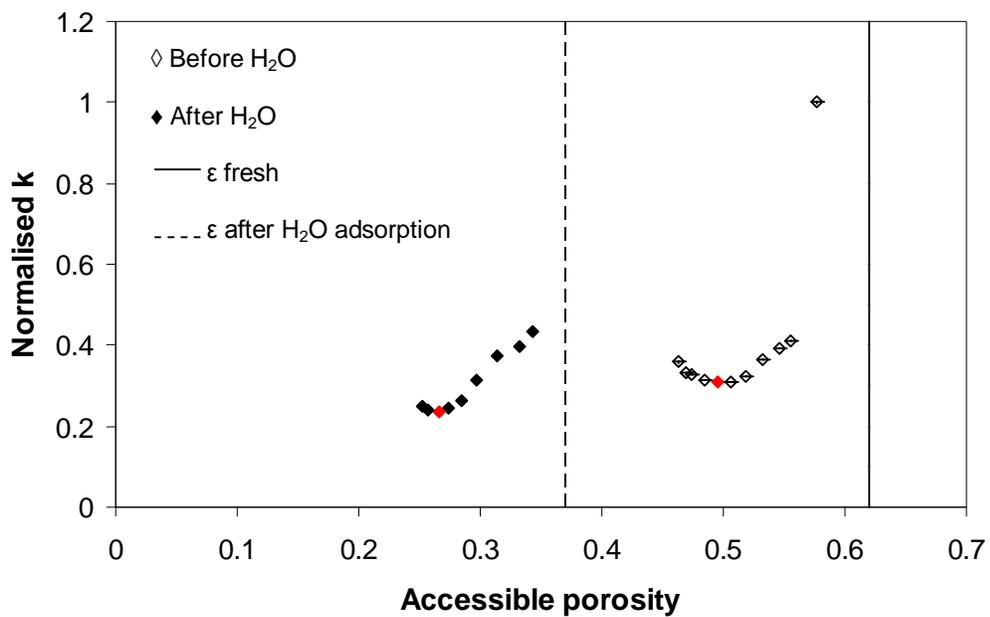
(b)
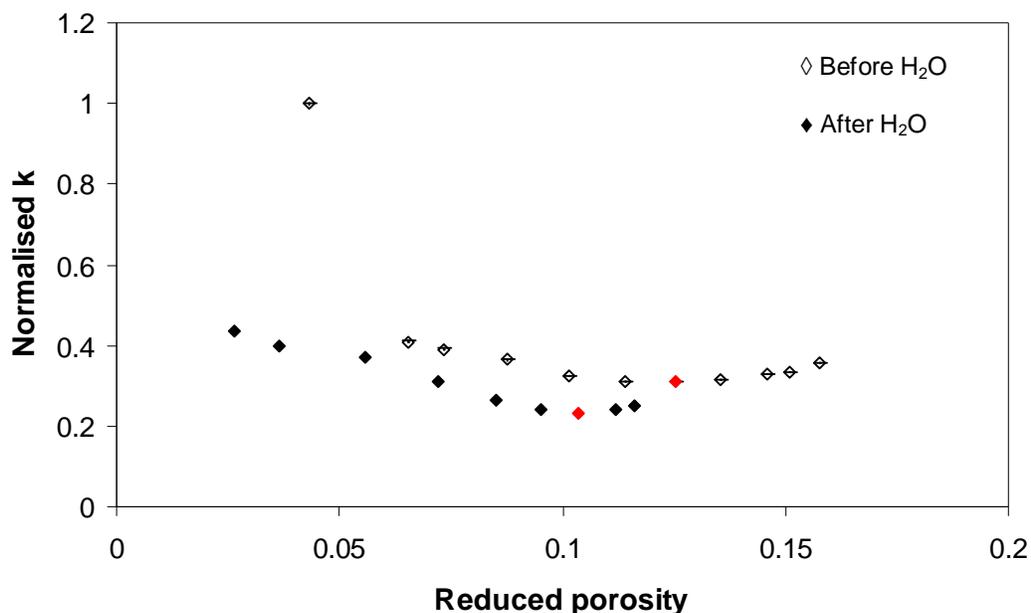
(c)

Fig. 4.7. (a) Variation in normalised mass transfer coefficient as a function of the fraction of the pore volume occupied by condensed liquid nitrogen before and after water adsorption in fresh catalyst sample A (whole). (b) Variation in normalised mass transfer coefficient as a function of the accessible porosity before and after water adsorption in fresh catalyst sample A (whole). (c) Variation in normalised mass transfer coefficient as a function of the reduced porosity before and after water adsorption in fresh catalyst sample A (whole). The red diamonds in the three figures indicate the minimum in the transfer coefficients.
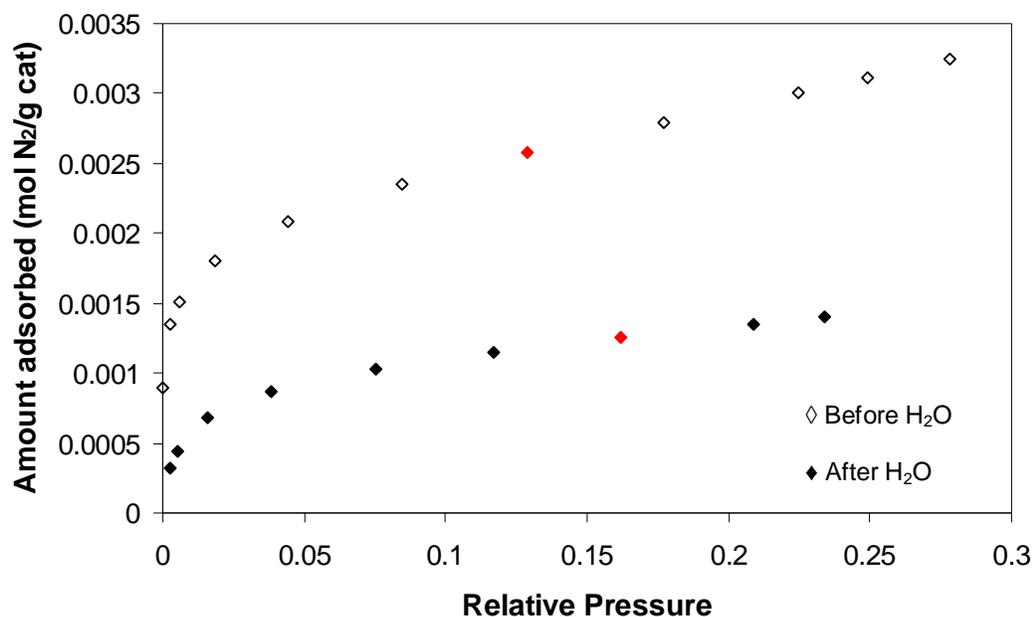
Fig. 4.8. Zoomed versions of nitrogen adsorption isotherms of fresh catalyst sample A (whole) before and after water adsorption.

4.4.2.2 Coked catalyst – Sample C1

The protocol followed for the fresh sample reported in the preceding section was repeated for the coked catalyst sample C1. Adsorption kinetics in the Knudsen

124

diffusion region were once again used to determine the adsorption mass transfer coefficients by employing the LDF equation as given by Eq. (4.4). The mass transfer coefficient was determined by analysing the individual mass uptake vs. time data for each relative pressure point in the isotherms given in Section 4.4.1. An example of the mass uptake vs. time data obtained at a relative pressure 0.081 is provided in Fig. 4.9. The fitting was done using the non-linear curve fitting program available in Origin 6.1. At this relative pressure, the LDF mass transfer coefficient was 0.51559 ± 0.0002. The R^2 value obtained for the fit was 0.99988. Repeating this procedure for different relative pressures provided the respective LDF mass transfer coefficients.
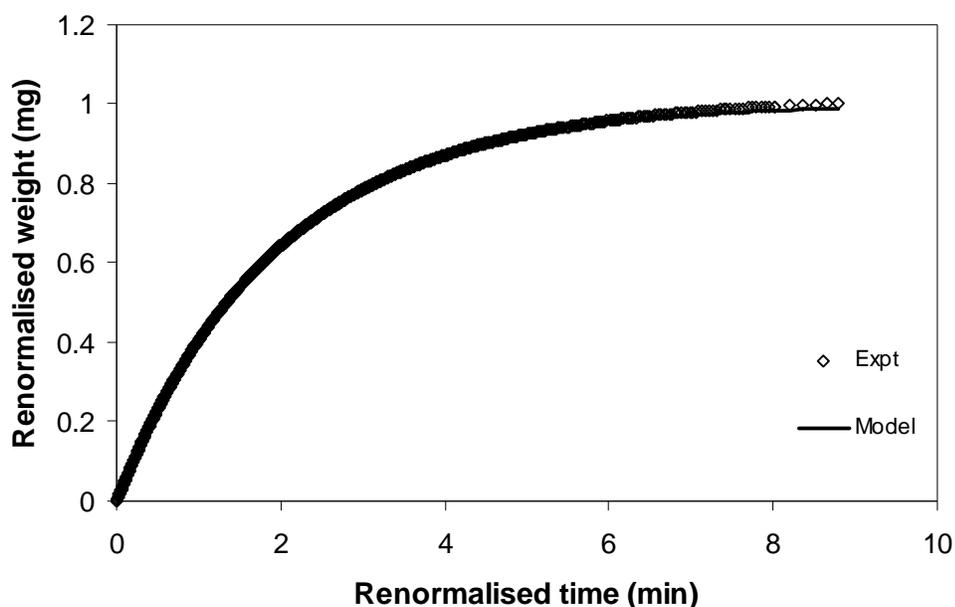
Fig. 4.9. Nitrogen mass uptake by coked sample C1 (whole) plotted as a function of time at a relative pressure of 0.081.

Following this, the respective LDF mass transfer coefficients were normalised for the variation in sample temperature using Eq. (4.8) (refer Section 4.2). This allowed plotting the variation in normalised mass transfer coefficient as a function of fraction of the pore volume occupied by condensed liquid nitrogen. The fraction of the pore volume occupied by condensed liquid nitrogen was obtained by taking the ratio of the amount condensed at a particular relative pressure to that obtained at the top of the isotherm or at saturation. Such a plot obtained for the coked catalyst sample C1 is presented in Fig. 4.10a for two conditions, i.e. before and after water adsorption. From Fig. 4.10a, it was noted that the normalised mass transfer coefficient seemed to fall as the fraction of the pore volume occupied by condensed liquid nitrogen increased before reaching a minimum and then again rising. This same pattern could

also be seen for catalyst sample C1 after water adsorption. Further, it was also observed that the first few points, at low occupancy of nitrogen, showed a much larger change in the normalised mass transfer coefficients compared to those at intermediate and greater nitrogen occupancies. More importantly, the normalised mass transfer coefficients were less than that obtained before water adsorption.

It must be noted that starting point for the two data sets are not the same. Hence, the fraction of the pore space occupied by condensed liquid nitrogen in coked catalyst sample C1 before and after water adsorption would be different. To facilitate comparison between the two different conditions, the normalised mass transfer coefficient was plotted as a function of the accessible porosity in Fig. 4.10b. Accessible porosity of the coked catalyst C1 can be defined by the following expression:

$$\text{Accessible porosity} = \left[1 - \left(\begin{array}{c} \left(fraction\,occupied\,by\,coke\right) + \\ \left(fraction\,occupied\,by\,liquid\,N_2\right) \end{array} \right) \right] \varepsilon_{fresh}, \quad (4.11a)$$

$$\text{Accessible porosity} = \left[1 - \left(\begin{array}{c} \left(\dfrac{TPV_{fresh} - TPV_{C1}}{TPV_{fresh}}\right) + \\[2mm] \left(\dfrac{vol\,of\,condensed\,liquid\,N_2}{TPV_{C1}}\right) \end{array} \right) \right] \varepsilon_{fresh}, \quad (4.11b)$$

for nitrogen adsorption before water adsorption, and by:

$$\text{Accessible porosity} = \left[1 - \left(\begin{array}{c} \left(fraction\,occupied\,by\,coke\right) + \\ \left(fraction\,occupied\,by\,H_2O\right) + \\ \left(fraction\,occupied\,by\,liquid\,N_2\right)_{after\,H_2O\,adsorption} \end{array} \right) \right] \varepsilon_{fresh}, \quad (4.12a)$$

$$\text{Accessible porosity} = \left[1 - \left(\begin{array}{c} \left(\dfrac{TPV_{fresh} - TPV_{C1}}{TPV_{fresh}}\right) \\[2mm] + \\[1mm] \left(\dfrac{vol\,of\,condensed\,liquid\,N_{2\,before\,H_2O\,adsorption} - vol\,of\,condensed\,liquid\,N_{2\,after\,H_2O\,adsorption}}{TPV_{C1\,before\,H_2O\,adsorption}}\right) \\[2mm] + \\[1mm] \left(\dfrac{vol\,of\,condensed\,liquid\,N_2}{TPV_{C1}}\right)_{after\,H_2O\,adsorption} \end{array} \right) \right] \varepsilon_{fresh}, \quad (4.12b)$$

for nitrogen adsorption after water adsorption. In the above equations, TPV_{fresh} is the total pore volume of the fresh catalyst and ε_{fresh} is the porosity of the fresh catalysts and $TPV_{C1\,after\,H_2O\,adsorption}$ is the total pore volume of nitrogen after water adsorption in

material C1. Additionally, the starting conditions or the starting porosities have been marked by vertical lines in Fig. 4.10b. For the coked catalyst C1, before water adsorption, the starting porosity was 0.53. On the other hand, after water adsorption and freezing, the starting porosity was 0.33. Thus, it was found that following water adsorption, there was a shift in the normalised mass transfer coefficients to lower porosities. The two conditions can be compared by transforming this plot into the one given in Fig. 4.10c where reduced porosity represented the change in porosity due to the adsorption of nitrogen, i.e. difference between the starting porosity and the accessible porosity at each experimental point. From Fig. 4.10c, it was found that for the same changes in porosity, the normalised mass transfer coefficient was lower following water adsorption and there seemed to be greater change in the mass transfer coefficients initially than at intermediate and later stages.

As said previously, it was also found that the normalised mass transfer coefficient decreases reaching a minimum and then again rises gradually. This fall and rise was observed for normalised mass transfer coefficients before and after water adsorption. The red diamonds in Fig. 4.10 correspond to the minimum in the normalised mass transfer coefficients. Referring the isotherms of coked catalysts sample C1 reported earlier (zoomed isotherms are presented in Fig. 4.11), it was noted that the minimum in the normalised mass transfer coefficient was obtained after the completion of the formation of the monolayer.
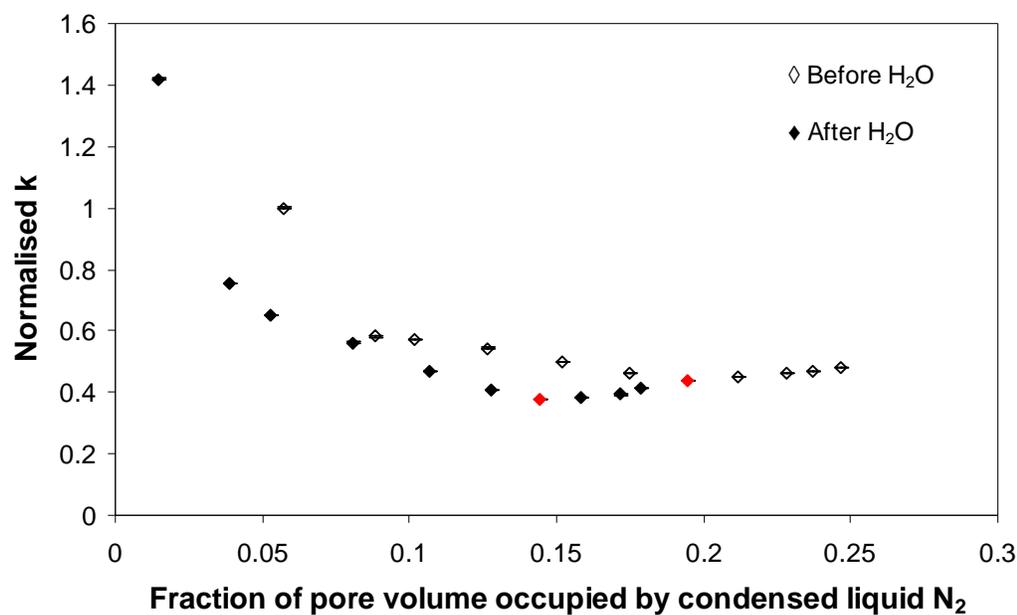
(a)
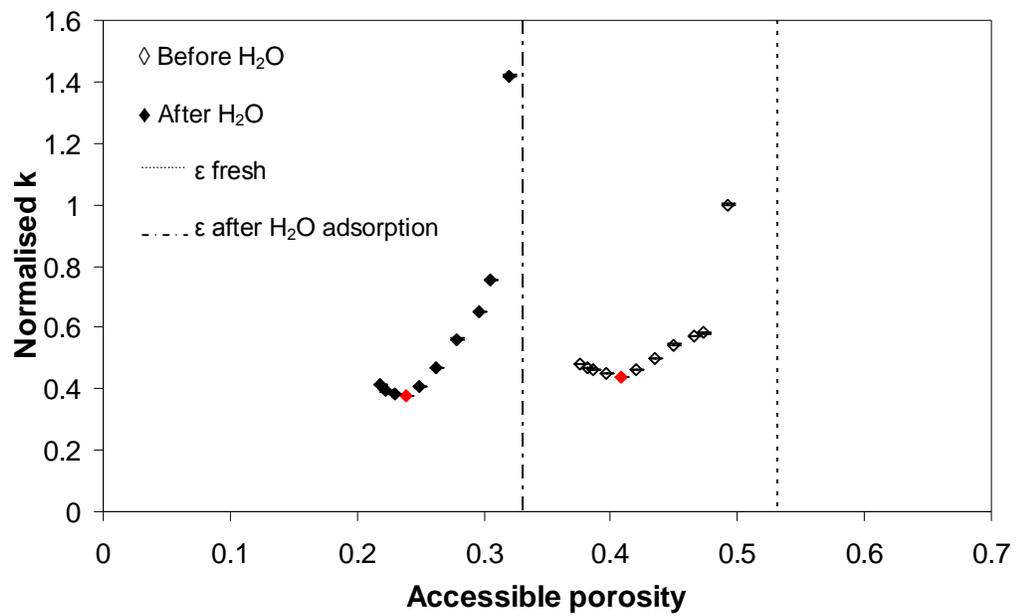
(b)
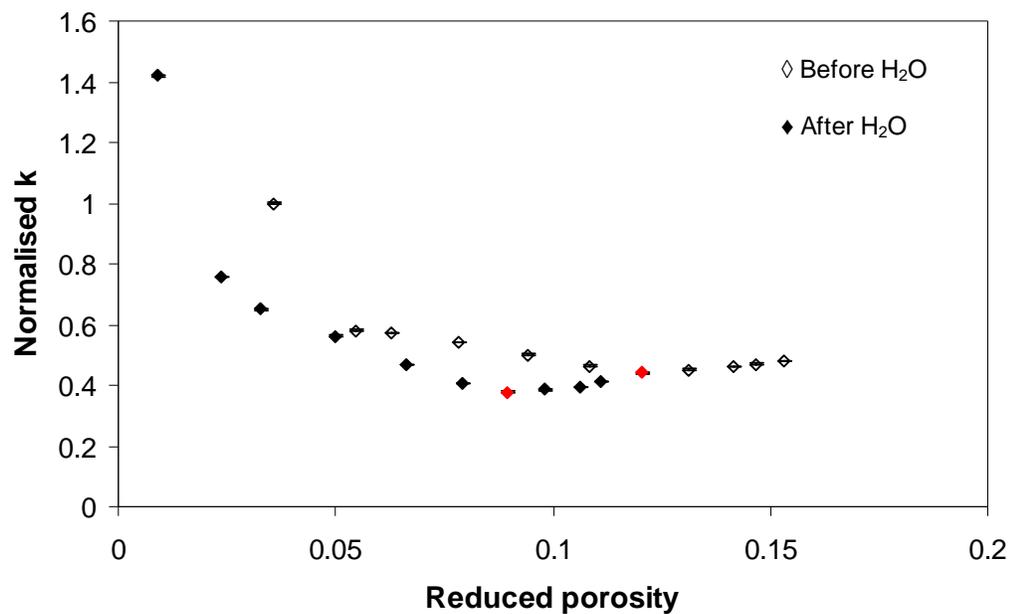
(c)

Fig. 4.10. (a) Variation in normalised mass transfer coefficient as a function of the fraction of the pore volume occupied by condensed liquid nitrogen before and after water adsorption in coked catalyst C1 (whole). (b) Variation in normalised mass transfer coefficient as a function of the accessible porosity before and after water adsorption in coked catalyst C1 (whole). (c) Variation in normalised mass transfer coefficient as a function of the reduced porosity before and after water adsorption in coked catalyst C1 (whole). The red diamonds in the three figures indicate the minimum in the transfer coefficients.
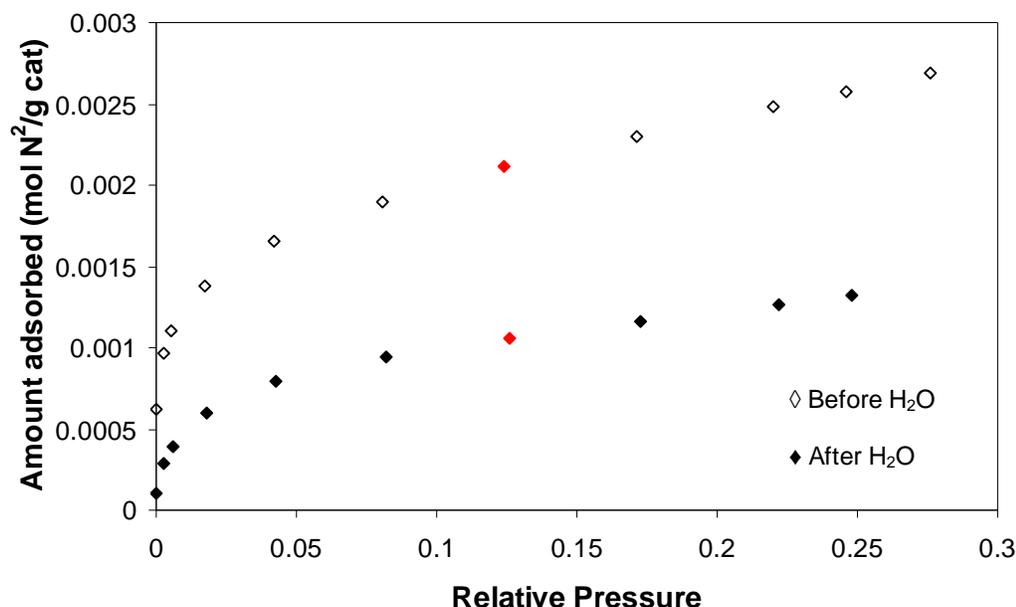
Fig. 4.11. Zoomed versions of nitrogen adsorption isotherms of coked catalyst C1 (whole) before and after water adsorption.

4.4.2.3 Fresh catalyst A and Coked catalyst C1

The effect of coke on the transport of nitrogen molecules in the Knudsen diffusion regime was detected by comparing the results obtained for the fresh catalyst sample A and coked catalyst sample C1. Fig. 4.12a presents the variation in the normalised mass transfer coefficient as a function of the pore volume occupied by condensed liquid nitrogen. The fraction of the pore volume occupied by condensed liquid nitrogen was obtained by taking the ratio of the amount condensed at a particular relative pressure to that obtained at the top of the isotherm or at saturation. From Fig. 4.12a, it was noted that the normalised mass transfer coefficient seemed to fall as the fraction of the pore volume occupied by condensed liquid nitrogen increased before reaching a minimum and then again rising. This same pattern could also be seen for the coked catalyst sample C1. It was also found that the first few points, at low occupancy of nitrogen, showed a much larger change in the normalised transfer coefficients compared to those at intermediate and greater nitrogen occupancies. More importantly, the normalised mass transfer coefficients were less than that obtained for the fresh catalyst.

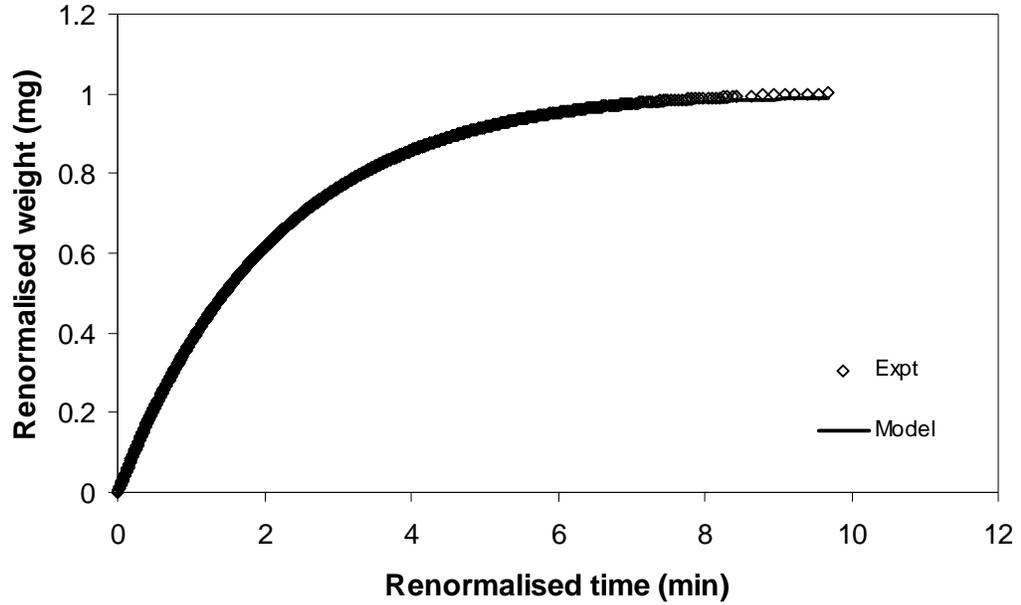It must be noted that starting point for the two data sets are not the same. Hence, the fraction of the pore space occupied by condensed liquid nitrogen in the fresh catalyst sample A and coked catalyst sample C1 would be different. To facilitate comparison between the two different samples, the normalised mass transfer coefficient was plotted as a function of the accessible porosity in Fig. 4.12b.

129

Accessible porosity can be defined by Eq. (4.9) for nitrogen adsorption on the fresh catalyst sample A, and by Eq. (4.11) for nitrogen adsorption on the coked catalyst sample C1. Additionally, the starting conditions or the starting porosities have been marked by vertical lines in Fig. 4.12b. For the fresh catalyst sample A, the starting porosity was 0.62. On the other hand, after reaction, the starting porosity was 0.53. Thus, it was found that following reaction, there was a shift in the normalised mass transfer coefficients to lower porosities. The two conditions can be compared by transforming this plot into the one given in Fig. 4.12c where reduced porosity represented the change in porosity due to the adsorption of nitrogen, i.e. difference between the starting porosity and the accessible porosity at each experimental point. From Fig. 4.12c, it was found that for the same changes in porosity, the normalised mass transfer coefficient was lower following reaction, i.e. the normalised mass transfer coefficients were lower for the coked catalyst sample C1. There also seemed to be a greater change in the mass transfer coefficients initially than at intermediate and later stages.

Fraction of pore volume occupied by condensed liquid N$_2$
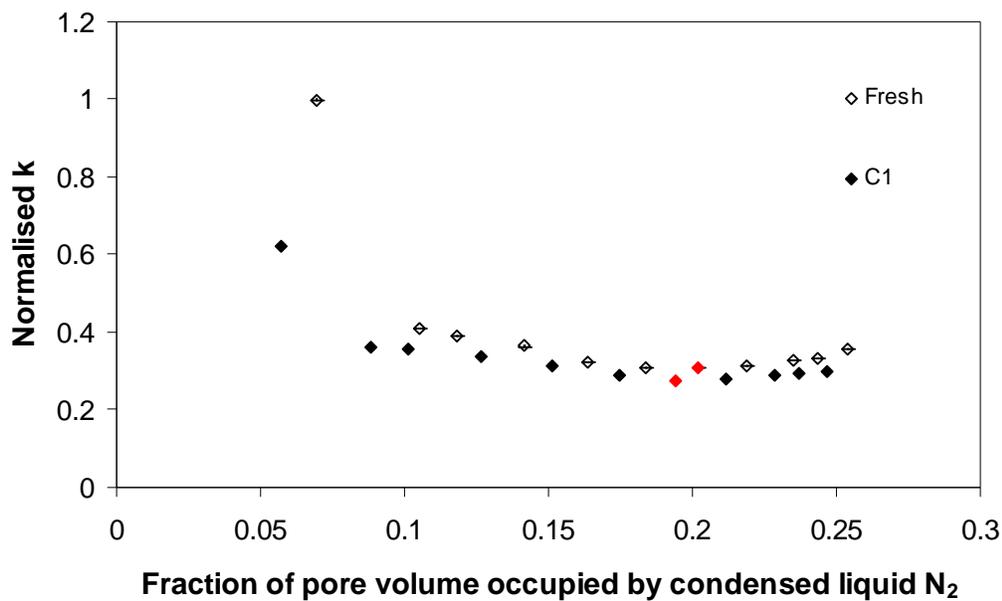
(a)
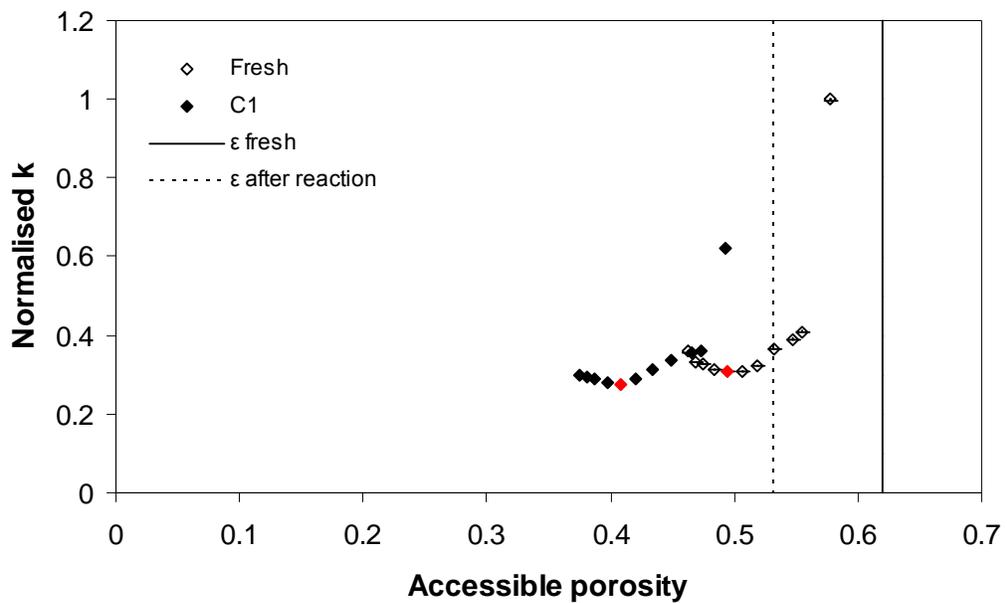
(b)
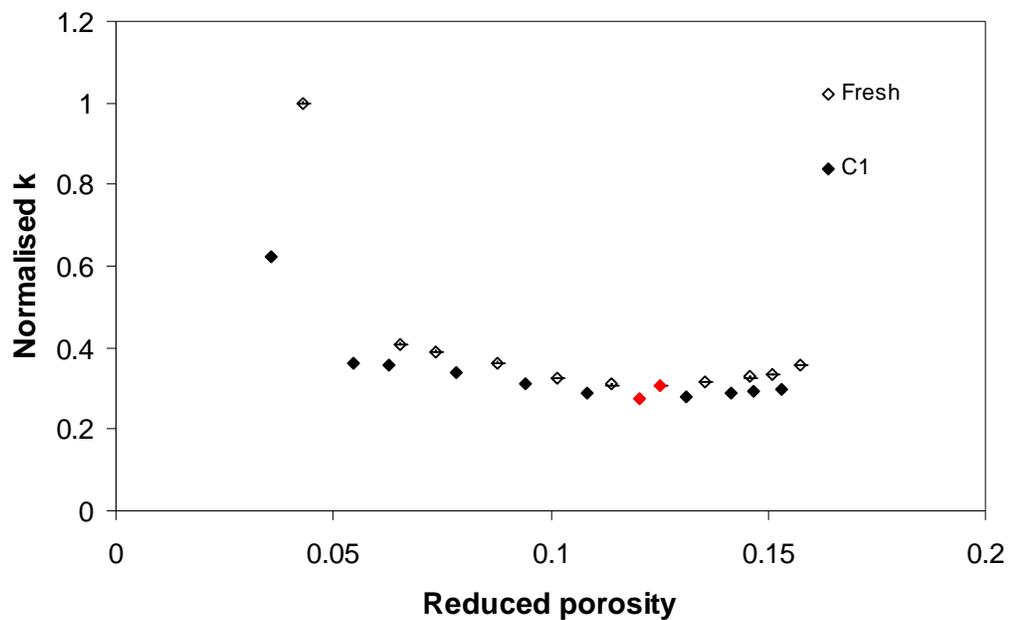
(c)

Fig. 4.12. (a) Variation in normalised mass transfer coefficient as a function of the fraction of the pore volume occupied by condensed liquid nitrogen for the fresh catalyst A (whole) and the coked catalyst C1 (whole). (b) Variation in normalised mass transfer coefficient as a function of the accessible porosity for the fresh catalyst A (whole) and the coked catalyst C1 (whole). (c) Variation in normalised mass transfer coefficient as a function of the reduced porosity for the fresh catalyst A (whole) and the coked catalyst C1 (whole). The red diamonds in the three figures indicate the minimum in the transfer coefficients.

As said previously for the two sample sets before and after water adsorption, it was found that the normalised mass transfer coefficient decreased reaching a minimum and then again rose gradually for the fresh and coked catalysts. The red diamonds in Fig. 4.12 correspond to the minimum in the normalised mass transfer

131

coefficients. Referring the isotherms of fresh and coked catalysts reported earlier (zoomed isotherms are presented in Fig. 4.13), it was noted that the minimum in the normalised mass transfer coefficient was obtained after the completion of the formation of the monolayer.
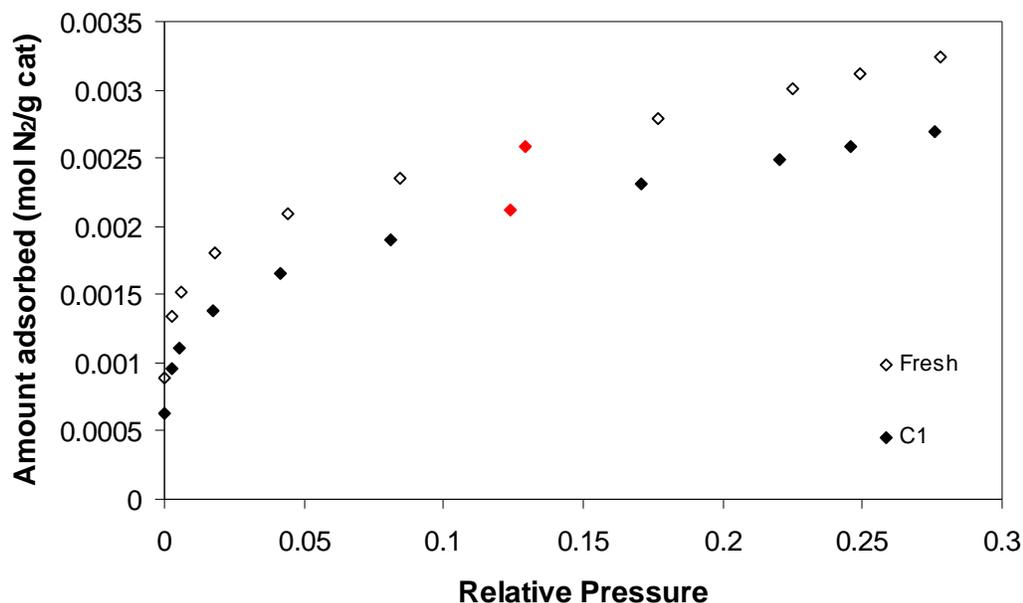
Fig. 4.13. Zoomed versions of nitrogen adsorption isotherms of the fresh catalyst sample A (whole) and the coked catalyst C1 (whole).

4.5 DISCUSSION

Preliminary analyses of three nitrogen gas adsorption isotherms in Fig. 4.1 indicated that there were drastic changes in the pore volumes for the fresh and coked samples. Such changes in pore volumes for different subsets within the same batch indicated variability in carbon/coke deposition along the reactor. It is likely that the different properties of coked catalysts are due to their different locations within the microreactor. For example, sample C2 may comprise extrudates that were probably located at the top of the reactor. As a result, during the reaction, they were directly exposed to the oil feed, while sample C1 may contain pellets taken from the bottom of the reactor. Another scenario that could explain the variability in carbon/coke deposition would be if sample C2 comprised catalyst extrudates taken from regions which had direct contact with oil while sample C1 contained catalyst extrudates that had oil channel past it contacting only some of the catalyst pellets. Unfortunately, such segregation was not made during the recovery of catalysts from the microreactor.

For the integrated N_2-H_2O-N_2 experiments performed on the fresh catalyst (sample A), it was found that the filling mechanism of water was similar to nitrogen over the investigated relative pressure range. This was established by a match in the increasing trend of the cumulative change in the amount adsorbed of nitrogen and water adsorbed as condensed liquids. This filling mechanism was also in line with the theory of the Kelvin equation (Eq. (3.8) in Section 3.1.5). It was found that the proportionality constant between the logarithm of the relative pressure and the reciprocal of pore size was the same for nitrogen adsorption at 77 K and water adsorption at 298 K (see Appendix C for more details). This implied that for a parallel pore bundle model, both nitrogen and water should condense in any given pore size at the same relative pressure. Apart from this, the nitrogen pore volumes before and after water adsorption could be reconciled with the pore volume occupied by water. This indicated the absence of any pore blocking caused by water adsorption and freezing. FHH fractal analysis revealed that the nitrogen molecules detected no significant change in the fractal dimension from the initial value to that following water adsorption. If water molecules were adsorbing uniformly across all the entire surface of the catalyst, then nitrogen molecules would certainly have detected a surface different to the initial surface giving a different FHH value. Apparently, this was not the case for sample A.

Unlike the fresh catalyst sample A, integrated experiments performed on the coked catalyst C1 showed a different filling mechanism. For the coked catalyst C1, water seemed adsorb at regions that were filled at higher pressures by nitrogen as indicated by the increasing trend in the cumulative change in Fig. 4.5. Thus, the presence of carbon deposits/coke seemed to cause condensation of water at larger pressures unlike that in fresh catalyst sample A. This can be interpreted as follows. It can be expected that carbon deposition caused a decrease in the size of the pore bodies present in the original fresh catalyst such that any adsorption in the narrower neighbouring necks at relative pressures below 0.7 also caused the filling of pore bodies via advanced adsorption/condensation at that same pressure. In the fresh sample, these pore bodies required a relative pressure greater than 0.7 and were unfilled by water. The results showed that nitrogen could fill large pores in the fresh catalysts following water adsorption, but less amount of nitrogen was adsorbed in the coked catalysts above a relative pressure of 0.7 following water adsorption. Thus, according to this interpretation the pore bodies and necks fill independently for nitrogen but not for water. This interpretation is also supported by earlier work of Rigby and Chigada (2009). They showed that that the critical pore neck to pore body

ratio that permits advanced adsorption is not a fixed value of 2 as propounded by Esparza et al. (2004). Advanced adsorption also depends on the properties of the probe fluid and the probe fluid-surface interaction strength. Under the investigated conditions, the nitrogen pore volumes before and after water adsorption in the coked sample was close to the pore volume occupied by water. This indicated the absence of any pore blocking caused by water adsorption and freezing. It was also revealed from FHH analysis that the nitrogen molecules detected a relatively smoother surface following water adsorption. Thus, the initial roughness caused by the presence of coke was not detected by nitrogen molecules. It was likely that polar groups on the coke attracted water molecules causing their condensation on carbon deposits. This may possibly be the other reason behind the different filling pattern in the C1 catalyst relative to the fresh sample. Water when frozen on C1 provided a uniform icy surface leading to a reduction in the FHH fractal dimension. The presence of polar groups on carbon deposits in hydroprocessing catalysts has been reported earlier in work done by Snape et al. (2001). Shah (2011) also reported the presence of polar groups on coked catalysts which underwent THAI®-CAPRI® reactions.

Analyses of nitrogen adsorption kinetics after water adsorption and after reaction showed that both water and coke caused a lowering of the normalised mass transfer coefficients relative to those obtained before water adsorption or before reaction. Water adsorption did cause a slightly greater fall in the normalised mass transfer coefficients than the presence of carbon deposits. However, this can be attributed to the difference in the amount of water and coke present in the catalysts.

(a)   (b)
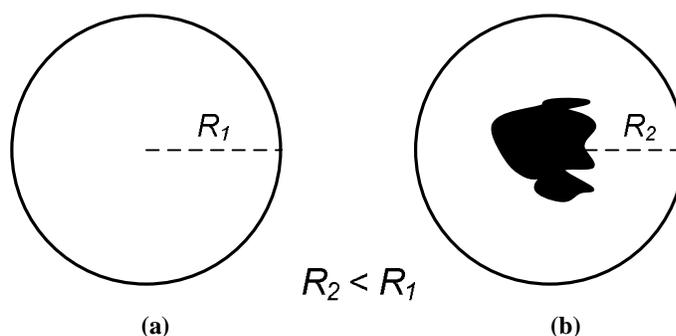
Fig. 4.14. An example of a fresh catalyst pellet (a) and a coked catalyst pellet (b). In the coked catalyst pellet, carbon deposition has taken place in the centre. The diffusion path length $R_2 < R_1$ causing the mass transfer coefficient to increase in the coked catalyst pellet relative to the fresh catalyst pellet.

It was mentioned in Section 4.2 that the mass transfer coefficient is dependent on the diffusion coefficient and the diffusion path length (see Eq. 4.3). Consider Figs. 4.14a and b showing a fresh catalyst pellet and its coked counterpart. It is assumed that in the coked catalyst carbon deposition has taken place internally at the centre of

134

the catalyst[27]. As seen in the Fig. 4.14, it is clear that the diffusion path lengths R_1 and R_2 would be different for the two catalysts. Since $R_2 < R_1$, the effective mass transfer coefficient (of nitrogen) will increase (according to Eq. 4.3) in the coked catalyst pellet. However, experimental evidence reported in Section 4.3.2 showed no evidence of an increase in the normalised mass transfer coefficient either following water adsorption or following the reaction. The initial drops in the normalised mass transfer coefficients were much larger than those at intermediate and later stages. The larger initial drops in the normalised mass transfer coefficients can be attributed to the sites adsorbed by water and coke in the pore space of the catalyst. The normalised mass transfer coefficient was only found to increase after a certain point in Figs 4.7, 4.10, 4.12, i.e. after the data point marked in red. This gradual rise in the normalised mass transfer coefficient can be attributed to a decrease in the diffusion path length due to completion of the monolayer formation and subsequent multilayer adsorption of nitrogen molecules such that enough condensate is present to block or seal off some pores completely. Thus, after the data point marked in red, the influence of the nitrogen condensate caused the normalised mass transfer coefficients to increase. Since the mass transfer coefficients (and diffusion coefficients) determined belong to the Knudsen diffusion regime, they would be influenced by the pore structure of the catalyst.

For greater fractions of the pore space occupied by condensed liquid nitrogen, molecular diffusion predominates. Since no evidence of increase in the normalised mass transfer coefficient was evident from the experiments conducted on the fresh catalyst sample A and coked catalyst C1, this indicated that most of the carbon deposition in C1 was away from the centre and interior portions of the catalysts. This implied that the carbon deposits are more likely to be dispersed and randomly distributed towards the outer regions of the catalyst, or more near the surface. Such an interpretation is agreed by the observation of a fall in the value of the normalised mass transfer coefficients. Further, this effect was not unique to carbon deposition in C1 as seen in Section 4.4.2. Water adsorption in sample A also caused a similar fall in the normalised mass transfer coefficients. This therefore indicates that water molecules were likely to be adsorbing at sites where carbon deposition also takes place following reaction. Clearly, from the preceding statements, if water adsorption takes place at different regions to that occupied by coke, then a different effect/trend would have been evident in the normalised mass transfer coefficients. For example, invoking Fig.

---

[27] Carbon deposition at the centre of the catalyst pellet is possible. An example of such an occurrence can be seen in the work of Chua et al. (2010).

4.14, if instead of carbon deposition, all of the water adsorption took place in the interior central region of the catalyst, an increase in the mass transfer coefficient would have been evident. As reported in Section 4.4.2, this was not found in the experiments conducted. Hence, experimental evidence suggested that water adsorption and carbon deposition took place at similar sites, which were likely to be located away from the interior central regions of the catalyst extrudates and are more likely to be dispersed and distributed closer to the external surface. This also means that the integrated N_2-H_2O-N_2 adsorption experiments are suitable for predicting the carbon deposition locations/patterns in sample A.

4.6 CONCLUSIONS

The work presented in this chapter is likely to be the first application of the integrated N_2-H_2O-N_2 adsorption experiments to distinguish between fresh and coked catalysts. It is concluded from the above work that cooperative effects in adsorption can be significant and must be considered when characterising fresh and coked catalysts. This is especially important as a general approach of comparing the pore size distributions may not be valid or accurate. When water molecules are pre-adsorbed in a manner such that it partially saturates the available pore space in the fresh catalyst sample A, it tends to serve as a good probe for the detecting the location of probable and likely sites of carbon deposition. The carbon deposits in the catalyst studied here were found to be away from the interior central regions of the catalyst. This possibly also hints at the diffusion limitations faced by the reactants in these catalysts under the investigated reaction conditions.

REFERENCES

CHUA, L. M., VAZHNOVA, T., MAYS, T. J., LUKYANOV, D. B. & RIGBY, S. P. 2010. Deactivation of PtH-MFI bifunctional catalysts by coke formation during benzene alkylation with ethane. *Journal of Catalysis,* 271, 401-412.

CRITTENDEN, B. D. 2006. CE 40131 Advanced Materials and Porous Solids Lectures. University of Bath.

ESPARZA, J. M., OJEDA, M. L., CAMPERO, A., DOMINGUEZ, A., KORNHAUSER, I., ROJAS, F., VIDALES, A. M., LOPEZ, R. H. & ZGRABLICH, G. 2004. N_2 sorption scanning behavior of SBA-15 porous substrates. *Colloids and Surfaces A: Physicochemical and Engineering Aspects,* 241, 35-45.

GARCÍA-OCHOA, F. & SANTOS, A. 1996. Coke effect in mass transport and morphology of $Pt\text{-}Al_2O_3$ and $Ni\text{-}Mo\text{-}Al_2O_3$ catalysts. *AIChE Journal,* 42, 524-531.

GEANKOPLIS, C. J. 2003. *Transport processes and separation process principles : (includes unit operations),* Upper Saddle River, NJ, Prentice Hall Professional Technical Reference.

GLUECKAUF, E. 1955. Theory of Chromatography .10. Formulae for Diffusion into Spheres and Their Application to Chromatography. *Transactions of the Faraday Society,* 51, 1540-1551.

GLUECKAUF, E. & COATES, J. I. 1947. Theory of Chromatography .4. The Influence of Incomplete Equilibrium on the Front Boundary of Chromatograms and on the Effectiveness of Separation. *Journal of the Chemical Society,* 1315-1321.

HUA, D. W. & SMITH, D. M. 1992. Pore-Size and Surface Texture Modification of Silica Via Trialkylsilylation. *Langmuir,* 8, 2753-2757.

KARNAUKHOV, A. P. 1985. Improvement of Methods for Surface-Area Determinations. *Journal of Colloid and Interface Science,* 103, 311-320.

LOWELL, S., SHIELDS, J. E., THOMAS, M. A. & THOMMES, M. 2006. *Characterization of Porous Solids and Powders: Surface Area, Pore Size and Density,* Dordrecht, Kluwer Academic Publishers.

MAYAGOITIA, V., ROJAS, F. & KORNHAUSER, I. 1985. Pore Network Interactions in Ascending Processes Relative to Capillary Condensation. *Journal of the Chemical Society-Faraday Transactions I,* 81, 2931-2940.

MENÉNDEZ, M. & BRAÑA, A. 1994. Variations in the Porous Structure of a Cr_2O_3/Al_2O_3 Catalyst by Coke Deposition. *Canadian Journal of Chemical Engineering,* 72, 926-928.

MORISHIGE, K. & KANZAKI, Y. 2009. Porous Structure of Ordered Silica with Cagelike Pores Examined by Successive Adsorption of Water and Nitrogen. *Journal of Physical Chemistry C,* 113, 14927-14934.

MORISHIGE, K. & YOSHIDA, K. 2010. Neck Size of Ordered Cage-Type Mesoporous Silica FDU-12 and Origin of Gradual Desorption. *Journal of Physical Chemistry C,* 114, 7095-7101.

NAVE, C. R. 2010. *Mean Free Path* [Online]. Georgia State University. Available from: http://hyperphysics.phy-astr.gsu.edu/hbase/kinetic/menfre.html#c3 [Accessed 6 May 2012].

NEIMARK, A. V., HANSON, M. & UNGER, K. K. 1993. Fractal Analysis of the Distribution of High-Viscosity Fluids in Porous Supports. *Journal of Physical Chemistry,* 97, 6011-6015.

PATTON, A., CRITTENDEN, B. D. & PERERA, S. P. 2004. Use of the linear driving force approximation to guide the design of monolithic adsorbents. *Chemical Engineering Research & Design,* 82, 999-1009.

PFEIFER, P., JOHNSTON, G. P., DESHPANDE, R., SMITH, D. M. & HURD, A. J. 1991. Structure-Analysis of Porous Solids from Preadsorbed Films. *Langmuir,* 7, 2833-2843.

RIGBY, S. P. & CHIGADA, P. I. 2009. Interpretation of integrated gas sorption and mercury porosimetry studies of adsorption in disordered networks using mean-field DFT. *Adsorption-Journal of the International Adsorption Society,* 15, 31-41.

RIGBY, S. P. & FLETCHER, R. S. 2004. Experimental evidence for pore blocking as the mechanism for nitrogen sorption hysteresis in a mesoporous material. *Journal of Physical Chemistry B,* 108, 4690-4695.

RIGBY, S. P., FLETCHER, R. S. & RILEY, S. N. 2004. Characterisation of porous solids using integrated nitrogen sorption and mercury porosimetry. *Chemical Engineering Science,* 59, 41-51.

RIGBY, S. P., WATT-SMITH, M. J. & FLETCHER, R. S. 2005. Integrating gas sorption with mercury porosimetry. *Adsorption-Journal of the International Adsorption Society,* 11, 201-206.

SHAH, A. A. 2011. *Experimental Optimization of the CAPRI Process.* PhD, University of Birmingham.

SIRCAR, S. & HUFTON, J. R. 2000. Why does the Linear Driving Force model for adsorption kinetics work ? *Adsorption-Journal of the International Adsorption Society,* 6**,** 137-147.

SNAPE, C. E., DIAZ, M. C., TYAGI, Y. R., MARTIN, S. C., HUGHES, R., MURRAY, I. P. & HALL, P. J. 2001. Characterisation of coke on deactivated hydrodesulfurisation catalysts and a novel approach to catalyst regeneration. *In:* SPIVEY, J. J., ROBERTS, G. W. & DAVIS, B. H., eds. *9th International Symposium on Catalyst Deactivation (ISCD),* 13-15 October 2001. Lexington, Kentucky. Studies in Surface Science and Catalysis, 139, Amsterdam: Elsevier Science BV, 359-365.

THOMAS, W. J. & CRITTENDEN, B. D. 1998. *Adsorption technology and design,* Oxford, Butterworth-Heinemann.

WASHBURN, E. W. (ed.) 1926 - 1930; 2003. *International Critical Tables of Numerical Data, Physics, Chemistry and Technology* Knovel. Available from: http://www.knovel.com/web/portal/browse/display?_EXT_KNOVEL_DIS PLAY_bookid=735&VerticalID=0 [Accessed 26 May 2012].

WYPYCH, G. 2008. Knovel Solvents - A Properties Database. ChemTec Publishing. Available from: http://www.knovel.com/web/portal/browse/display?_EXT_KNOVEL_DIS PLAY_bookid=635&VerticalID=0 [Accessed 26 May 2012].

YANG, R. T. 1987. *Gas separation by adsorption processes,* Boston, Butterworths.

CHAPTER 5 – CATALYST CHARACTERISATION BY NUCLEAR MAGNETIC RESONANCE

Chapter 5 of this thesis introduces the reader to catalyst characterisation methods that involve application of nuclear magnetic resonance (NMR) techniques. This chapter first provides the reader with a basic description of NMR spectroscopy, through some essential theory, which discusses NMR parameters such as T_1 and T_2 relaxation times, and molecular diffusion coefficients. This is followed by an overview of the current porous media characterisation techniques that use NMR. From this overview and in the light of limitations of conventional catalyst characterisation techniques (from previous chapters), the need for a robust characterisation technique is established. A new method termed liquid-liquid exchange (LLE) is proposed as a characterisation technique that is likely to meet the stringent requirements for characterising both fresh and coked catalysts. Experiments are conducted on a model silica material, and Pt/Al_2O_3 catalysts in their fresh and coked states. The significance of the results discussed here is found to lie in their ability to reveal the spatial location of coke deposits within catalysts.

5.1 NUCLEAR MAGNETIC RESONANCE – CONCEPT AND THEORY

The development of NMR spectroscopy has allowed it to become an indispensable tool in all branches of chemistry due to its ability to elucidate molecular structures and study chemical reactions. Today, apart from chemists, it is widely used by physicists, biologists and medical doctors. The magnetic properties of atomic nuclei form the basis of NMR spectroscopy (Günther, 1995; Levitt, 2006; Atkins and Paula, 2010). Apart from fundamental properties like mass and charge, nuclei have angular momentum P and a magnetic moment μ, which are related to each other by:

$$\mu = \gamma P \, , \tag{5.1}$$

where γ is the magnetogyric ratio, a constant characteristic of a specific nucleus. The magnitude of the angular momentum is given by $\{I(I+1)\}^{1/2}\dfrac{h}{2\pi}$ where I is the spin quantum number and h is Planck's constant. I can hold values of either a integer or half integer, i.e. 0, $\dfrac{1}{2}$, 1, $\dfrac{3}{2}$, 2, $\dfrac{5}{2}$, etc. The orientation of angular momentum P is

quantized and its component along the *z*-direction of Cartesian coordinates is given by:

$$P = \frac{h}{2\pi} m_I ,$$
(5.2)

where m_I is the magnetic quantum number and can take values from $+I$, $I-1$, ...$-I$ (Günther, 1995; Atkins and Paula, 2010). Thus, a magnetic moment with a constant magnitude and orientation can be obtained for any nuclei with $I > 0$. Protons (^1H), the nuclei of interest in this work, have a spin quantum number of $\frac{1}{2}$. This means that each proton can exist in two spin states with magnetic quantum numbers $+\frac{1}{2}$ and $-\frac{1}{2}$ and its magnetic moments in the *z*-direction are given by:

$$\mu = \gamma \frac{h}{2\pi} m_I = \pm \gamma \frac{h}{2\pi} \left(\frac{1}{2} \right) .$$
(5.3)

Thus, the proton is essentially a magnetic dipole with magnetic moments in a parallel or anti-parallel orientation with respect to the main field, i.e. along the *z*-direction of the coordinate system. In the absence of a magnetic field, the spin states of the nuclei have the same energy, i.e. they are degenerate. However, in the presence of a static magnetic field B_0, this degeneracy is destroyed and the microscopic magnetic moments align themselves relative to the field, either in a parallel or anti-parallel direction (see Fig. 5.1).
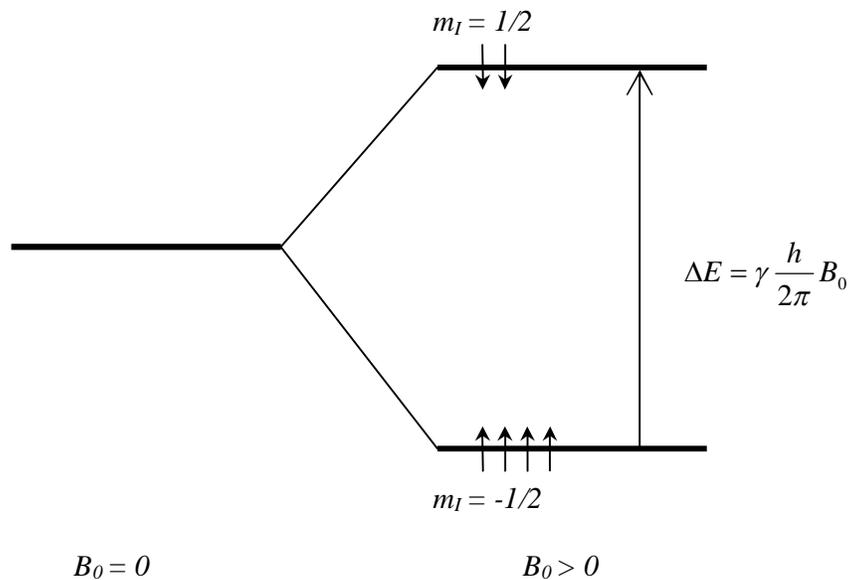
Fig. 5.1. Splitting of energy states of a proton in the presence of a magnetic field.

The static magnetic field exerts a torque on the magnetic moment forcing it to trace a circular path about the applied field. This motion of the magnetic moment is called the Larmor precession (Günther, 1995; Atkins and Paula, 2010). The energy difference ΔE between the two spin states of protons in a magnetic field B_0 is given by:

$$\Delta E = \gamma \frac{h}{2\pi} \left[\left(\frac{1}{2} \right) - \left(-\frac{1}{2} \right) \right] B_0 = \gamma \frac{h}{2\pi} B_0 . \tag{5.4}$$

Nuclei have a tendency to occupy the lower energy state, giving this state a slight population excess relative to the higher energy state. Considering the Bohr frequency condition $\Delta E = h\nu$, a photon of the exact frequency is necessary to enable the nuclei to undergo a transition from the lower energy state to the higher energy state. This helps to achieve the state of nuclear magnetic resonance as expressed in:

$$h\nu_0 = \gamma \frac{h}{2\pi} B_0 , \tag{5.5a}$$

and the frequency that exactly matches this energy gap is called the Larmor frequency ν_0 (Günther, 1995; Atkins and Paula, 2010):

$$\nu_0 = \frac{\gamma B_0}{2\pi} . \tag{5.5b}$$

Eq. (5.5b) may also be written in the following form:

$$\omega_0 = \gamma B_0 , \tag{5.5c}$$

where ω_0 is the angular frequency and is equal to $2\pi\nu_0$. The most important parts of an NMR spectrometer are the magnet, radiofrequency (r.f.) transmitter and detector. A Bruker NMR spectrometer was used in this work and it employs a static magnetic field strength of 9.4 T. For protons, the magnetogyric ratio, γ is 2.675×10^8 $T^{-1}s^{-1}$. This yields a Larmor frequency of 400 MHz. Thus, on application of the Larmor frequency, the populations of the two spin states become equal and in the absence of this r.f. frequency, the protons go back to equilibrium conditions with the emission of energy that produces the NMR spectrum.

For a collection of protons exposed to an external magnetic field B_0, the individual protons will align with or against the magnetic field. Since as mentioned earlier, there is a slight excess of nuclei in the lower energy state, the resultant of individual nuclear magnetic moments produces a macroscopic magnetization M along the z-axis parallel to the external magnetic field (see Fig. 5.2). This resultant magnetization along the z-axis can be deflected towards the y-axis by the application of a strong r.f. pulse. The longer (or stronger) the r.f. pulse, the more the magnetization is tipped towards the y-axis. After a certain amount of time, the

magnetization *M* will have been deflected by 90°. Here 90° is the pulse or flip angle[28]. The length of the pulse can be varied to direct the magnetization in different orientations. Thus, a 180° pulse (i.e. a pulse with twice the duration of a 90° pulse) would point the magnetization in the negative *z*-axis (Günther, 1995).
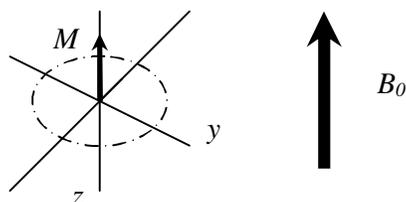
Fig. 5.2. Development of macroscopic magnetization *M* along the *z*-axis in the presence of a static magnetic field *B₀*.

At resonance, or the Larmor frequency, the interaction of this r.f. pulse with the magnetization thus causes a deflection of the resultant magnetization from its equilibrium position along the *z*-axis. This in turn creates a transverse magnetization in the *xy* plane. As mentioned earlier, the static magnetic field, along the *z*-axis, exerts a torque on the magnetic moments in the *xy* plane, forcing them to trace a circular path about the applied field, at their Larmor frequency. This transverse magnetization therefore rotates in the *xy* plane, inducing a voltage that can be picked up by the NMR spectrometer's detector coils. This signal, detectable for several milliseconds to several seconds, depending on the sample, is then Fourier transformed to yield the frequency signal (Günther, 1995). The signal will disappear over time due to relaxation, as shown in the next section.

5.1.1 NMR RELAXATION

The phenomenon by which nuclei return back to their original spin states with the transfer of energy is called relaxation. It can be understood from preceding paragraphs that there are two macroscopic magnetization components that can be achieved in a nuclear magnetic resonance experiment. Both longitudinal magnetization (along the *z*-axis) and transverse magnetization (along the *xy* plane) undergo time dependent relaxation phenomena. The spins present in a sample exposed to an external magnetic field are initially in a non-equilibrium state because

---

[28] The pulse or flip angle α for the macroscopic magnetization *M* is given by the relation: $\alpha = (\gamma/2\pi)B_1 t_p$ where B_1 is the r.f. pulse in the form a strong magnetic field, $(\gamma/2\pi)B_1$ is the amplitude or power of the pulse and t_p is its length or width (Günther, 1995).

all the spin states are equally populated. Longitudinal relaxation time (T_1) is the time constant during which the z-component of the magnetization reverts to the equilibrium state, i.e. with a population excess aligned with the magnetic field. Energy is transferred from the spins to the environment or lattice during this process. Hence, longitudinal relaxation is also called spin-lattice relaxation. The variation of the z-component of magnetization for each nuclear environment during this phenomenon obeys (assuming a uniform a magnetic field) a first-order differential equation:

$$\frac{dM_z(t)}{dt} = \frac{(M_0 - M_z(t))}{T_1}, \tag{5.6a}$$

$$M_z(t) - M_0 \propto e^{-t/T_1}. \tag{5.6b}$$

The longitudinal relaxation time is measured by the application of the inversion recovery technique. Initially, a 180° pulse is applied to the sample which rotates the magnetization vector M by 180°, pointing it in the negative z-direction. Since the vector points in the negative z-direction, no signal will be detected by the coil, which only detects magnetization in the xy plane. As the spins relax back to their original equilibrium state, the magnetization vector shrinks exponentially through zero to its the thermal equilibrium value M. To generate a free induction decay (FID) signal, the decaying magnetization vector is rotated into the xy plane by applying a 90° pulse after an interval τ. As the interval τ is increased, the length of the magnetization vector detected by the coil also changes allowing the intensity of the spectrum to change exponentially with increasing τ. An exponential curve can then be fitted to the series of spectra obtained with different values of τ to obtain the longitudinal relaxation time T_1 (Günther, 1995; Atkins and Paula, 2010). The pulse sequence used for the determination of longitudinal relaxation time is illustrated below in Fig. 5.3.
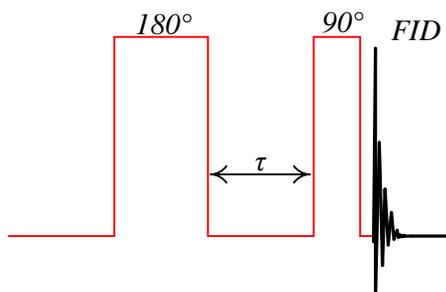
Fig. 5.3. Pulse sequence employed for determining T_1 relaxation time constant using the principle of inversion recovery. τ is the time delay between the 180° and 90° r.f. pulses.

On the other hand, if instead of a 180° pulse, a 90° pulse is applied, then the magnetization vector M is tipped onto the xy plane. As mentioned earlier, M will subsequently precess around the z-axis. However, the spins are in phase only for an instant after the pulse. This coherence of spins is not at equilibrium and even if there were no longitudinal relaxation, the individual spins would fan out until they were uniformly distributed with all possible angles around the z-axis. At this stage, the overall magnetization vector present in the xy plane is averaged to zero. This randomization of spin directions occurs exponentially with a time constant called the transverse relaxation time T_2. Since this relaxation process involves the energy transfer between individual spins, it is also called spin-spin relaxation (Günther, 1995; Atkins and Paula, 2010). The variation of the xy-component of magnetization obeys a first order differential equation:

$$\frac{dM_{xy}(t)}{dt} = -\frac{M_{xy}(t)}{T_2}, \tag{5.7a}$$

$$M_{xy}(t) \propto M_{xy}(0)e^{-t/T_2}. \tag{5.7b}$$

The measurement of transverse relaxation time can be accomplished by performing the spin echo experiment. Once equilibrated within a magnetic field, the macroscopic magnetization vector M is initially along the z-axis. A 90° pulse applied along the y-axis will tip the magnetization vector into the x-axis. Over time, the magnetization vector (which is precessing about the z-axis) decays and fans out since the nuclear spins experience magnetic field inhomogeneities and/or varying intermolecular or intramolecular interactions[29]. Therefore, some spins may experience a slightly greater local field causing them to have a higher frequency and creep ahead (fast) while other spins may experience a relatively lower local field and lag behind (slow). After an interval τ, a 180° pulse is applied which exchanges the position of the fast and slow spins in the frame of reference. The same time delay τ is again allowed to pass. Since the spins follow or traverse the same path as before, they are bound to meet and produce a refocused magnetization vector at 2τ. This refocused magnetization vector can be detected in the receiver coil and is called a spin echo signal. To reduce the effect of diffusion during the measurement of transverse relaxation time, the amplitude of spin echo is recorded repeatedly at 2τ, 4τ, 6τ, etc. (Günther, 1995; Atkins and Paula, 2010). Such a pulse sequence is called the CPMG (Carr-Purcell-Meiboom-Gill) pulse train and it is illustrated below in Fig. 5.4.

---

[29] This decay of the magnetization vector is visible in the rotating frame of reference.

Porous media properties like surface/volume ratio, permeability, wettability, etc. can be determined by relating them to spin-lattice and/or spin-spin relaxation times of imbibed fluids. In this work, only spin-spin relaxation times are used to estimate porous media properties. These properties are determined using a probe liquid which is imbibed within the material of interest. In a bulk medium, liquid molecules are surrounded by other liquid molecules. However, the presence of a surface causes liquid molecules near the surface, within a thin layer of thickness λ, to experience different intermolecular forces relative to those molecules away from the surface. The presence of a surface causes a change in the kinetics of the molecules relative to those away from the surface due to variable fluid-solid interactions caused by the presence of different surface functional groups. This difference in forces usually results in an enhancement of the relaxation rate of a liquid within a porous medium. The catalysts studied in this work are mesoporous.
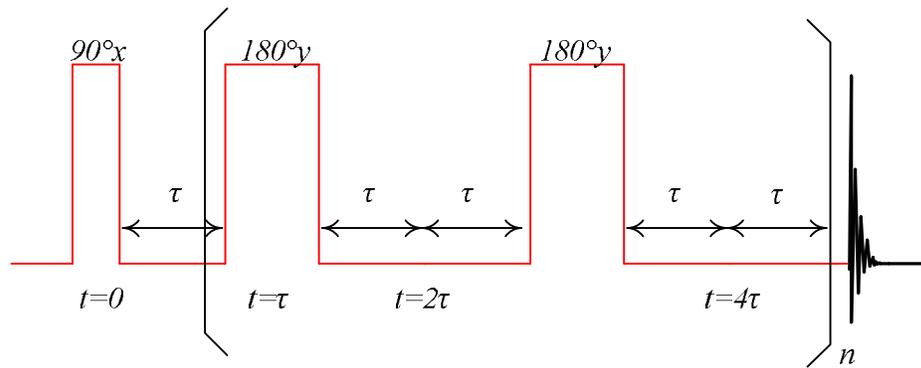
Fig. 5.4. CPMG pulse train employed to determine the T_2 relaxation time constant.

During a typical NMR experiment, the mean square displacement of the nuclei is of the order of tens of microns, which is much larger than the typical pore size of the catalyst, usually of the order of nanometres. This means that liquid molecules traverse paths that contain a number of pores and there is rapid exchange between molecules near the surface of the pore and those within the centre of the pore. Such an exchange regime is referred to as the fast-exchange limit (Brownstein and Tarr, 1977) and the expression for the transverse relaxation rate corresponding to a single pore in this regime is given by:

$$\frac{1}{T_2} = \frac{p_b}{T_{2b}} + \frac{p_s}{T_{2s}}, \tag{5.8a}$$

$$\frac{1}{T_2} = \frac{1-p_s}{T_{2b}} + \frac{p_s}{T_{2s}}, \tag{5.8b}$$

146

$$\frac{1}{T_2} = \frac{1}{T_{2b}} + p_s\left(\frac{1}{T_{2s}} - \frac{1}{T_{2b}}\right), \tag{5.8c}$$

where T_2 is the average relaxation time of the liquid molecules within the pore, T_{2b} is the relaxation time of the bulk liquid, T_{2s} is the surface relaxation time of the liquid, p_b and p_s are the bulk and surface fractions respectively of the liquid present in the pore. For a cylindrical pore seen in Fig. 5.5, where $\lambda <<$ pore size r, the above expression becomes:

$$\frac{1}{T_2} = \frac{1}{T_{2b}} + \frac{\lambda s}{v}\left(\frac{1}{T_{2s}} - \frac{1}{T_{2b}}\right), \tag{5.8d}$$

$$\frac{1}{T_2} = \frac{1}{T_{2b}} + \frac{\lambda 2}{r}\left(\frac{1}{T_{2s}} - \frac{1}{T_{2b}}\right). \tag{5.8e}$$

λ is the thickness over which the surface relaxation of the fluid takes place within the pore and s/v is the surface to volume ratio of the pore, for a cylindrical pore $s/v = 2/r$.
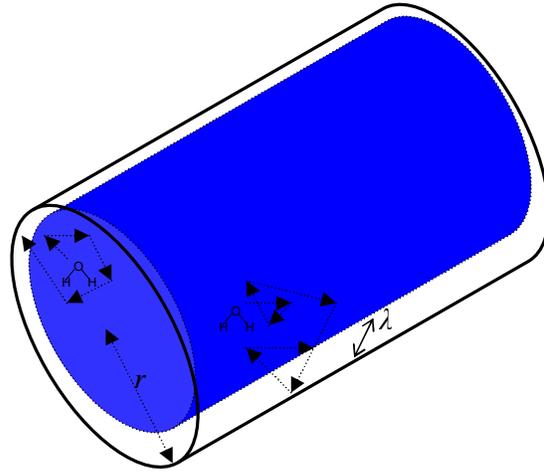
Fig. 5.5. Relaxation of water molecules near the surface of a cylindrical pore of radius r having a volume v and surface area s. Water molecules undergo enhanced relaxation in a thin surface layer of thickness λ.

Eq. (5.8e) is normally written in the following form:

$$\frac{1}{T_2} = \frac{1}{T_{2b}} + \rho\frac{2}{r}, \tag{5.8f}$$

where ρ is called the surface relaxivity parameter for spin-spin relaxation. As $T_{2b} >> T_{2s}$, Eq. (5.8f) becomes:

$$\frac{1}{T_2} \approx \rho\frac{2}{r}, \tag{5.8g}$$

for a cylindrical pore. In general:

$$\frac{1}{T_2} \approx \rho\frac{s}{v}. \tag{5.8h}$$

Thus, the T_2 relaxation time is proportional to the pore size r. Hence, large relaxation times correspond to large pore sizes while smaller relaxation times correspond to smaller pore sizes. Earlier in Eq. (5.7b), it was seen that the spin-spin relaxation time is described by an exponential decay model. In the fast-exchange regime, spin-spin relaxation is described by a mono-exponential model and it will be seen that this is the regime that is observed for the work discussed here.

5.1.2 DIFFUSION NMR

A significant advantage of NMR is its ability to non-invasively probe the Brownian motion or translational properties of fluids within a porous medium or in their bulk nature. The traditional spin echo sequence can be further modified by the addition of spatial and time dependent magnetic field gradients which label molecules and detect their displacements without intrinsically affecting their diffusion. This labelling is achieved by utilising the Larmor precession of nuclear spins. Hence, by determining the starting and final positions of nuclei, the diffusion coefficient of a fluid can be determined. In this work, NMR in the form of pulsed field gradient (PFG) experiments was used to study the diffusion of liquids within model catalyst supports and an industrially relevant catalyst. Self diffusion or translational diffusion is driven by the internal energy of molecules and is considered to be the most fundamental means of transport in chemical and biochemical systems. For example, reactions within catalysts take place by the diffusion of reactants.

In contrast to the earlier discussion on the basic principles of NMR and relaxation phenomena, where the external applied field B_0 was homogenous, the determination of diffusion coefficients is made possible by the addition of small magnetic field gradients G to the uniform field. This causes the resultant field B and the Larmor frequency ω_{0z} to vary along the direction of the applied gradient:

$$\frac{\partial B}{\partial z} = G_z, \tag{5.9a}$$

$$\omega_{0z} = \gamma\left(B_o + G_z z\right). \tag{5.9b}$$

Only a brief outline and introduction to the pulsed field gradient NMR is provided here. Further details can be seen in reviews and articles by Gladden (1994), Hollewand and Gladden (1995), Price (1997), Stallmach and Kärger (1999), Barrie (2000), Kärger (2008), and Kärger et al. (2009). From Eq. (5.9), it can be seen that the Larmor frequency becomes dependent on the position of the spins, when a gradient G is applied along the same direction as the static field. Hahn (1950) was first to

recognise this. Later, Stejskal and Tanner (1965) advanced the method by advocating the use of gradient pulses instead of continuous steady gradients, thus circumventing the limitations of the Hahn technique.

In Fig. 5.6, application of the 90° pulse shifts the net magnetization onto the xy plane. The introduction of the first gradient pulse at time t_1 imparts a phase shift on the magnetization and at the end of the first τ period, a 180° pulse is applied which exchanges the position of the fast and slow spins. Then, at time $t_1 + \Delta$, another gradient equal in magnitude to the initial gradient, is applied for the same duration thereby reversing the phase shift. Therefore, if diffusion was present, the spin echo intensity would be attenuated, since the phase shift would not be completely reversed because each diffusing nuclei would not experience equal gradients. On the other hand, if there was no diffusion, maximum signal would be obtained, as the two gradient pulses cancel and all spins refocus.
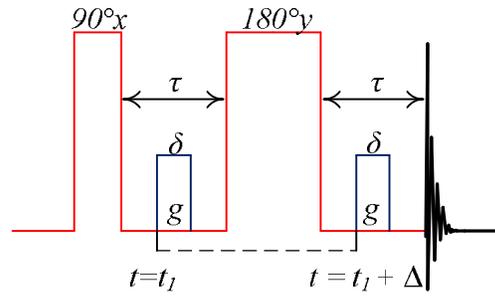
Fig. 5.6. Stejskal and Tanner NMR pulse sequence to determine the diffusion coefficient. τ is the time delay between the 90° and 180° r.f. pulses, g indicates the gradient pulse applied for a duration δ, and Δ is the time allowed for diffusion.

An advanced version of the Stejskal and Tanner pulse sequence that uses a stimulated echo and bipolar gradient pulses is used to measure diffusion coefficients in this work. The change in echo intensity R for PFG experiments is given by:

$$R = \frac{I}{I_0} = \exp\left[-D\gamma^2 g^2 \delta^2 \left(\Delta - \frac{\delta}{3} - \frac{\tau}{2}\right)\right],$$ (5.10a)

$$R = \frac{I}{I_0} = \exp\left[-D\Psi\right],$$ (5.10b)

where D is the diffusion coefficient, γ is the gyromagnetic or magnetogyric ratio, g is the gradient strength, δ is the duration of the applied gradient pulse, Δ is the diffusion time and τ is the correction time between the bipolar gradients and $\Psi = \gamma^2 g^2 \delta^2 \left(\Delta - \frac{\delta}{3} - \frac{\tau}{2}\right)$. The above equation displays an exponential decay and a plot of the relative intensity against Ψ yields the diffusion coefficient (Kerssebaum, 2002). The diffusion coefficient measured for a liquid within a porous material is the

average of the individual diffusion coefficients experienced by the labelled spins. This is directly related to the voidage or porosity of the material. Thus, the diffusion coefficient measured by PFG NMR, D_{PFG}, is given by:

$$D_{PFG} = \frac{D_b}{\tau_p},$$ (5.11)

where D_b is the free or bulk diffusion coefficient of liquid studied at the same temperature at which the PFG NMR experiment is conducted, and τ_p is the tortuosity of the pore space traversed by the liquid molecules (Hollewand and Gladden, 1995). It must be stressed that the above equations are acceptable only when molecular displacements during field gradient pulses are negligibly smaller than the time delay between them, i.e. when $\delta << \Delta$. Therefore, optimal values of δ and Δ must be selected such that δ is much less than the T_2 relaxation time while Δ is less than the T_1 relaxation time. An estimate of the mean square displacement $\langle r^2 \rangle$ undertaken by nuclei during the diffusion process can be obtained from the Einstein equation:

$$\langle r^2 \rangle = 6 D_{PFG} \Delta .$$ (5.12)

In the characterization of porous materials with diffusion NMR, any of three diffusion regimes are likely to be observed. They include free diffusion, restricted diffusion and partially constrained diffusion. Unlike free fluids, where $\langle r^2 \rangle$ increases with increase in diffusion time, keeping the diffusion coefficient a constant at a given temperature, the presence of a pore surface and its interaction with fluid molecules causes a dramatic change in the self diffusion coefficient. It is possible to gain a sense of the architecture of the pore surface by conducting PFG NMR experiments at different diffusion times. At very short diffusion times, $\langle r^2 \rangle$ is far less than the typical pore size of the sample; this implies that the fluid molecules do not experience the pore walls or any restrictions. Hence, the diffusion coefficient may be similar to, or less than, the free fluid diffusion coefficient. On the other hand, at long diffusion times, molecules may be trapped or restricted within pores or a particular region of pores. In these conditions, $\langle r^2 \rangle$ is a constant determined by the pore or region size, and the diffusion coefficient will vary inversely with time. A model given by Eq. (5.13):

$$\Re = \left(5D \left(\Delta - \frac{\delta}{3} \right) \right)^{0.5},$$ (5.13)

from Callaghan et al. (1983) can be used to determine the spherical cavity radius $\Re$ in which molecules undergo restricted diffusion. Under partially constrained conditions,

only a fraction of the molecules feel the surface and the apparent diffusion coefficient measured will be a function of the diffusion time. The fraction of molecules that feel the effects of the boundary will be dependent on the surface to volume ratio. From Eq. (5.10), it is seen that the change in echo intensity R during a PFG experiment is also described by an exponential decay model. Therefore, a plot of $\ln R$ vs. Ψ will yield a straight line with slope equal to the negative of the diffusion coefficient. However, the straight line is usually observed only when molecules are in the free diffusion regime. Divergence from a straight line is observed as soon as the molecules begin to feel the presence of the wall or be restricted in certain regions (Barrie, 2000). This may cause the diffusion coefficient to be described by a multi-exponential decay equation instead of the original mono-exponential decay equation, see Eq. (5.14a). This implies that the liquid molecules are experiencing a range of diffusion coefficients with no exchange between populations of different diffusion coefficients (Hollewand and Gladden, 1995). For example, when the experimental data is described by a bi-exponential decay model (as will be seen in this work), this is consistent with a region where the liquid molecules undergo fast diffusion and another region where the liquid is undergoing slow diffusion. Such a model is usually described by Eq. (5.14b) and the log-attenuation plot data has the form of an ice-hockey stick.

$$R = \sum_i p_i \exp[-D_i \Psi],$$ (5.14a)

$$R = p_a \exp[-D_a \Psi] + (1 - p_a) \exp[-D_b \Psi],$$ (5.14b)

where p_i represents the liquid fraction having a diffusion coefficient $D_{i,}$, p_a and p_b are the two fractions of liquids having diffusion coefficients D_a and D_b respectively, p_a and p_b are related to each other such that $p_a + p_b = 1$.

5.2 INTRODUCTION TO CATALYST CHARACTERISATION WITH NMR

Before considering the work conducted using the above discussed NMR methods, a succinct overview of the literature in the context of the work presented here is given below. Earlier in Chapter 1 of this thesis, it was mentioned that displacement methods formed the basis of oil recovery. This was either achieved by reducing the oil-water interfacial tension or mobility ratio aiding the recovery of oil, or reducing the oil viscosity by the application of heat. Examples of the former include primary water flooding of light oil and mobile heavy oil reservoirs, secondary

water flooding, chemical flooding and immiscible CO_2 flooding of thin heavy oil formations while the latter include thermal oil recovery techniques such as SAGD, CSS and ISC. The salient feature of these techniques is that they are either a liquid-liquid or a gas-liquid displacement process. With the advent of NMR, reservoir plugs and cores have been characterised and an understanding of fluid flow in different conditions has been achieved. This provided a unique understanding of how fluid displacement actually takes place within the medium and what roles pressure, surface tension, pore size, connectivity, and rock wettability play during oil recovery.

Previous work by Holmes et al. (2001) and Holmes and Packer (2002, 2003, 2004) include an investigation of the surface wetting film in a two phase saturated porous medium and the phase entrapment of the hydrocarbon phase with the aid of PFG NMR and relaxometry. They found that the displacement of water usually occurred by the development of a thin surface film along the pore edges and crevices which then grew to encapsulate and trap the hydrocarbon phase. As water saturation increased within the medium, the mean square displacement for water transformed from one that was initially centred on zero displacement to a Gaussian spread. This form of displacement is essentially similar to the standard mercury porosimetry extrusion process where air displaces mercury within a porous medium causing the entrapment of non-wetting mercury in certain regions. Hertzog et al. (2007) described the use of NMR T_2 relaxation time measurements to characterise the presence of dense non-aqueous phase liquids (DNAPL) and moisture within subsurface soils. They used columns of fine sand and clay which were saturated with water and trichloroethylene to different degrees. They found that the drainage of water usually resulted in its removal from larger pores. Following this, saturation with trichloroethylene restricted them to these empty large pores. Displacement by water flooding led to the washing out of the majority of trichloroethylene and an increase in their relaxation times. Hence, there was some entrapment of trichloroethylene in very large pores. This mechanism is similar to mainstream oil recovery methods and hence structure related factors, wettability, interfacial tension, etc. also play a major role in the flow of organic contaminants and pollutants.

Qualitative and quantitative information on immiscible displacements can also be achieved through the use of NMR imaging techniques as seen in the work of Majors et al. (1997) and Chu et al. (2004). Majors et al. (1997) developed an imaging technique where the displacement could be detected by changes to T_2 relaxation times. Depending on saturation conditions, they observed either a piston displacement (when silicone oil displaced water) or finger based displacement (when water

152

displaced silicone oil). Chu et al. (2004) investigated the removal of non-aqueous phase liquid (NAPL) decane by soil vapour extraction (SVE) from heterogeneous porous media using magnetic resonance imaging (MRI). They found that NAPL recovery rates were high when the NAPL flowed from low permeability zones to high permeability zones. However, once the NAPL reached residual saturation, then diffusion controlled the volatilization of NAPL and mass recovery rates decreased. Once again, these observations are similar to entrapment of oil during its recovery or mercury during its extrusion from a catalyst. Thus, information available from NMR is also vital to understanding soil remediation and ground water pollution.

Like reservoir plugs or rock cores, catalysts have a significant level of physical and chemical heterogeneity which makes their physical characterisation extremely complex. It is essential to examine the physical properties of catalysts and optimise their properties to ensure optimum use during chemical reactions. The characterisation becomes even more difficult once they are aged, coked, or spent as physical and chemical heterogeneity undergo a drastic change relative to fresh catalysts. This makes the necessity for the availability of a robust method that is equally applicable for fresh and coked catalysts. Presently available characterisation techniques like gas adsorption (seen in Chapter 3 and Chapter 4), mercury porosimetry (seen in Chapter 2) and thermoporometry have limitations which make it essential for the development of a new method. Consider nitrogen gas adsorption; the highly heterogeneous surface of the catalyst can lead to specific interactions with nitrogen gas molecules. Thus, on a highly polar surface, there tends to be a tighter packing of nitrogen molecules relative to a homogeneous surface. Further, this method cannot be used for characterising macroporous samples since a proper control of pressure near the saturation pressure is not possible. More significantly, recent work by Hitchcock et al. (2010) and earlier work in Chapter 4 has shown that the phenomena of advanced adsorption must also be considered, as it can cause significant errors in pore size distribution measurements.

On the other hand, mercury porosimetry, though applicable over the macropore and mesopore range, cannot be used in the conventional way for microporous materials. Further, the high pressures generated by the apparatus to push mercury into the porous medium can generate undue stress and result in structure deformation or buckling. Sample destruction in such a manner inevitably leads to inaccurate pore structure information. Mercury porosimetry utilises the property that it is non-wetting to most porous materials. However, with certain materials like Cu, Al, and Pt, mercury wets the surface and even forms amalgams (Catchpole, 2009;

Hadden and Moss, 2010; Rigby et al. 2011). This results in a complete change in contact angle causing a change in the determined pore size. Mercury porosimetry is also not feasible for characterising coked catalysts as the high pressures generated by the apparatus can cause the movement of coke deposits, thereby once again generating false pore properties. Finally, the fact that samples cannot be reused necessitates the need for a large amount of sample which eventually requires safe disposal. This and the health hazard that mercury presents has led to a fall in the consumption of high levels of mercury for research.

Thermoporometry in its conventional, or NMR form, determines the pore size by measuring the freezing and/or melting point depression of the probe fluid imbibed within the porous medium. This technique is able to provide only limited spatial information on the location of coke within the pore space depending on the width of the freezing-melting hysteresis loop. An understanding of the coking process and optimisation of the catalyst structure can only be pursued if an accurate understanding of the location of coke laydown is achieved. Hence, it is essential to understand if the coking took place within the interior of the pellet, towards the surface, or all throughout the catalyst.

The above limitation calls for the requirement of a catalyst characterization technique that is applicable for all pore size ranges, i.e. micropores, mesopores, and macropores. It must simultaneously account for physical and chemical heterogeneity of the surface and must convey information on the degree of difference between fresh and coked catalysts. The variety of experiments offered by NMR and its ability to perform rapid, non-destructive and non-invasive measurements make it an extremely powerful technique that may be exploited to understand catalyst pore structure properties. A liquid-liquid exchange (LLE) or liquid-liquid displacement mechanism has the potential to provide spatial information/location for different sized pores by virtue of the displacement mechanism. In such experiments, the porous medium is already filled by a liquid, and another liquid then penetrates from outside of the pellet displacing the former liquid. As envisaged, the external liquid follows a path that is very similar to the diffusion path taken by reactant molecules while moving towards the catalytically active sites. The presence of coke residues in spent catalysts will certainly disturb the path traversed by the displacing liquid. It is proposed that this effect can be detected by the application of ^{1}H NMR spectroscopy, NMR relaxation and NMR diffusion experiments. Further, it also has immense potential to be developed further.

Previous work on the application of NMR to study the pore structure of catalysts include T_1 relaxation dispersion experiments (where the static magnetic field strength or Larmor frequency was varied) by Ren et al. (2010) on fresh, coked and regenerated Pt/Re-Al$_2$O$_3$ catalysts using n-heptane and water at room temperature. These experiments provided an indication of the surface interaction of the probe fluid molecules with the catalyst surface by detecting changes in the surface roughness and adsorbate properties. They observed that for fresh catalysts, n-heptane showed weak frequency dependence while water displayed a strong dependence. For coked catalysts, water displayed a similar strong dispersion in T_1 relaxation times in addition to a reduction in the T_1 values depending on the coke concentration. With regenerated samples, a similar reduction of T_1 relaxation times dependent on coke concentration was observed. However, n-heptane T_1 relaxation times showed significant differences in the frequency dependence for coked and regenerated catalysts relative to fresh catalysts indicating its high affinity to coke. Thus, the different surface interactions of two liquids, one polar and the other non-polar, help in understanding surface properties such as surface fractal dimension and the heterogeneity in coke distribution. Diffusometry experiments were also done by Ren et al. (2010) using n-heptane as a probe fluid. They found a 33% increase in tortuosity when 16 wt-% coke was introduced on to the fresh catalyst surface. However, on regeneration, the catalyst tortuosity was higher than that for a fresh catalyst indicating hysteresis.

NMR imaging experiments on different coked catalysts were performed by Cheah et al. (1994) to reveal significant heterogeneity in coke distribution that was related to heterogeneity in the porosity of the pellet. Other related works include PFG NMR studies on the transport properties of fluid catalytic cracking catalysts and hydroprocessing catalysts. Kortunov et al. (2005) used n-octane and 1,3,5-triisopropylbenzene as probe liquids and showed that the intra-particle diffusion coefficient controlled the rate of molecular exchange between catalyst particles and their surroundings. Using pentane and heptane as probe fluid molecules, Wood and Gladden (2003) found that heptane experienced larger tortuosities than pentane, which had a tendency to increase with increasing coke content. Most work done to date involves the study of only a single fluid (either polar or non-polar) in a pore filled state and do not provide any spatial information on pore characteristics apart from the imaging work done by Stapf et al. (2005) and Cheah et al. (1994). In this chapter, a liquid-liquid exchange (LLE) or displacement mechanism will be used to characterise a simple mesoporous sol-gel silica catalyst support and a bidisperse macro-mesoporous catalyst. The catalysts will be studied in its fresh state and following

155

reaction. The technique will provide spatial information that is of significant importance to catalyst structural design.

5.3 MATERIALS AND METHODS

The two materials studied in this work are commercially available sol-gel silica spheres G1 (2-4 mm dia), and Pt/Al_2O_3 cylindrical catalyst pellets Pt-E1 (3 mm dia. and 3.5 mm long). Material G1 has a uni-modal system with most pores centred at ~10 nm and material Pt-E1 has a bidisperse macro-mesoporous structure with 0.5 wt-% Pt loading and modal pore sizes at ~1 μm and ~8 nm. The LLE technique was applied to fresh and coked Pt-E1 catalysts. Coked Pt-E1 catalysts were obtained after performing the supercritical isomerisation of 1-hexene in a fixed bed reactor. The reaction was carried out under a constant liquid flow rate of 1.5 mlmin^{-1}. Two conditions are investigated as shown by the circled crosses in Fig. 5.7. The conditions denoted ISO_014 and ISO_008 represent the supercritical isomerisation of 1-hexene for 2 h at 235 °C and 4 MPa (40 bar), and for 8 h at 270 °C and 4 MPa (40 bar). Further details regarding the reaction can be found in Wang et al. (2009).

The nitrogen adsorption Gurvitsch pore volumes for fresh G1 and fresh Pt-E1 are 1 cm^{3}g^{-1} and 0.233 cm^{3}g^{-1} respectively while the BET surface areas for the same materials are 425 m^{2}g^{-1} and 109 m^{2}g^{-1} respectively. Each sample was initially dried under vacuum at 423 K for ~12 h, and for the coadsorption experiment, at time $t = 0$, suspended in a vial above separate reservoirs containing cyclohexane[30] and water[31] as seen in Fig. 5.8. This setup was then sealed using parafilm and insulation tape, and immersed in a water bath maintained at 298 K. After the method was developed with model sol-gel silica spheres, it was improved by exposing material Pt-E1 (and their coked counterparts) initially to only cyclohexane vapours. Once Pt-E1 (or their coked counterparts) was pore-filled with cyclohexane, a separate water reservoir was introduced into the vial containing cyclohexane. Thus, a water-cyclohexane displacement or exchange process was initiated. Periodically, prior to NMR relaxometry and diffusion experiments, the sample was transferred from the vial to a 5 mm NMR tube. The NMR tube contained a cyclohexane reservoir at the bottom and a water wet tissue at the top, ensuring that the sample experienced the same atmosphere as in the vial (see Fig. 5.8). A glass spacer was added such that there was no direct contact between the cyclohexane reservoir and the sample. The cyclohexane

---

[30] ACS reagent grade ($\geq$ 99%) cyclohexane used for the LLE experiments was sourced from Sigma Aldrich.
[31] Ultrapure water having a resistivity of 18.2 MΩ-cm was used for the LLE experiments.

present in the reservoir also did not give a detectable NMR signal. Susceptibility plugs were used to reduce the effect of the magnetic field distortions. The duration of NMR measurements was very short compared to the overall timescale of the LLE processes.

NMR relaxometry and diffusion experiments were performed, at 298 K, on a Bruker Avance spectrometer with static field strength of 9.4 T, corresponding to a resonance frequency of 400 MHz for ^{1}H nuclei. Proton intensities were also obtained using a simple spin-echo sequence before and after relaxation or diffusion experiments. T_2 relaxation time experiments were performed using a CPMG (Carr-Purcell-Meiboom-Gill) pulse sequence. The echo times used in the relaxation experiments were 0.0015 s for G1, and between 0.0002 and 0.0009 s for Pt-E1 (and its coked counterparts). All relaxation time experiments were conducted with at least 8 scans. Diffusion experiments were performed using a stimulated echo pulse sequence with bipolar gradient pulses for different diffusion times, Δ = 0.025 to 0.075 s for G1, and Δ = 0.025 to 0.3 s for Pt-E1 (and its coked counterpart). The gradient duration time δ was set to 2000 μs and the delay for gradient recovery τ was set to 100 μs. The field gradient strength was varied between 0.698 and 33.14 Gcm^{-1} using at least 8 steps. All diffusion experiments were conducted with at least 8 scans. The recycle time was selected as 5 s for G1 and 10 s for Pt-E1 (and it coked counterparts) as determined from the respective T_1 relaxation times. The data obtained were then analysed to determine the variation in T_2 relaxation times and diffusion coefficients as the LLE progressed. The recording, Fourier transformation and analysis were done using TOPSPIN 2.1.
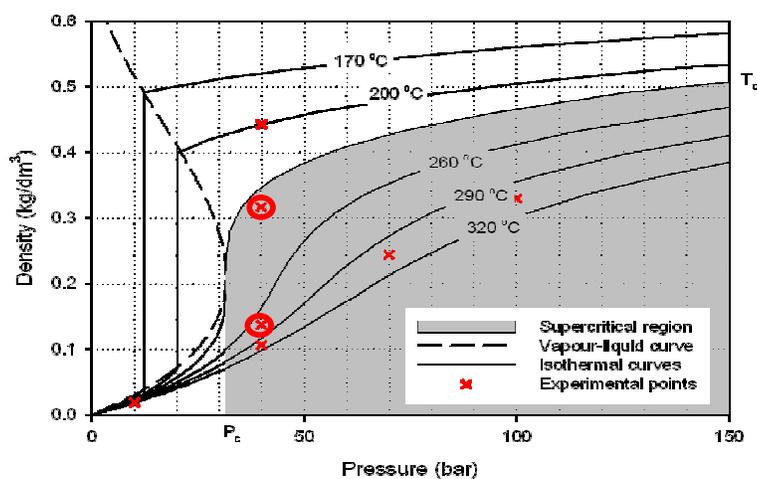
Fig. 5.7. Conditions under which the supercritical reaction was performed. The circled crosses represent the conditions under which Pt-E1 catalysts underwent reaction and were also studied by LLE. The figure was adapted from Wang et al. (2009).
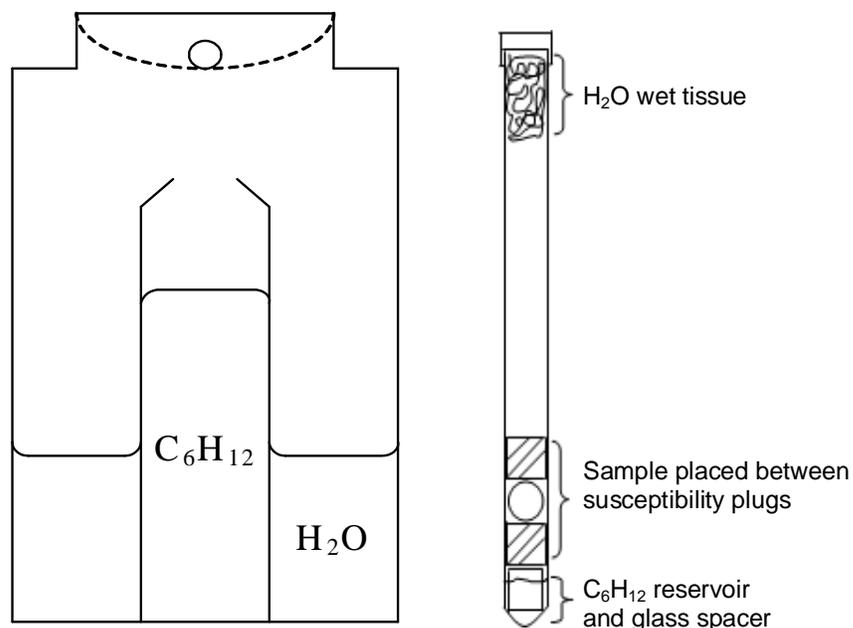
Fig. 5.8. Experimental set up for the coadsorption of cyclohexane and water on the different materials studied.

5.4 RESULTS

5.4.1 MATERIAL G1

The pore filling of uni-modal material G1 with cyclohexane was tested gravimetrically and by checking the T_2 relaxation times at 298 K. As the pore volume of material G1 (~1 cm^{3}g^{-1}) was known independently from traditional methods, namely, nitrogen gas adsorption porosimetry and mercury porosimetry (see Fig. 5.10), only the weight of the dried sample and its weight after exposure to cyclohexane vapours at different times was required (see Table 5.1). This helped to calculate the density of condensed cyclohexane confined within material G1. The density obtained (0.668 gcm^{-3}) was similar to values present in the literature (0.773 gcm^{-3} at 298 K) (Yaws, 2003). The little difference can be attributed to the evaporation of cyclohexane during its transfer from the vial into the NMR tube and vice versa. T_2 relaxation times for cyclohexane in material G1 remained the same for more than a day as seen in Table 5.1. This indicated that G1 was completely pore filled by cyclohexane when exposed to a cyclohexane atmosphere within a couple of hours. The test also helped to ensure that the sample experienced the same environment within the NMR tube as in the vial.

Table 5.1
Gravimetric analysis of the filling of cyclohexane within material G1.

Weight (g)	Cumulative Time (h)	T_2 (s)
0.0121	0	
0.02	2:13:04	0.23
0.0193	18:04:54	0.21
0.0203	25:45:16	0.23
0.0208	42:56:29	0.25
0.0205	51:48:38	0.24

Average weight of all measurements after time $t = 0$ is 0.0202g

Average T_2 of all measurements after time $t = 0$ is 0.23s

The trends of the ^{1}H NMR intensities of water and cyclohexane during a typical LLE experiment within material G1 are illustrated in Fig. 5.9. As can be seen in the figure, the sample is initially pore filled with cyclohexane. This happens quickly due to the high vapour pressure of cyclohexane relative to water[32].
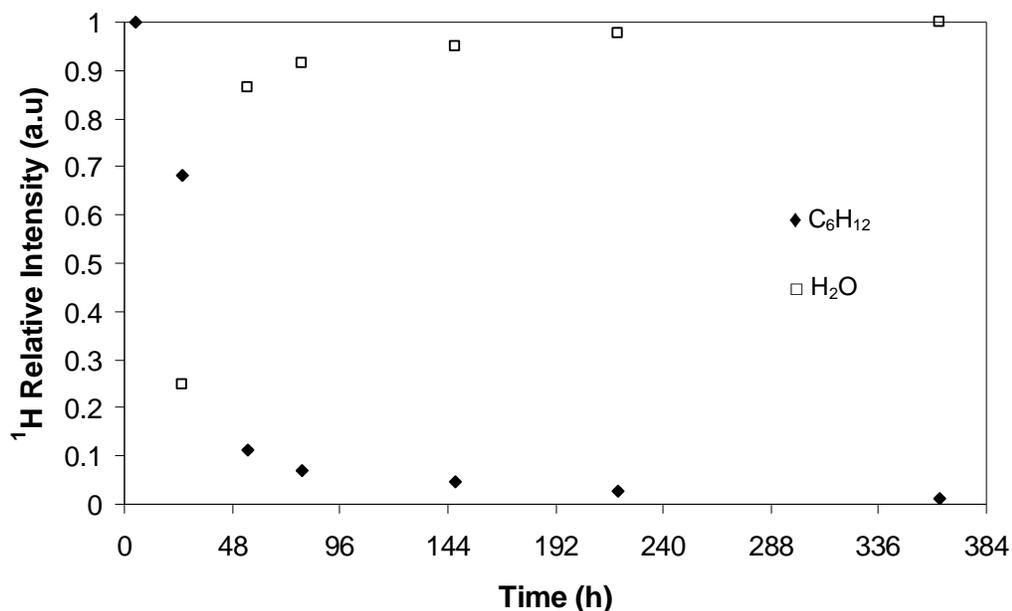
Fig. 5.9. Variation of proton intensities for cyclohexane and water in material G1 against experimental time.

However, as time passes, the cyclohexane content in the sample falls at a high rate initially and then decreases gradually. This occurs due to its displacement by water. The water saturation rises quickly initially and then gradually displaces most of the cyclohexane present in the material. Further, at ~78 h, the cyclohexane content

---

[32] The vapour pressure of cyclohexane and water are 12.96 kPa and 3.142 kPa respectively at 298 K (Rowley et al., 2007a, cited by Perry and Green 2008, p.2-56 and p.2-60)

within the material is ~7%. This is similar to mercury entrapment values (~10-12%) obtained for material G1 as seen in Fig. 5.10.
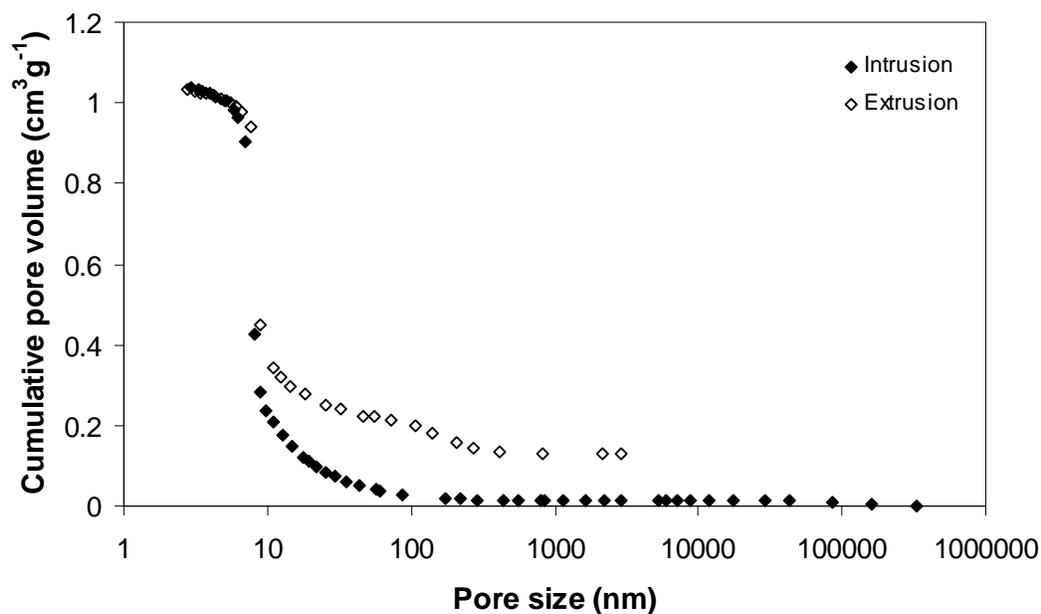
Fig. 5.10. Mercury porosimetry data for material G1. Equilibration time was 5 s.

T_2 relaxation times and diffusion coefficients for water and cyclohexane were also determined when the ^{1}H NMR signal intensities of the two liquids were obtained. This helped to determine the size and location of cyclohexane ganglia, the displacement mechanism and the variation of tortuosity τ with time within material G1. The variation in the T_2 relaxation time of the two liquids during the same experiment can be seen in Fig. 5.11. Once again, it is seen that the T_2 relaxation times for the two liquids follow a similar trend to that shown earlier in Fig. 5.9 for ^{1}H NMR intensities.

It is found that the T_2 relaxation time for the cyclohexane phase decreases sharply for the first ~48 h. At the same time period, the relaxation time for the water phase also increases sharply. After the first 48 h, the relaxation time for the cyclohexane phase remains unchanged for times greater than 240 h. However, the relaxation time for the water phase increases over this time interval. Since the T_2 relaxation time is proportional to the pore size (Eq. 5.8g), one can estimate the size of entrapped cyclohexane globules.
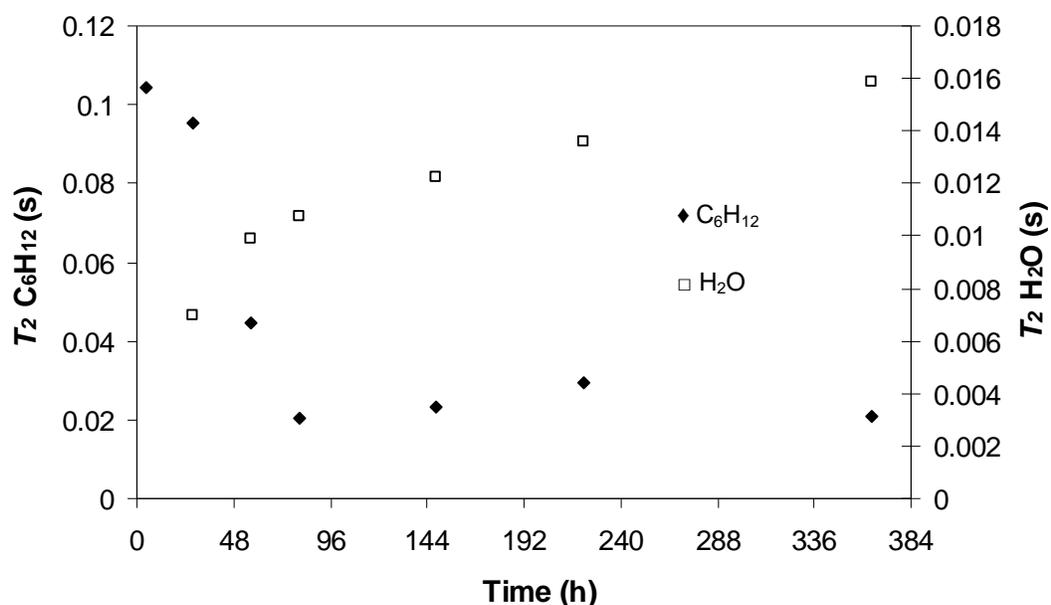
Fig. 5.11. Variation in the T_2 relaxation times of cyclohexane and water in material G1 as a function of the experimental duration.

It is independently known from gas adsorption and mercury porosimetry that all pores in this material are ~10 nm in size. When fully filled with cyclohexane, the T_2 relaxation time would be characteristic of this pore size. It can be seen from Fig. 5.11 that entrapped cyclohexane phase has lesser relaxation times. This is likely to mean that the entrapped cyclohexane ganglia are likely to be surrounded by water that wets the silica surface.

PFG NMR experiments conducted at different diffusion times allowed the observation of the change in tortuosities of the two liquids during the displacement experiment. For the diffusion times investigated (Δ = 0.025, 0.05 and 0.075 s), both liquids did not experience complete or partial restriction at any stage in the LLE experiment. The diffusion log attenuation plots at the 27 h time point were characterised by straight lines as shown in Fig. 5.12 for the cyclohexane phase and Fig. 5.13 for the water phase. Slopes of straight line fits yield their respective diffusion coefficients. Tables 5.2 and 5.3 present the diffusion coefficients and tortuosities for the cyclohexane and water phases obtained from Figs. 5.12 and 5.13 respectively. As seen in Tables 5.2 and 5.3, the diffusion coefficients in G1 are reduced relative to the bulk diffusion coefficient. There was only a slight variation in tortuosity of the two liquids with increase in diffusion time Δ, indicating little change in ganglia structure. As the experiment evolves, for Δ = 0.075 s, it is found that the tortuosity of the cyclohexane phase increases in the first 27 h. This is due to the ingress of the water phase into material G1 as seen in Fig. 5.14. More, importantly, the tortuosity of the

161

water phase is more than twice that of the cyclohexane phase at this point. Thereafter, the tortuosity of the water phase decreases (implying that the connectivity of the water phase increases) and becomes similar to that when the material is fully filled with water. It can be expected that the tortuosity of the cyclohexane phase would increase further during this time period since the cyclohexane phase would get more disconnected (as it gets displaced by the more connected water phase). However, it was not practical to measure this because of the very low signal and its rapid attenuation.
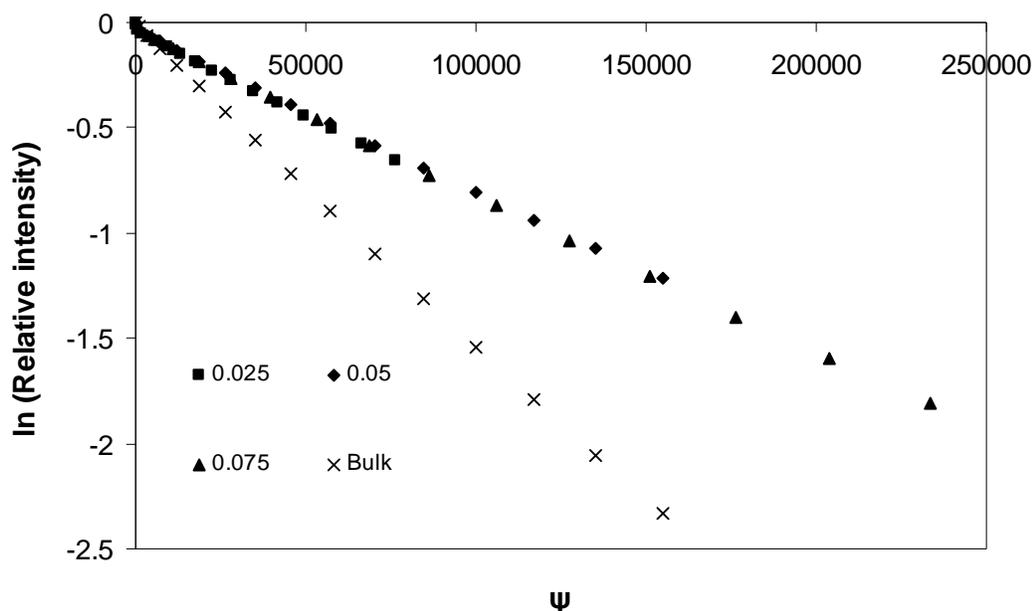
Fig. 5.12. NMR diffusion data for cyclohexane in material G1 for Δ = 0.025, 0.05 and 0.075 s. The result was obtained approximately 27 h after beginning the experiment. The straight line indicates that little restriction was detected by the cyclohexane phase within material G1 in this timescale. However, the diffusion coefficient of the cyclohexane phase was less than that in the bulk.

Table 5.2
Diffusion coefficients and tortuosities of the cyclohexane phase within material G1 for different values of the diffusion time Δ approximately 27 h after the start of the experiment.

Δ (s)	$D_p \times 10^{10}$ (m^{2}s^{-1})	$D_b \times 10^{9}$ (m^{2}s^{-1})	τ_{C6H12}
0.025	8.20(0.112)	1.511(0.007)	1.84(0.03)
0.05	7.70(0.056)		1.96(0.02)
0.075	7.68(0.058)		1.97(0.02)

( ) Errors are quoted in brackets.
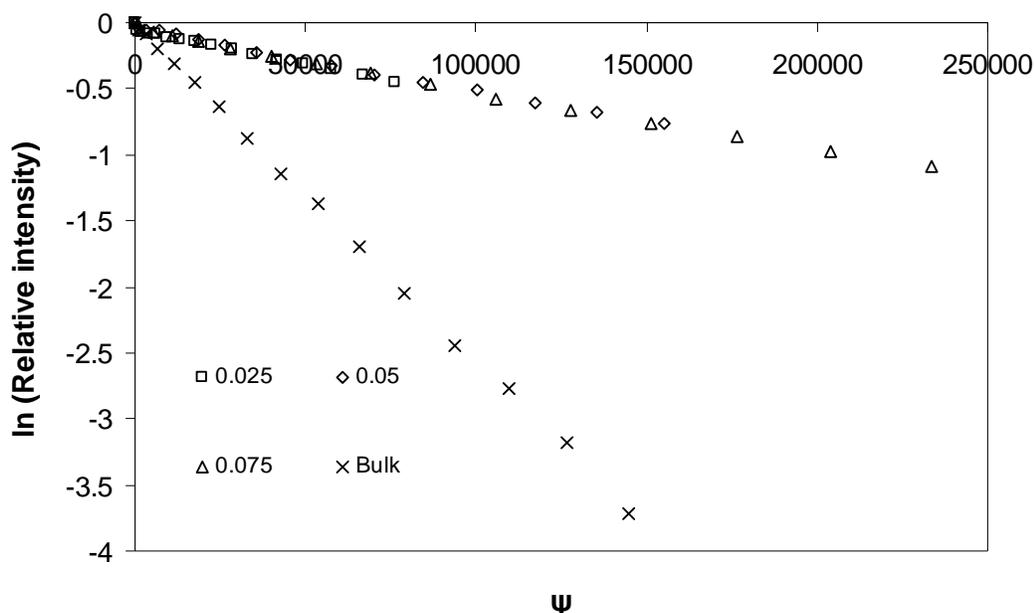
Fig. 5.13. NMR diffusion data for water in material G1 for Δ = 0.025, 0.05 and 0.075 s. The result was obtained approximately 27 h after beginning the experiment. The straight line indicates that little restriction was detected by the water phase within material G1 in this timescale. However, the diffusion coefficient of the water phase was less than that in the bulk.

Table 5.3
Diffusion coefficients and tortuosities of the water phase within material G1 for different values of the diffusion time Δ approximately 27 h after the start of the experiment.

Δ (s)	$D_p \times 10^{10}$ (m^{2}s^{-1})	$D_b \times 10^9$ (m^{2}s^{-1})	τ_{H2O}
0.025	5.26(0.158)	2.54(0.013)	4.82(0.15)
0.05	4.82(0.074)		5.26(0.08)
0.075	4.59(0.062)		5.59(0.08)

( ) Errors are quoted in brackets.
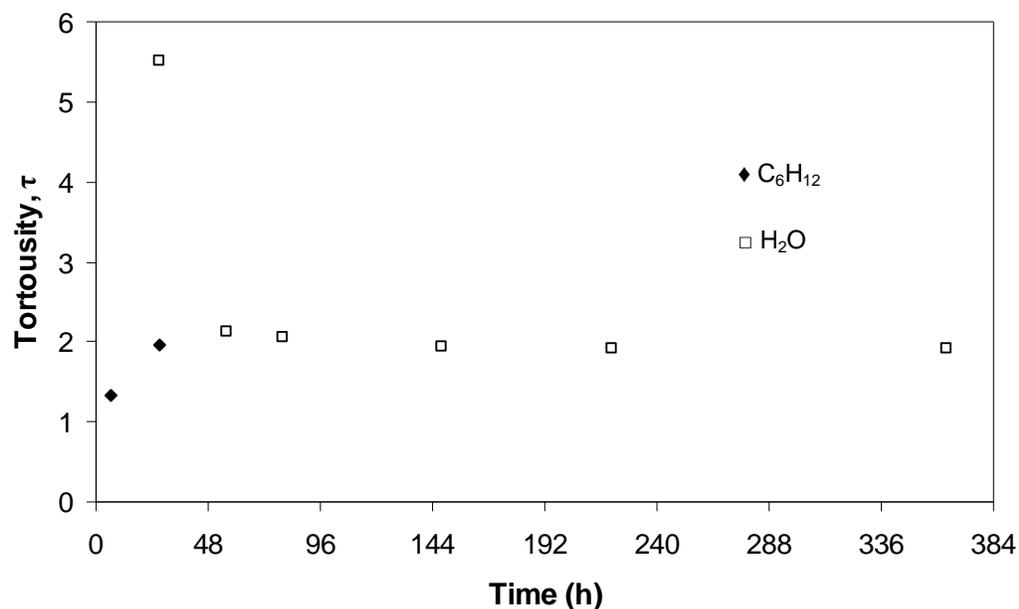
Fig. 5.14. Variation in tortuosity τ of cyclohexane and water phases (at Δ = 0.075 s) in material G1 with experimental time during the LLE process.

163

5.4.2 MATERIAL Pt-E1 (FRESH AND COKED)

Material G1 is a mono-modal catalyst support with a homogenous surface and served as a test bed to determine the characteristics of the LLE method. Pt/Al_2O_3 catalysts, i.e. material Pt-E1 in their fresh and coked forms were next studied by the same technique. Their characterisation results from mercury porosimetry and nitrogen gas adsorption are presented in Figs. 5.15, 5.16 and 5.17. From the nitrogen gas adsorption isotherms (Fig. 5.16) and BJH pore size distributions (Fig. 5.17), it was evident that coking resulted in a loss of the mesopores. However, no major change was visible in the shape of the hysteresis loop of the different isotherms. The isotherms were eye shaped and did not achieve complete saturation at high relative pressures. Hence, information regarding macropores was not available due to the absence of capillary condensation in these regions. These macropores can however be detected by mercury porosimetry as seen in Fig. 5.15. But, as mentioned in Section 5.2, coked catalysts cannot be accurately characterised using mercury porosimetry. In previous work done by Rigby et al. (2011), it was found from computerised X-ray tomography (CXT) images that most of the Pt metal crystallites were mainly located in the form of an annular region in the periphery of the catalyst pellet. This layer also caused the non-recoverability of mercury from these regions since mercury wetted the Pt layer (see Figs. 11, 12a and b, and 13a and b in Rigby et al. (2011)).
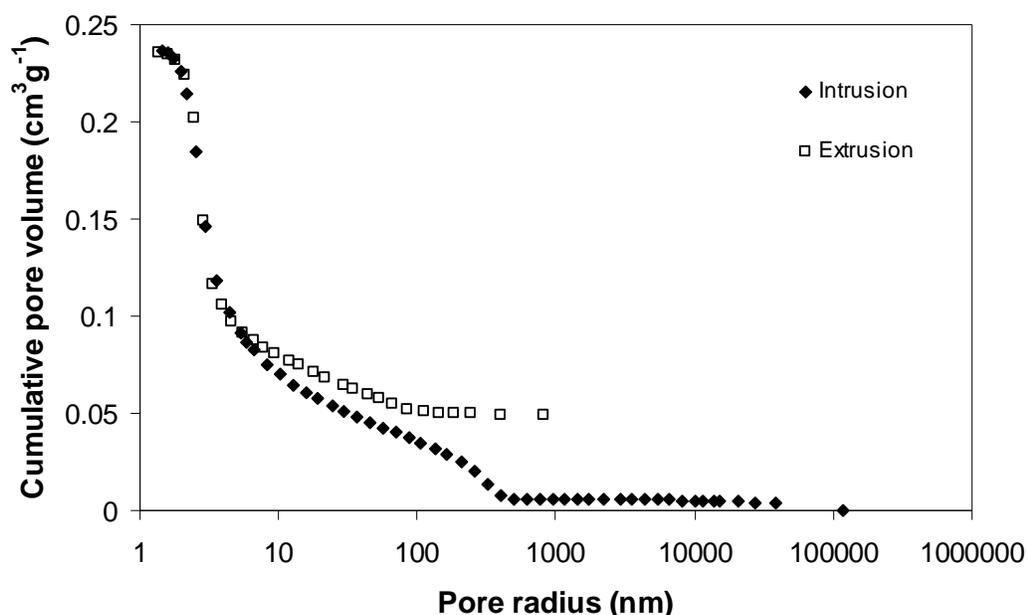
Fig. 5.15. Mercury porosimetry data for fresh Pt-E1 catalysts. Equilibration time was 10 s.
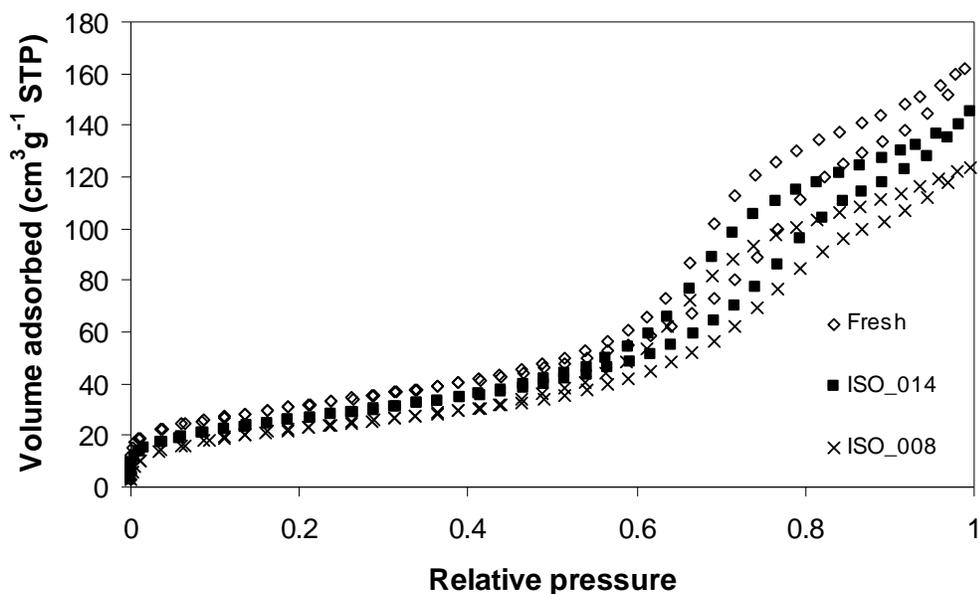
Fig. 5.16. Nitrogen gas adsorption isotherms for fresh and coked Pt-E1 catalysts obtained from runs conducted under different reaction conditions.
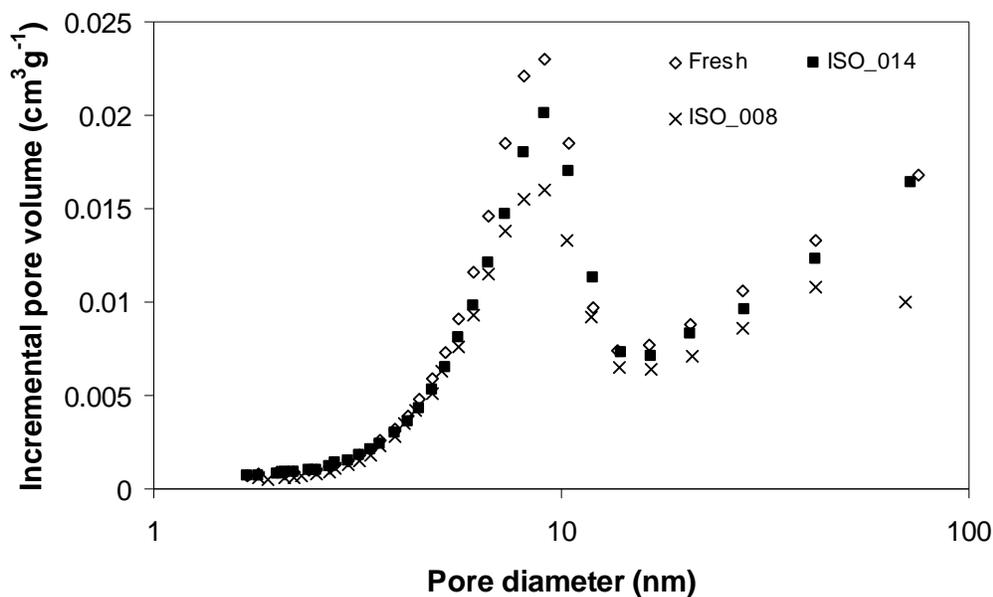
Fig. 5.17. BJH pore size distribution obtained from the nitrogen gas adsorption isotherms presented in Fig. 5.16.

On the other hand, LLE experiments provide a larger picture when the T_2 relaxation times of cyclohexane and water phases present in Pt-E1 catalysts are plotted against the water content within them. Water T_2 relaxation times are illustrated in Fig. 5.18 for a typical fresh and coked sample. As the displacement time of cyclohexane by water for fresh and coked samples are different, comparison between the two can only be achieved if both samples were based on a single

165

parameter. Water concentration within the catalyst pellet served as the abscissa since it grew with time or progress of the experiment. All further results in this section will be displayed in this manner. It can be seen that as the water content within the catalyst pellets increased from ~7% to 100%, the coked catalyst exhibited systematically larger water T_2 relaxation times than the fresh catalyst. A similar set of data for another fresh and coked sample from the same batch can be seen in Fig. 5.19.
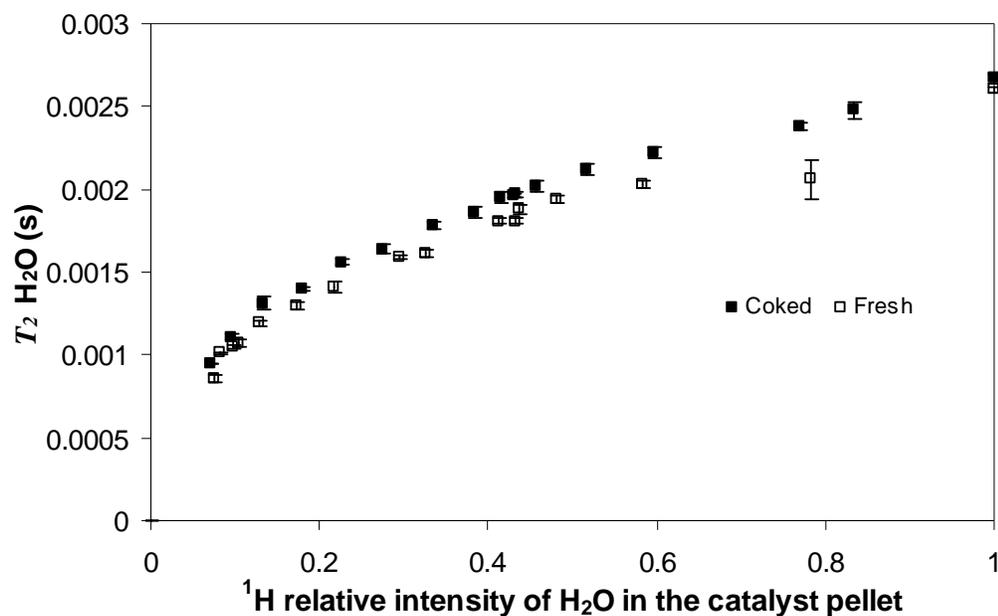
Fig. 5.18. Variation in the T_2 relaxation times of the water phase as a function of the water content within a fresh and coked catalyst Pt-E1 pellet. The coked catalyst was obtained under conditions denoted by ISO_014.

Figs. 5.18 and 5.19 clearly represent the repeatability of the experiments. Also, it is seen that the water T_2 relaxation times rises relatively quickly for the coked catalyst in Fig. 5.19. Each water T_2 relaxation time in Figs. 5.18 and 5.19 were defined by a mono-exponential decay equation. The water T_2 relaxation time constants were obtained by using the non-linear curve fitting program available in Origin 6.1 (see Appendix D for more details). An example of the raw water T_2 relaxometry data at 15% and 51% water content within a fresh and coked catalyst is presented in Fig. 5.20 and Table 5.4 presents the respective T_2 values.

Fig. 5.19. Variation in the T_2 relaxation times of the water phase as a function of the water content within another fresh and coked catalyst Pt-E1 pellet. The coked catalyst was obtained under conditions denoted by ISO_014.

Fig. 5.20. Raw T_2 relaxometry data obtained for the water phase in a fresh and coked catalyst Pt-E1 pellet (from Fig 5.19). Each experimental dataset was fitted by a mono-exponential decay model. The number within brackets in the legend indicates the water fraction within the catalyst pellet.

Table 5.4
Water T_2 relaxation times for a fresh and coked catalyst Pt-E1 pellet obtained from Fig. 5.20.

Water content within the catalysts pellet	T_2 H$_2$O (s) for Fresh Pt-E1	R^2	T_2 H$_2$O (s) for Coked Pt-E1	R^2
0.15	0.00106(6.60×10^{-6})	0.99999	0.0012(0.00003)	0.9999
0.51	0.00175(0.00002)	0.99996	0.00209(0.00002)	0.99998

( ) Errors are quoted in brackets.

The approach adopted to study the variation in water T_2 relaxation times as the experiment evolved was also used to study the cyclohexane T_2 relaxation times. Cyclohexane T_2 relaxation times were also plotted as a function of the water content within the catalyst pellet. Unlike the growth observed in the water T_2 relaxation times in fresh and coked catalysts, the variation in the cyclohexane T_2 relaxation times as seen in Fig. 5.21 are distinctly different. Fig. 5.21 corresponds to the results shown earlier for water in Fig. 5.18. It was seen that as the water content within the catalyst pellets increased from 30% to complete saturation, the cyclohexane T_2 relaxation times for the fresh catalyst were lower than the coked catalyst pellet. This agreed with the trend displayed by water T_2 relaxation times in the same range as given in Figs. 5.18 and 5.19. However, at low water contents (~0.1-0.25), it was found that there was a significant rise and fall in the cyclohexane T_2 values for the fresh sample. In Fig. 5.21, the cyclohexane T_2 relaxation times for the fresh catalyst increased from 0.00718 ± 0.00024 s at 0% water content to 0.00826 ± 0.00052 s at 17% water content before returning back to 0.0073 ± 0.00023 s at 21% water content. Thus, there was approximately a 15% increase in the cyclohexane T_2 value before falling back to the same level. Unlike the fresh sample, the coked catalyst pellet did not experience such a rise and fall in the cyclohexane T_2 relaxation times. The cyclohexane T_2 relaxation times of the coked catalyst pellet were fairly constant over this region and remained so up to a water fraction of ~0.3, before gradually falling of at higher water contents (~38-100% water content). It is this pattern that was found to be repeatable in other fresh and coked catalyst pellets from the same batch, i.e. there is an initial rise and fall in the cyclohexane T_2 relaxation times for fresh catalysts but none for coked catalysts. This is shown in Fig. 5.22 (for the same fresh and coked catalyst pellets as displayed in Fig. 5.19) and in Fig. 5.23.
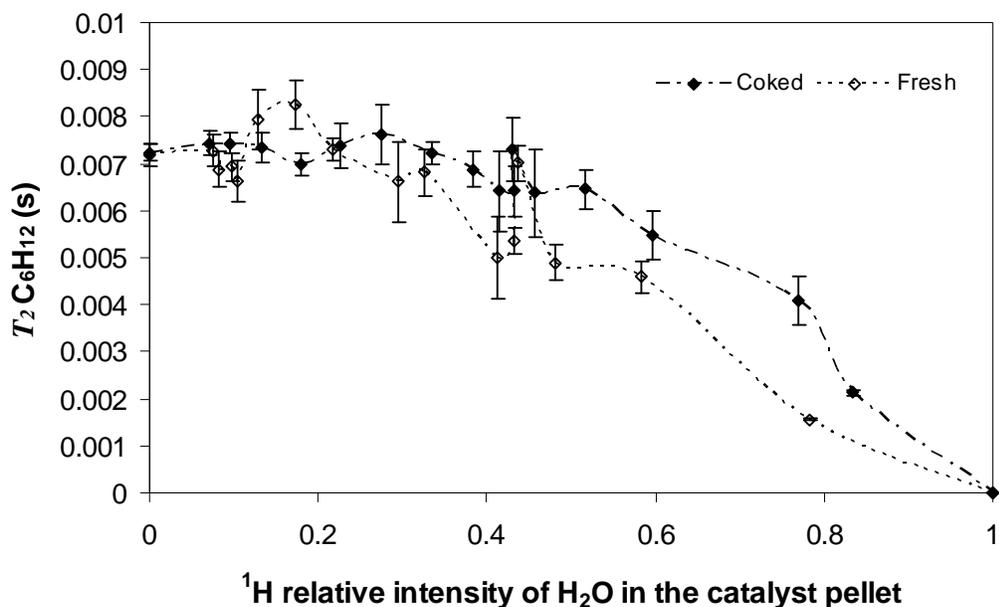
Fig. 5.21. Variation in the T_2 relaxation times of the cyclohexane phase as a function of the water content within a fresh and coked catalyst Pt-E1 pellet. The coked catalyst was obtained under conditions denoted by ISO_014.
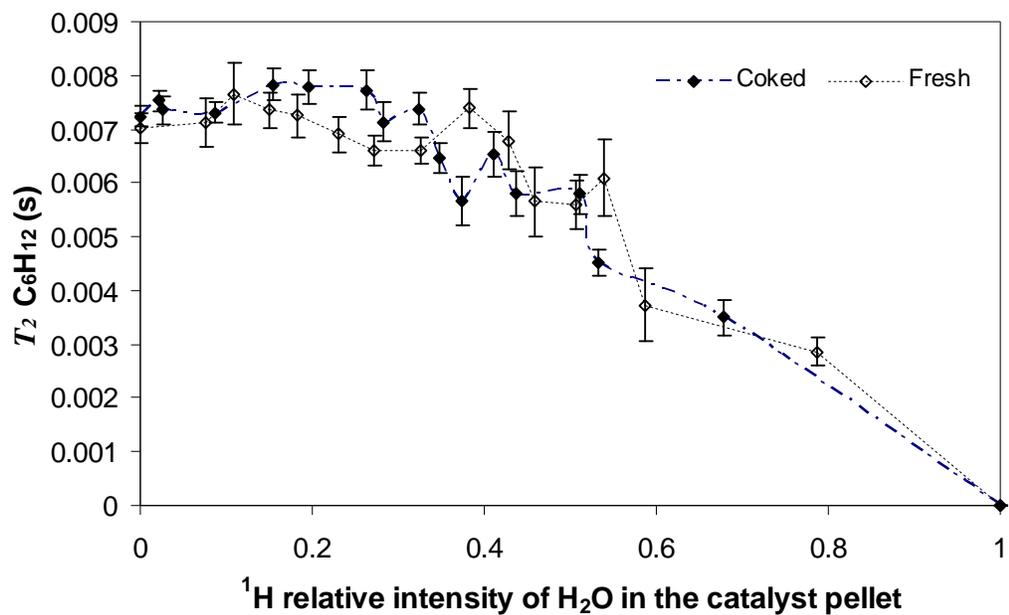
Fig. 5.22. Variation in the T_2 relaxation times of the cyclohexane phase as a function of the water content within another fresh and coked catalyst Pt-E1 pellet. The coked catalyst was obtained under conditions denoted by ISO_014.
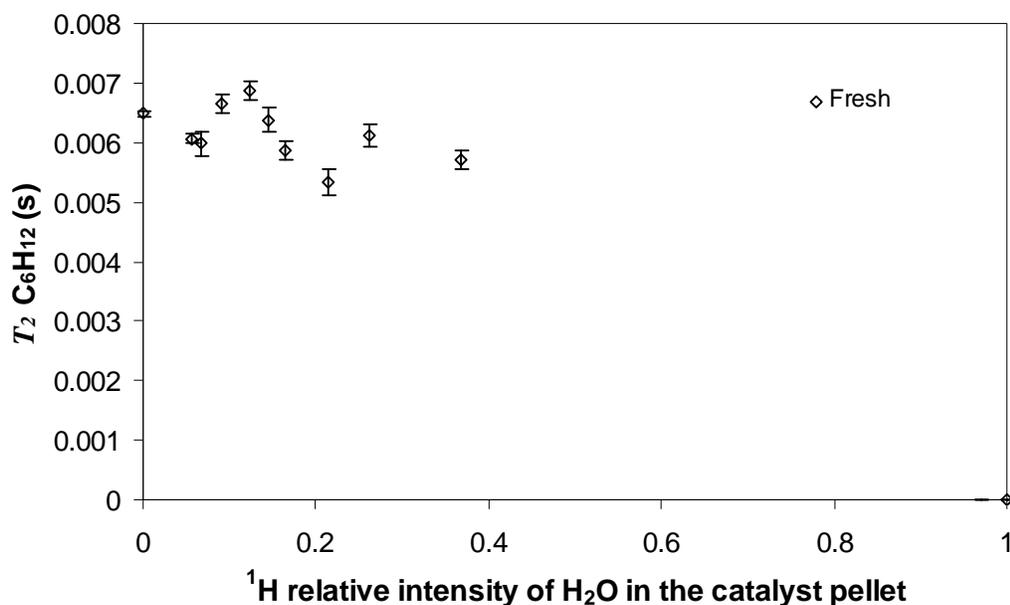
Fig. 5.23. Variation in the T_2 relaxation time of the cyclohexane phase as a function of the water content for another fresh catalyst Pt-E1 pellet. The initial rise and fall can be seen at low water contents.

The reader may argue that there is very little rise and fall, or even no rise and fall in the cyclohexane T_2 data displayed in Fig. 5.22. In this case, the reader is directed to Fig. 5.23, where as suggested, at low water contents there is clear evidence of a rise and fall in cyclohexane T_2 relaxation times. To back this observation, further analysis was done by completing straight line linear regression analysis of the different data sets of cyclohexane T_2 values for fresh and coked catalysts at water contents in the range from 0-0.3. The constructed residual plots are shown in Fig. 5.24 and Fig. 5.25 for the fresh and coked samples respectively. Considering the residual plots for the fresh samples, it can be seen that the signs of the residual vary in a manner such that they are generally negative at first, then positive and then negative again. Further, it is also noted that the spread in residual values for the fresh catalyst is larger than that for coked samples. The standard deviations for the different sets of catalysts are presented in Table 5.5.

Table 5.5
Standard deviation for fresh and coked Pt-E1 catalysts obtained from linear regression fits to the cyclohexane T_2 relaxation times at water fractions between 0 and 0.3.

Catalyst	Standard deviation σ
Fresh	0.062204
Coked/ISO_014	0.030778
Coked/ISO_008	0.035345
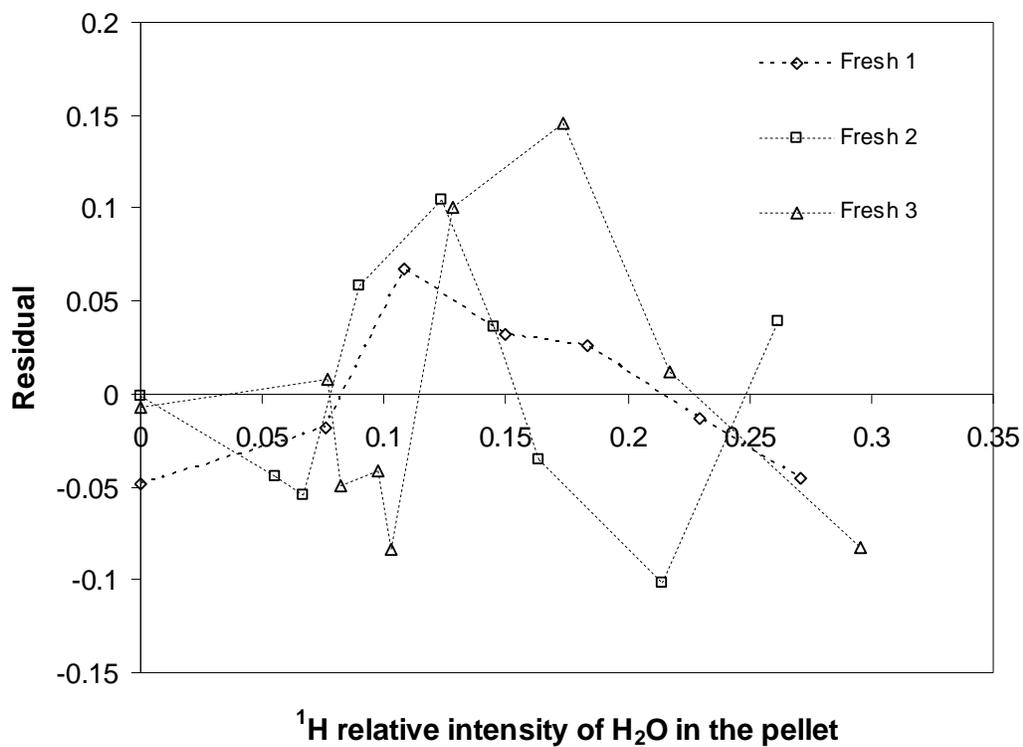
Fig. 5.24. Residuals obtained for cyclohexane T_2 relaxation times at low water contents for fresh Pt-E1 catalysts.
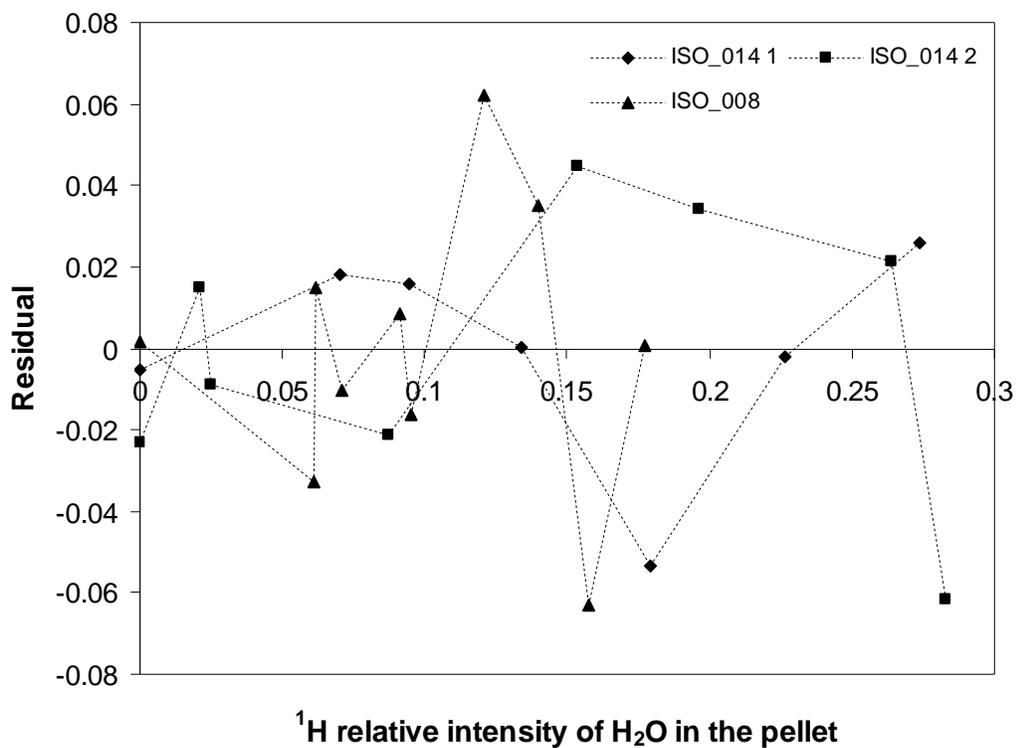
Fig. 5.25. Residuals obtained for cyclohexane T_2 relaxation times at low water contents for coked Pt-E1 catalysts.

At intermediate water contents (~0.3-0.5), it can be seen that the cyclohexane T_2 values for coked catalysts are higher than that observed for fresh catalysts in Fig. 5.21 agreeing well with trend observed for water T_2 relaxation times. A peak in T_2 values is seen when the water fraction is between 0.4 and 0.5 in Fig. 5.21 and in Fig. 5.22 (though slightly shifted to lower water contents). At higher water contents, the trend of higher cyclohexane T_2 relaxation times for coked catalysts continues in Fig. 5.21. Thus, the second peak was found to be common to the fresh and coked catalysts tested.

Each cyclohexane T_2 relaxation time in Figs. 5.21, 5.22 and 5.23 were defined by a mono-exponential decay equation (just as for water). The cyclohexane T_2 relaxation time constants were obtained by using the non-linear curve fitting program available in Origin 6.1 (see Appendix D for more details). An example of the raw cyclohexane T_2 relaxometry data at 15% and 51% water content within a fresh and coked catalyst is presented in Fig. 5.26 and Table 5.6 presents the respective T_2 values.
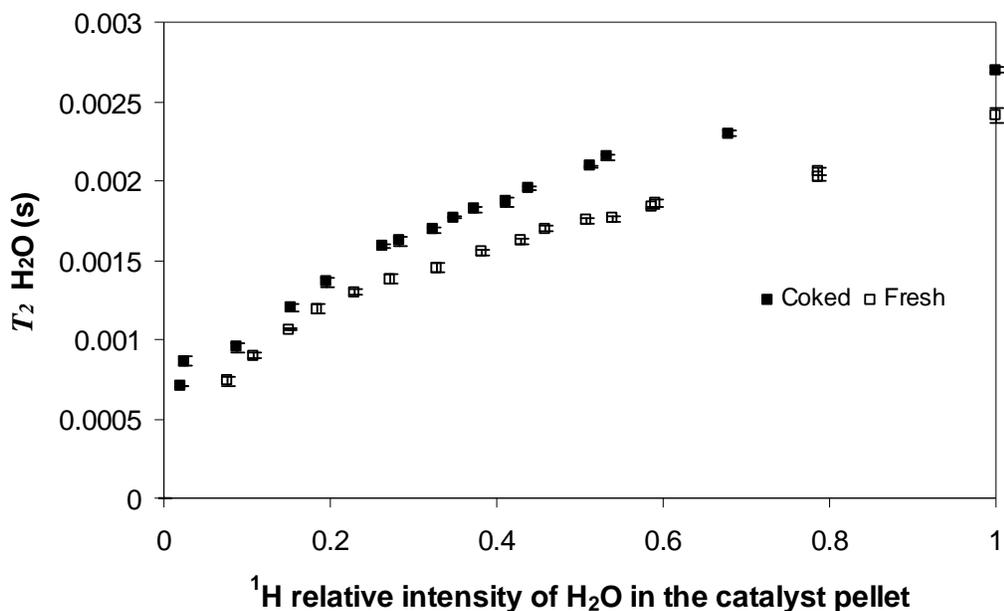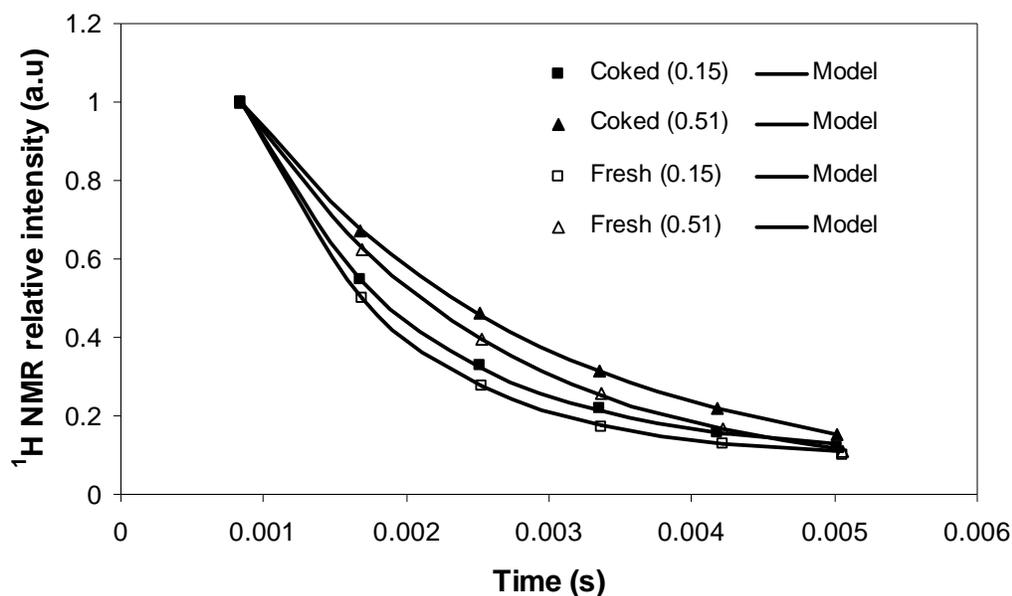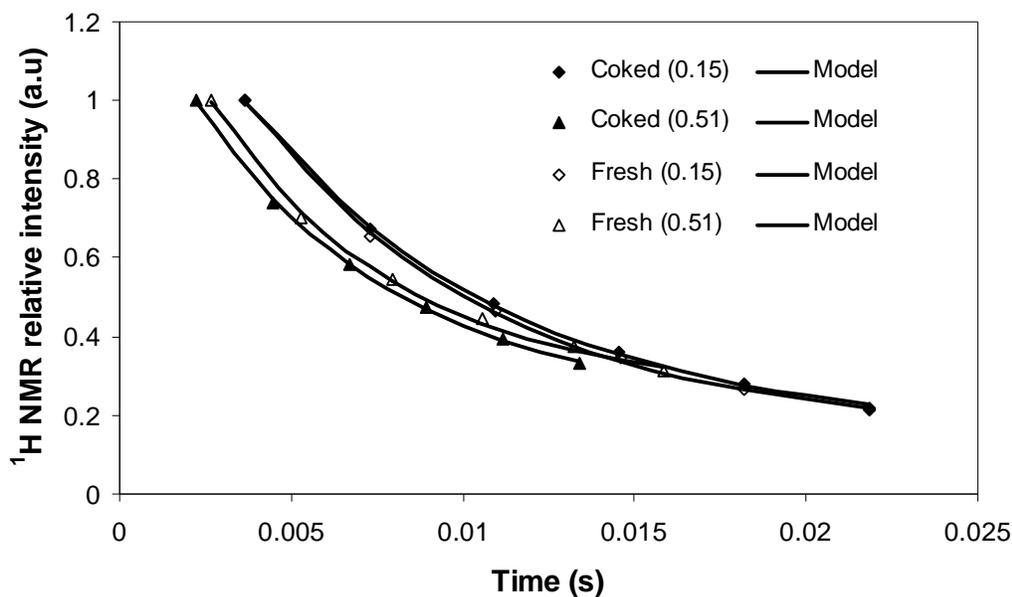

Fig. 5.26. Raw T_2 relaxometry data obtained for the cyclohexane phase in a fresh and coked catalyst Pt-E1 pellet from Fig. 5.21. Each experimental dataset was fitted by a mono-exponential decay model. The number within brackets in the legend indicates the water fraction within the catalyst pellet.

Table 5.6
Cyclohexane T_2 relaxation times for a fresh and coked catalyst Pt-E1 pellet obtained from Fig. 5.21.

Water content within the catalyst pellet	T_2 C_6H_{12} (s) for Fresh Pt-E1	R^2	T_2 C_6H_{12} (s) for Coked Pt-E1	R^2
0.15	0.00735(0.00033)	0.99948	0.00783(0.0003)	0.99965
0.51	0.00559(0.00045)	0.99841	0.00579(0.00036)	0.9993

( ) Errors are quoted in brackets.

As with material G1, PFG NMR enabled the study of the entrapment mechanism of cyclohexane within fresh and coked Pt-E1 catalysts. Along with the variation in cyclohexane and water T_2 relaxation times as reported earlier, shown in Fig. 5.27 is another set where periodic PFG NMR experiments were also performed. There was a 10% increase in cyclohexane T_2 values as water fraction within the catalyst pellet increased from 0-0.56. At this point, PFG NMR experiments were performed and they revealed data shown in Fig. 5.28. As the data shown in Fig. 5.28 did not show a straight line relationship between ln (^{1}H NMR relative intensity) and Ψ, the data was fitted to a two-component diffusion model (Eq. 5.14b), as shown in Fig. 5.29. The fitting was done using the non-linear curve fitting program available in Origin 6.1. The residual of the fits are provided in Fig. 5.30. Tables 5.7 and 5.8 respectively contain the results obtained from the bi-exponential fits to the cyclohexane diffusion data for fresh and coked Pt-E1 catalysts when the diffusion time Δ was changed from 0.05 to 0.1 s.
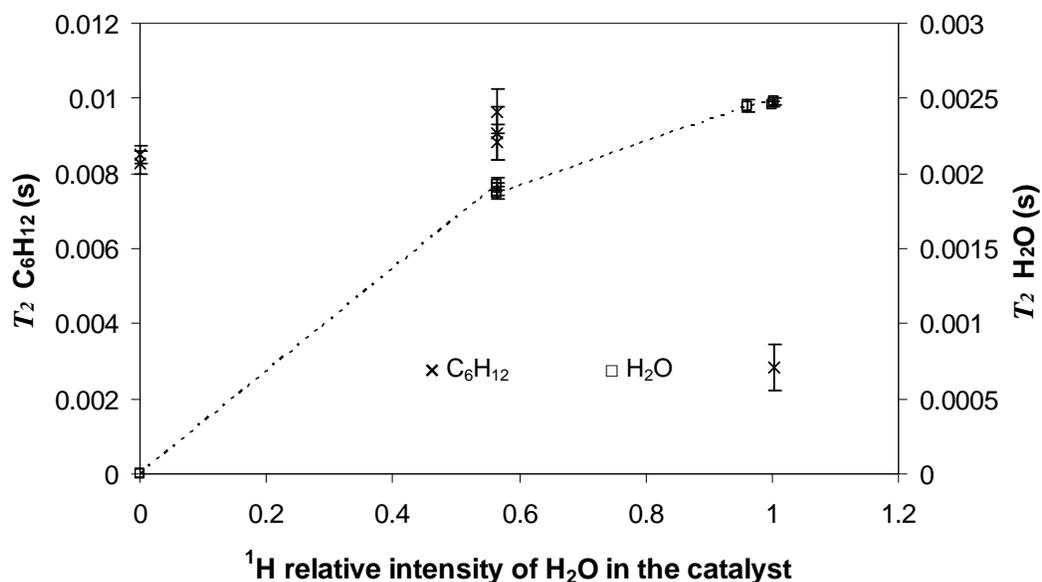
Fig. 5.27. Variation of cyclohexane and water T_2 relaxation times for another fresh Pt-E1 catalyst where periodic diffusion experiments were performed.
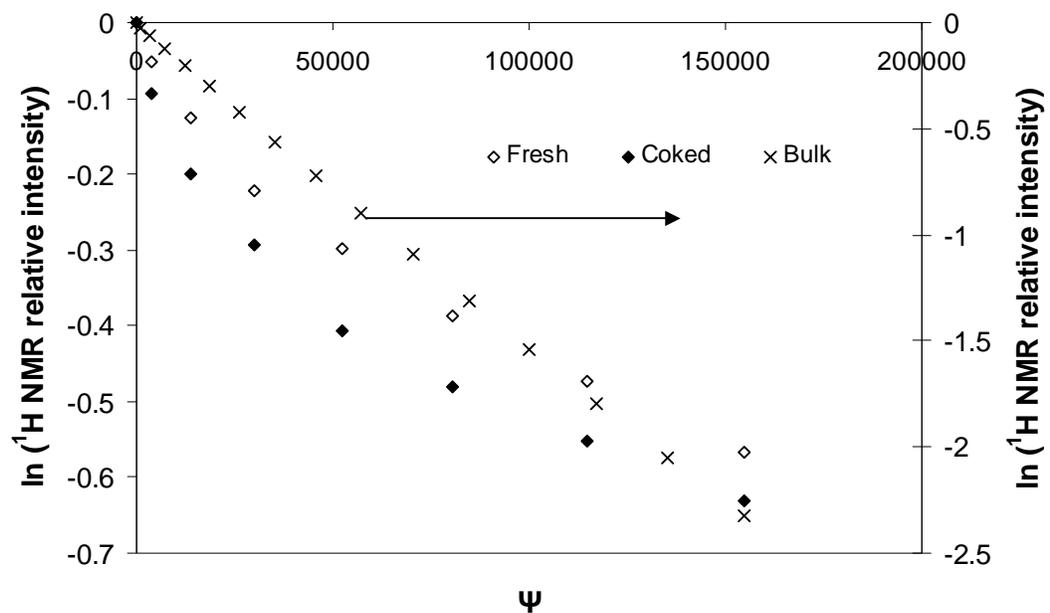
Fig. 5.28. Raw cyclohexane diffusion data for fresh and coked catalyst Pt-E1 pellet when the water fraction within the catalyst was 0.56. The bulk cyclohexane diffusion data has been shown for reference.
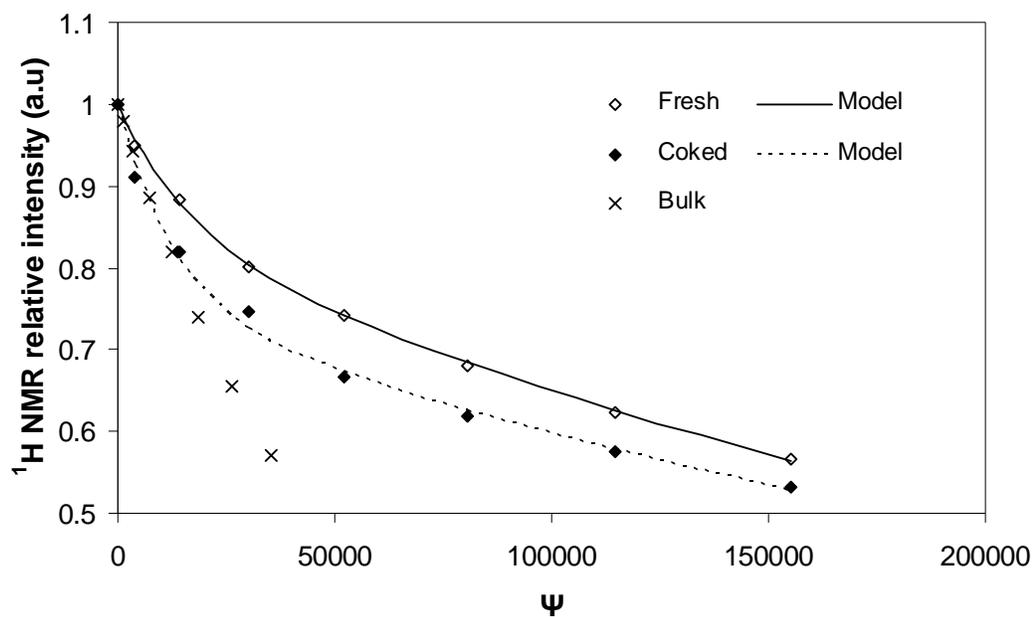
Fig. 5.29. Raw cyclohexane diffusion data with the respective bi-exponential fits for fresh and coked catalyst Pt-E1 pellet when the water fraction within the catalyst was 0.56. The bulk cyclohexane diffusion data has been shown for reference.

174
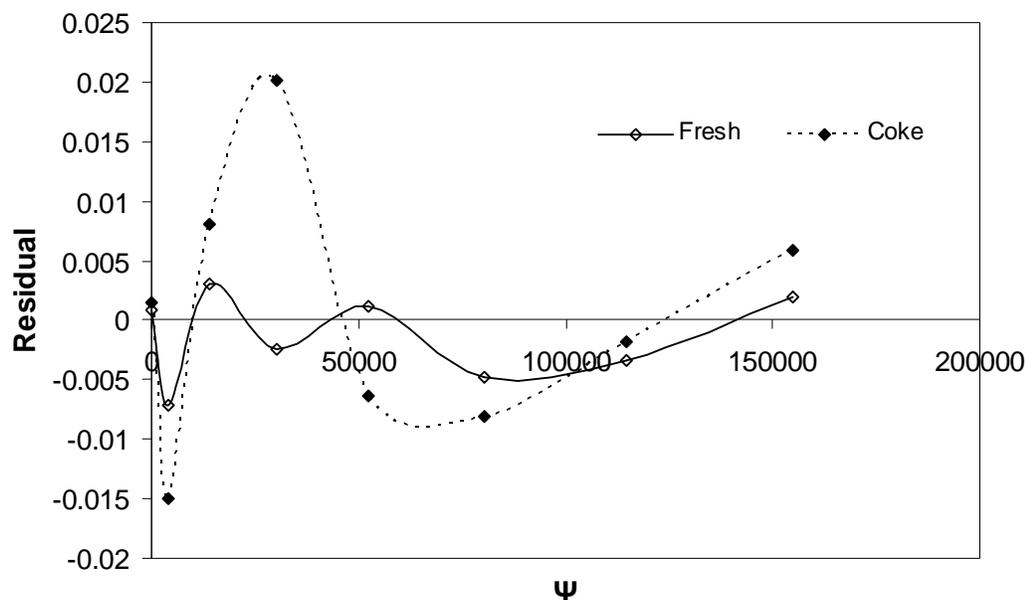
Fig. 5.30. Residuals of the bi-exponential fits presented in Fig. 5.29. The standard deviations for the fresh and coked catalyst are 0.003657 and 0.0121 respectively.

Table 5.7
Results obtained from bi-exponential fits to experimental cyclohexane diffusion data for a fresh catalyst Pt-E1 pellet when the diffusion time Δ was changed from 0.05 to 0.3 s.

Δ (s)	p	$D_a C_6H_{12} \times 10^{10}$ (m^2s^{-1})	$D_b C_6H_{12} \times 10^{9}$ (m^2s^{-1})	τ_a	τ_b	R^2	Water content
0.05	0.84(0.01)	2.56(0.12)	6(0.7)	5.90(0.27)	0.25(0.03)	0.99938	0.56
0.1	0.67(0.02)	1.71(0.14)	3(0.3)	8.86(0.74)	0.5(0.05)	0.99908	0.56
0.2	0.43(0.02)	0.78(0.09)	1(0.07)	19.28(2.28)	1.51(0.11)	0.99958	0.56
0.3	0.35(0.03)	0.67(0.15)	1(0.14)	22.48(5.18)	1.51(0.21)	0.99762	0.56

( ) Errors are quoted in brackets.

Table 5.8
Results obtained from bi-exponential fits to experimental cyclohexane diffusion data for a coked catalyst Pt-E1 pellet when the diffusion time Δ was 0.05 and 0.1 s. The coked catalyst was obtained under conditions denoted by ISO_014.

Δ (s)	p	$D_a C_6H_{12} \times 10^{10}$ (m^2s^{-1})	$D_b C_6H_{12} \times 10^{9}$ (m^2s^{-1})	τ_a	τ_b	R^2	Water content
0.05	0.76(0.02)	2.38(0.3)	8(1)	6.50(0.83)	0.19(0.02)	0.9959	0.56
0.1	0.60(0.03)	1.17(0.20)	4(0.51)	12.9(2.2)	0.38(0.05)	0.99661	0.56

( ) Errors are quoted in brackets.

Both, Figs. 5.28 and 5.29 also show the experimental diffusion data for bulk liquid cyclohexane at 298 K for reference. The difference between bulk diffusion and pore diffusion was clearly evident. While bulk liquid cyclohexane diffusion revealed a straight line plot in Fig. 5.28, cyclohexane diffusion within the catalyst pores was non-linear. This was preliminary evidence for cyclohexane molecules detecting some

175

restrictions or boundaries during diffusion within pores of the catalysts. Further analysis was completed by interpreting the obtained results in the form of Fig. 5.31, where the product of the apparent cyclohexane diffusivity and diffusion time ($D\Delta$) was plotted as a function of the diffusion time Δ. $D\Delta$ was found to be approximately constant as the diffusion time Δ was varied from 0.05-0.3 s. This indicated evidence of restricted diffusion. Restricted diffusion can also be seen in Tables 5.7 and 5.8 where there is a doubling of tortuosity τ of the cyclohexane phase with a doubling in diffusion time Δ (see Section 5.1.2 for more details on restricted diffusion). The major component was the slower component and had a volume fraction that varied from ~84-35% as the diffusion time increased from ~0.05-0.3 s in the fresh catalyst. Using the restricted diffusion model in a spherical cavity given by Eq. (5.13), the typical cavity radius $\mathfrak{R}$ was found to be 8.8 ± 0.4 μm. This is consistent with observation from Fig. 5.31, where there was a transition to a horizontal plateau between diffusion times of ~0.025-0.05 s and lasted even when the diffusion time was 0.3 s. The rms displacement over this time period increased from ~6 μm to ~10 μm. However, for the coked catalyst, though cyclohexane diffusion was restricted at the same water content, the corresponding cavity size was 7.6 ± 0.03 μm for diffusion times 0.05-0.1s. Table 5.9 lists the cavity radii $\mathfrak{R}$ obtained for fresh and coked Pt-E1 catalysts. Thus, from Table 5.9, coking leads to statistically significant decrease in the apparent cavity size of cyclohexane ganglia.
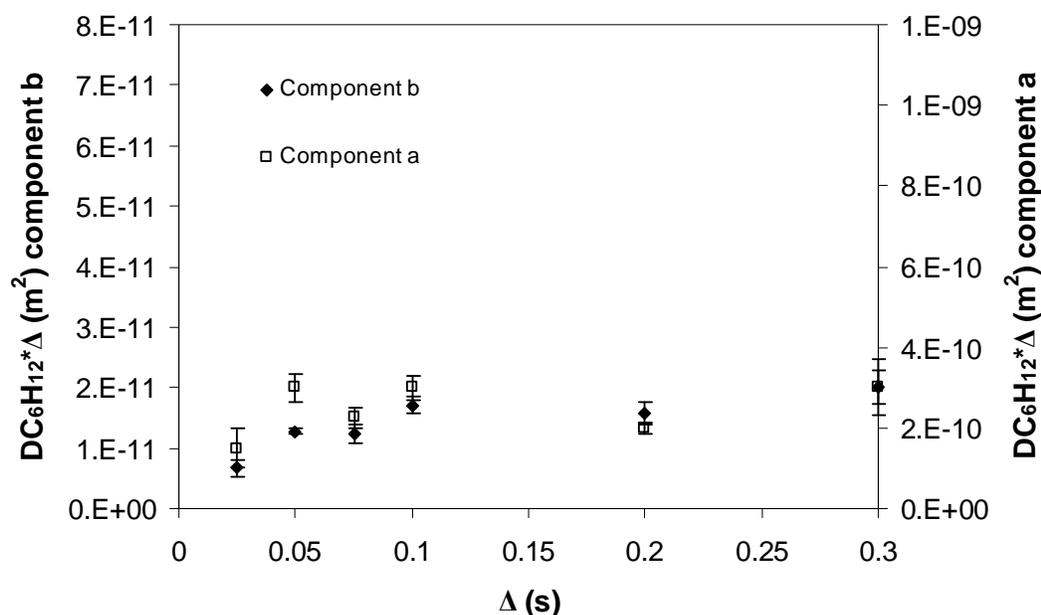
Fig. 5.31. The product of cyclohexane diffusion coefficient and diffusion time ($DC_6H_{12}\Delta$) is plotted against the diffusion time Δ when ~56% of the catalyst pore space is occupied by water.

Table 5.9
Cavity radius obtained for fresh and coked Pt-E1 catalysts according to the restricted diffusion model given by Eq. (5.13).

Catalyst Pt-E1	Δ (s)	$\Re$ (µm)
Fresh	0.1	9.2(0.4)
Coked	0.1	7.6(0.6)

( ) Errors are quoted in brackets.

5.5 DISCUSSION

The gravimetric analysis performed for material G1 showed that cyclohexane pore-filled the material. It is the high vapour pressure of cyclohexane that ensured material G1 was rapidly filled with cyclohexane initially which then undergoes gradual displacement by water. Water wets the surface of the silica material and has a far stronger affinity than cyclohexane due to the presence of hydroxyl groups on the silica surface. The presence of water allows hydrogen bonding to take place (Scott, 1980) which paves the way for more water to seep in and displace the cyclohexane confined within the material. Unlike water, cyclohexane only forms a few hydrogen bonds. Hence, cyclohexane will pore-fill the sample initially, but will have less affinity for the silica surface compared to water. It can be expected that the opposite will be true for carbonised surfaces (as is evident from the work of Mattia et al. (2006) where they found that the contact angle for water (79°) on carbon films was greater than that of non-polar liquids like cyclohexane (10°)[33]).

For the model material G1, the non-linear change in T_2 relaxation times and the variability found in tortuosity values during the LLE experiment indicate the presence of conditions similar to capillary flow where the boundary between cyclohexane and water moves down a pore just as the movement of a piston in a pump. For material G1, as seen in Fig. 5.14, initially the tortuosity of the water phase increased to more than twice that of the cyclohexane phase. This indicated the presence of highly disconnected globules of water trying to imbibe from different regions of the material, while major portions of the cyclohexane phase remained connected. Later, the connectivity of the water phase grows and becomes similar to that for a material completely filled with water. This must cause the connectivity of the cyclohexane phase to diminish (or the tortuosity of the cyclohexane phase increases). The similarity in the entrapment values to that obtained from mercury porosimetry brings into light that this technique may be a possible replacement

---

[33] See Table 2 in Mattia et al. (2006) for further details.

candidate for mercury porosimetry. This is especially important, as in LLE experiments benign liquids are used compared to harmful or hazardous mercury.

For Pt-E1 catalysts investigated with the same method, it was seen that when the water content was ~0.1-0.3, a peak observed in the cyclohexane T_2 values for the fresh catalyst was absent in the coked catalyst. The T_2 values in the first peak were larger than the initial starting value for a sample fully saturated with cyclohexane indicating that cyclohexane was being displaced by water from small pores. As the displacement continued, the cyclohexane fraction was restricted to larger than average pores resulting in higher T_2 relaxation times. If water partially occupied any of the pores containing cyclohexane, then the rise in the cyclohexane T_2 relaxation time would not have taken place. Another peak was observed when the water content reached between 0.4 and 0.5 in Figs. 5.21 and 5.22. However, this peak was observed in both fresh and coked catalysts. This was presumably due to displacement of cyclohexane from another set of small pores which had a different accessibility from the outside. As the second peak appeared when the water fraction was between 0.4 and 0.5, this implied that more time was required for water to reach this portion of the pore network. This could be due to the deeper location of these pores within the network away from the water front or these pores were located behind pores where transport was slower, such as other relatively smaller diameter pores. The absence of the first peak in cyclohexane T_2 values for coked catalysts indicates the unavailability of the same set of pores available in the fresh catalyst for cyclohexane displacement. This may be because these sets of pores are now fully blocked by coke or partially covered making it much harder for cyclohexane to be displaced by water. Since the second peak was observed for fresh and coked catalysts, this possibly points to a region of the pore network unaffected by coking. These results also concurred with those from nitrogen gas adsorption which show that coking resulted in a loss of some mesopores. Hence, it was likely that the pores which were lost by coking as seen in the nitrogen adsorption BJH pore size distribution in Fig. 5.17 correspond to those giving rise to the first peak in the cyclohexane T_2 relaxation times. Further, as these mesopores were detected at low water fractions and had greater accessibility from the pellet exterior, they were likely to be at the edge of the pellet. Thus, the location of coke in these catalysts was determined.

This independent method of determining the location of coke also agreed with the results from earlier work done by Wang et al. (2009) and Rigby et al. (2011). Wang et al. (2009) found from pulse CO chemisorption studies that Pt-metal dispersion (%) decreased by more than ~80% for coked catalysts relative to fresh

catalysts. Thus, coke laydown was restricted to the Pt-metal sites. Rigby et al. (2011) captured CXT images which showed the location of the band of Pt crystallites in the form of an annular region at the periphery of the catalyst pellet (see Figs. 11, 12a and b, 13a and b of Rigby et al. (2011)). Thus, the interpretations are in line with each other.

Both relaxometry and PFG NMR results suggested that during the displacement experiment as the cyclohexane content decreased, it became preferentially confined to larger pores. These larger pores were concentrated in cavities which had a radius of ~9 μm which is much larger than the size of a single macropore. Additionally, PFG NMR results in Table 5.7 and 5.8 also revealed that the diffusion regime was highly restricted diffusion within these regions. This clearly implied low connectivity and poor accessibility. The decrease in the cavity radius for coked catalysts relative to fresh catalysts is conceivable considering that the presence of coke residues can block or reduce access to other pores which are likely to be accessible in fresh catalysts. This is also supported by previous experimental work on liquid entrapment by Wardlaw and McKellar (1981). They showed that liquid entrapment was influenced by pore to throat size ratio, throat to pore coordination number and the extent of random and non-random heterogeneities in the pore network.

The above work clearly shows that the LLE experiment along with NMR spectroscopy, relaxometry and diffusometry is a potential novel characterisation tool that addresses the drawbacks of conventional catalyst characterisation techniques. The results confirm that network connectivity is extremely important and must be accounted for to achieve optimum catalyst design, enabling greater lifespan for catalysts.

5.6 CONCLUSIONS

A new method, that uses two liquids (cyclohexane and water) of different affinities, has been developed and employed to determine the difference between fresh and coked catalysts with the aid of NMR. The LLE method was developed on a sol-gel silica material where a similarity was found in the percentage entrapment value of cyclohexane and that of mercury from an air-mercury displacement process. On application of the method to industrially relevant bidisperse catalysts, it was found that different displacement patterns occurred for the fresh and coked Pt/Al$_2$O$_3$ catalysts. While water initially displaced cyclohexane from a set of small pores in the

fresh catalyst, these set of pores were no longer available in the coked catalyst. Since these set of pores are filled at low water fractions, they must be located nearer the pellet surface, i.e. at the periphery. Their non-availability in coked Pt/Al_2O_3 catalysts suggests that these small pores were coked during the reaction. Thus, the LLE method was found to address some of the drawbacks of traditional, widely and industrially prevalent catalyst pore characterisation techniques and also additionally revealed the location of coke within coked catalysts.

REFERENCES

ATKINS, P. & PAULA, J. D. 2010. *Atkins' physical chemistry,* Oxford, Oxford University Press.

BARRIE, P. J. 2000. Characterization of porous media using NMR methods. *Annual Reports on NMR Spectroscopy, Vol 41,* 41, 265-316.

BROWNSTEIN, K. R. & TARR, C. E. 1977. Spin-Lattice Relaxation in a System Governed by Diffusion. *Journal of Magnetic Resonance,* 26, 17-24.

CALLAGHAN, P. T., JOLLEY, K. W. & HUMPHREY, R. S. 1983. Diffusion of Fat and Water in Cheese as Studied by Pulsed Field Gradient Nuclear Magnetic-Resonance. *Journal of Colloid and Interface Science,* 93, 521-529.

CATCHPOLE, S. 2009. Mercury removal in hydrocarbon streams *Petroleum Technology Quarterly* 14, 39-45.

CHEAH, K. Y., CHIARANUSSATI, N., HOLLEWAND, M. P. & GLADDEN, L. F. 1994. Coke Profiles in Deactivated Alumina Pellets Studied by Nmr Imaging. *Applied Catalysis A: General,* 115, 147-155.

CHU, Y. J., WERTH, C. J., VALOCCHI, A. J., YOON, H. & WEBB, A. G. 2004. Magnetic resonance imaging of nonaqueous phase liquid during soil vapor extraction in heterogeneous porous media. *Journal of Contaminant Hydrology,* 73, 15-37.

GLADDEN, L. F. 1994. Nuclear-Magnetic-Resonance in Chemical-Engineering - Principles and Applications. *Chemical Engineering Science,* 49, 3339-3408.

GÜNTHER, H. 1995. *NMR SPECTROSCOPY Basic Principles, Concepts, and Applications in Chemistry,* Chichester, John Wiley & Sons Ltd.

HADDEN, R. & MOSS, T. 2010. Dealing with mercury in refinery processes. *Petroleum Technology Quarterly,* 15, 29-37.

HAHN, E. L. 1950. Spin Echoes. *Physical Review Series II,* 80, 580.

HITCHCOCK, I., CHUDEK, J. A., HOLT, E. M., LOWE, J. P. & RIGBY, S. P. 2010. NMR Studies of Cooperative Effects in Adsorption. *Langmuir,* 26, 18061-18070.

HOLLEWAND, M. P. & GLADDEN, L. F. 1995. Transport Heterogeneity in Porous Pellets – I. PGSE NMR Studies. *Chemical Engineering Science,* 50, 309-326.

HOLMES, W. A. & PACKER, K. J. 2004. Investigation of phase trapping by secondary imbibition within Fontainebleau sandstone. *Chemical Engineering Science,* 59, 2891-2898.

HOLMES, W. M., GRAHAM, R. G. & PACKER, K. J. 2001. Diffusion in surface-wetting films in a two-phase saturated porous solid characterised by pulsed magnetic field gradient NMR. *Chemical Engineering Journal,* 83, 33-38.

HOLMES, W. M. & PACKER, K. J. 2003. Investigation of two phase flow and phase trapping by secondary imbibition within fontainebleau sandstone. *Magnetic Resonance Imaging,* 21, 389-391.

KÄRGER, J. 2008. Diffusion Measurements by NMR Techniques. *In:* KARGE, H. & WEITKAMP, J. (eds.) *Adsorption and Diffusion.* Springer Berlin / Heidelberg.

KÄRGER, J., CARO, J., COOL, P., COPPENS, M. O., JONES, D., KAPTEIJN, F., RODRIGUEZ-REINOSO, F., STOCKER, M., THEODOROU, D., VANSANT, E. F. & WEITKAMP, J. 2009. Benefit of Microscopic Diffusion Measurement for the Characterization of Nanoporous Materials. *Chemical Engineering & Technology,* 32, 1494-1511.

KERSSEBAUM, R. 2002. DOSY and Diffusion by NMR. *In:* SALNIKOV, G. (ed.) *Acquistion Application Manuals.* Rheinstetten, Germany: Bruker BioSpin GmbH.

KORTUNOV, P., VASENKOV, S., KARGER, J., ELIA, M. F., PEREZ, M., STOCKER, M., PAPADOPOULOS, G. K., THEODOROU, D., DRESCHER, B., MCELHINEY, G., BERNAUER, B., KRYSTL, V., KOCIRIK, M., ZIKANOVA, A., JIRGLOVA, H., BERGER, C., GLASER, R., WEITKAMP, J. & HANSEN, E. W. 2005. Pulsed-field gradient nuclear magnetic resonance study of transport properties of fluid catalytic cracking catalysts. *Magnetic Resonance Imaging,* 23, 233-237.

LEVITT, M. H. 2006. *Spin dynamics - basics of nuclear magnetic resonance,* Chichester, John Wiley & Sons, Ltd.

MAJORS, P., LI, P. & PETERS, E. 1997. NMR imaging of immiscible displacements in porous media. *SPE Formation Evaluation,* 12, 164-169.

MATTIA, D., BAN, H. H. & GOGOTSI, Y. 2006. Wetting of CVD carbon films by polar and nonpolar liquids and implications for carbon nanopipes. *Langmuir,* 22, 1789-1794.

PACKER, K. J. & HOLMES, W. M. 2002. Investigation of thin surface-wetting films in two-phase saturated porous media. *Magnetic Resonance in Chemistry,* 40**,** S20-S28.

PERRY, R. H. & GREEN, D. W. 2008. *Perry's chemical engineers' handbook,* New York, McGraw-Hill Professional ; London : McGraw-Hill [distributor].

POLING, B. E., THOMSON, G. H., FRIEND, D. G., ROWLEY, R. L. & WILDING, W. V. 2008. Physical Properties of Organic Compounds. *In:* PERRY, R. H. & GREEN, D. W. (eds.) *Perry's chemical engineers' handbook.* 8th ed. / prepared by a staff of specialists under the editorial direction of editor-in-chief, Don W. Green, late editor, Robert H. Perry. ed. New York: McGraw-Hill Professional ; London : McGraw-Hill [distributor].

PRICE, W. S. 1997. Pulsed-field gradient nuclear magnetic resonance as a tool for studying translational diffusion .1. Basic theory. *Concepts in Magnetic Resonance,* 9**,** 299-336.

REN, X., STAPF, S. & BLÜMICH, B. 2010. *RE: Multiscale Approach to Catalysts Design.* Type to NAVIN.

RIGBY, S. P., CHIGADA, P. I., WANG, J. W., WILKINSON, S. K., BATEMAN, H., AL-DURI, B., WOOD, J., BAKALIS, S. & MIRI, T. 2011. Improving the interpretation of mercury porosimetry data using computerised X-ray tomography and mean-field DFT. *Chemical Engineering Science,* 66**,** 2328-2339.

ROWLEY, R. L., WILDING, W. V., OSCARSON, J. L., YANG, Y., ZUNDEL, N. A., DAUBERT, T. E. & DANNER, D. P. 2007a. DIPPR® Data Compilation of Pure Chemical Properties New York Design Institute of Physical Properties, AIChE.

ROWLEY, R. L., WILDING, W. V., OSCARSON, J. L., YANG, Y., ZUNDEL, N. A., DAUBERT, T. E. & DANNER, D. P. 2007b. DIPPR® Data Compilation of Pure Chemical Properties New York Design Institute of Physical Properties, AIChE.

SCOTT, R. P. W. 1980. The silica-gel surface and its interactions with solvent and solute in liquid chromatography. *Faraday Symposia of the Chemical Society,* 15**,** 49-68.

STALLMACH, F. & KÄRGER, J. 1999. The potentials of pulsed field gradient NMR for investigation of porous media. *Adsorption-Journal of the International Adsorption Society,* 5**,** 117-133.

STAPF, S., REN, X. H., TALNISHNIKH, E. & BLUMICH, B. 2005. Spatial distribution of coke residues in porous catalyst pellets analyzed by field-cycling relaxometry and parameter imaging. *Magnetic Resonance Imaging,* 23, 383-386.

STEJSKAL, E. O. & TANNER, J. E. 1965. Spin Diffusion Measurements: Spin Echoes in the Presence of a Time-Dependent Field Gradient. *The Journal of Chemical Physics,* 42, 288-292.

WANG, J., CHIGADA, P. I., RIGBY, S. P., AL-DURI, B. & WOOD, J. 2009. Prolonging catalyst lifetime in supercritical isomerization of 1-hexene over a platinum/alumina catalyst. *Chemical Engineering Science,* 64, 3427-3436.

WARDLAW, N. C. & MCKELLAR, M. 1981. Mercury Porosimetry and the Interpretation of Pore Geometry in Sedimentary-Rocks and Artificial Models. *Powder Technology,* 29, 127-143.

WOOD, J. & GLADDEN, L. F. 2003. Effect of coke deposition upon pore structure and self-diffusion in deactivated industrial hydroprocessing catalysts. *Applied Catalysis A: General,* 249, 241-253.

YAWS, C. L. 2003. Yaws' Handbook of Thermodynamic and Physical Properties of Chemical Compounds. 1st Feb 2003 ed.: Knovel. Available from: http://www.knovel.com/web/portal/browse/display?_EXT_KNOVEL_DISPLAY_bookid=667&VerticalID=0 [Accessed 24 November 2011].

CHAPTER 6 – SUMMARY AND FUTURE WORK

From the work presented in this thesis, it has been found that the traditional methods of catalyst pore characterisation have limitations and thus require further development. The analyses methods must consider coupling between pores, and the probe fluid-surface interaction, so that a better understanding of the evolution of the pore structure, especially during coking, can be achieved. In this context, the research conducted by the author makes valuable contributions to the field of catalyst pore characterisation by proposing and applying the integrated N_2-H_2O-N_2 adsorption experiments, and developing and using the novel LLE experiments employing NMR, to fresh and coked catalysts. Thus, the methods developed and used in Chapter 4 and Chapter 5 are alternatives to the more general and traditional approach seen in the literature. However, the work completed for this thesis has also opened avenues that require further research aiding the development of the new characterisation techniques. Below, a summary of each of the chapters discussed in this thesis is presented and recommended future work along with some preliminary experimental data are also added. First, results related to mercury porosimetry and gas adsorption porosimetry are presented, following which the NMR work is summarised and some preliminary data related to LLE in ISO_008 catalyst is added. The melting and freezing point depression in porous materials has been investigated using NMR to understand pore properties of porous materials. Some preliminary data related to this method are also presented as it may be possible to combine this aspect with LLE experiments and help provide a greater insight into the pore structure of catalysts.

6.1 MERCURY POROSIMETRY AND GAS ADSORPTION POROSIMETRY

Summary: In Chapter 2 and Chapter 3, the technique of mercury porosimetry and nitrogen gas adsorption porosimetry were respectively used to determine the structural properties of catalyst samples A, B and C. It was found that the mercury porosimetry was not applicable, or rather was not able to give sufficient pore structure information, for sample A and sample C. Both samples were characterised by flat extrusion curves indicating ~100% entrapment of mercury, i.e. mercury intruded into the sample could not be recovered. For both catalysts (sample A and sample C), the presence of large atoms contributing significant van der Waals forces was highlighted. These high

dispersion forces can change the surface tension and contact angle of mercury confined within pores. This is likely to give rise to an enhancement in structural and contact angle hysteresis. The work done on sample A and sample C therefore questions the approach of using the classical Washburn equation (Eq. 2.1) to determine the pore size. The classical Washburn equation (Eq. 2.1) need not be applicable for all catalysts as it does not account for the chemical heterogeneity present within them and only accounts for mechanical equilibrium.

Unlike samples A and C, mercury porosimetry was able to give more structural information for sample B. Part of the intrusion and extrusion curves could be superimposed to show the presence of reversible contact angle hysteresis and structural hysteresis. This was despite sample B being chemically heterogeneous with large metal atoms (see Table 2.1). Thus, the work conducted using mercury porosimetry showed that metal concentration within the catalyst was crucial for the determination of accurate pore properties.

The pore properties not understood clearly from mercury porosimetry were revealed through the use of nitrogen gas adsorption. Nitrogen gas adsorption was performed on samples A, B and C. They showed that all the samples were mesoporous confirming the results obtained from mercury porosimetry.

In case of sample A, nitrogen adsorption also showed the presence of some micropores and a rough texture which could be detected by the FHH fractal dimension. Some coked counterparts of sample A, subjected to THAI®-CAPRI® reactions for 1 h and 8 h, were also characterised by nitrogen adsorption. These samples produced straight line isotherms proving that all the porosity available in the catalyst was lost and the surface was weakly adsorbing. This implied that rapid coking took place under the reaction conditions investigated and indicated the need for the use of appropriate catalysts that have a meso-macroporous or macroporous character which allowed oil molecules to freely access the pore space and not face any hindrance.

Nitrogen adsorption on sample B also showed the presence of some micropores and hinted the presence of some shielded macropores. The presence of micropores and macropores interspersed amongst the mesopores also does not meet the requirements for the THAI®-CAPRI® reaction. Most of the oil molecules are unable to access the active sites present in the catalyst. This diffusion limitation causes coking.

Sample C was found to have the smallest pore volume and surface area amongst all the samples studied. In contrast to mercury porosimetry, where all the

mercury intruded was non-recoverable, the nitrogen adsorption-desorption isotherm revealed a narrow hysteresis loop suggesting good connectivity. The connectivity was greater than sample A. Further, amongst the different samples studied, only sample C showed a good fit to the Langmuir + BET model for adsorption in the micropore filling and multilayer adsorption regions. Unfortunately, the coked catalysts obtained after reactions were not feasible for analysis, because they could only be removed by damaging the reactor. Further, the products did not show any appreciable upgrading performance even though they had the largest pores amongst all the catalysts studied. This was mainly because sample C was an LTS catalyst which cannot handle the contaminants present in heavy oil. Thus, from catalyst characterisation studies conducted, it was understood that coking occurred rapidly (less than an hour) during the THAI®-CAPRI® process and, ideally, macroporous catalysts that do not present diffusion limitations to the oil molecules are required for running the process.

Future Work: Future work with mercury porosimetry and nitrogen gas adsorption porosimetry can be expected to involve further tests with powdered samples of the same catalysts and the use of scanning loops. This may aid in understanding the regions within the catalysts that give rise to the non-recoverability of mercury following intrusion and presence of pore-pore interactions. In addition to the above experiments, it is suggested to undertake investigations of mercury intrusion and especially mercury extrusion processes using computational techniques such as MFDFT calculations (Porcheron et al., 2005) and GCMC simulations (Porcheron and Monoson, 2005; Rigby et al., 2008) on chemically heterogeneous models. This is likely to give a further understanding as to how surface chemistry and pore size plays a role in the extrusion process causing non-recoverability of mercury. This would help answer the question is it the pore structure, or connectivity related effects, actually causing an entrapment of mercury. Similar work can also be done on nitrogen gas adsorption and desorption. This would help to understand the filling and emptying mechanisms of nitrogen in chemically heterogeneous models. Monson (2009), Rigby and Chigada (2009), and Rasmussen et al. (2012) have used MFT and MC simulations to study some of these effects. A chemically heterogeneous model was used by Rasmussen et al. (2012) but this investigation was limited to a single non-wetting site. These approaches, however, could not be pursued in this thesis primarily due to apparatus downtime issues and need for appropriate software and computing power. To further understand the evolution of coking during THAI®-CAPRI® reaction/process, short run time tests such as 15 min or 30 min run times will be

required along with the use of macroporous catalysts which do not present any diffusion limitations.

6.2 INTEGRATED N_2-H_2O-N_2 GAS ADSORPTION

Summary: Prior to the work presented in this thesis, new gas adsorption porosimetry methods such as successive or integrated gas adsorption had not been employed for catalyst characterisation, especially in distinguishing fresh and coked catalysts. Traditional approaches of using gas adsorption to distinguish fresh and coked catalysts tend to simply consider the respective pore size distributions (e.g. BJH pore size distribution). Such an approach is inaccurate, as it makes the critical assumption of thermodynamically independent pores. Integrated N_2-H_2O-N_2 adsorption experiments (one component was pre-adsorbed (H_2O) and immobilised (frozen) on the surface, followed by adsorption of a second component (N_2)) performed on fresh and coked catalysts can be used to better understand the pore structure evolution during coking. This was discussed in Chapter 4. The work done in this chapter highlighted the presence of advanced adsorption, and the need to consider it in pore characterisation using gas adsorption methods. This was understood by studying the filling pattern of nitrogen and water vapour condensates within fresh and coked catalysts of sample A. The filling pattern of the two fluids was identical for the fresh sample but different for the coked version. This difference was attributed to the presence of advanced adsorption (a pore to pore interaction effect), as a result of the decrease in size of the pore bodies. Thus, coupling (and connectivity) between pores is critical to understanding the pore structure of catalysts. The method also provided information on the location of carbon deposits in the coked catalysts which underwent reaction with a model feed decane. Analyses of the obtained mass transfer coefficients proved that all of the carbon deposition took place away from the central region of the catalyst. Further, this also agreed with deposition pattern of water in the fresh catalysts. The work importantly also showed that water preadsorption was a good probe to determine the location of carbon deposits in sample A.

Future Work: However, the work presented in Chapter 4 did not discuss desorption isotherms. In fact, desorption isotherms were also obtained when the adsorption experiments were performed pre- and post-water adsorption. Kinetic analysis showed that they were not in equilibrium. Further experiments could not be done mainly due to non-availability of equipment and the termination of experimental time in this project. Hence, future work regarding the development of this method would be to

determine equilibrated desorption isotherms and use them to obtain connectivity-related parameters as has been done in Chapter 3 for sample A and sample C.

Clearly, water need not be the only vapour to be adsorbed and frozen. Hydrocarbons are also feasible for this technique. Non-polar hydrocarbons may give a different effect relative to that obtained from water. A test was conducted wherein cyclohexane was adsorbed on coked catalyst C2 and then frozen using the same protocol as mentioned in Chapter 4 for water. However, it seemed as though proper pressure control was not achieved during the freezing of cyclohexane. Thus, very little difference was observed in the nitrogen adsorption isotherms before and after cyclohexane adsorption, and although the method pursued in this thesis gave favourable results for samples tested with water, it did not do so for cyclohexane. Hence, more work is required to determine the optimal rate of drop in pressure and the degassing pressure required at the end of partial filling of the system and its freezing.

6.3 LLE, NMR CRYOPOROMETRY

Summary: In Chapter 5, an alternative novel method, LLE, was developed and its use was demonstrated for the characterisation of fresh and coked Pt-E1 catalysts using NMR. LLE was achieved by the coadsorption of two liquids, namely, cyclohexane and water. The traditional methods of catalyst pore characterisation such as gas adsorption porosimetry and mercury porosimetry have several disadvantages that lead to inaccuracies in the information obtained. Inaccurate information can be highly critical for the optimisation of any given reaction. The LLE method was developed to meet and, to a certain extent, overcome the disadvantages of traditional characterisation techniques. The method was first developed on a model silica material and the results obtained were found to be comparable to those obtained from mercury porosimetry. T_2 relaxation times and diffusion coefficient measurements helped understand the displacement mechanism of cyclohexane by water in the silica material. The method was then applied to fresh Pt-E1 catalysts and coked Pt-E1 catalysts obtained from the supercritical isomerisation of 1-hexene. The variation of the cyclohexane and water T_2 relaxation times, and cyclohexane diffusion coefficients as a function of the water content within the catalyst pellets was used to determine the location of coke deposits within Pt-E1 catalysts. In the coked catalysts, carbon deposits were found to be deposited in the periphery of the pellet. This result was also found to agree with the work done using other independent methods.

Future Work: The variation of cyclohexane and water T_2 relaxation times as a function of the water content within the ISO_008 catalyst pellet (coked catalysts obtained from reaction conducted in different conditions)[34] was not presented in Section 5.4.2. This will be discussed below. Time constraints allowed the investigation of only a catalyst pellet from the batch, hence, the reason for including this result here. This pellet showed a distinctly different behaviour to the batch ISO_014 confirming the sensitivity of the LLE technique.

Fig. 6.1 presents the cyclohexane and water T_2 relaxation times as a function of the water content within the coked catalyst pellet from batch ISO_008. It can be seen in Fig. 6.1, that the cyclohexane T_2 relaxation time was 0.00182 ± 0.00019 s when the water content within the catalyst pellet was ~80%. In terms of experimental duration, the time required for displacement up to this point was more than 141 h. Such large experimental timescales clearly imply the difficulty of water in displacing cyclohexane from the ISO_008 catalyst pellet.
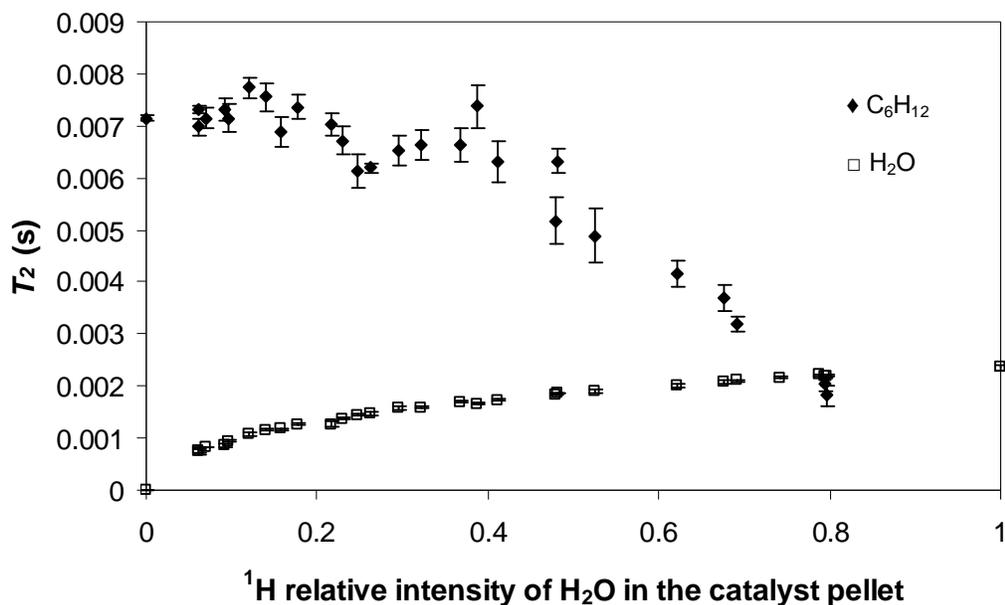
Fig. 6.1. Variation in the T_2 relaxation times of cyclohexane phase and water phase as a function of the water content within a coked catalyst Pt-E1 pellet. The coked catalyst pellet was obtained under conditions denoted by ISO_008.

The water T_2 relaxation time when the water content within the catalyst pellet was 100% was obtained after re-preparing the sample and then exposing it to pure water vapour. In contrast to the large displacement time observed for the ISO_008 catalyst pellet, the displacement time observed for fresh Pt-E1 and coked ISO_014

---

[34] Refer to Section 5.3 for details of reaction conditions.

catalysts was much less. Previous work done by Mattia et al. (2006) showed that non-polar liquids (cyclohexane) confined in carbon nanopipes had greater retention times than polar liquids like water. They also found that the cyclohexane contact angle was less than that of water on carbon surfaces, indicating greater affinity of cyclohexane for carbonised surfaces than water. Coking impacts the physical properties of the catalyst. This would mean that the very large experimental time required for the displacement of cyclohexane was likely to be due to the deposition of coke and the ability of cyclohexane to be attracted to these carbon deposited surfaces. As a result, water finds greater difficulty in displacing cyclohexane in the coked catalyst pellet ISO_008 than in ISO_014. This also leads to the greater entrapment of cyclohexane within this sample. Future work must be directed to investigate if the entrapment of hydrocarbons can be related to coking and/or experimental duration. This is especially important as the LLE method uses relatively benign liquids and also has potential to replace the mercury porosimeter. Today, mercury is being highly regulated in its use, due to the serious environmental and health hazards that it presents (Lassen and Maxson, 2008).

Apart from the above, there are other dimensions that can be introduced to the LLE process which require detailed examination so that the technique may be developed further. This would also provide light on the filling patterns of polar and non-polar liquids. The catalyst pellets (fresh and coked) investigated in this thesis was exposed to the saturation vapour pressures of the two liquids. Catalysts can also be exposed to lower vapour pressures of cyclohexane and/or water. Aqueous solutions with different concentrations of solutes can be prepared which provide a supply of water vapour at different pressures (see Poling et al. (2008) for relevant datasets). Lower vapour pressures are achieved with increasing solute concentrations (as it is a colligative property). These lower vapour pressures imply lower filling fractions on exposed samples. Similarly, earlier work has also shown that cyclohexane saturation vapour pressure can also be controlled by the addition of a non-volatile solute. Fisher and Israelachvili (1981) validated the Kelvin equation (Eq. 3.8) for cyclohexane menisci on mica surfaces. They used n-hexadecane and n-dodecane as non-volatile solutes in their experiments. Though control of the vapour pressure of cyclohexane was achieved, they also found that over long periods of equilibration, contamination of the non-volatile solute took place. Hence, a detailed investigation will be required where filling patterns of water and cyclohexane within catalysts are individually studied at different vapour pressures. This may be followed by a study where water vapour pressure is controlled and cyclohexane is left at saturation conditions and vice

versa. These studies would also reveal whether the extent of contamination was significant in the timescale of the experiment.

Another approach would be to deuterate one of the solutions used in the LLE process, i.e. use deuterated water and non-deuterated cyclohexane or vice versa. Deuterated components are invisible to ^{1}H NMR experiments, thus simplifying the experiment and giving greater light as to how the displacement of cyclohexane by water proceeds with time. Further, apart from cyclohexane, other hydrocarbons may also be feasible for LLE experiments. However, kinetics factors may arise. Cyclohexane has a high vapour pressure and can quickly fill the sample at atmospheric conditions. It can be expected that the above set of experiments in combination with NMR relaxometry and diffusometry will provide greater insights on the filling and displacement/exchange mechanisms or patterns within porous materials. A combination of the above experiments with MRI sequences also holds potential since this provides direct qualitative and quantitative data on the location and saturation of entrapped fluid (displaced fluid) and the displacing fluid. These experiments could not be pursued mainly due to non-availability of the equipment within the university.

Thirdly, apart from NMR relaxometry and diffusometry, thermoporometry in its NMR form (i.e. NMR cryoporometry) can also be used in combination with the aforementioned techniques to understand pore structure information. Preliminary studies of this technique were carried out by performing freeze-melt experiments and T_2 relaxatometry studies on water[35], and hydrocarbons[36] (including cyclohexane, decane and cyclooctane) imbibed within pellets of sample G1. Typical NMR cryoporometry freeze-thaw curves obtained for material G1 imbibed in water, cyclohexane, cyclooctane and decane for more than 24 hours are displayed in Figs. 6.2a, b, c, and d. They are illustrated as the variation of the mobile fluid signal strengths against temperature after an equilibration time of 10 minutes[37] at each temperature. After obtaining the proton intensity of water (or any of the other liquids) in G1 at room temperature, the sample was cooled to ~257 K (~187 K for cyclohexane, ~199 K for cyclooctane, and ~183 K for decane) when no signal was obtained. This indicated the absence of any mobile fluid within the system. Next, a melting step was initiated that gradually progressed to ~271 K (~267 K for

---

[35] Ultrapure water having a resistivity of 18.2 MΩ-cm was used for the freeze-melt experiments

[36] ACS reagent grade ($\geq$ 99%) cyclohexane, ($\geq$ 99%) cyclooctane, and ($\geq$ 99%) decane sourced from Sigma Aldrich were used for the freeze-melt experiments.

[37] Fig. 6.2d for decane was obtained using an equilibration interval of 5 min. The results are similar to those obtained with an equilibration time of 10 min. Each temperature was repeated twice and intensities were recorded at a time interval of 5 min.

cyclohexane, ~283 K for cyclooctane, and ~242 K for decane). At this point, most of the pores in G1 were already molten and the temperature cycle was reversed. Thus, the freezing mechanism of water (or any of the other liquids) in G1 could also be studied. The freezing cycle was continued back to ~ 257 K (~188 K for cyclohexane, ~199 K for cyclooctane, and ~185 K for decane) after which the melting step was again repeated. It was found that the second melting cycle followed exactly the same path as the first melting step. Thus, no destruction of pore pathways or the structure had taken place. The second melting cycle was allowed to progress fully and continued till room temperature. As a result of this step, the bulk melting point of water - 273.1 K (and other fluids, cyclohexane - 279.4 K, cyclooctane - 286.3 K and decane - 243.5 K) was also observed. Also shown in Figs. 6.2b, c, d are the melting curves for pure bulk cyclohexane, cyclooctane and decane.

(a)

193
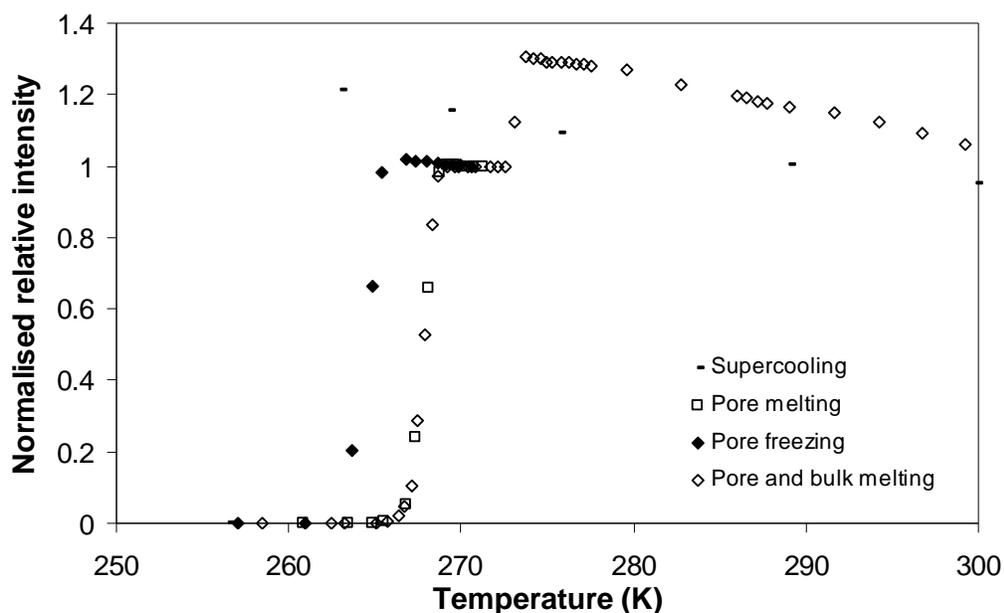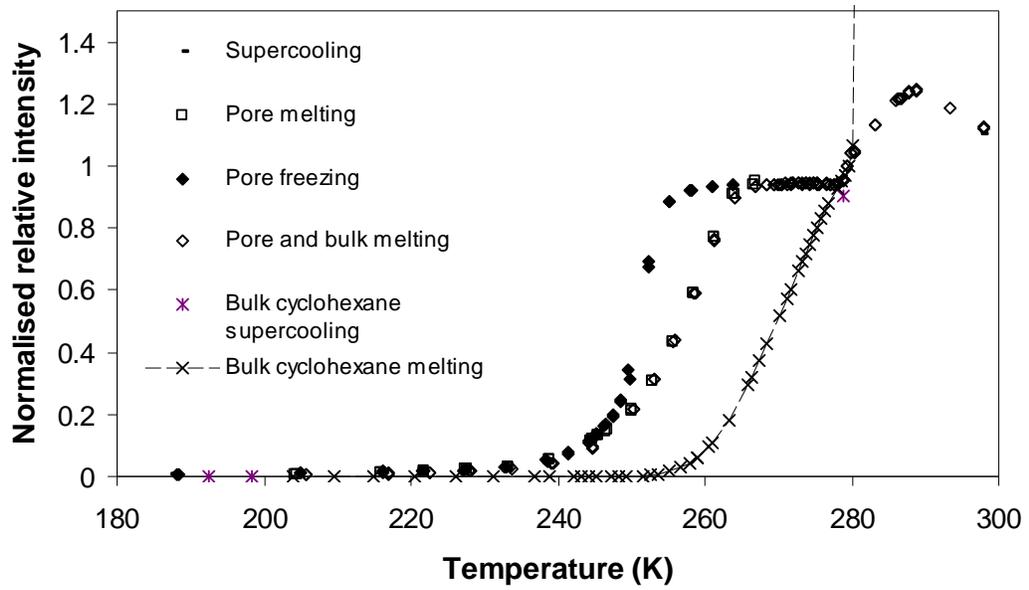
(b)
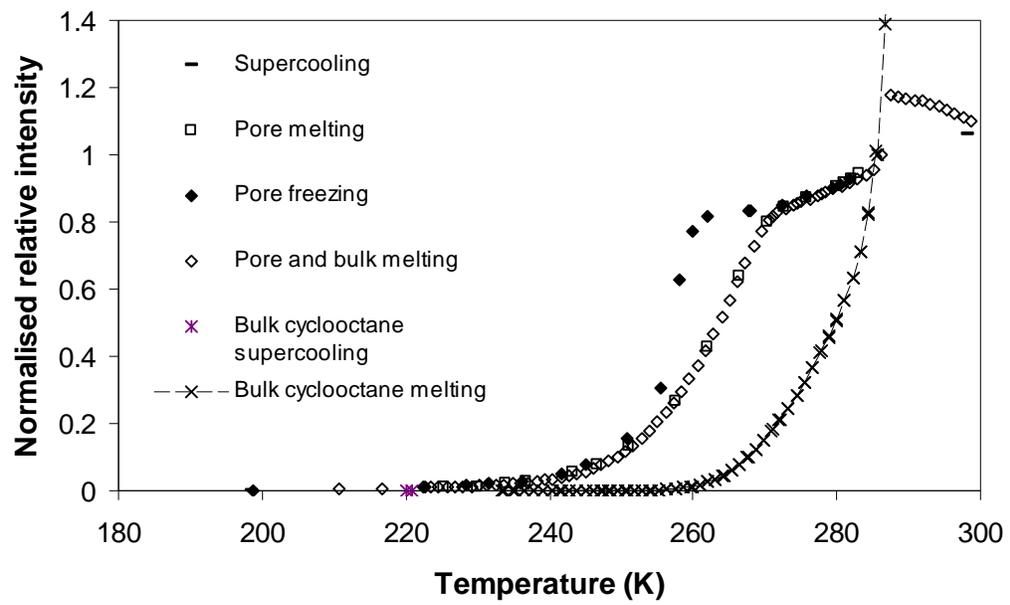
(c)
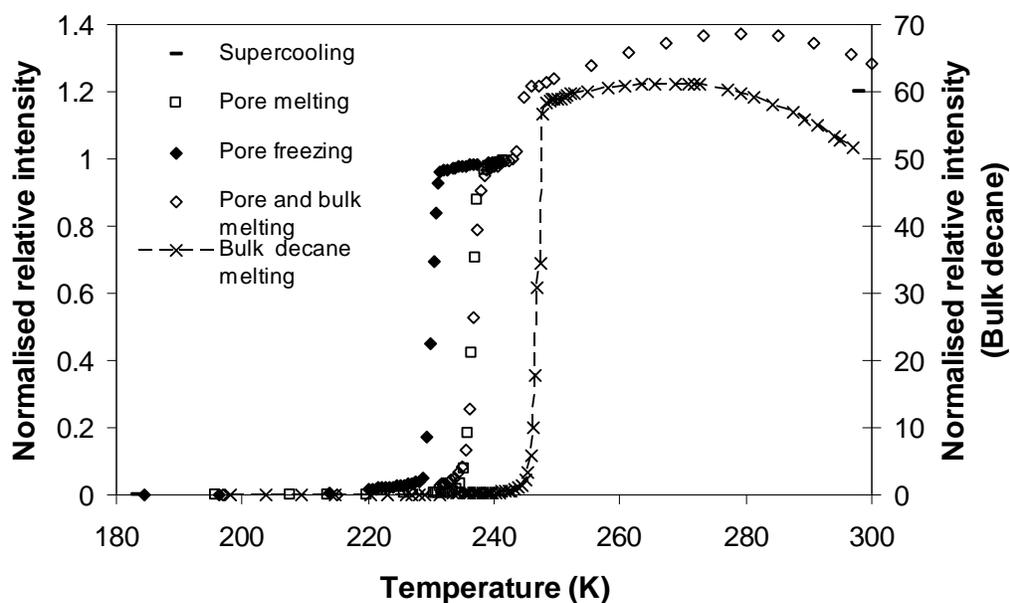
(d)
Fig. 6.2. NMR cryoporometry chart for sample G1 imbibed in (a) water, (b) cyclohexane, (c) cyclooctane and (d) decane with an effective equilibration time of 10 minutes. The dashed line with crosses (x) indicates the melting cycle for pure bulk liquids.

Clear differences were observed in the melting and freezing behaviour of all liquids when confined within material G1. It was noted that unlike water which began to melt at ~266 K, the hydrocarbons thawed at much lower temperatures (cyclohexane and cyclooctane at ~222 K, decane at ~235 K). While water melted in all the pores of G1 with a temperature difference of ~5 K, decane melted in all the pores with a temperature difference of ~8.5 K, cyclohexane with a temperature difference of ~57 K and cyclooctane with a temperature difference of ~63 K. This was clear evidence of the greater melting point depression provided by hydrocarbons relative to water. This has also been pointed out in the literature (Mitchell et al., 2008). More importantly, it was found that that the melting steps of cyclohexane and cyclooctane in G1 were more gradual relative to the melting steps of water and decane. This gradual diffuse melting cycle of cyclohexane provided a broad pore size distribution for G1 which was very unlike the results obtained from water and decane cryoporometry or even mercury porosimetry. It is not possible for G1 to have different pore size distributions dependent on the imbibed fluid. Sample damage during the freeze-thaw process cannot be a reason, as re-melting step always followed the initial melting step. In Chapter 2, it was mentioned that pore shielding can contribute significantly in skewing the pore size distribution to smaller pore sizes during the mercury intrusion cycle. However, shielding does not effect the extrusion cycle and a

distribution obtained from an extrusion cycle superimposed on that obtained from a typical cyclohexane melting curve can be seen in Figure 6.3.
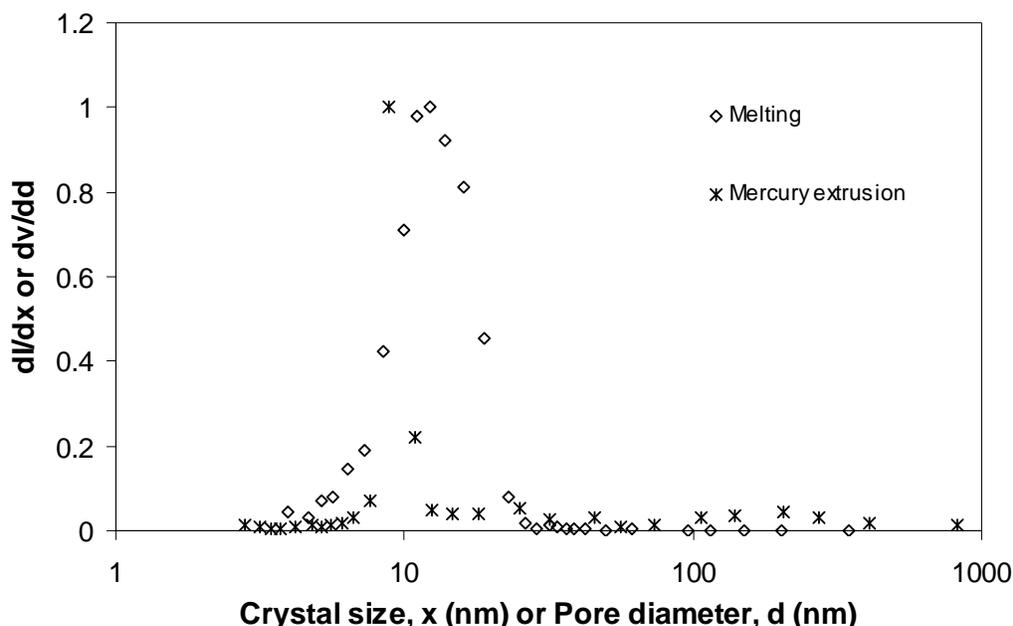
Fig. 6.3. Pore size distributions obtained from the melting of cyclohexane and the extrusion of mercury from material G1.

It was noted that peaks were located at ~12 nm for the pore size distribution obtained from the cyclohexane melting curve and at ~9 nm for the mercury extrusion curve. Also it was found that the widths of the size distributions were significantly different. Previous workers (Overloop and Van Gerven, 1993) have suggested the presence of a liquid film along the solid-substrate interface and that only the interior of the pore freezes. This allowed the melting transition to be an independent process unaffected by pore shielding. However, recent experiments by Hitchcock et al. (2011) show the presence of advanced melting effects similar to advanced adsorption (discussed in Chapter 4) that skew the pore size distribution to smaller sizes. Since both extrusion and melting are not affected by pore shielding, it is surprising that very different size distributions were obtained.

A review of the literature has shown that the broad pore size distribution for cyclohexane can be attributed to the fact that cyclohexane is a non-polar globular molecule that undergoes two distinct phase transitions. First, at ~186 K, it undergoes a solid-solid phase transition from a monoclinic rigid lattice structure to a face centred cubic plastic crystal structure. This plastic crystalline state of cyclohexane allows it to gain mobility with increasing temperatures. The diffusion coefficients for cyclohexane in this state are larger than those of a typical solid. At the normal melting point of

196

cyclohexane, ~279.65 K, the mobility of the plastic crystal has increased to a state where it becomes very similar to that corresponding to a liquid. This transition of cyclohexane from the plastic phase to the liquid phase within G1 is diffuse and is likely to be the reason for the broadness in the pore size distribution. Hence, a relaxation filter must be employed that should be optimised to remove the plastic ice phase and detect the presence of only molten liquid in G1 (Dore et al. 1989; Booth and Strange, 1998; Aksnes et al. 1998; Aksnes and Gjerdaker, 1999; Aksnes and Kimtys, 2002). Similar reasons can also be attributed to the presence of the broad melting step for cyclooctane in G1.

On other hand, bulk decane is known to freeze into a triclinic structure at 243 K (Malhotra et al., 1992). Fig. 6.4 shows the pore size distributions obtained for decane and water from the freeze-thaw curves in Fig 6.2. Both liquids seem to probe the same structure. Unlike water, which expands on freezing, the advantage of using hydrocarbons is their greater melting point depression giving more resolution and also the ice phases of hydrocarbons contract on freezing causing no damage to the pore structure at termination of the experiment.
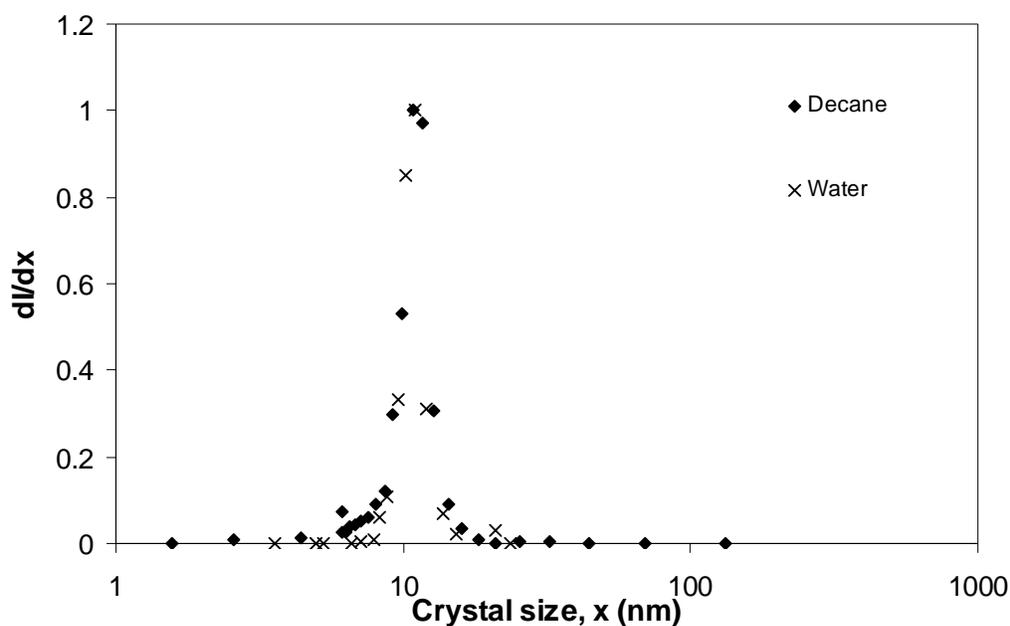
Fig. 6.4. Pore size distributions obtained for the melting of decane and water within material G1.

In addition to the above NMR cryoporometry experiments, T_2 relaxation time experiments were also performed to gain an understanding of the confinement effect of water and hydrocarbons (cyclohexane, cyclooctane, and decane) within material G1. Fig. 6.5 shows the raw relaxation data obtained for water and hydrocarbons

(cyclohexane, cyclooctane, and decane) imbibed within material G1 when the entire pore liquid was molten (i.e. at 100% melt) but bulk liquid melting had not taken place. The differences in the T_2 relaxation time behaviour of the liquids can be clearly seen (see Table 6.1). Water relaxed faster than hydrocarbons due to its wetting properties. Further, it was also found that as the molecular weight increased, greater time was required for relaxation. Also it was found that the mono-exponential attenuation equation was not applicable for T_2 relaxation of decane within material G1. The intensity attenuation was described by two components, representing two regions with ~42% of the pore space contributing to the greater relaxation time and the remaining ~58% of the pore space contributing to the lower relaxation time.
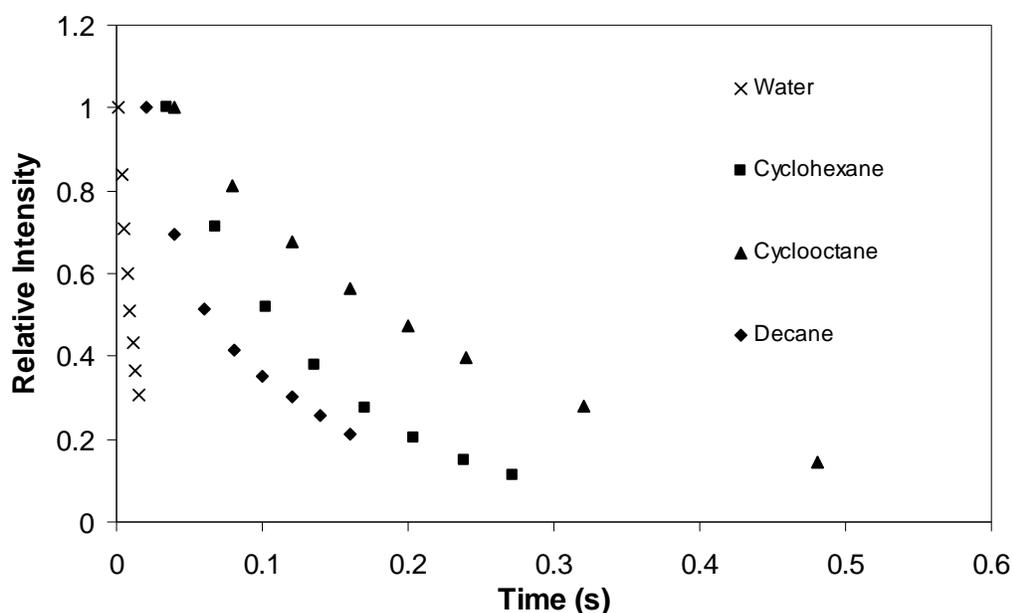
Fig. 6.5. Raw T_2 relaxometry data obtained for water, cyclohexane, cyclooctane and decane in material G1 when the entire pore liquid was molten.

Table 6.1
T_2 relaxation times of different probe liquids within material G1 when the entire pore liquid was molten.

Liquid	T_2 (s) (at 100% melt)
Water	0.01058(0.00013)
Cyclohexane	0.10027(0.00153)
Cyclooctane	0.2011(0.00624)
	0.14039(0.01392)
Decane	$p = 0.41655(0.02997)$
	0.02353(0.00308)

( ) Errors are quoted in brackets.

Variable temperature T_2 relaxation data for water within material G1 along the freezing and melting cycles was always defined by a mono-exponential attenuation equation. A difference in the T_2 relaxation times during the melting and freezing steps was clear evidence of the different paths taken during the freezing and melting process. Table 6.2 contains the water T_2 relaxation times at different molten fractions along the melting and freezing cycles. For hydrocarbons, it was found that the melting process for cyclohexane and cyclooctane was usually defined by a mono-exponential equation. However, the freezing cycle exhibited both mono-exponential and bi-exponential characteristics. Further investigation is required to see if the bi-exponential character seen in the freezing cycle for cyclohexane and cyclooctane is due to the formation of different ice phases or due to the presence of mobile liquids within different pore subsets. Unlike water and globular liquids (cyclohexane and cyclooctane), linear hydrocarbon decane showed bi-exponential characteristics over the entire melting and freezing process (except at very low molten fractions). Table 6.3 contains the decane T_2 relaxation time data at different molten fractions along the melting and freezing cycles.

Table 6.2
Water T_2 relaxation times at different molten fractions during the melting and freezing cycles.

Water intensity	T_2 (s) (melting cycle)	T_2 (s) (freezing cycle)
0.75	0.00517(0.00021)	0.00745(0.00033)
0.5	0.00215(0.00008)	0.00576(0.00039)
0.25	0.00157(0.00005)	0.00294(0.00142)

( ) Errors are quoted in brackets.

To the knowledge of the author, the literature does not contain any comparison of the effect of confinement of different polar and non-polar liquids within porous media and how they influence freezing point or melting point depression and what effect the freezing or melting cycles have on the T_2 relaxation times and other NMR parameters such as diffusion coefficients. It is these differences that need to be further explored so as to arrive at an understanding of the interaction of different liquids with porous solids and use them in the further development of the LLE process for catalyst characterisation. Such an investigation will presumably require access to a neutron or x-ray source (e.g. neutron reactor or synchrotron) where different neutron or x-ray diffraction experiments can be performed (as seen in Sliwinska-Bartkowiak et al. (2008) and Jelassi et al. (2011)). This will serve as an

independent method to distinguish the different ice phases of water and hydrocarbons confined in porous media. Such experiments are likely to be beyond the scope of this thesis.

Table 6.3
Decane T_2 relaxation times at different molten fractions during the melting and freezing cycles.

Decane intensity	T_2 (s) (melting cycle)	Decane intensity	T_2 (s) (freezing cycle)
	0.00259(0.00002)		0.11917(0.01868
0.11	$p = 0.54234(0.00315)$	0.86	$p = 0.30335(0.05055)$
	0.00056(0.000005)		0.02607(0.00247)
	0.00676(0.00031)		0.1282(0.03135)
0.38	$p = 0.61359(0.002658)$	0.68	$p = 0.22601(0.05692)$
	0.00128(0.0001)		0.0274(0.0235)
	0.01384(0.0001)		0.20359(0.1104)
0.66	$p = 0.55429(0.00062)$	0.44	$p = 0.13409(0.04639)$
	0.00379(0.000025)		0.02932(0.00186)
			0.1569(0.07649)
		0.27	$p = 0.11873(0.04773)$
			0.02802(0.0017)
		0.14	0.02457(0.00005)
		0.05	0.02096(0.00006)

( ) Errors are quoted in brackets.

REFERENCES

AKSNES, D. W. & GJERDAKER, L. 1999. NMR line width, relaxation and diffusion studies of cyclohexane confined in porous silica. *Journal of Molecular Structure,* 475, 27-34.

AKSNES, D. W., GJERDAKER, L., ALLEN, S. G., BOOTH, H. F. & STRANGE, J. H. 1998. Diffusion processes in confined materials. *Magnetic Resonance Imaging,* 16, 579-581.

AKSNES, D. W. & KIMTYS, L. 2002. ^{1}H NMR studies of cyclohexane confined in mesoporous solids: Melting point depression and pore size distribution. *Applied Magnetic Resonance,* 23, 51-62.

BOOTH, H. F. & STRANGE, J. H. 1998. Organic nanocrystals: an NMR study of cyclohexane in porous silica. *Molecular Physics,* 93, 263-269.

DORE, J. C., DUNN, M., HASEBE, T. & STRANGE, J. H. 1989. Orientationally Disordered Crystals in Porous Silica - Cyclohexane. *Colloids and Surfaces,* 36, 199-207.

FISHER, L. R. & ISRAELACHVILI, J. N. 1981. Experimental Studies on the Applicability of the Kelvin Equation to Highly Curved Concave Menisci. *Journal of Colloid and Interface Science,* 80, 528-541.

HITCHCOCK, I., HOLT, E. M., LOWE, J. P. & RIGBY, S. P. 2011. Studies of freezing-melting hysteresis in cryoporometry scanning loop experiments using NMR diffusometry and relaxometry. *Chemical Engineering Science,* 66, 582-592.

JELASSI, J., GROSZ, T., BAKO, I., BELLISSENT-FUNEL, M. C., DORE, J. C., CASTRICUM, H. L. & SRIDI-DORBEZ, R. 2011. Structural studies of water in hydrophilic and hydrophobic mesoporous silicas: An x-ray and neutron diffraction study at 297 K. *Journal of Chemical Physics,* 134.

LASSEN, C. & MAXSON, P. 2008. Options for reducing mercury use in products and applications, and the fate of mercury already circulating in society. European Commission. (Contract: ENV.G.2/ETU/2007/0021) Available from:http://ec.europa.eu/environment/chemicals/mercury/pdf/study_report 2008.pdf [Accessed 28 May 2012].

MALHOTRA, V. M., MU, R. & NATARAJAN, A. 1992. Effects of Surfaces on the Melting Freezing Behavior of Fluids in Derivatized-Porous and Nude-Porous Silica. *In:* DRAKE, J. M., KLAFTER, J., KOPELMAN, R. & AWSCHALOM, D. D., eds. *Symp on Dynamics in Small Confining Systems, at*

the 1992 MRS Fall Meeting, 30 November – 04 December 1992. BOSTON, MA. Materials Research Society Symposium Proceedings, 290, Pittsburgh: Materials Research Soc, 121-126.

MATTIA, D., BAN, H. H. & GOGOTSI, Y. 2006. Wetting of CVD carbon films by polar and nonpolar liquids and implications for carbon nanopipes. *Langmuir,* 22, 1789-1794.

MITCHELL, J., WEBBER, J. B. W. & STRANGE, J. H. 2008. Nuclear magnetic resonance cryoporometry. *Physics Reports-Review Section of Physics Letters,* 461, 1-36.

MONSON, P. A. 2009. Dynamic Mean Field Theory for Fluids Confined in Porous Materials: Application to an Inkbottle Pore Geometry. *In:* KASKEL, S., LLEWELLYN, P., RODRIGUEZ-REINOSO, F., SEATON, N. A., eds. *IUPAC Symposium on Characterisation of Porous Solids (COPS VIII),* 10-13 June 2008. Edinburgh, Scotland. Royal Society of Chemistry Special Publications, 318, Cambridge: Royal Soc Chemistry, 103-110.

OVERLOOP, K. & VAN GERVEN, L. 1993. Freezing Phenomena in Adsorbed Water as Studied by NMR. *Journal of Magnetic Resonance, Series A,* 101, 179-187.

POLING, B. E., THOMSON, G. H., FRIEND, D. G., ROWLEY, R. L. & WILDING, W. V. 2008. Physical and Chemical Data - Vapour pressures of solutions. *In:* GREEN, D. W. & PERRY, R. H. (eds.) *Perry's chemical engineers' handbook.* 8th ed. / prepared by a staff of specialists under the editorial direction of editor-in-chief, Don W. Green, late editor, Robert H. Perry. ed. New York: McGraw-Hill Professional ; London : McGraw-Hill [distributor].

PORCHERON, F. & MONSON, P. A. 2005. Dynamic aspects of mercury porosimetry: A lattice model study. *Langmuir,* 21, 3179-3186.

PORCHERON, F., MONSON, P. A. & THOMMES, M. 2005. Molecular Modeling of mercury porosimetry. *Adsorption-Journal of the International Adsorption Society,* 11, 325-329.

RASMUSSEN, C. J., GOR, G. Y. & NEIMARK, A. V. 2012. Monte Carlo Simulation of Cavitation in Pores with Nonwetting Defects. *Langmuir,* 28, 4702-4711.

RIGBY, S. P. & CHIGADA, P. I. 2009. Interpretation of integrated gas sorption and mercury porosimetry studies of adsorption in disordered networks using mean-field DFT. *Adsorption-Journal of the International Adsorption Society,* 15, 31-41.

RIGBY, S. P., CHIGADA, P. I., EVBUOMVAN, I. O., CHUDEK, J. A., MIRI, T., WOOD, J. & BAKALIS, S. 2008. Experimental and modelling studies of the kinetics of mercury retraction from highly confined geometries during porosimetry in the transport and the quasi-equilibrium regimes. *Chemical Engineering Science,* 63, 5771-5788.

SLIWINSKA-BARTKOWIAK, M., JAZDZEWSKA, M., HUANG, L. L. & GUBBINS, K. E. 2008. Melting behavior of water in cylindrical pores: carbon nanotubes and silica glasses. *Physical Chemistry Chemical Physics,* 10, 4909-4919.

APPENDIX A – SUPPORTING INFORMATION FOR MERCURY POROSIMETRY

This appendix contains extra information on how major catalyst pore properties were calculated from raw data. Information concerning the removal of contact angle hysteresis is also given.

A.1 SURFACE AREA USING THE ROOTARE-PRENZLOW EQUATION

Below in Table A.1.1, the pressure and the incremental volume intruded obtained from the raw experimental data are presented. Their product PV_i is calculated in the third column. This is then summed and substituted in the Rootare-Prenzlow equation:

$$A = -\frac{1}{\gamma \cos \theta} \int_0^V P dV ,$$ (A.1.1)

as derived by Rootare and Prenzlow (1967). The surface tension γ was assumed as 0.485 Nm^{-1} and contact angle θ as 130° to obtain the surface area. Substituting the values in Eq. (A.1.1):

$$A = -\frac{1}{0.485\cos130}(93.299) ,$$

$A = 299.1743$ m^{2}g^{-1}.

Table A.1.1
Raw pressure and volume data for mercury intrusion in sample B (whole). The final column contains the product of the pressure and incremental volume which is summed in the last row.

Pressure P (MPa)	Incremental volume V_i (cm^{3}g^{-1})	PV_i
4.637414	0.0022	0.010202
5.619572	0.002	0.011239
7.158275	0.0028	0.020043
8.564736	0.002	0.017129
10.68949	0.0021	0.02248
13.34329	0.0022	0.029355
16.56989	0.002	0.040609
20.30451	0.002	0.040609
24.93048	0.0023	0.05734
31.30716	0.0027	0.084529
38.56148	0.0029	0.111828
47.41497	0.0034	0.161211

59.0287	0.0043	0.253823
72.95784	0.0066	0.481522
90.69674	0.0077	0.698365
101.5976	0.0067	0.680704
113.066	0.0188	2.125641
137.4089	0.2495	34.28351
171.7911	0.2003	34.40975
206.5993	0.0662	13.67687
240.4278	0.015	3.606417
275.0285	0.005	1.375142
308.9188	0.0018	0.556054
345.0803	0.0016	0.552129
378.5676	0	0
413.8099	0	0
	$\sum P_i V_i$	93.299

A.2 DECONVOLUTION OF CONTACT ANGLE HYSTERESIS

Liabastre and Orr (1978) compared the pore diameters obtained from mercury porosimetry and electron microscopy for CPG. Kloubek (1981) used this data to determine the variation of the $\gamma \cos \theta$ factor present in the Washburn equation:

$$P = -\frac{2\gamma \cos \theta}{r},$$
(A.2.1)

with pore radius r. During the intrusion process, i.e. for the advancing mercury menisci, Kloubek (1981) obtained the following expression:

$$\gamma \cos \theta_A = -302.533 + \frac{-0.739}{r},$$
(A.2.2a)

and for the extrusion process, i.e. for the receding mercury menisci, Kloubek (1981) obtained:

$$\gamma \cos \theta_R = -68.366 + \frac{-235.561}{r},$$
(A.2.2b)

where θ_A and θ_R are the advancing and receding mercury contact angle. All other terms are previously defined in Section 2.1. However, the original constants determined by Kloubek (1981) had to be changed to that in Eq. (A.2.2c):

$$\gamma \cos \theta_R = -5 + \frac{-135}{r},$$
(A.2.2c)

in order to remove contact angle hysteresis in catalyst sample B. This can be expected as the equations Kloubek (1981) originally derived were for CPG. Sample B is a hydroprocessing catalyst which is chemically and physically more heterogeneous.

205

Thus, it can be expected to have a different pore structure compared to the CPG used by Liabastre and Orr (1978). The pore radius can then be obtained by substituting Eq. (A.2.2a) and (A.2.2c) into Eq. (A.2.1) and solving the quadratic equations to determine the radius. Therefore, for the mercury intrusion and extrusion processes when contact angle hysteresis has been removed, the pore radius r is given by Eq. (A.2.3a):

$$r = \frac{302.533 + \sqrt{91526.216 + 1.478P}}{P},$$ (A.2.3a)

and Eq. (A.2.3b):

$$r = \frac{5 + \sqrt{25 + 270P}}{P},$$ (A.2.3b)

respectively.
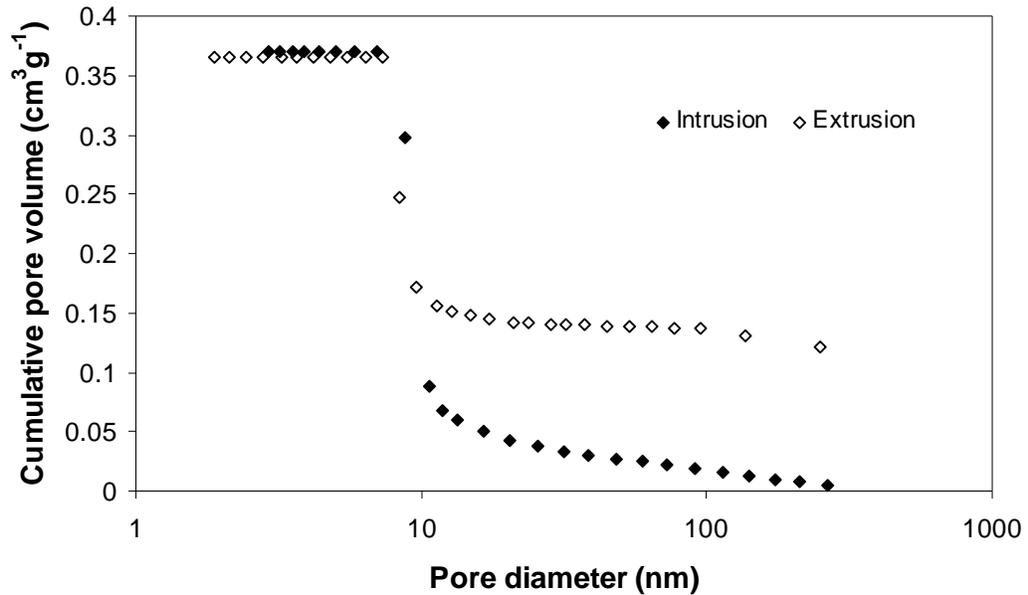
Fig. A.2.1. An example of the application of the Rigby-Edler equation used to remove contact angle hysteresis for sample B (powder) using the constants in Table 2.4. The equilibration time was 30 s.

A.3 WITHDRAWAL EFFICIENCY/MERCURY ENTRAPMENT

Withdrawal efficiency (W_E) is the percentage ratio of the amount extruded at minimum pressure to the total amount intruded. Percentage entrapment will therefore be 100 – W_E. Consider Fig. 2.4 in Section 2.3, the total intruded volume is 0.41 cm^{3}g^{-1} and no amount could be extruded on minimising the pressures during the extrusion process.

$$W_E = \left(\frac{0.41 - 0.41}{0.41}\right) \times 100,$$

$$W_E = 0,$$

$$\therefore \% \, Mercury \, entrapment = 100 - 0 = 100.$$

All the mercury intruded remained irreversibly trapped within the pores of catalyst sample A.

P. S. The details of the quoted references can be seen in the **REFERENCES** section in Chapter 2.

APPENDIX B – SUPPORTING INFORMATION FOR GAS ADSORPTION POROSIMETRY

This appendix contains extra information on how major catalyst pore properties were calculated from raw gas adsorption porosimetry data.

B.1 CALCULATION OF BET SURFACE AREA AND BET C CONSTANT

The raw nitrogen gas adsorption data presented in Fig. 3.2 for catalyst sample A had a linear uptake in the pressure range 0.06-0.28. This region represented the multilayer adsorption region. The straight line equation of the BET isotherm (Eq. 3.3a) was used to construct a plot of $1/(Volume\ adsorbed(P_0/P\text{-}1))$ vs. P/P_0. A straight line fit gave the slope and the intercept. These values were solved by using Eq. (3.3b) and Eq. (3.3c) to obtain the value of the BET C constant and the monolayer capacity V_m. For example, consider the plot in Fig. 3.3a:

$$Slope = \frac{C-1}{V_m C} = 0.01984,\ \text{and:}$$

$$Intercept = \frac{1}{V_m C} = 0.00020.\ \text{From the former two expressions:}$$

$C = 100.1846,$

$V_m = 49.9001\ \text{cm}^3\text{g}^{-1}(\text{STP}).$

According to Fig. 7 in Karnaukov (1985), the BET C value of 100 corresponds to a nitrogen molecular area of ~0.16 nm^2. Using this value, it was possible to estimate the surface area A_{BET} of catalyst sample A.

$$A_{BET} = \frac{V_m}{22414}\sigma N_A = n_m \sigma N_A,$$

$$A_{BET} = \left(\frac{49.9001}{22414}\right)\left(0.16\times10^{-18}\right)\left(6.023\times10^{-23}\right) = 214.5432\ m^2 g^{-1}.$$

Table B.1.1
Nitrogen molecular area for the catalysts investigated (derived from Fig. 7 in Karnaukhov (1985)).

Catalysts	BET C constant	Molecular area (nm^2)
Sample A	108(4)	0.16
Sample B	146(16)	0.14
Sample C	187(27)	0.13

( ) Errors are quoted in brackets.

The surface areas of other catalysts studied in this thesis were also determined in a similar manner. The BET C constant was taken into consideration to determine the molecular area of nitrogen for all catalysts. Please refer Table B.1.1 for nitrogen molecular areas at different BET C constants.

B.2 CALCULATION OF FHH FRACTAL DIMENSION

The raw gas adsorption data presented in Fig. 3.17a for catalyst sample C was transformed into $\ln \dfrac{V}{V_m}$ vs. $\ln[\ln(P_0/P)]$ plot (Fig. 3.19a) where the monolayer capacity V_m was obtained by the method mentioned in section B.1. In the van der Waals regime, i.e. in the early stages of multilayer formation:

$$Slope = \frac{D-3}{3} = \text{-0.407},$$

D = 1.779 which is unphysical, as D is supposed to be a value between 2 and 3. On the other hand, if the surface tension regime is considered:

$$Slope = D - 3 = \text{-0.407},$$

D = 2.59 which is a physical value between 2 and 3.

To test if surface tension effects were negligible, the difference $\delta = 3(Slope+1)-2$ was determined. If $\delta < 0$, then surface tension effects were non-negligible. For this sample, δ = -0.221. Thus, surface tensions effects were significant. The number of layers of molecules determined from Eq. (3.5c) was ~4. The thickness of one layer of nitrogen molecules can be related to the size of a nitrogen molecule ~0.35 nm. Therefore, the fractal dimension D was existent over length scales of ~0.35-1.4 nm. This procedure was followed for all the catalysts studied here. It was found that surface tension effects were significant for all catalysts and thus this regime was applied to determine the surface fractal dimension.

B.3 COKED CATALYST THERMOGRAVIMETRY

Thermogravimetric analysis of the coke content of the spent sample A catalyst was performed in a SETARAM TGA92 thermogravimetric analyzer. Coked samples were heated from room temperature to 1000 °C at a rate of 5 °Cmin^{-1} in flowing dry air. The same protocol was also followed for fresh sample A.
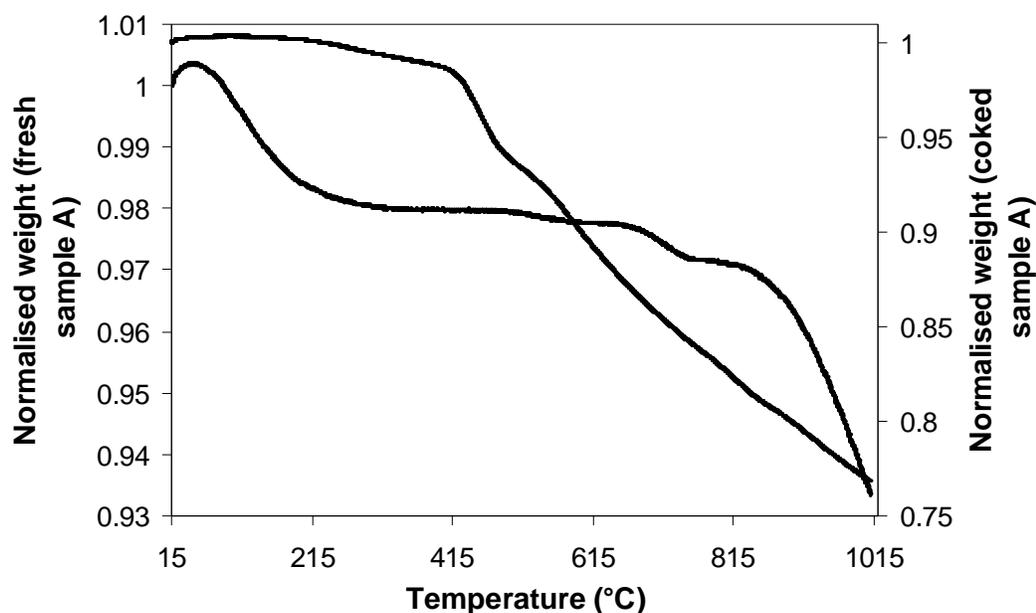
Fig. B.3.1 Thermogravimetric profile of catalyst sample A in its fresh and coked form.

The raw data presented in Fig. B.3.1 represents the change in mass of the fresh and coked catalysts as a function of increasing temperature. The lower profile belongs to the fresh catalyst while the upper profile belongs to the coked catalyst. They have been normalized to facilitate comparison. As seen in Fig. B.3.1, it was found that the fresh sample had a loss in mass once the temperature exceeded 50 °C. This is probably due to water adsorbed on the fresh catalyst. It was also found that between ~300 °C and 515 °C there was no mass loss for the fresh catalysts confirming that the sample preparation technique followed in Section 3.3 was acceptable. In contrast, for the coked catalyst, no major loss in mass was observed till the temperature exceeded 215 °C. This was likely to be due to the nature of the coke which then started burning off giving a rapid loss in mass especially after 415 °C. Since no major mass loss was observed initially, it was decided to heat the coked sample to 150 °C for more than 12 h under vacuum conditions before performing the nitrogen gas adsorption experiments. The results are presented in Fig. 3.9a. As a linear adsorption isotherm was obtained for 1 h TOS samples, a similar isotherm was also expected for 8 h TOS samples. This was confirmed by the data presented in Fig. 3.9b.

B.4 PORE SIZE DISTRIBUTION FROM MERCURY POROSIMETRY AND NITROGEN GAS ADSORPTION FOR SAMPLE B

The pore size distributions obtained from mercury porosimetry for sample B seemed to be detecting the presence of different subsets of pores. During the mercury intrusion process, no evidence of macropores was detected (see Fig. B.4.1). Mercury intrusion only detected the presence of ~10 nm pores. However, mercury extrusion detected the presence of larger pores (~80 nm). This implied that the larger pores were shielded by smaller pores. In Section 2.6, it was shown using the Rigby-Edler equations (Eq. A.2.3a and A.2.3b) that a part of the pore volume in sample B displayed reversible contact angle hysteresis. The structural hysteresis evident in the remaining pore space giving rise to entrapment was likely to be due to the connection between the large pores and small pores.
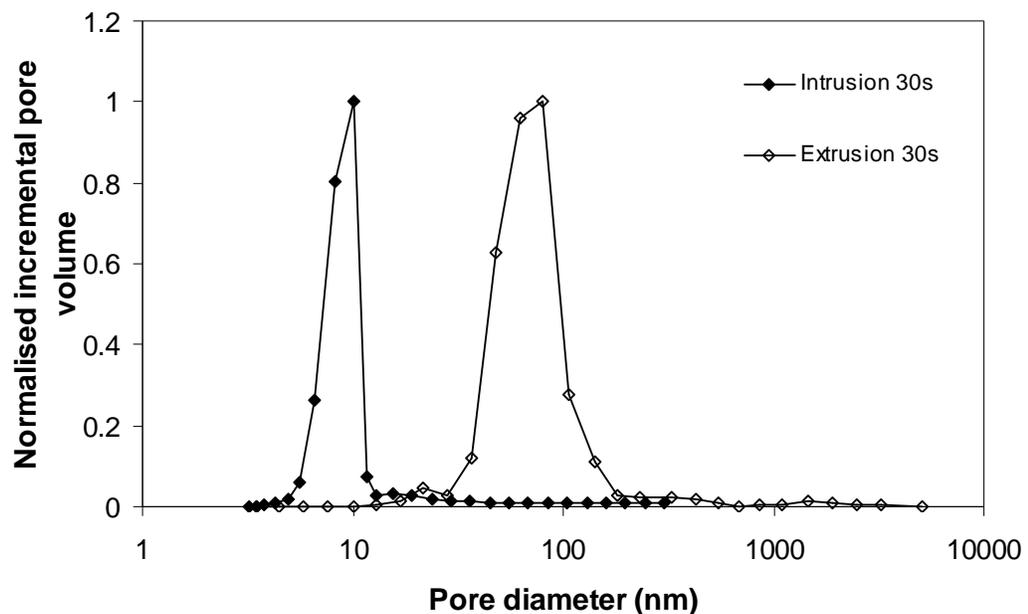
Fig. B.4.1. Incremental pore size distributions obtained from mercury intrusion and extrusion branches for sample B (whole).

There also seemed to be a match in the peaks of the BJH pore size distribution (with the film thickness defined by the Harkins-Jura equation (Eq. 3.8e)) obtained from the nitrogen desorption branch and the pores size distribution obtained from the mercury intrusion cycle as seen in Fig. B.4.2. Both desorption and intrusion processes are controlled by pore shielding or blocking effects.
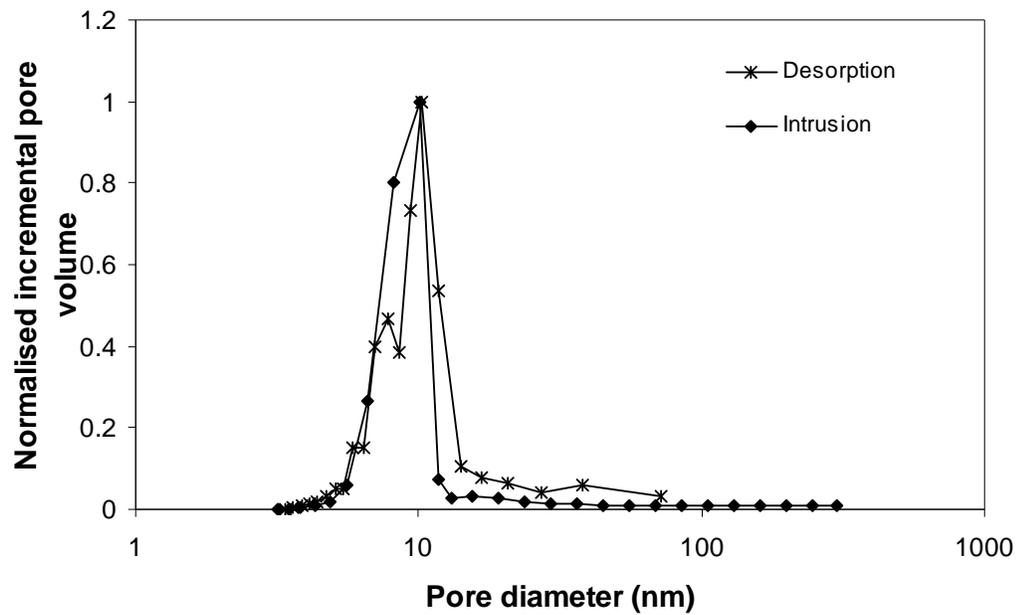
Fig. B.4.2. Incremental pore size distributions obtained from the nitrogen desorption branch and mercury intrusion process for sample B (whole).

B.5 DETERMINATION OF CONNECTIVITY AND LATTICE SIZE (SEATON, 1991)

Consider Fig. B.5.1 and first two columns of Table B.5.1 which respectively present a typical nitrogen adsorption isotherm obtained for sample A and the BJH pore size distribution data for the adsorption branch using the Harkins-Jura thickness equation (Eq. 3.8e).

Fig. B.5.1. Nitrogen adsorption isotherm obtained for sample A using an equilibration time of 90s.

212

Table B.5.1
Data required for calculating the pore connectivity Z and lattice size L using the Seaton (1991) method.

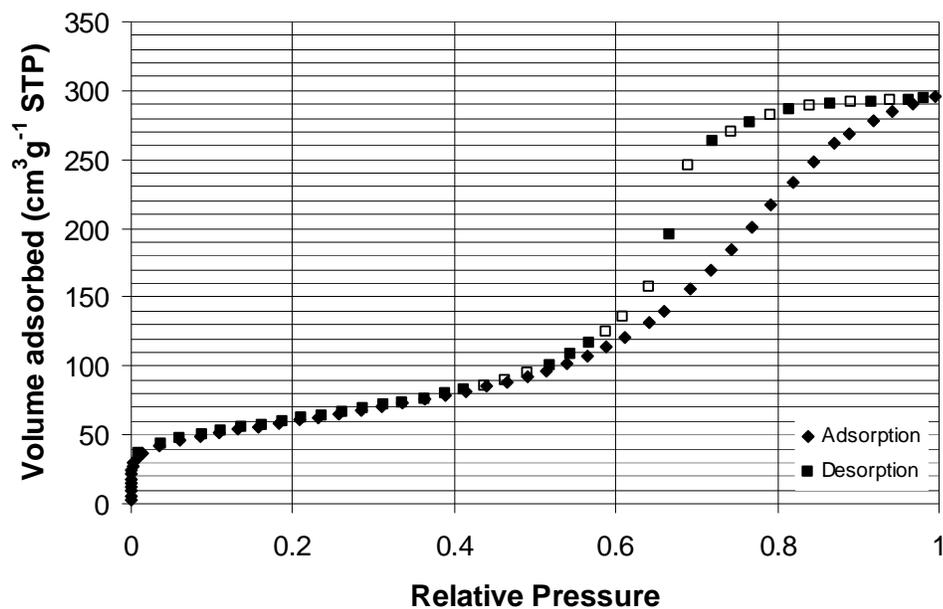| Average diameter D (nm)	Incremental pore volume V_c (cm^{3}g^{-1})	V_c/D^2	$\int(V_c/D^2)$	f	F/f	F
70.2	0.008204	1.66476E-6	1.66476E-6	0.000158577		
40.9	0.010377	6.20333E-6	7.86809E-6	0.000749475	0.230281322	0.00017259
28.5	0.010911	1.34331E-5	2.13012E-6	0.00202904		
20.8	0.019114	4.41799E-5	5.54811E-5	0.006237395	0.156719101	0.000977519
17.1	0.014512	4.96289E-5	0.00011511	0.010964798		
14.4	0.027095	0.000130666	0.000245776	0.023411425	0.142968906	0.003347106
12.2	0.030382	0.000204125	0.000449902	0.042855362		
10.6	0.034031	0.000302875	0.000752776	0.071705672	0.163191932	0.0011701787
9.4	0.034124	0.000386193	0.001138969	0.108492449		
8.4	0.03357	0.000475765	0.001614735	0.153811445	0.223950044	0.03444608
7.6	0.032908	0.000569737	0.002184471	0.208081694		
6.9	0.029614	0.000622012	0.002806484	0.264331427	0.358284939	0.095780824
6.2	0.03356	0.000873049	0.003679532	0.350493649	0.847370512	0.296997983
5.8	0.016475	0.000489744	0.004169277	0.397144218	0.914545046	0.363206277
5.3	0.022667	0.000806942	0.004976219	0.474009427		
4.9	0.013597	0.000566306	0.005542545	0.527952843	0.935374318	0.493833531
4.6	0.011153	0.000527079	0.006069604	0.57815976		
4.3	0.009412	0.000509032	0.006578636	0.626647564		
4	0.00774	0.00048375	0.007062386	0.672727141	0.988317472	0.664867988
3.8	0.006056	0.000419391	0.007481776	0.712676166	0.992973713	0.707668699
3.5	0.004947	0.000403837	0.007885613	0.75114361	0.99587112	0.748042229
3.3	0.004001	0.000367401	0.008253014	0.786140398		
3.1	0.003215	0.000334547	0.008587562	0.818007685		
2.9	0.002523	0.0003	0.00887562	0.846584167		
2.8	0.002097	0.000267474	0.009155036	0.872062434		
2.6	0.001899	0.000280917	0.009435953	0.898821181		
2.4	0.00152	0.000263889	0.0009699842	0.923957902		
2.3	0.001149	0.000217202	0.009917045	0.944648868		
2.1	0.000926	0.000209977	0.010127022	0.964648868		
2	0.000608	0.000152	0.010279022	0.979127619		
1.9	0.00047	0.000130194	0.010409216	0.991529232		
1.7	0.000257	8.89273E-5	0.010498143	1		

The ratio of the percolation probability to the bond occupation probability F/f was initially calculated from the adsorption and desorption isotherms. This was obtained for the each of desorption points that are not darkened in Fig. B.5.1 as they have a corresponding adsorption point (at the same relative pressure). The ratio is given as:

$$\frac{F}{f} = \frac{N_F - N_D}{N_F - N_A},$$

(B.5.1)

where N_F is the number of moles of nitrogen which would have been present in the pores at pressure P during the desorption experiment if no nitrogen had vaporised from the pores which contain nitrogen below its condensation pressure (i.e. at the start of desorption), N_D is the number of moles of nitrogen which are present in the pores at pressure P during the desorption experiment and N_A the is the number of moles of nitrogen which are present in the pores at pressure P during the adsorption experiment. For example, at relative pressure $P/P_0 = 0.89$:

$$\frac{F}{f} = \frac{295.2715 - 291.0871}{295.2715 - 268.5715} = 0.156719.$$

By the above procedure, as one goes down the desorption isotherm in Fig. B.5.1, F/f can be obtained as a function of P/P_0. This can then be related to the pore size by using the Kelvin equation (Eq. 3.8 with a hemispherical meniscus so that r_1 and r_2 become r) with the film thickness defined by the Harkins-Jura equation (Eq. 3.8e). The BJH pore size distribution (first two columns in Table B.5.1) can be used to calculate the bond occupation probability f. First V_c/D^2 is determined. This is then integrated, which can then be used to determine f. Each of the ratio (F/f) previously obtained are then inserted into the above table next to the respective f, as related by the pore size. Then the percolation probability F is obtained. Fig. B.5.2 presents the percolation probability F as a function of the bond occupation probability f.

The scaling relation (Eq. 3.9) was then taken; the terms on the LHS and RHS of the equality were evaluated using the obtained percolation and bond occupation probabilities, i.e. F and f. A plot of $\left[(Zf - 3/2)L^{1/\nu}\right]$ vs. $L^{\beta/\nu}ZF$ provided the experimental scaling relation for sample A. The theoretical generalised scaling relation was generated using the data given in Fig. 8 of Seaton (1991) who used the simulation data of Kirkpatrick (1979, cited by Seaton 1991, p.1899). The values of the terms on the x and y axes are provided in Table B.5.2. The best fit was then obtained by fitting the experimental scaling data (f, F) to the generalised scaling relation h, given by Eq. (3.9), between f and F. It is this fit that is presented in Fig. 3.8.
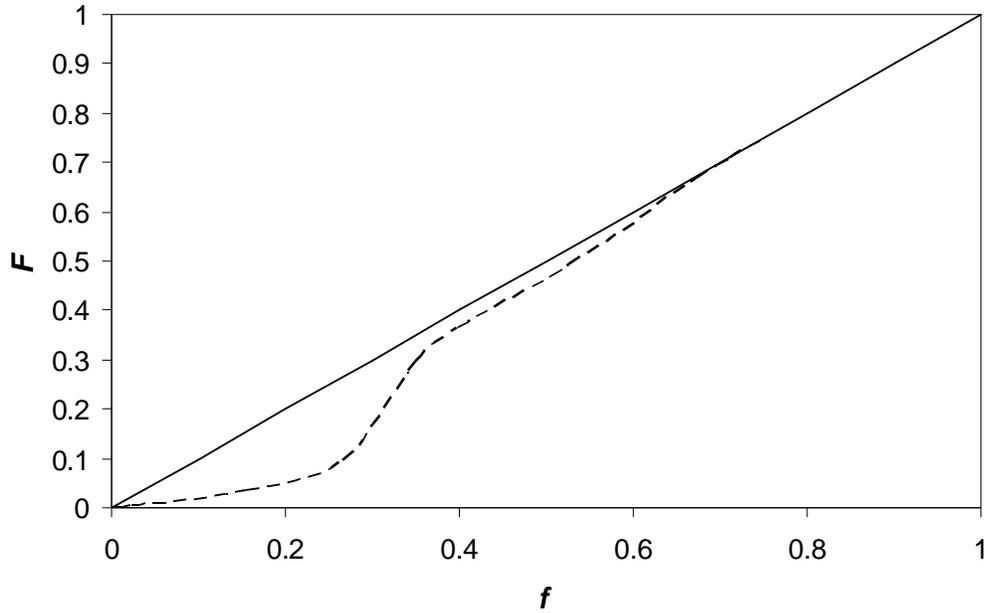
Fig. B.5.2. Percolation probability F as a function of the bond occupation probability f for sample A (whole).

Table B.5.2
Theoretical data that describe the generalised scaling function from Fig. 8 in Seaton (1991), who used the simulation data of Kirkpatrick (1979, cited by Seaton 1991, p.1899).

$L^{\beta/\nu}ZF$	$(Zf-3/2)L^{1/\nu}$
0.271186	-7.5
0.40678	-5
0.508475	-3.75
0.881356	-2.5
1.288136	-1.25
2	0
2.83333	1.25
3.7	2.5
4.241379	3.75
4.724138	5
5.137931	6.25
5.5517	7.5
5.896552	8.75
6.237288	10
6.77966	12.5
8.2712	20

P. S. The details of the quoted references can be seen in the **REFERENCES** section in Chapter 3 (and Chapter 2).

APPENDIX C – SUPPORTING INFORMATION FOR INTEGRATED N_2-H_2O-N_2 ADSORPTION EXPERIMENTS

This appendix contains extra supporting information for experiments conducted using the integrated N_2-H_2O-N_2 adsorption experiments.

C.1 THERMOGRAVIMETRY

Thermogravimetric analysis of the coke content of the spent sample investigated in Chapter 4 was performed using a SETARAM TGA92 thermogravimetric analyzer. Coked samples were heated from room temperature to 1000 °C at a rate of 1 °Cmin^{-1} in flowing dry air. A similar protocol was also followed for fresh sample A except that the temperature was ramped at 5 °Cmin^{-1}.
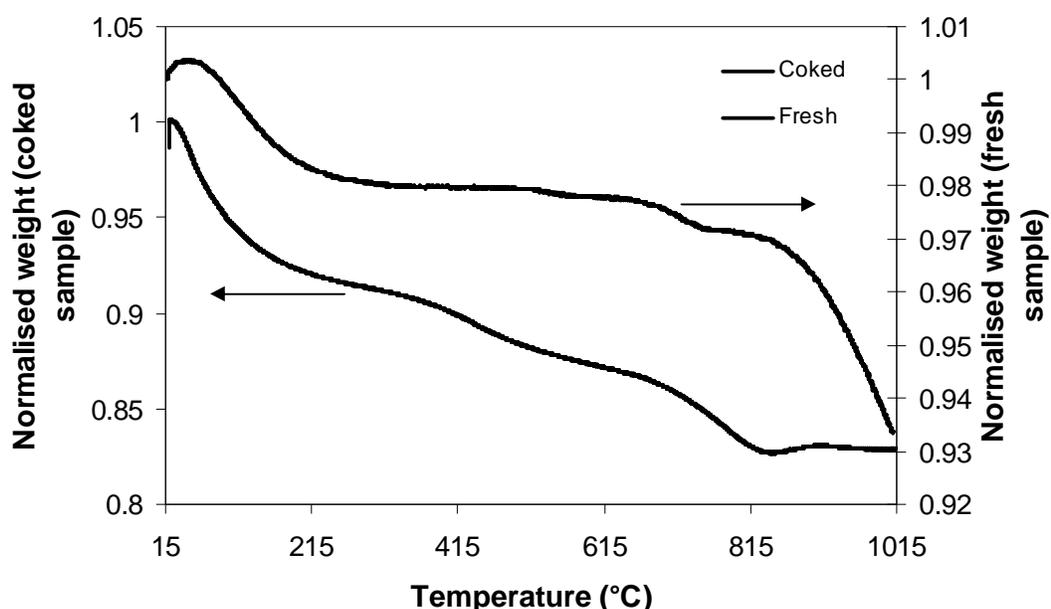

Fig. C.1.1. Thermogravimetric profile of the fresh and coked samples investigated in Chapter 4.

The raw data presented in Fig. C.1.1 represents the change in mass of the fresh and coked catalysts as a function of increasing temperature. The upper profile belongs to the fresh catalyst while the lower profile belongs to the coked catalyst. They have been normalized to facilitate comparison. As seen in Fig. C.1.1, it was found that the fresh sample had a loss in mass once the temperature exceeded 50 °C. This is probably due to water adsorbed on the fresh catalyst. It was also found that between ~300 °C and 515 °C there was no mass loss for the fresh catalysts confirming that the sample

preparation technique followed in Section 4.3 was acceptable. In contrast, for the coked catalyst, mass loss was observed once the temperature exceeded 30 °C and continued even when the temperature exceeded 800 °C. However, the mass loss subsided as the temperature reached 900 °C and thereafter there was no mass loss. The loss in mass over such a large temperature range was likely to be due to the nature of the coke deposits. Since there was a loss in mass initially, it was decided to only heat the coked sample to 150 °C for 12 h under vacuum conditions before performing the nitrogen gas adsorption experiments. This would ensure that there would not be any water vapour present on the catalyst surface when nitrogen adsorption was performed on the coked samples. Further, a rough estimate of the amount of coke present in the sample was determined using the following relation:

$$Coke\% = \left(\frac{w_{150} - w_{1000}}{w_{1000}}\right)100, \tag{C.1.1}$$

where w_{150} and w_{1000} are the respective weights of the sample at 150 and 1000 °C. Taking these amounts from Fig. C.1.1 and substituting them in Eq. (C.1.1) gives the percentage coke content:

$$Coke\% = \left(\frac{28.46 - 25.31}{25.31}\right)100 = 12.45\% .$$

C.2 PYCNOMETRY

The AccuPyc 1330 gas displacement pycnometer was used to determine the porosity of the fresh sample A. The pycnometer determines the density and volume by measuring the pressure change of helium[38] in a calibrated volume. Initially, the empty sample cup weight was noted. The cup was filled to at least $\frac{2}{3}$ of its capacity with dried sample, following which the cup was again weighed to determine the sample weight. The cell chamber cap was removed so as to insert the sample cup containing the sample. The cell chamber cap was then replaced and the analysis parameters were set. 10 purges were performed and 20 runs were conducted to determine the average skeletal density of the sample which was 3.4094 gcm^{-3}. The pore volume of sample A was determined by nitrogen gas adsorption to be 0.47 cm^{3}g^{-1} in Chapter 3. Therefore, the porosity ε of sample A is $0.47/((1/3.4094) + 0.47) = 0.62$.

---

[38] Helium gas was sourced from BOC.

C.3 EVALUATION OF THE PROPORTIONALITY CONSTANT IN THE KELVIN EQUATION

The Kelvin equation given earlier in Eq. (3.8) in Section 3.1.5 relates the relative pressure and the pore size. It is expressed as follows:

$$\ln\left(\frac{P}{P_0}\right) = -\frac{\gamma V_M}{RT}\left(\frac{1}{r}\right), \tag{C.3.1}$$

for a cylindrical pore (with a cylindrical film of adsorbate). The proportionality constant in Eq. (C.3.1) is $\frac{\gamma V_M}{RT}$ where γ is the surface tension, V_M is the molar volume, R is the ideal gas constant and T is temperature. This constant can be evaluated for nitrogen and water adsorption by substituting the respective values available from the literature. For nitrogen, γ is 8.85×10^{-3} Nm^{-1}, V_M is 34.68 cm^{3}mol^{-1}, R is 8.31451×10^6 Pacm^{3}mol^{-1}K^{-1} and T is 77 K (Lowell et al., 2006). Substituting these values in Eq. (C.3.1) gives:

$$\ln\left(\frac{P}{P_0}\right)_{N_2} = -\frac{\left(8.85 \times 10^{-3}\right)\left(34.68\right)}{\left(8.31451 \times 10^6\right)\left(77\right)}\left(\frac{1}{r}\right), \tag{C.3.1a}$$

$$\ln\left(\frac{P}{P_0}\right)_{N_2} = -\frac{4.794 \times 10^{-10}}{r}.$$

On the other hand, for water, γ is 71.97×10^{-3} Nm^{-1} (Washburn, 1926 - 1930; 2003), V_M is 18 cm^{3}mol^{-1} (Wypych, 2008), R is 8.31451×10^6 Pacm^{3}mol^{-1}K^{-1} and T is 298 K. Substituting these values in Eq. (C.3.1) gives:

$$\ln\left(\frac{P}{P_0}\right)_{H_2O} = -\frac{\left(71.97 \times 10^{-3}\right)\left(18.05\right)}{\left(8.31451 \times 10^6\right)\left(298\right)}\left(\frac{1}{r}\right), \tag{C.3.1b}$$

$$\ln\left(\frac{P}{P_0}\right)_{H_2O} = -\frac{5.244 \times 10^{-10}}{r}.$$

Dividing Eq. (C.3.1b) and Eq. (C.3.1a) gives:

$$\frac{\ln\left(\frac{P}{P_0}\right)_{H_2O}}{\ln\left(\frac{P}{P_0}\right)_{N_2}} \sim 1.$$

P. S. The details of the quoted references can be seen in the **REFERENCES** section in Chapter 4.

APPENDIX D – SUPPORTING INFORMATION FOR LLE EXPERIMENTS

This appendix contains extra supporting information that the reader may find beneficial in understanding the LLE experiments performed on materials – G1 and Pt-E1 (fresh and coked).

D.1 BULK DIFFUSION – CYCLOHEXANE AND WATER

The bulk diffusion coefficient of cyclohexane and water at 298 K was determined by performing PFG NMR experiments with only cyclohexane or water in its bulk form in the NMR tube (see Figs. D.1.1 and D.1.2). The linear diffusion attenuation plots indicate that cyclohexane and water molecules are in the free diffusion regime. The bulk diffusion coefficient of cyclohexane and water are obtained from the slope of the straight line fits. They are $1.511 \pm 0.007 \times 10^{-9}$ m^2s^{-1} and $2.540 \pm 0.013 \times 10^{-9}$ m^2s^{-1} respectively.
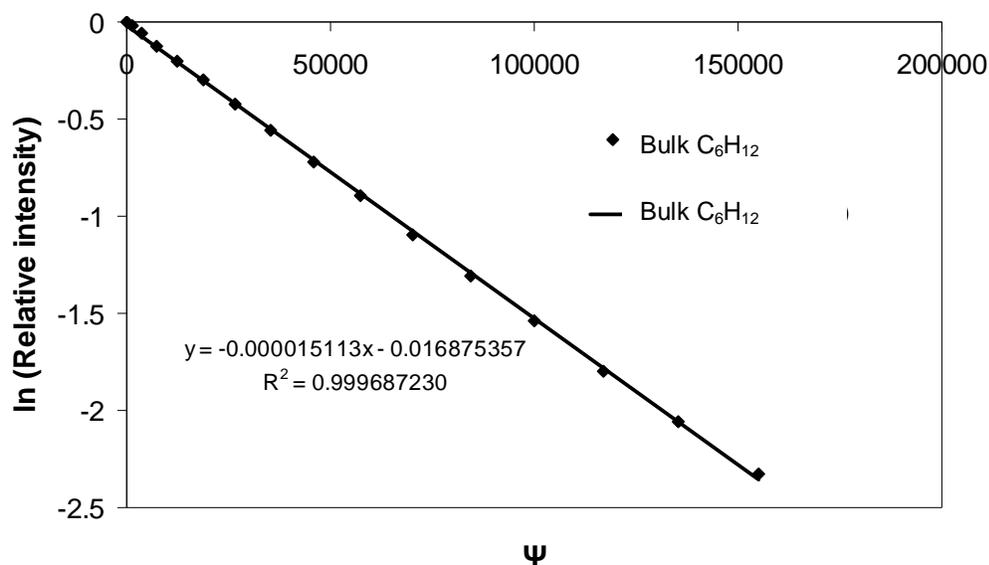

Fig. D.1.1. NMR diffusion data for bulk cyclohexane at 298 K. A linear graph implies molecules are experiencing the free diffusion regime.
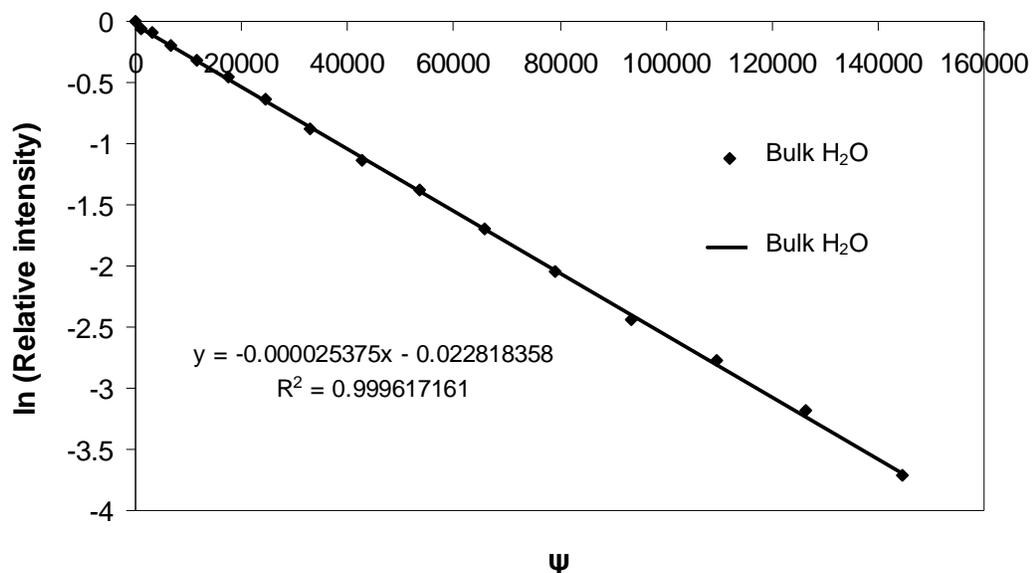
Fig. D.1.2. Raw NMR diffusion data for bulk water at 298 K. A linear graph implies molecules are experiencing the free diffusion regime.

Similar straight line fits yield the pore diffusion coefficients of cyclohexane and water (for the data presented in Fig. 5.12 and 5.13). The tortuosity factor τ was then determined from the ratio D_b/D_p, where D_b is the bulk diffusion coefficient and D_p is the diffusion coefficient within the pore.

D.2 DATA REPRESENTATION – Pt-E1 (FRESH AND COKED)

The water fraction present in the catalyst was used as the abscissa in Figs. 5.18 and 5.21. This was obtained from Fig. D.2.1 and Fig. D.2.2. They represent ^{1}H NMR spectra that contain peaks for water and cyclohexane stacked together. The coked catalyst is from batch ISO_014. In both figures, the first spectrum on the nearer side contains only one peak and belongs to cyclohexane. Once water seeps into the catalyst, the intensity of the cyclohexane peak reduces due to its displacement by water. The water intensity therefore grows gradually eventually kicking (displacing) out all the cyclohexane. The water content presented in Figs. 5.18 and 5.21 in Section 5.4.2 can be obtained by integrating the water peaks. Since the time for LLE or displacement varies for different catalysts, water content as determined from ^{1}H NMR intensity was used as the abscissa. The protocol while running the experiment was to first obtain a ^{1}H NMR spectrum and then perform a relaxometry or diffusion experiment followed by another ^{1}H NMR spectrum. The initial and final ^{1}H NMR spectrum can be superimposed to see any changes in experimental conditions. They were found to be coincident in all of the work discussed in this thesis. An example for

220

the similar proton spectra obtained for the coked catalyst is presented in Fig. D.2.3. The similarity in the proton spectra indicates that there is no evidence of coke dissolution during the experiment. The spectra were obtained initially when the catalyst contained only cyclohexane (i.e. before introducing water vapour into the system).
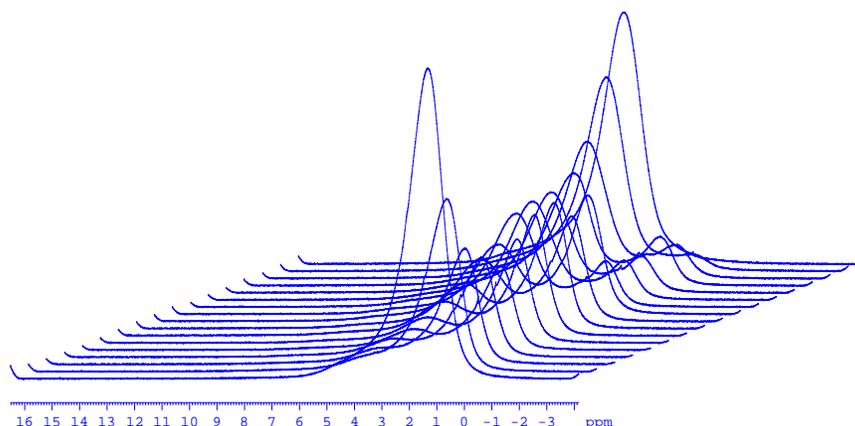

Fig. D.2.1. ^{1}H NMR spectra obtained for the fresh catalyst Pt-E1 shown in Fig. 5.18 and Fig. 5.21 in Section 5.4.2.
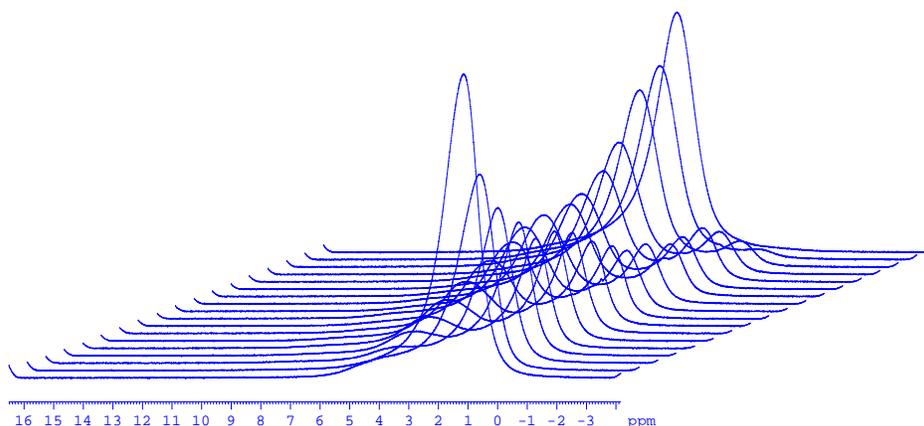

Fig. D.2.2. ^{1}H NMR spectra obtained for the coked catalyst Pt-E1 shown in Fig. 5.18 and Fig. 5.21 in Section 5.4.2.

Raw T_2 relaxometry data for water and cyclohexane within fresh and coked catalysts Pt-E1 were obtained after fitting a mono-exponential decay equation as given by:

$$I = I_0 e^{-t/T_2} + C .$$
(D.2.1)

The fitting was performed using the non-linear curve fitting program available in Origin 6.1. The mono-exponential fits provided the T_2 relaxation time constants presented in Figs. 5.18, 5.19, 5.21, 5.22 and 5.23.
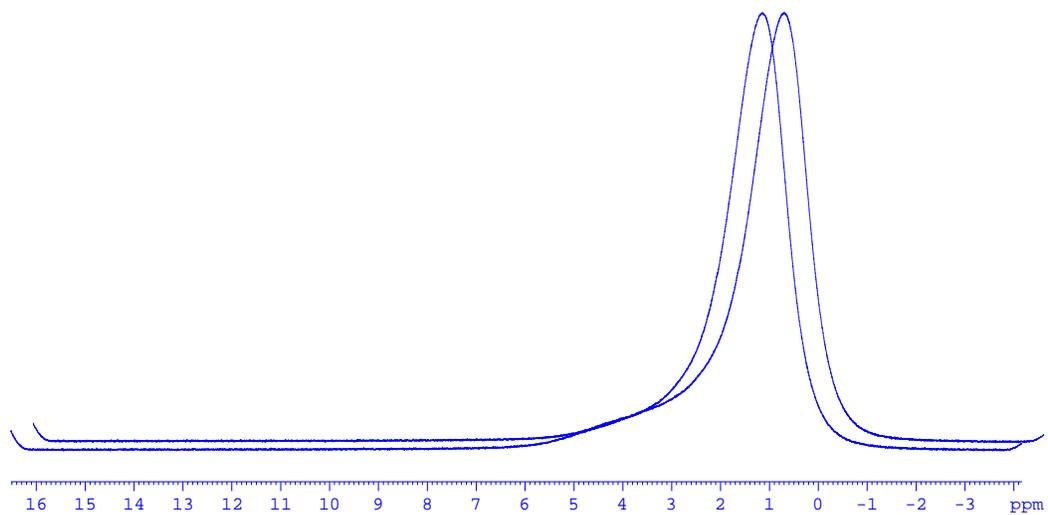
Fig. D.2.3. ^{1}H NMR spectra of cyclohexane phase obtained before and after a cyclohexane T_2 relaxation experiment for the coked catalyst Pt-E1 shown in Fig 5.18 and Fig 5.21. The similarity of spectra indicates that there is no dissolution of coke in the timescale of the experiment.